

Design, Testing and Simulation of GFRP Cruciform Test Specimen in Biaxial Fatigue



4th SEMESTER
DMS4 - 2.209A
FIBIGERSTRÆDE 16
DESIGN OF MECHANICAL SYSTEMS
AALBORG UNIVERSITY
10th OF JUNE 2014

Faculty of Engineering
and Science
Fibigerstræde 16
DK - 9220 Aalborg Øst
Tlf. 99 40 93 09
swe@me.aau.dk
www.industri.aau.dk

Title:

Design, Testing and Simulation of GFRP
Cruciform Test Specimen in Biaxial Fa-
tigue

Semester: 4

Semester theme: Master Thesis

Project period:

03/02-2014 - 10/06-2014

ECTS: 30

Supervisors:

Lars Chr. T. Overgaard &
Jens Ammitzbøll Glud

Project group: DMS4-2.209A

Jens Jakob Bender

Nikolai Kirkensgaard Grishauge

Søren Voldby Pedersen

Copies: 6

Number of pages: max. 99

Appendix: 72

Synopsis:

This project contains design, testing and simulation of a GFRP cruciform specimen subjected to biaxial fatigue. A study of state-of-the-art literature is conducted, where previous designs of cruciform specimens subjected to biaxial fatigue are studied. A specimen geometry and lay-up optimization is conducted in MATLAB which interacts with a solid FE model in ANSYS, wherein a gauge zone is embedded into the specimen with a predefined lay-up, specified by Siemens Wind Power A/S.

Designed specimens are tested in biaxial fatigue at different stress levels until failure occurs in the gauge zone. Video camera, DIC and strain gauges are utilized to monitor failure during the fatigue tests.

A state-of-the-art fatigue life prediction algorithm, called FADAS, is implemented into an ANSYS programmable subroutine. The algorithm involves a progressive strength degradation, Puck's failure criteria and a stiffness degradation in order to estimate fatigue life of FRP. FADAS is utilized on an FE shell model of the designed specimen. Simulations of the fatigue test are conducted in order to verify if the FADAS algorithm can predict the fatigue life of these.

It is concluded that this version of the implemented FADAS algorithm can not estimate fatigue life within an acceptable tolerance.

By signing this document every group member confirms that everyone has participated equally in the project work, and everyone hereby are responsible for the content of this report.

Resume

Dette projekt indeholder design, test og simulering af GFRP krydsformede testemner udsat for bi-aksial udmattelse.

Ud fra den nyeste litteratur, omhandlende bi-aksial udmattelsetests, undersøges forskellige typer af krydsformede emner udsat for bi-aksial udmattelse. Fordeler og ulemper undersøges og ud fra disse medtages erfaring i designet af et testemne. Følgende emner er berørt i designet af testemnet; overordnet geometri, udformning af måleområde på testemnet samt implementering af stivhedsovergange (ply drops).

Testemnet er designet ud fra ovenævnte erfaringer fra litteraturen samt en geometri-og oplægsoptimering hvori der er implementeret et måleområde i testemnet som har et fastlagt GFRP-oplæg, specificeret af Siemens Wind Power A/S. Optimeringen er anvendt til at opnå et optimum i forbindelse med ydre geometri, som omhandler diameter størrelse samt placering på rundinger mellem armene. Derudover optimeres GFRP-oplægget som omhandler tykkelser på de enkelte tilførte lag ud over det i forvejen implementerede oplæg for måleområdet. Målet med optimeringen er at testemnerne skal fejle i måleområdet under bi-aksial udmattelse. Optimeringen er udført med en af MATLAB's indbyggede optimeringsalgoritmer som interagerer med en solid finite element (FE) model lavet af testemnerne i ANSYS.

Det er ud fra litteraturen og på baggrund af intuitiv forståelse samt måden hvor på testemnerne skal produceres (VARTM), bestemt at anvende interne "ply drops" i testemnerne. Der er fundet et optimum ud fra geometri- og oplægsoptimeringen hvorudfra arbejdstegninger udarbejdes således testemnerne kan produceres af Siemens Wind Power A/S. De producerede testemner tilpasses efterfølgende af projektgruppen således de passer i den anvendte testmaskine hvori de bliver udsat for bi-aksial udmattelse.

Inden udmattelses test igangsættes, bestemmes den statiske styrke vha. et testemne, der overrides ved at øge den bi-aksiale pålagte last kontinuert. Ud fra den statiske bestemte styrke af testemnet bestemmes et "setup" for de efterfølgende udmattelsestest. Disse udføres ved forskellige spændingsniveauer idet glasfibrene i måleområdet af testemnerne udsættes for et specifikt tøjningsforhold, specificeret af Siemens Wind Power A/S. Udmattelsestest monitoreres vha. Digital Image Correlation (DIC), strain gauge samt almindeligt video kamera. En af de nyeste udmattelsesalgoritmer inden for FRP området, kaldet "FAtigue DAmage Simulator (FADAS)" er implementeret i en programmerbar subrutine til ANSYS, skrevet i programmeringssproget FORTRAN. Udmattelsesalgoritmen er anvendt på en FE lagopdelt skal-model lavet af testemnerne i ANSYS, hvormed de førsttalte udmattelsestest simuleres.

FADAS udmattelsesalgoritmen indeholder styrkedegradering, Pucks fejl kriterier samt stivhedsdegradering, og disse evalueres i hvert enkelt lag af skal-modellen for hvert enkelt element. Styrkedegraderingen er afhængig af antallet af udmattelsesgentagelser, Pucks fejlkriterier anvendes til bestemmelse af om der forekommer fejl og hvilken fejltype der er tale om, og ud fra fejlkriteriets størrelse og type degraderes stivheden af det enkelte lag i det enkelte element i FE modellen.

Test og simuleringer er sammenlignet for at verificere om FADAS algoritmen kan estimere levetiden på GFRP emner udsat for bi-aksiale laster. Det konkluderes at afvigelsen på algoritmen

er for stor til, at den kan bruges som et egentligt design værktøj i forbindelse med udmattelse, men der kan opnås en nogenlunde forståelse for hvordan fejltyperne interagerer.

Preface

This report serves to document the work of group DMS4-2.209A from the Department of Mechanical and Manufacturing Engineering at Aalborg University in the period 03/02/2014 - 10/06/2014. This report concludes the master thesis program stated in Curriculum for the Master's Program in Design of Mechanical Systems.

A special thanks is given to Design Engineer at Siemens Wind Power A/S and former Ph.D student at Aalborg University Steffen Laustsen who has supported the project group with knowledge regarding the used test equipment in the project. Siemens Wind Power A/S has delivered test specimens and GFRP material properties which is gratefully acknowledged.

Reading guide

The report is written using American English spelling. Source references in the report are made using the Harvard method [Surname, Year]. The bibliography is placed at the end of the report. If a source is used for an entire chapter, the source is mentioned in the start of the chapter.

Headlines, equations, tables, and figures are numbered. Headlines are in the format x.y.z; x representing the number of the chapter, y representing the number of the section, and z representing the number of the subsection. Equations, tables and figures are in the format x.w; x representing the number of the chapter and w representing a consecutive number throughout the chapter. Symbols and units used in the report are defined in the respective sections.

All quotes are written in italic together with quotation marks and a source reference.

The report is written such that it can be read without additional material, but in the back of the report an appendix and CD are available, in which clarifications and further work are accessible. Throughout the report references to the appendix and CD are made. The CD contains an electronic version of this report, FE models, working drawings and FORTRAN files including a guide to implement the material routine in ANSYS.

Content

Part I Introduction to Biaxial Tests and Design of GFRP Test Specimen	1
Chapter 1 Introduction	3
1.1 Cooperation with Siemens Wind Power	4
1.2 Terminology	4
1.3 Requirements	8
1.4 Project Clarification	8
Chapter 2 Specimen Design	11
2.1 State-of-the-art Cruciform Test Specimens	11
2.2 Specimen Geometry	12
2.3 Finite Element Modeling	15
2.4 Geometry and Lay-up Optimization	16
2.5 FE Solid Model	23
2.6 Sub-Conclusion	24
Part II Fatigue Test	25
Chapter 3 Procedure for Fatigue Test	27
3.1 Test Equipment	28
3.2 Adaptation of SWP Manufactured Specimen	30
Chapter 4 Static Pilot Test	33
4.1 Static Test of Specimen	33
4.2 Camera Observations	34
4.3 Failure Mode Investigation	35
4.4 Measurements	38
4.5 Comparison	45
Chapter 5 Fatigue Tests	49
5.1 General Setup for Fatigue Tests	49
5.2 Fatigue Test 1	50
5.3 Fatigue Test 2	55
5.4 Fatigue Test 3	57
5.5 Fatigue Test 4	60
5.6 Fatigue Test Summary	61
Part III Simulation of Fatigue Test	63
Chapter 6 Introduction to FADAS	65
Chapter 7 Failure Criteria	67

CONTENT

7.1 Fiber Failure (FF)	68
7.2 Inter Fiber Failure (IFF)	69
Chapter 8 FADAS Implementation	73
8.1 Initial Strength Initial Stiffness	74
8.2 Constitutive Equations	74
8.3 Cycles to Failure	75
8.4 Update Palmgren-Miner Coefficient	76
8.5 Cycle Jump Procedure	77
8.6 Strength Degradation	78
8.7 Failure Calculations	78
8.8 Stiffness Degradation	79
Chapter 9 Validation of FADAS algorithm	81
9.1 Validation of Stress-Strain Relation	81
9.2 Validation of Strength Degradation	82
9.3 Comparison of FADAS Algorithm to Coupon Tests	84
9.4 Sub-Conclusion	85
Chapter 10 Simulation of Fatigue Tests	87
10.1 Simulation of FT1	87
10.2 Simulation of FT2	93
10.3 Simulation of FT3	95
10.4 Simulation of FT4	97
10.5 Sub-Conclusion	98
Part IV Closure	99
Chapter 11 Conclusion	101
Chapter 12 Future Work	103
Bibliography	105
Part V Appendix	1
Appendix A Specimen Manufacturing	3
A.1 Manufacturing Process	3
A.2 Gained Experience regarding the manufacturing process	4
A.3 Sources of Error Due to Manufacturing Process	5
Appendix B Finite Element	9
B.1 The Solid Model	10
B.2 The Shell Model	13
B.3 Comparison of the Solid and Shell Model	15

B.4 Validation of FE Shell Model	18
B.5 Properties	22
B.6 Validation of BIAX Ply	24
B.7 Convergence Study	26
B.8 Force and Stress Distribution in Specimen	29
B.9 Calculations of Bolt Connections	32
Appendix C Test Results	35
C.1 Static Pilot Test	36
C.2 Fatigue Test 1	38
C.3 Fatigue Test 2	40
C.4 Fatigue Test 3	42
C.5 Fatigue Test 4	46
Appendix D Experimental Log	51
D.1 Asynchronous Load Configuration	52
D.2 Mounting Plates for Secondary Direction	52
D.3 Bolt Failure in Bushing	53
D.4 Arm Failure	54
D.5 Changing the Suspension System for the Secondary Actuator	56
D.6 Rod End Failure	56
D.7 DIC Data for the Secondary Directions	58
D.8 Strain Gauge Configuration	61
Appendix E Specifications for Measurement Equipment	63
E.1 Test Rig	64
E.2 Video Camera	64
E.3 Strain Gauge	65
E.4 DIC	67
E.5 Thermal Camera	69
E.6 Thermocouple	70
Appendix F Working Drawings	71
F.1 Specimen Geometry	72
F.2 Specimen Ply Drop Boundaries	73
F.3 Ply Drop Specifications	74
Appendix G CD	75

Nomenclature

Symbol:	Description:	Unit:
C	Optimization parameter, $(0.34 - R_{strain})$	[\cdot]
$D_{j,l}$	Palmgren-Miner Coefficient	[\cdot]
E_{f1}	Stiffness of fiber material	[GPa]
$N1$	Current guess for number of cycles for failure	[\cdot]
$N2$	Resulting guess for number of cycles for failure	[\cdot]
N_i	Number of cycles for failure at the i 'th stress level	[\cdot]
$R_{\perp\perp}^A$	Fracture resistance of the fracture plane against $\tau_{\perp\perp}$	[MPa]
R_{\perp}^c	Fracture resistance of the fracture plane against σ_{\perp}^c	[MPa]
R_{\perp}^t	Fracture resistance of the fracture plane against σ_{\perp}^t	[MPa]
R_{CL1}	R_{CL} for the first set of S-N data used in the numeric determination of N_i	[\cdot]
R_{CL2}	R_{CL} for the second set of S-N data used in the numeric determination of N_i	[\cdot]
R_{CL}	Cyclic load ratio between minimum and maximum load in each direction	[\cdot]
R_{Load}	Ratio between secondary and primary load	[\cdot]
$R_{Opti,load}$	Ratio between secondary and primary load used in the optimization	[$\%$]
R_{int1}	Dependent variable used in the numeric determination of N	[\cdot]
R_{int2}	Dependent variable used in the numeric determination of N	[\cdot]
R_{int}	Dependent variable used in the numeric determination of N	[\cdot]
R_{strain}	Ratio between ε_x and ε_y in gauge zone	[\cdot]
$S1$	Maximum stress amplitude in the expression for the first set of S-N data used in the numeric determination of N_i	[MPa]
$S2$	Maximum stress amplitude in the expression for the second set of S-N data used in the numeric determination of N_i	[MPa]
S_{21r}	Residual shear strength	[MPa]
$S_{MAX,Fillet}$	Failure index at the fillet corner determined using maximum stress failure criteria	[\cdot]
$S_{MAX,GZ}$	Failure index in the gauge zone determined using maximum stress failure criteria	[\cdot]
$S_{MAX,Pri-Arm}$	Failure index in primary arm determined using maximum stress failure criteria	[\cdot]

Continued on next page

NOMENCLATURE

Symbol:	Description:	Unit:
$S_{MAX,Sec-Arm}$	Failure index in secondary arm determined using maximum stress failure criteria	[\cdot]
Δn	The number of cycles jumped in the FADAS algorithm	[\cdot]
η_r	Factor representing a small remaining stiffness	[\cdot]
η	Factor to determine stiffness degradation after IFF	[\cdot]
γ_{12}	In-plane shear strain	[\cdot]
ν_{12}	Poisson's ratio of lamina	[\cdot]
ν_{f12}	Poisson's ratio of fiber material	[\cdot]
$\sigma_{j,l_{max}}$	Maximum stress	[MPa]
σ_{max}	Maximum stress in cyclic loading	[MPa]
σ_{min}	Minimum stress in cyclic loading	[MPa]
τ_{21c}	Shear stress at the 'turning point' of the fracture envelope	[MPa]
τ_{21}	Shear stress parallel to the fiber direction, acting on a plane perpendicular to the transverse direction	[MPa]
θ_{fp}	The angle of the fracture plane	[\cdot]
ξ	Parameter used to fit η -curve to experimental data	[\cdot]
c_{Puck}	Parameter used to fit η -curve to experimental data	[\cdot]
d_{fillet}	Diameter of the fillet corner used in the optimization	[$m \cdot 10^{-3}$]
$f_{E(IFF)}^A$	Stress exposure factor for IFF mode A	[\cdot]
$f_{E(IFF)}^B$	Stress exposure factor for IFF mode B	[\cdot]
$f_{E(IFF)}^C$	Stress exposure factor for IFF mode C	[\cdot]
$f_{E(FF)}$	Stress exposure factor for FF	[\cdot]
$f_{E(IFF)}$	Stress exposure factor for IFF	[\cdot]
$fval$	Objective function value	[\cdot]
j	Subscript to indicate tension (t) or compression (c)	[\cdot]
$k1$	Exponent in the expression for the first set of S-N data used in the numeric determination of N_i	[\cdot]
$k2$	Exponent in the expression for the second set of S-N data used in the numeric determination of N_i	[\cdot]
k_{weight}	Weighting factor in the objective function	[\cdot]
k	Sudden death eksponent	[\cdot]
l	Subscript to indicate direction, parallel (p) or transverse (t) to fibers or shear (s)	[\cdot]

Continued on next page

Symbol:	Description:	Unit:
$m_{\sigma,f}$	Fiber/Matrix interface stress magnification factor	[\cdot]
n_i	Number of simulated cycles at the i 'th stress level	[\cdot]
t_{BIAX}	Total thickness of the BIAX layer group in the arms used in the optimization	[$m \cdot 10^{-4}$]
t_{UD_0}	Total thickness of the UD ₀ layer group used in the optimization	[$m \cdot 10^{-4}$]
$t_{UD_{90}}$	Total thickness of the UD ₉₀ layer group used in the optimization	[$m \cdot 10^{-4}$]

Part I

INTRODUCTION TO BIAXIAL TESTS AND DESIGN OF GFRP TEST SPECIMEN

Introduction

1

Composite materials are used in more and more applications in the automobile, airplane and wind turbine industries. In the automobile industry car bumpers have been made of composites for many years and nowadays BMW has constructed a composite chassis for the BMW i3 model [Miel, 2013]. Composite parts together with metals etc. have been used for decades in airplanes. The trend shows an increase in the number of composite parts in new designed airplanes, which can be seen in the Boeing 787, where composite parts contribute 50 [%] to the total structural weight of the airplane [Freissinet, 2011]. In manufacturing and design of wind turbine blades, monolithic- and sandwich laminated composites have been used as the only structural components for decades.

Some of the main topics concerning structural parts these days, are performance and production cost. The performance needs to be as high as possible, but at the same time keeping the production cost as low as possible. This also applies to structural monolithic- and sandwich laminated composite parts. To ensure that no failure occurs in these materials it is necessary to determine the material properties, this is done through static and fatigue tests. Different types of tests are conducted, involving scaled coupon tests (from lamina to laminate level) to full scale tests. Not only the material properties are determined, but also the failure modes. The failure modes express the different ways in which a composite material can fail. Depending on the load conditions and the failure type, the material can maintain some of its load carrying capabilities after failure. The different modes considered in this project are described in detail in Chapter 7 on page 67.

To estimate whether or not a designed component can withstand its time of operation, a life time estimation is performed. The life time estimation is performed with the use of an S-N curve, which can be created by employing a fatigue model. A general approach for life time estimation for anisotropic materials does not exist, since these are more complicated than what is known for isotropic materials, thus numerous fatigue models are created in an attempt to estimate the reality. The fatigue models can be divided into three groups: Empirical models, Phenomenological models and Mechanistic models. [V.A. Passipoulaeridis, P. Brøndsted, 2009]

Empirical models are considered models that introduce a damage parameter with no physical interpretation as a means of accumulating fatigue damage until total failure of the material occurs [V.A. Passipoulaeridis, P. Brøndsted, 2009]. These fatigue models use approaches similar to what is used for isotropic materials, thus the Palmgren-Miner Linear Damage Rule is widely used for empirical models.

The phenomenological models differ from the empirical models, because these try to correlate physically measurable quantities such as stiffness and/or strength into the fatigue damage of the material. Experimental parameters have to be determined before phenomenological fatigue models can be employed [V.A. Passipoulaeridis, P. Brøndsted, 2009].

Mechanistic models are complex compared to empirical and phenomenological models, because

these take the actual fatigue damage of the material into account. This yields that the mechanistic fatigue models are computationally heavy. Due to their complexity they can only be employed for simple laminate structures and load conditions, since they are not fully developed today. The theoretical advantage of mechanistic models is the ability to predict life time with only a minor amount of parameters determined experimentally [V.A. Passipoularidis, P. Brøndsted, 2009]. The fatigue model used in this project falls somewhere in between the phenomenological- and mechanistic models, which is described in Chapter 6 on page 65.

1.1 Cooperation with Siemens Wind Power

This project is established in cooperation with Siemens Wind Power (SWP) in Aalborg, where the Blade department is located. SWP has produced blades in Glass Fiber Reinforced Polymers (GFRP) for more than two decades.

A lack of accuracy is present in the current fatigue life prediction methods for laminated GFRP materials at SWP. Large safety margins are introduced, thus the blades are often over-engineered, resulting in time consuming prototype testing. Therefore SWP has interest in extending and improving the modeling and simulation capabilities, meaning that the performance of the blades remain satisfactory, while reducing the production cost. [Overgaard, 2014]

The purpose of this project is to design a test specimen, which is manufactured using Vacuum Assisted Resin Transfer Molding (VARTM). The test specimen has to allow testing of multiaxial stress states in a lay-up specifically designed for wind turbine blade testing. The designed specimen is tested in a multiaxial fatigue stress state, and the observed number of cracks at given cycles is obtained together with the mode of failure. The data from the fatigue tests is then compared to simulations in ANSYS where a state-of-the-art fatigue life prediction algorithm is implemented. The goal of this comparison is to conclude whether this fatigue life prediction algorithm can be used by SWP when designing blades to get a better estimate of the fatigue life of the used GFRP. Furthermore if the algorithm proves to be accurate, a reduction in time required for experimental testing can be achieved.

The overall content of the project is described in the following:

1. **Specimen design:** A draft specimen design is found, based on literature and finalized through a geometry and lay-up optimization.
2. **Specimen fatigue test:** The designed specimen is manufactured by SWP and tested in a biaxial test rig at Aalborg University.
3. **Simulation of specimen fatigue test:** Finite element simulations are performed, where a fatigue life prediction algorithm is implemented in a material routine. The simulation results are compared with the experimental results.

1.2 Terminology

The different definitions and terms are presented in this section to give the reader a better understanding of the project.

1.2.1 Specimen

The designed specimen tested in this project has a cruciform geometry, which is cut from a square plate. This is shown in Figure 1.1 and 1.2.

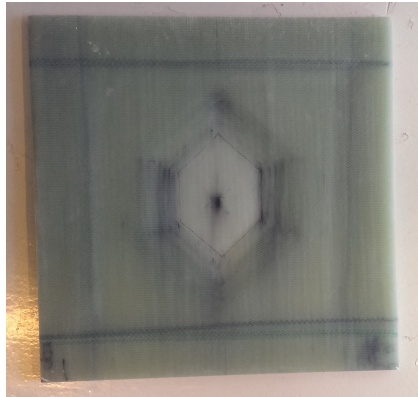


Figure 1.1 Square GFRP plate

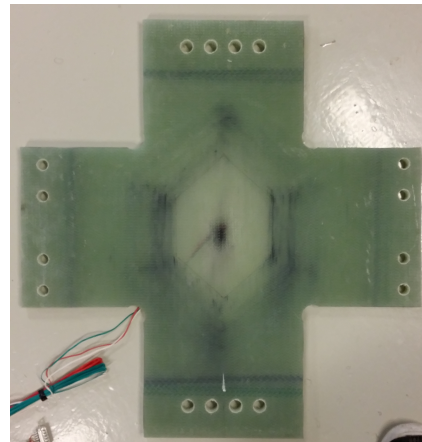


Figure 1.2 Cruciform geometry

An area in the specimen is predefined to have a specific GFRP lay-up. This area is called the gauge zone. The specified lay-up in this zone is the one of interest and this is where the failure initiation is supposed to happen. The rest of the geometry is designed to distribute the loads into the gauge zone and not fail under the applied loads. The gauge zone is vaguely shown with the bright area in the specimen in Figure 1.2 and it is sketched in Figure 1.3.

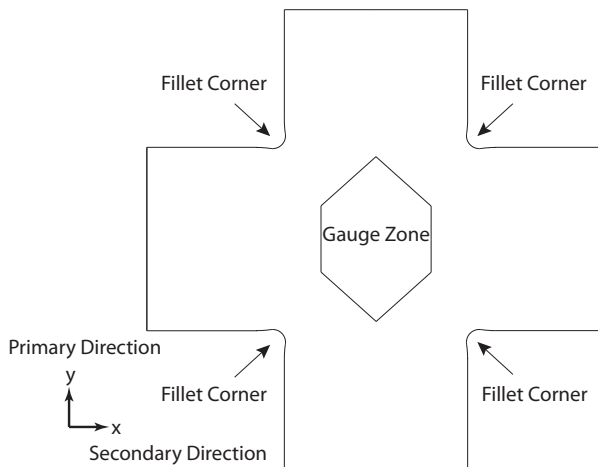


Figure 1.3 Cruciform specimen, gauge zone and fillet corners

The global reference frame used throughout the project is shown in Figure 1.3. The y-axis correspond to the primary direction and the x-axis correspond to the secondary direction. These directions originate from the test setup which is described in Section 1.2.3.

1.2.2 Definition of Failure

As mentioned earlier GFRP has different failure modes, therefore it is relevant to define what kind of failure modes are considered in this report. To determine when a specimen fails a term called first failure is introduced. The definition of this term is based on the experience gained from the static test as described in Chapter 4 on page 33.

By first failure is meant the first matrix crack, parallel to the fiber direction and the primary load direction, in the gauge zone that is visible to the naked eye. This means that all cracks in the fillet corners are ignored in this respect, and only cracks that initiate in the gauge zone, or initiate in the ply drops and propagate into the gauge zone are considered.

1.2.3 Test Setup

The test setup used in this project involves a biaxial test rig as show in Figure 1.4.

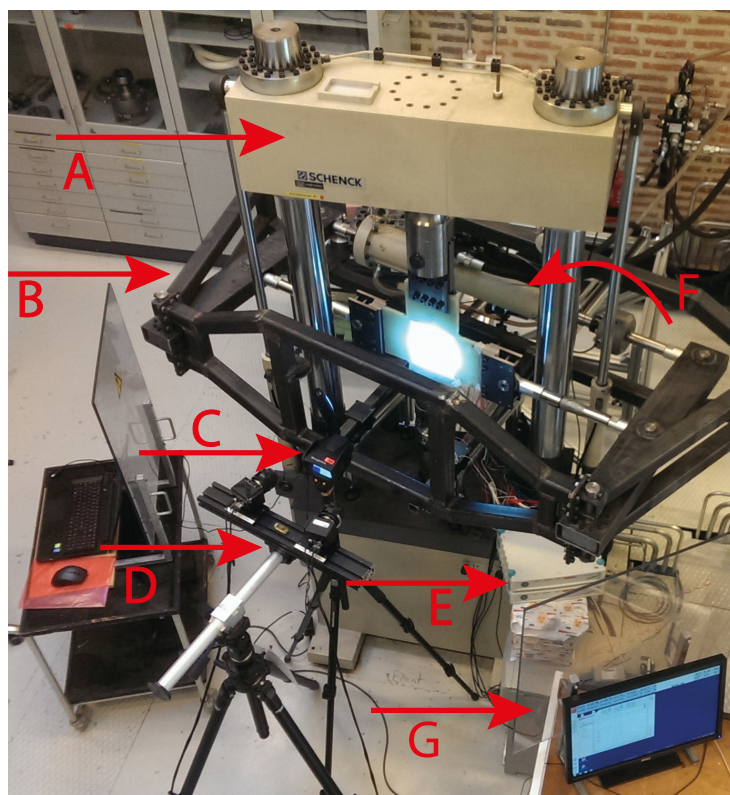


Figure 1.4 The test rig used for testing

The primary load frame and actuator is a uni-axial servo-hydraulic 400 [kN] (Instron Hydropuls® PL 400) testing machine (A) which has been extended with an additional secondary 63 [kN] horizontal actuator (Instron Hydropuls® PL 63) and associated loading frame (B). [Laustsen, 2014]

To monitor heat during fatigue tests a thermal camera (C) is used. For the monitoring of strains both (D) Digital Image Correlation (DIC) and strain gauges (E) are used. (E) indicates the control box which is the connection between the strain gauges on the specimen and the computer, where the data is stored. Furthermore a regular white light camera (F) is mounted on the back of the test rig. The test rig is controlled by the actuator controller (G), where programming for the movement of the test rig is performed.

1.2.4 Strain Ratio

A strain ratio is utilized throughout this project and it is defined as the ratio between the strain in the secondary and the primary direction, measured in the gauge zone of the specimen with a

strain gauge. The ratio is shown in Equation (1.1).

$$R_{strain} = \frac{\varepsilon_x}{\varepsilon_y} = 0.34 \quad (1.1)$$

where:

R_{strain}	Ratio between ε_x and ε_y in gauge zone, [-]
--------------	--

The magnitude of the strain ratio is specified by SWP and the aim is to obtain this strain ratio in the gauge zone. The strain ratio is abbreviated to R_{strain} and used henceforth in the report.

1.2.5 Load Ratio

Throughout the project a load ratio is employed, which describes the ratio between the load in the secondary and the primary direction. Henceforth, the load ratio is abbreviated to R_{Load} and determined as shown in Equation (1.2).

$$R_{Load} = \frac{F_x}{F_y} \quad (1.2)$$

where:

R_{Load}	Ratio between secondary and primary load, [-]
F_x	Force in the secondary direction, [kN]
F_y	Force in the primary direction, [kN]

1.2.6 Cyclic Loading Ratio

The fatigue tests are performed with a cyclic loading ratio specified by SWP of 0.1. It is defined as the ratio between the minimum and the maximum stress for a fatigue test. Henceforth the cyclic loading ratio is abbreviated to R_{CL} and determined as shown in Equation (1.3).

$$R_{CL} = \frac{\sigma_{min}}{\sigma_{max}} \quad (1.3)$$

where:

R_{CL}	Cyclic load ratio between minimum and maximum load in each direction, [-]
σ_{min}	Minimum stress in cyclic loading, [MPa]
σ_{max}	Maximum stress in cyclic loading, [MPa]

1.2.7 Ply, Lamina and Laminate

This section defines how the terms: ply, lamina and laminate are defined throughout the report and appendix.

Ply is used when a single fiber mat is mentioned, e.g. the BIAX ply.

Lamina is used when multiple identical plies are mentioned, e.g. the UD lamina in the gauge zone, which consists of five UD plies.

Laminate is used when multiple laminae are mentioned, e.g. the laminate in the gauge zone, which consists of two BIAX laminae and one UD lamina.

1.3 Requirements

In this section the requirements for the project is defined. The requirements are presented as bullet points:

- Specimen design
 - The specimen shall fit into the test rig, as shown in Figure 1.4, i.e. the outer geometry and the bolt connections shall be similar to previous specimens tested in the test rig, as in Laustsen et. al. [2013]
 - The test equipment shall be able to deliver enough force to develop static total failure in the specimen
 - The specimen shall have the specified lay-up from SWP in the gauge zone
 - The failure shall initiate inside the gauge zone and possible failures from the fillet corners shall not propagate into the gauge zone
- Specimen fatigue test
 - Perform the test with the SWP specified parameters:
 - * $R_{strain} = 0.34$ in the gauge zone
 - * R_{CL} of 0.1
 - Shall be able to monitor strain using strain gauges and DIC
 - Shall be able to monitor crack initiation and propagation with regular white light camera, due to transparency of GFRP.
- Simulation of specimen fatigue test
 - Implement the state-of-the-art fatigue life prediction algorithm, FADAS, in an ANSYS material routine
 - Simulate the performed fatigue tests

1.4 Project Clarification

This section describes the project approach which is employed to give the reader an overview of the report and the project work. The project approach is shown in Figure 1.5.

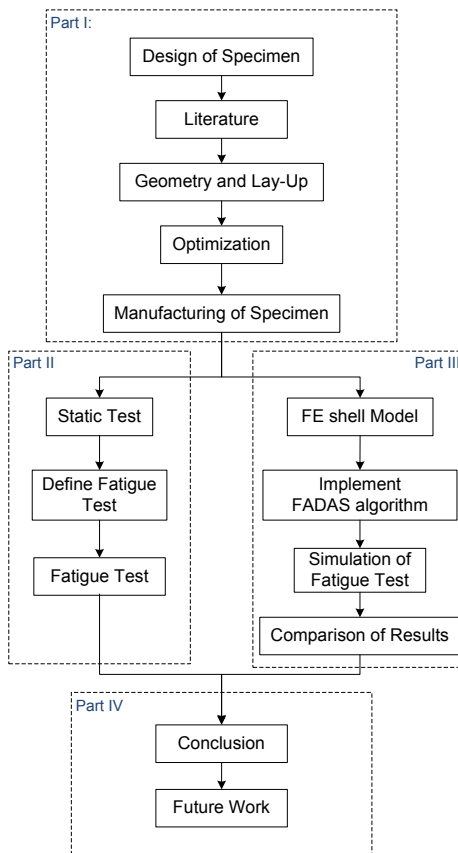


Figure 1.5 The project approach

The project is divided into 4 parts, part I, II, III and IV. These divisions are employed for the project work as well as for the report structure. Part II and III are performed simultaneously.

1.4.1 Part I: The Initial Phase

In the initial phase the objective is to design a specimen, which can be manufactured by SWP and used for the experimental fatigue test in part II and the simulated fatigue tests in part III.

Literature is studied to incorporate state-of-the-art knowledge w.r.t. design, testing and simulation of cruciform test specimens in biaxial fatigue. Furthermore, former Ph.D. student at Aalborg University, Steffen Laustsen, who designed the secondary test rig, is consulted regarding the test rig, specimen design and manufacturing.

Geometry and lay-up is based on the knowledge gained from the literature study. However, the diameter of the fillet corners, and the position of these along with the number of plies in each lamina is determined through an optimization.

Design optimization is performed to determine the final configuration of the fillet corner diameter and lay-up.

Manufacturing of specimen is started when an optimized design has been obtained.

1.4.2 Part II: Fatigue Test

Part II is the experimental part of the project, where the objective is to determine a feasible test setup and perform the fatigue tests.

Static pilot test is performed to calibrate (fine tune) R_{Load} to obtain the specified R_{strain} in the gauge zone. Furthermore, the static test is performed until total failure is achieved. This knowledge is used to estimate what level of loads are necessary to obtain failure after a given number of cycles and the failure modes that are to be expected during the fatigue tests. Experience with using the test rig, the strain gauges and the DIC equipment is acquired through the static test as well.

Define fatigue test is done on the basis of the static pilot test. From this test an estimate of the fatigue loading configuration is found. Furthermore a method for detecting and monitoring failure in the gauge zone is obtained.

Fatigue tests are performed in order to verify if it is possible to simulate these with a state-of-the-art fatigue life prediction algorithm.

1.4.3 Part III: Simulation of Fatigue Test

The objective is to simulate the fatigue test, by performing finite element (FE) analysis, using a state-of-the-art fatigue life prediction algorithm in ANSYS.

FE shell model is created to represent the designed specimen, i.e. outer geometry, lay-up and boundary conditions (BC) are similar.

Implement FE material routine in ANSYS to simulate fatigue damage in the specimen. The material routine uses a fatigue life prediction algorithm, wherein Puck's failure criteria indicate the different failure modes.

Fatigue test simulation is performed, where the defined fatigue test configurations from Part II are employed.

Comparison of results between the performed fatigue tests and simulations.

1.4.4 Part IV: Closure

The objective for the closure is to conclude on the comparison of results in part III together with a final conclusion for the project. The comparison yields a conclusion of how well the fatigue life prediction algorithm simulates the reality, which indicates whether or not the algorithm is applicable when designing wind turbine blades. Furthermore, it is concluded whether the requirements in Section 1.3 are fulfilled.

Different topics are discussed in future work, which can be used for inspiration if a second iteration of the project is conducted.

Specimen Design 2

In this chapter the specimen is presented and it is described how the specimen geometry and lay-up is determined. Some of the available and relevant literature is presented in Section 2.1, the designed specimen is presented in Section 2.2 where the design is based on the knowledge gained from the literature. The designed specimen is modeled in the commercial finite element software ANSYS, described in Section 2.3, and a geometry and lay-up optimization is described in Section 2.4. Initially the general outer geometry is determined together with the three ply drop boundaries and finally an optimization is performed to determine the final dimensions, such as fillet corner diameter and number of plies in each lamina.

2.1 State-of-the-art Cruciform Test Specimens

Biaxial testing is relevant because it is rare that a structure experiences pure uniaxial loads. Cruciformed specimens are used for biaxial tests to determine static- and fatigue strengths of different composites and lay-ups. So far, no one has managed to design a specimen that is suited to become a standard geometry for biaxial testing [Lamkanfi et. al., 2010]. Which is why these specimens are constructed with different geometries and lay-ups, and why extensive research is conducted to optimize the geometry of the specimens. In the article Laustsen et. al. [2013] tests are performed for a sandwich panel, which represents the outer shell of a wind turbine blade, i.e. it is curved due to the aerodynamic outer shape of the blade, as shown in Figure 2.1. The sandwich panel is analyzed numerically and the results are compared to the experimental results.

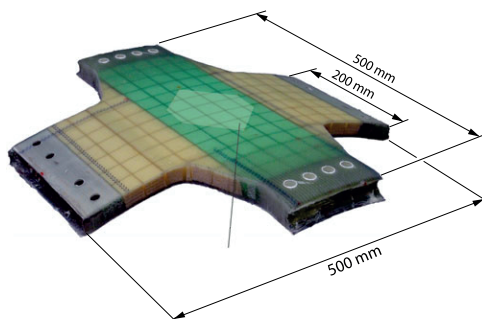


Figure 2.1 General geometry and dimensions [Laustsen et. al., 2013]

In the article a normal force and a moment are applied in the primary and secondary directions, respectively. This load condition is realized in the same test rig as the one used in this project, which is described in Section 1.2.3 on page 6.

A hexagonal gauge zone geometry is used to increase the length of the ply drop, and hereby increase the area over which the load is distributed, as shown in Figure 2.2 and 2.3. Furthermore, the strain distribution in the center of the gauge zone is more uniform when using angled ply drops.

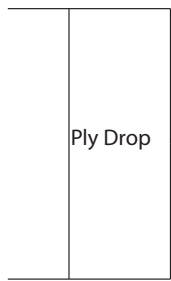


Figure 2.2 Straight ply drop

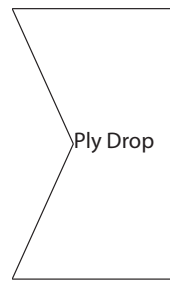


Figure 2.3 Angled ply drop

OptiDAT wind turbine materials research database [Nijssen, 2011] has developed a cruciform test specimen, shown in Figure 2.4 which has been extensively used by other researchers.

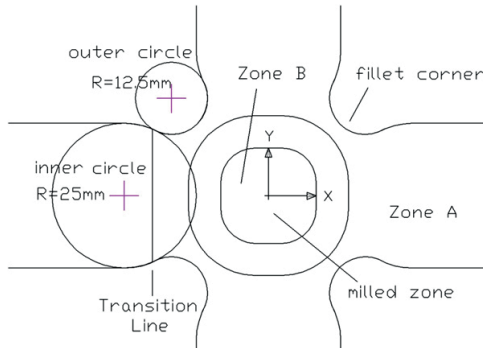


Figure 2.4 Cruciform test specimen [Lamkanfi et. al., 2010]

This geometry is used in the experiments described in the article Lamkanfi et. al. [2010] where a study of detailed FE modeling is performed in order to determine whether a simple 2D model is enough to capture the failure modes seen in the biaxial experiments or if it is necessary to introduce a more detailed 3D model. The results obtained in the experiments are gathered using DIC.

The gauge zone of this specimen is milled, which leads to crack initiation and delamination at the ply drops. However, the manufacturing of the specimen is eased compared to a specimen with internal ply drops.

2.2 Specimen Geometry

Based on the literature study above, the specimen geometry shown in Figure 2.5 is designed. The geometry is a mix of the two geometries mentioned, and some new ideas are implemented as well. The overall dimensions from Laustsen et. al. [2013] are chosen along with the position of the mounting holes. This is done to ensure that the designed specimen can fit in the test rig. However, since it is expected to experience some load transfer between the load directions, it is impractical to use the exact outer geometry from Laustsen et. al. [2013]. Therefore it is chosen to incorporate the fillet corner geometry described in Lamkanfi et. al. [2010] with a slight moderation so it fits the enlarged specimen. This means that the diameters of the circles are 200 [mm] for the ones placed in each of the four arms of the specimen, and 28 [mm] for the circles that connect the larger circles.

With respect to the gauge zone, it is decided to use internal ply drops, to avoid milling and the corresponding cracks, as described in Lamkanfi et. al. [2010]. When using internal ply drops for a gauge zone it is necessary to cut the plies by hand, which means that a circular gauge zone is very difficult to manufacture, which leads to the use of a hexagonal gauge zone as described in Laustsen et. al. [2013].

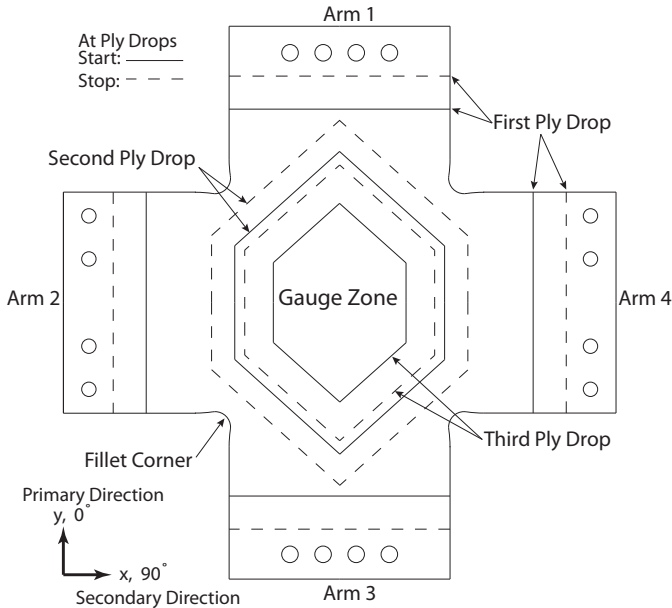


Figure 2.5 Specimen geometry

The start and stop boundaries of ply drops illustrate areas where a number of plies are dropped. The specimen is designed to fail in the gauge zone, by increasing the amount of plies outside it, i.e. increasing the strength of areas outside the gauge zone, but at the same time not increasing the stiffness too much. If the stiffness, especially around the fillet corners, is increased, then these areas will carry more of the load. This results in less load being transferred through the gauge zone and hereby less likeliness of cracks to initiate and propagate in the gauge zone. The lay-up in the gauge zone is specified by SWP and consists of four BIAX 0° and five UD 0° plies $[(\pm 45)_2, 0_5, (\pm 45)_2]$, as shown in Figure 2.6. Each BIAX ply consist of fibers in $\pm 45^\circ$.

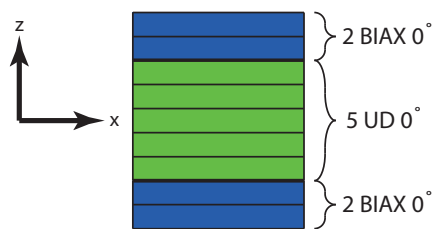


Figure 2.6 Gauge zone lay-up

2.2.1 Layer Groups

To increase the strength in the areas around the gauge zone three groups of GFRP layers are added to the SWP specified lay-up, as shown in Figure 2.7. The three added groups are group 2, 3 and 4. Group 2 consists of BIAX 0°, group 3 of UD 90° and group 4 consists of UD 0°. The lay-up is symmetric around the 5 UD° in group 1, i.e. group 2,3,4 and 5 are mirrored around

group 1. This yields that group 5 (BIAX 0°) in the gauge zone is used to enclose all the added layer groups together with layer group 1 at the gauge zone in order to obtain internal ply drops.

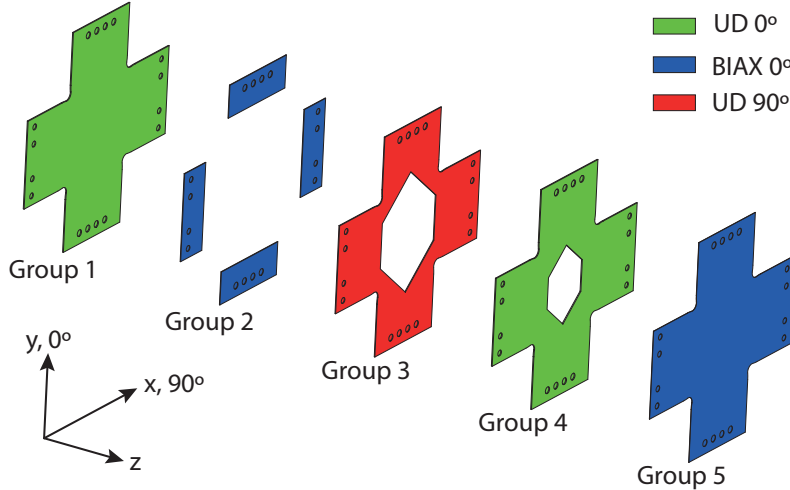


Figure 2.7 The symmetric fiber lay-up. The symmetry is w.r.t. group 1, which is the 5 UD 0° mid lamina

To ensure that the arms do not fail due to the forces applied in the primary or secondary directions, layer group 4 and 3 are used, respectively. Both groups are present in all arms, thus the UD 0° lamina in arm 2 and 4 in Figure 2.5 do not contribute significantly to the strength in the secondary direction, i.e. horizontal direction in Figure 2.5. Vice versa for the UD 90° lamina in arm 1 and 3 in Figure 2.5. Layer group 4 starts at the third ply drop boundary, shown in Figure 2.5, and ends at the outer geometry. This is also the approach for layer group 3, but this starts at the second ply drop boundary.

Furthermore, layer group 3 and 4 are selected in an attempt to reduce the shear stress in the fillet corners, which entails a reduction in the force transfer between the arms. A study is performed to clarify the relation between the stiffness and load transfer in the fillet corners, which is described in Appendix B.8. The results from the study shows that a high fillet corner stiffness yields high load transfer in the fillet corners and low load transfer for a low fillet corner stiffness. Furthermore, the study shows that the stresses in the gauge zone are decreased with a high fillet corner stiffness. Thus it is of interest to decrease the fillet corner stiffness, but at the same time ensure failure in the gauge zone instead of in the fillet corners.

Layer group 2 is only present in the arms, to ensure that the bolt connections do not fail during test, i.e. tearout of the bolts.

2.2.2 Ply Drops

The number of plies in layer group 2, 3 and 4 is determined in the optimization, described in Section 2.4. It is decided to use internal ply drops, since these reduce the risk of delamination compared to a specimen with external ply drops. In Figure 2.8 an external ply drop is shown, where delamination can occur due to out-of-plane stresses which only are constrained by the strength of the matrix material. By using an internal fiber layer contributes together with the matrix material to prevent delamination at the ply drop,

i.e. out-of-plane stresses are decreased at the ply drop. Thus internal ply drops are beneficial compared to external ply drops, but delamination cannot be prevented completely.

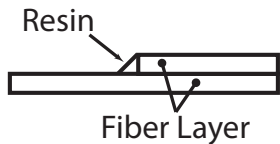


Figure 2.8 External ply drop

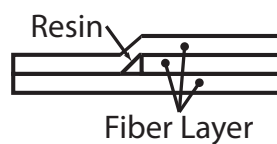


Figure 2.9 Internal ply drop

The optimization result showed that layer group 2, 3 and 4 consists of multiple layers, which yield that a multiple layer ply drop is used in the design, as shown in Figure 2.10.

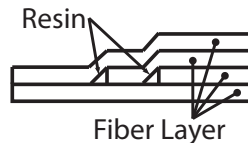


Figure 2.10 Internal ply drop of multiple layers

The designed specimen has three ply drop boundaries as shown in Figure 2.5, where start and stop boundaries can be seen. Between two ply drops a general design guideline is followed to determine the length until the next drop, as illustrated in Figure 2.11. The guideline states that: $l \geq 10 \cdot \Delta t$ [ESA, 1994]. The lay-up for the specimen is shown in Figure 2.22.

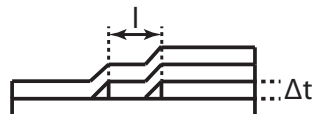


Figure 2.11 Design guideline for length between ply drops

2.3 Finite Element Modeling

The FE modeling of the specimen is performed in ANSYS 14.5 and scripted in PEDAL. In the FE model the geometry, i.e. layers of GFRP etc., are built of volumes and meshed with a 3D solid element, called SOLID186. This element is a higher order element consisting of 20 nodes, which makes it computationally heavy, but at the same time it is possible to calculate out-of-plane strains and stresses, compared to the use of a shell element [ANSYS, 2011a]. This is beneficial, when simulating complex structural parts such as ply drops and fillet corners. A more detailed explanation of the solid model can be found in Appendix B.1 and a mesh convergence study in Appendix B.7.

To reduce the computational time, the symmetry of the specimen is utilized, making it necessary to only model a quarter of the geometry. The quarter of the specimen with boundary conditions is shown in Figure 2.12.

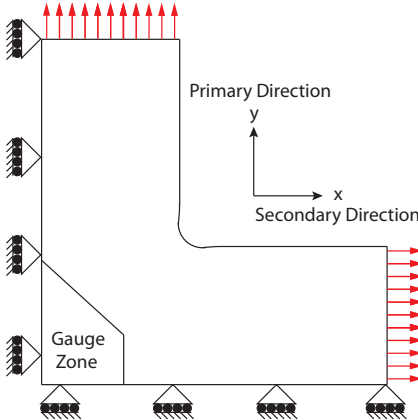


Figure 2.12 FE geometry

As shown in Figure 2.12 the normal forces are applied at the end of the two arms, i.e. in the primary and secondary directions. Symmetric boundary conditions are utilized at the edges. Furthermore, the specimen is mounted in the test rig by bolt connections in each arm, i.e. four bolt holes in each arm. In the primary direction M14 bolts are used and M12 bolts in the secondary direction. The bolt connections are prestressed during all testing, but the mounting holes are not modeled since it is assumed that these do not fail before the gauge zone, which is supported by calculations presented in Appendix B.9.

2.4 Geometry and Lay-up Optimization

2.4.1 Objective Function

As mentioned earlier, the aim is to make the specimen fail in the gauge zone before anywhere else, and diminish shear stress in the fillet corners and thereby reduce the load transfer between the arms. This is done by evaluating the effect of key design parameters, which yield an initial design which is then refined to ease manufacturing. Furthermore SWP requested that $R_{strain} = 0.34$, as described in Section 1.3 on page 8, is utilized in the gauge zone. The above is expressed in a conventional optimization form in Equation (2.1), (2.2) and (2.3).

$$\begin{aligned}
 \text{Minimize : } & S_{MAX,Pri-Arm}(t_{BIAx}, t_{UD_0}, t_{UD_{90}}, d_{fillet}, R_{Opti,load}) \\
 & S_{MAX,Sec-Arm}(t_{BIAx}, t_{UD_0}, t_{UD_{90}}, d_{fillet}, R_{Opti,load}) \\
 & S_{MAX,Fillet}(t_{BIAx}, t_{UD_0}, t_{UD_{90}}, d_{fillet}, R_{Opti,load}) \\
 & C(t_{BIAx}, t_{UD_0}, t_{UD_{90}}, d_{fillet}, R_{Opti,load})
 \end{aligned} \tag{2.1}$$

$$\text{Maximize : } S_{MAX,GZ}(t_{BIAx}, t_{UD_0}, t_{UD_{90}}, d_{fillet}, R_{Opti,load}) \tag{2.2}$$

$$\begin{aligned}
 \text{subject to : } & 3.2 [m \cdot 10^{-4}] \leq t_{BIAx} \leq 16.0 [m \cdot 10^{-4}] \\
 & 4.1 [m \cdot 10^{-4}] \leq t_{UD_0} \leq 20.5 [m \cdot 10^{-4}] \\
 & 4.1 [m \cdot 10^{-4}] \leq t_{UD_{90}} \leq 20.5 [m \cdot 10^{-4}] \\
 & 10 [mm] \leq d_{fillet} \leq 29 [mm] \\
 & 5 [\%] \leq R_{Opti,load} \leq 90 [\%]
 \end{aligned} \tag{2.3}$$

where:

t_{BIAX}	Total thickness of the BIAX layer group in the arms used in the optimization, [$m \cdot 10^{-4}$]
t_{UD_0}	Total thickness of the UD_0 layer group used in the optimization, [$m \cdot 10^{-4}$]
$t_{UD_{90}}$	Total thickness of the UD_{90} layer group used in the optimization, [$m \cdot 10^{-4}$]
d_{fillet}	Diameter of the fillet corner used in the optimization, [$m \cdot 10^{-3}$]
$R_{Opti,load}$	Ratio between secondary and primary load used in the optimization, [%]
$S_{MAX,Pri-Arm}$	Failure index in primary arm determined using maximum stress failure criteria, [-]
$S_{MAX,Sec-Arm}$	Failure index in secondary arm determined using maximum stress failure criteria, [-]
$S_{MAX,Fillet}$	Failure index at the fillet corner determined using maximum stress failure criteria, [-]
$S_{MAX,GZ}$	Failure index in the gauge zone determined using maximum stress failure criteria, [-]
C	Optimization parameter, $(0.34 - R_{strain})$, [-]

As expressed above, 5 design parameters are chosen. These parameters are the thickness of layer group 2, 3 and 4, i.e. the number of UD_0° , UD_{90° and BIAX plies, together with the diameter of the fillet corner and the load ratio. The load ratio has a huge influence on the strain ratio in gauge zone, it is included in the optimization to ensure that the requirement regarding the strain ratio is met at all times during the optimization. By doing this, a specimen that is optimized with $R_{strain} = 0.34$ is designed, and not a specimen where the load ratio is changed after the optimization to obtain the required strain ratio.

The first three parameters are converted from discrete ply numbers to continuous lamina thicknesses, to achieve a smoother optimization. This means that after the optimization, the parameters are converted back to discrete ply numbers. The diameter of the fillet corner is constrained because otherwise there is a possibility of too much load transfer between the arms, due to shear stress. The parameters used in the optimization do not have the same units, they have been multiplied by factors of 10 to have more or less the same order of magnitude. This is done to ensure that a similar step size for all the parameters can be utilized.

The shear stress is not included in the optimization. However, since the lay-up around the fillet corners is dominated by $[0^\circ, 90^\circ]$ plies, it is assessed that the shear stress is lower than if it was dominated by $[\pm 45^\circ]$ plies.

From the problem described in Equation (2.1) and (2.2) the objective function in Equation (2.4) is constructed.

$$fval = \frac{S_{MAX,Pri-Arm} + S_{MAX,Sec-Arm} + S_{MAX,Fillet}}{S_{MAX,GZ}} + k_{weight} \cdot C^2 \quad (2.4)$$

where:

$fval$	Objective function value, [-]
k_{weight}	Weighting factor in the objective function, [-]

All the S -values can be gathered in one fraction since they all are positive. First ply failure is considered in the optimization because the maximum stress failure criterion is used. This failure criterion simply evaluates stresses compared to strengths. It is assumed that first ply failure can be used as an indication of total failure as well. All the maximum stress failure criteria values are extracted from predefined areas or points in the model, as shown in Figure 2.13.

$S_{MAX,Pri-Arm}$ and $S_{MAX,Sec-Arm}$ are calculated based on values from a single point in the primary and secondary arm, respectively. The values used in the objective function are the ones with the highest failure indices through the thickness. The same is done with $S_{MAX,Fillet}$ and $S_{MAX,GZ}$, except that instead of a single point, a line and an area is chosen, respectively, as shown in Figure 2.13.

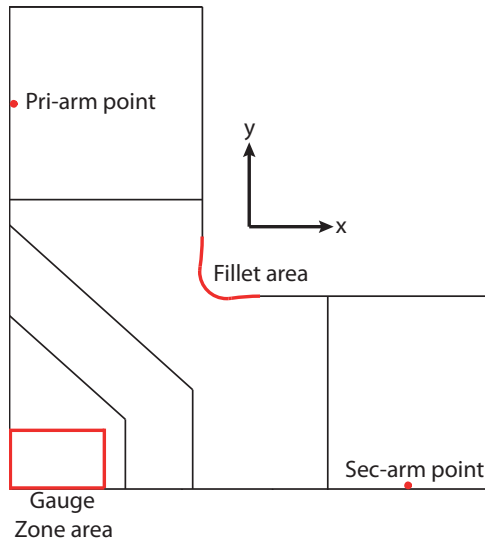


Figure 2.13 Areas on specimen used in objective function

From the objective function it can be seen that the failure indices above the fraction are to be minimized, while the failure index under the fraction is to be maximized. This means that for every iteration a new maximum from each of the areas outside the gauge zone is found, and the optimization attempts to decrease these values. This decreases the overall failure index in the specified areas, ensuring that failure does not occur here. Inside the gauge zone the optimization algorithm attempts to increase the highest value of the failure index, to ensure that failure occurs in this area.

The last part in the objective function, Equation (2.4), ensures that the strain ratio is as close to 0.34 as possible. The exponent of 2 is included to make sure that C is always positive. The factor, k_{weight} , is used to ensure that the optimization minimizes the difference between the wanted strain ratio and the actual strain ratio to a higher extend than the rest of the parts in the objective function, since the strain ratio is a direct requirement for the specimen. The strain ratio is calculated as the mean value of the ratio between the 20 highest strains in the x-direction and the corresponding strains in the y-direction. The strains are found in the gauge zone area, shown in Figure 2.13.

2.4.2 Used Solvers

To find an optimized solution to the problem, the MATLAB optimizer "fmincon" is used. This solver is used to find the minimum of constrained non-linear multivariable functions. A sequential quadratic programming algorithm called "sqp" in MATLAB, has been chosen, and a forward difference method is used to determine the gradients. The algorithm represents the state-of-the-art within non-linear programming methods [MathWorks, 2014].

The basics of this optimization configuration is that an initial start guess is provided and for each iteration of the optimization, an approximated Hessian of the Lagrangian function is estimated. The Hessian is then used in a quadratic programming sub-problem which is solved in order to find the search direction. To be able to use the "sqp" algorithm, the objective function and constraint functions need to be twice differentiable. [MathWorks, 2014]

However, due to the nature of the problem, fmincon is not enough to find a global minimum. Depending on the initial guess, different values for the objective function (Figure 2.14 and 2.15) and parameters (Figure 2.16 and 2.17) are obtained, which indicates that several local minima exists. The units of the parameters in the figures below are as described in Equation (2.3).

In Figure 2.14 and 2.15 the function values are plotted as a function of the iteration number.

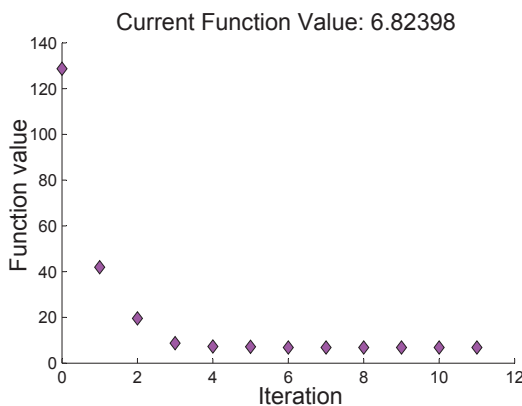


Figure 2.14 Function value from fmincon with the initial guess: [6.4 10.25 8.2 14 22.5]

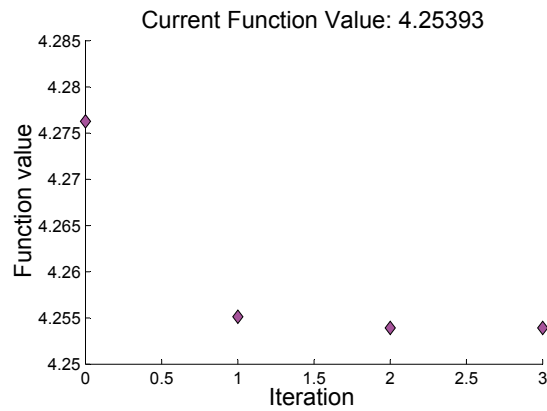


Figure 2.15 Function value from fmincon with the initial guess: [12.8 20.5 16.4 28 45]

In Figure 2.16 and 2.17 the values of the individual parameters at the final iteration are shown.

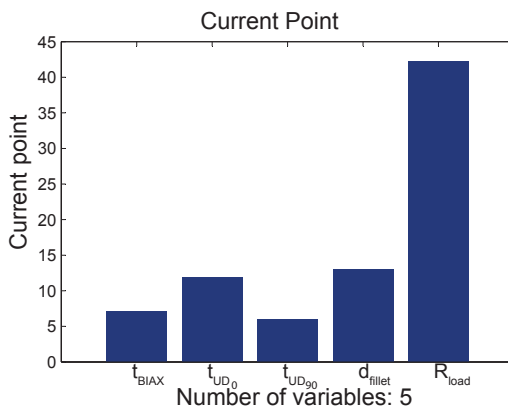


Figure 2.16 Final parameters from fmincon with the initial guess: [6.4 10.25 8.2 14 22.5]

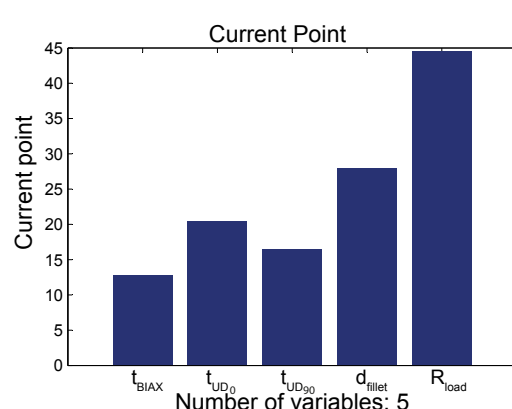


Figure 2.17 Final parameters from fmincon with the initial guess: [12.8 20.5 16.4 28 45]

As shown in Figure 2.18 and 2.19, the optimization converges at a minimum for both cases since the final step size for both of them is very small. However, the function values and the corresponding parameters are different. This means that there are at least two different local minima.

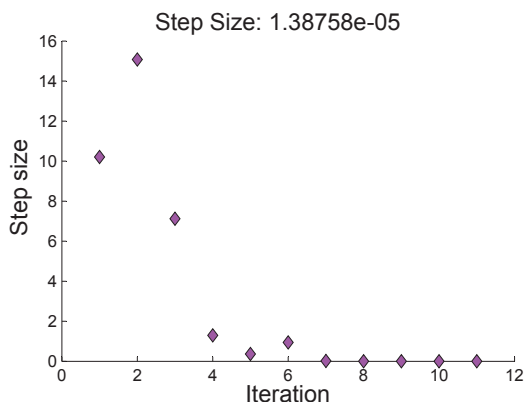


Figure 2.18 Step size of fmincon with the initial guess: [6.4 10.25 8.2 14 22.5]

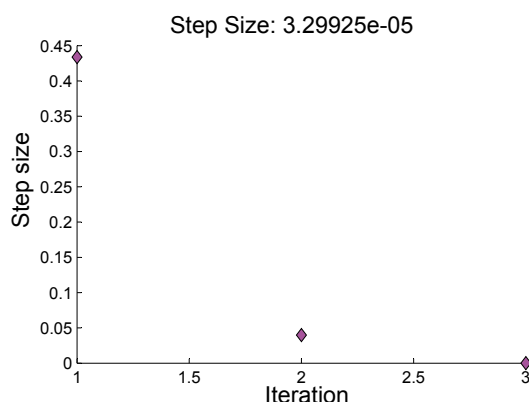


Figure 2.19 Step size of fmincon with the initial guess: [12.8 20.5 16.4 28 45]

To verify that the best result obtained with the fmincon is actually a global minimum, or close to, the MATLAB function "GlobalSearch" is used. The GlobalSearch algorithm basically starts the local solver, which in this case is the fmincon, from different points using a scatter-search algorithm [MathWorks, 2014]. This means that if another minimum can be obtained from another starting point, the GlobalSearch algorithm will initiate the local solver from this other starting point. To determine whether a new minimum will be reached from the new starting point, the GlobalSearch algorithm uses Basins of Attraction to exclude starting points that lead to a previously discovered local minimum. The radii of these Basins of Attraction are defined based on the distance from the start point to the local minimum point, as shown in Figure 2.20. [MathWorks, 2014]

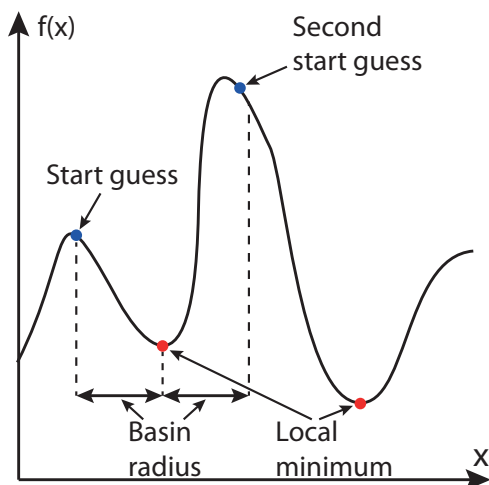


Figure 2.20 Definition of radii of Basins of Attraction

If another start guess is within the radius of a previous Basin, then it will not be used for further analysis. The GlobalSearch algorithm assumes that the Basins of Attraction are spherical, which can mean that some start guesses that can lead to other minima, will not be considered, which is shown in Figure 2.20 at the second start guess. The second start guess would yield another, and better minimum, but because it is within the Basin radius, the starting point is not considered. [MathWorks, 2014]

These Basins are useful in the given case, because the analyses take a lot of time to complete, so

by not obtaining the same local minimum again and again, time can be saved. It is assessed that the decreased computational time, is worth the possibility of not obtaining some local minima due to Basins of Attraction.

2.4.3 Results from the Optimization

The result from the GlobalSearch is shown in Figure 2.21

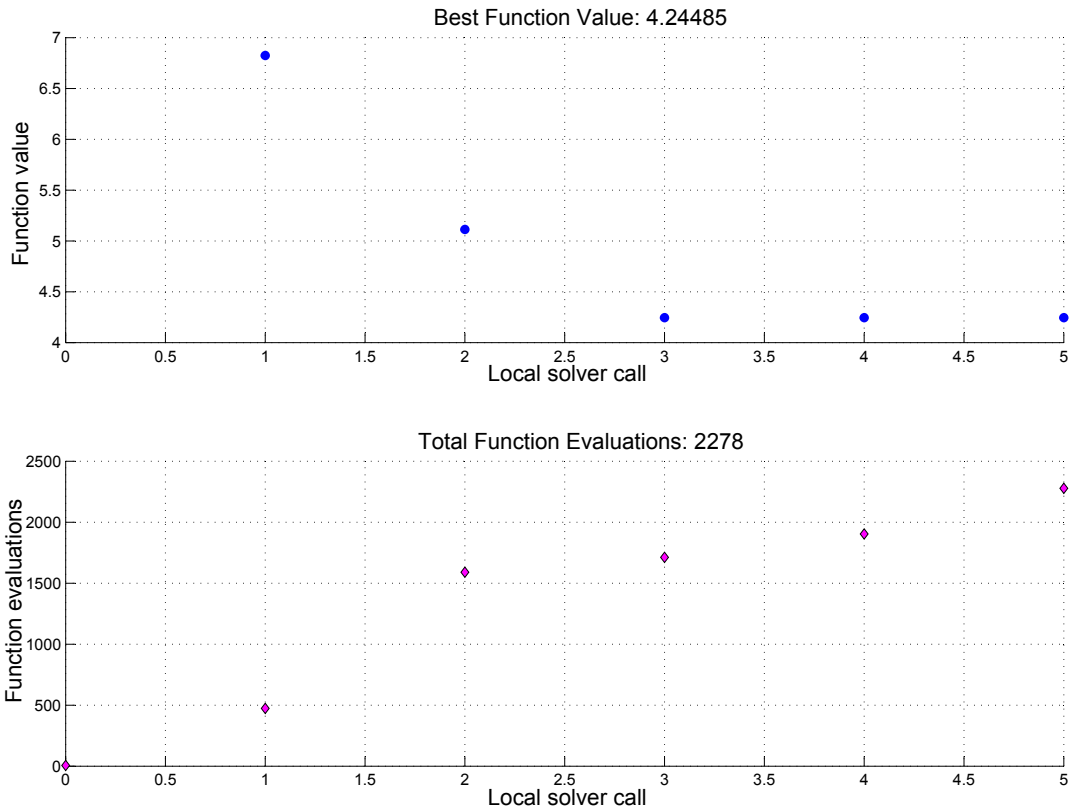


Figure 2.21 GlobalSearch result

As it is shown in Figure 2.21, the GlobalSearch algorithm finds three increasingly better solutions, and then finds two that are worse, so it returns to the previously found function value. The optimum solution found by the GlobalSearch is shown in Table 2.1. However, as mentioned earlier, the parameters have to be converted back to discrete values that can be used in the manufacturing of the specimen. This means that the first three parameters are rounded up or down to the nearest integer of plies. For the diameter of the fillet corner, the parameter is rounded to an integer, and the load ratio is rounded to a number with three decimals. A simulation is performed with the rounded values to determine the function value, which is shown in Table 2.1.

Table 2.1 Exact and rounded values of optimized solution

	BIAZ	UD _{0°}	UD _{90°}	Diameter	R _{Load}	fval
Exact Global	0.75130 [mm]	2.05 [mm]	1.82604 [mm]	29 [mm]	0.448736	4.2448
Exact fmincon	1.28089 [mm]	2.05 [mm]	1.64364 [mm]	28.0400 [mm]	0.445299	4.2539
Rounded	1.28 [mm]	2.05 [mm]	1.64 [mm]	28 [mm]	0.445	4.2627

As mentioned earlier, the GlobalSearch algorithm was implemented to verify that the result shown in Figure 2.15 and 2.17 is valid. As shown in Table 2.1 many of the values are close to each other if not identical. The largest difference is for the BIAX plies in the arms, where the result from the GlobalSearch indicates that 2 BIAX plies is best and the stand-alone fmincon indicates that 4 is best. It is easier and cheaper to manufacture the specimen with just 2 BIAX plies, but with 4 there is a higher safety against failure at the load introduction. Furthermore there is a very small difference between the function value from the GlobalSearch and the one from the stand-alone fmincon, actually the difference between them corresponds to a change in the maximum stress failure index of less than 0.01.

From the above optimization, the specimen has the lay-up shown in Figure 2.22.

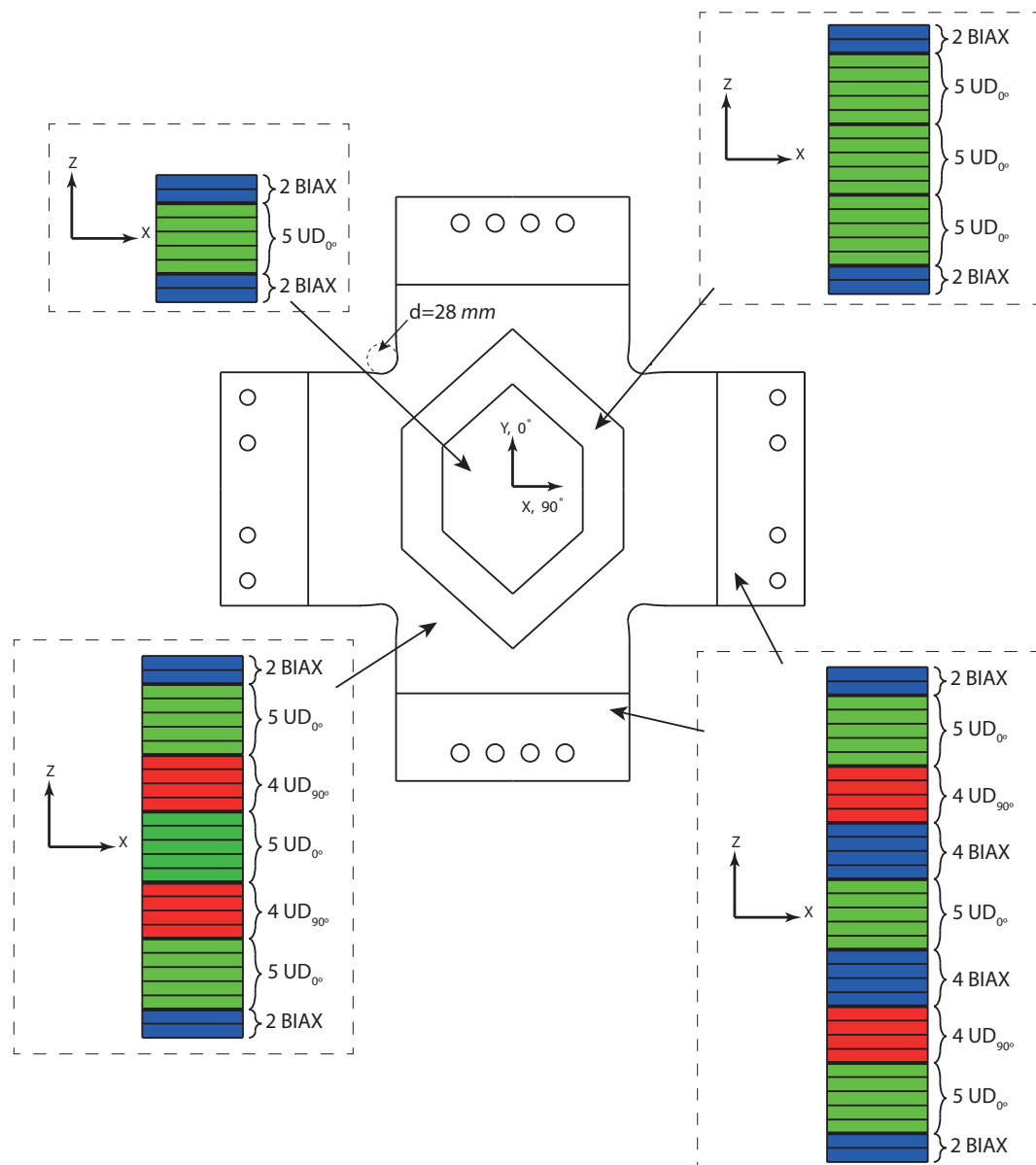


Figure 2.22 The designed specimen with lay-up

The specimen designed in this project has some features and combinations of features that have

not been tested in this context before. This is the internal ply drops in particular, but also the fillet corners in combination with the gauge zone shape that increases the force transferring area in the primary direction. The laminate around the fillet corners is dominated by $[\pm 45^\circ]$ in the article Lamkanfi et. al [2010], which means the laminate is capable of carrying a high shear stress. Hence, the transition from the arms to the center of the specimen has to be more pronounced. In this project the laminate is dominated by $[0^\circ, 90^\circ]$ close to the fillet corners, which means less shear stress occurs, and therefore the transition does not have to be as pronounced.

2.5 FE Solid Model

To give an idea of the behavior of the specimen with the specified lay-up, a static analysis of the solid model is conducted.

A force of 200 [kN] is applied in the primary direction and $R_{Load} = 0.445$ is utilized in the secondary direction. The force magnitude is randomly chosen as the analysis is linear. The following results are only used to indicate the behavior of the specimen.

In Figure 2.23 and 2.24 the maximum stress failure criteria are shown for the predefined gauge zone lay-up of the UD and BIAX laminae, respectively.

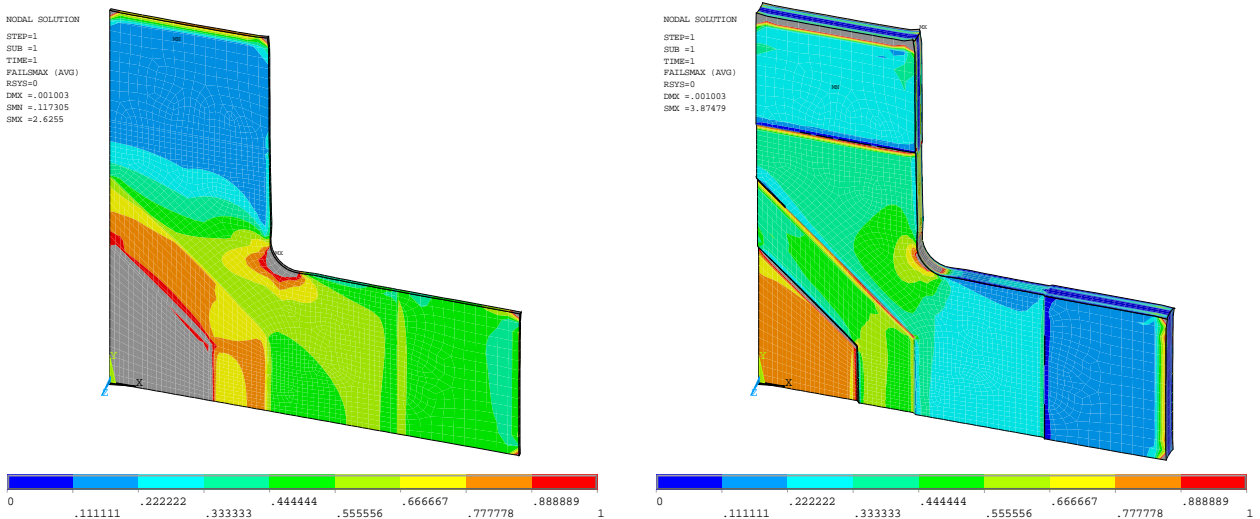


Figure 2.23 Maximum stress failure criteria for the predefined UD lamina

Figure 2.24 Maximum stress failure criteria for the predefined BIAX lamina

As shown in Figure 2.23 and 2.24 the gray areas indicate that the failure criterion is above one, meaning failure has occurred according to the utilized failure criterion. Only the maximum stress failure criterion is shown, as this has been utilized in the design optimization. The fillet corners show low safety against first ply failure, as expected, but the gauge zone also indicates low safety, which is intended.

The strain distribution in the gauge zone is shown in Figure 2.25 and 2.26.

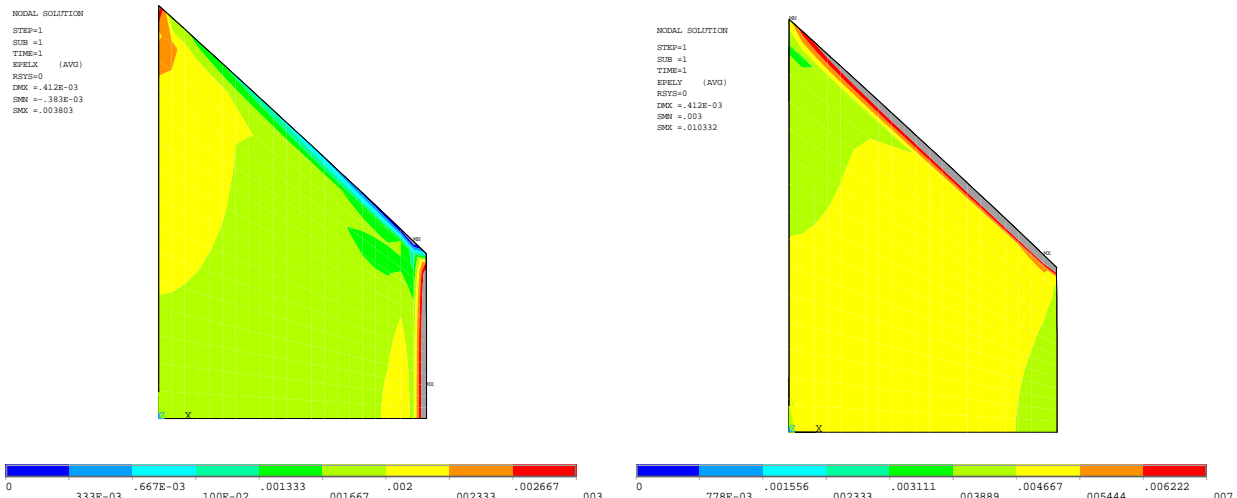


Figure 2.25 Strain in secondary direction in the gauge zone

Figure 2.26 Strain in primary direction in the gauge zone

The strains at the edges of the gauge zone, when excluding the symmetry boundaries, becomes relatively high compared to the rest of the gauge zone. This is to be expected, due to the ply drops at these edges.

For the simulations in this project a FE shell model is employed. This is due to a shell model is not as computational heavy as a solid model. Furthermore, the specimen modeling is easier for a shell model compared to a solid model. Thus it is selected to employ a shell model for the fatigue simulations in this project.

The FE shell model is compared to the FE solid model, in Appendix B.3, to ensure the calculated strain distribution, failure indices, etc. are similar for both models. This validates that the FE shell model can be used instead of the Solid model and be compared to the tested specimen and employed for the fatigue simulations. Furthermore, the FE shell model is validated w.r.t. experimentally determined strains in Appendix B.4.

2.6 Sub-Conclusion

A cruciform biaxial specimen is designed based on a literature study. The overall geometry is the result of a compromise between two test specimens, and the final geometry and lay-up is determined through an optimization. The specimen geometry of the fillet corners decrease the shear stress, which leads to decreased load transfer between the arms. Furthermore, the laminate at the fillet corners is dominated by $[0^\circ, 90^\circ]$ -laminae which also decreases the shear stress, compared to laminates dominated by $[\pm 45^\circ]$ -laminae. The ply drops are internal to increase the out-of-plane stiffness, which decreases the likeliness of crack initiation in the ply drops.

Part II

FATIGUE TEST

Procedure for Fatigue Test 3

Fatigue testing is a time consuming process, because a high number of cycles have to be achieved to achieve a complete understanding of the fatigue properties. To ensure that the first fatigue test in this project does not require weeks to complete, it is decided to perform a static test to determine the magnitude of loads that are appropriate to achieve a number of cycles between $1 \cdot 10^4$ and $1 \cdot 10^5$ for the fatigue tests. This amount is based on a compromise between the time required to test the specimens in high cycle fatigue, and having a reasonable spectrum of data points w.r.t. stress levels and cycles.

Normally an S-N curve, as the example shown in Figure 3.1, is derived by conducting multiple coupon tests at a given stress level. This is continued at different stress levels until a representative spectrum is obtained. The tendency line is obtained from the results by employing a general expression for the tendency line, e.g. $S_A = S_0 N^{-\frac{1}{b}}$, where the constants S_0 and b are determined by the least square method. S_A is the stress amplitude, S_0 is the line intersection with the y axis, N is the number of cycles for failure and b is the slope of the line. The least square method takes deviation between the data points into account, which is beneficial, since the difference between the data points for each stress level is normally not identical.

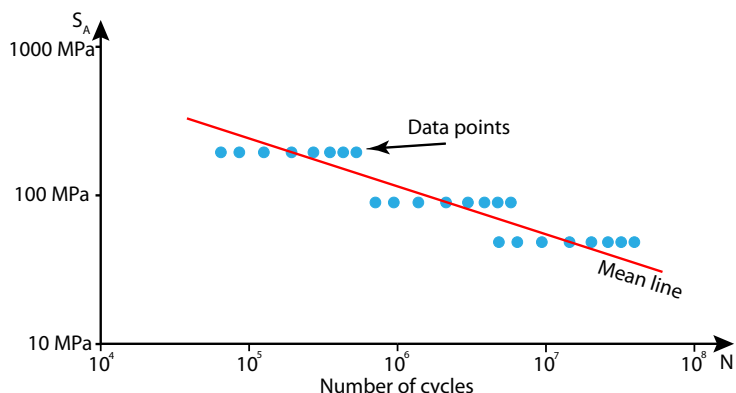


Figure 3.1 Example of S-N curve in log-log diagram

Due to the limited project period and specimens it has been prioritized to only conduct one test at each chosen stress level. However, because the first two tests failed before and after the considered fatigue life interval, respectively, it is decided to test the last two specimens at the same stress level. This is done to estimate the variance between the manufactured specimens. This yields that no S-N curve is derived in this project, due to the limited amount of fatigue data. To derive an accurate S-N curve a significant amount of fatigue data has to be available, which cannot be obtained for this project.

Failure in a composite specimen can occur due to multiple failure modes. Therefore, it is essential to be able to determine the failure modes and at which cycle these appear in the fatigue tests. The project goal for the fatigue tests is to be able to detect first failure. A definition of first failure is described in Section 1.2.2 on page 5.

3.1 Test Equipment

During the tests, measuring equipment is used to measure strain and to observe failures. Strain gauges and DIC equipment are used to measure strain. To observe failures in the specimen a regular white light camera and a thermal camera are utilized. The thermal camera used was the only one available during the test period. Furthermore, a thermocouple is used to monitor the specimen temperature. The used equipment is described in further details in Appendix E.

An overview of the test rig is shown in Section 1.2.3 on page 6, but in order to get a better understanding of the measurement equipment used during tests, Figure 3.2 is shown. Henceforth, when referring to the left or right side of the specimen, it is w.r.t. the front of the specimen.

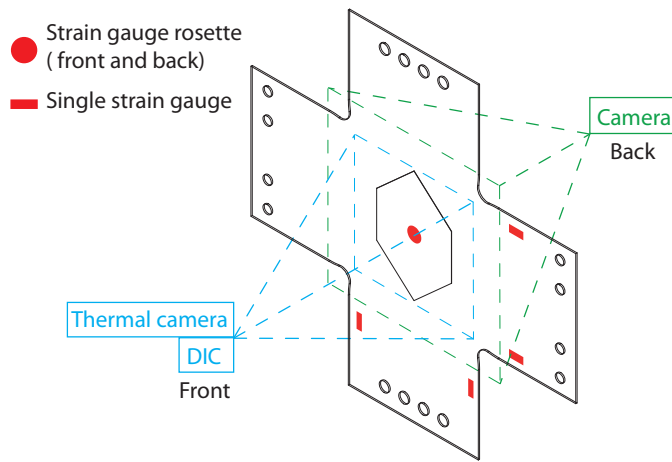


Figure 3.2 Setup of measurement equipment

Four single strain gauges are mounted on the arms to monitor whether or not the specimen is exposed to in-plane bending.

Furthermore, due to the manufacturing process of the specimen, described in Appendix A.3, one of the specimen sides have surface irregularities, thus a rosette strain gauge is applied on both sides to ensure that the obtained results are valid. This is experienced during the static pilot test where only a strain gauge rosette is attached to the back, because the entire strain field in the gauge zone is of interest for DIC.

This enables a comparison of the strain gauge measured strains on the front and back. DIC is used to monitor the strain field in the gauge zone and to monitor failures.

3.1.1 Strain Gauge

Strain gauges are a good measuring tool to determine strain on a surface, since a strain gauge is accurate and sensitive to small strain changes. The strain is measured over an area, which yields a mean measured strain value. Furthermore, a good adhesive bond between the strain gauge and the surface is essential.

The strain gauge results can be used to get the strain magnitudes within a minor area at the position of the strain gauge. If failure occurs somewhere in the specimen, the strain gauge result can include spikes, due to redistribution of loads within the specimen. However, it is not possible to get a distribution of the strains or an indication of where the failure occurs. This is possible with DIC equipment, as described in Section 3.1.2.

Strain gauges have a linear measurement range, in which a change in specimen strain yields a linear change in electric resistance in the strain gauge circuit and thereby the measured strain. If the strain within the specimen changes outside the linear measurement range it can result in a non-linear change in measured strain.

The linearity of a normal strain gauge is negligible compared to the uncertainty concerning the strain gauge K factor up until 5000 [μ strain]. It is only for strains as high as 50000 [μ strain] deviations from linearity can be a problem [Mouritsen, 2010]. Thus, for the strain magnitudes in this project, it is not necessary to take the non-linear effects into account, since the strains are below 5000 [μ strain] for the fatigue tests. Strain gauge uncertainties are described in Appendix E.3.1.

In this project strain gauges are the reference strain, because they are positioned on the surface, which yields a high level of accuracy and precision. Due to this, DIC and FE strains are compared to strain gauge measured strains for the static pilot test and the fatigue tests.

3.1.2 DIC

In contrast to strain gauges the DIC equipment can calculate strain in a field, e.g. the gauge zone. DIC is employed for tests in this project, because it is of interest to monitor the entire gauge zone and to clarify whether or not DIC can detect failure in the specimen.

The DIC is a non-contact measuring tool, which is beneficial compared to strain gauges, since no adhesive bonding can fail.

To prepare the specimen for DIC, a pattern has to be made on the surface, such that the DIC can recognize the pattern in different images. This is a simple process, compared to strain gauge where a position has to be determined and prepared. Furthermore, strain gauges and wires are glued on the specimen and it has to be ensured that the wires are undamaged during testing.

The size of the specimen is not a parameter, since the DIC equipment can be configured to calculate strains for all specimen sizes. However, a large field of interest could yield a decreased accuracy, compared to a small field of interest. For a large specimen monitored only by strain gauges, multiple strain gauges have to be employed on the specimen to measure the strain field, where DIC can monitor the entire field and calculate strains for all strain gauge positions at once.

The DIC is sensitive to the light applied to the area of interest, since a change in light can yield that the DIC software cannot recognize a part of the surface pattern. Thus, no strains can be calculated for this part.

The accuracy of the DIC results can be determined by looking into the DIC noise, which is a standard procedure to determine deviations for the DIC calculated strains.

A calibration is performed to "teach" the software where and how the cameras are positioned w.r.t. each other. This calibration is tedious, because it is performed by a 13 steps guide, where a calibration plate is held by hand in different positions. Two identical calibrations are almost impossible, because the calibration plate is held by hand.

The DIC calibration is comprehensive compared to the strain gauge calibration, which means a

higher probability of human errors is present.

3.1.3 Camera

A regular white light camera is used to be able to observe the specimen during cycles, when the specimen cannot be inspected. Furthermore, it is a method to store observations for later use. As illustrated in Figure 3.2 the camera is placed on the back, which is beneficial due to the DIC light. The specimen material is transparent, which makes it possible to detect failure in the specimen during testing, because cracks change the transparency of the specimen.

The camera observes the light through the specimen and can only monitor if the reflection of the light changes. Thus, it is assumed that not all failures can be observed, since some failure modes, sizes or locations do not result in changed reflection.

3.1.4 Thermal Camera

Crack surfaces appear during a fatigue test, due to specimen failure, i.e. first failure. Increased temperatures can occur in the area around the failure, because the crack surfaces are rubbed against each other due to the cyclic load.

To clarify whether or not heat changes occur during the fatigue tests a thermal camera is employed. The thermal camera is not used for the static pilot test, since no cyclic load is applied to the specimen.

3.1.5 Thermocouple

To monitor the specimen temperature during tests a thermocouple is placed on the back of the gauge zone. The temperature information can be used to evaluate if the cycle frequency used in the fatigue tests are high enough to introduce increased temperatures in the specimen, i.e. if temperature has to be taken into account for evaluation of the measured strains and for the fatigue simulations.

3.2 Adaptation of SWP Manufactured Specimen

The SWP manufactured specimens are delivered as square GFRP plates as the one shown in Section 1.2.1 on page 5. The cruciform geometry is created by the project group and the workshop at Aalborg University by drilling 20 holes, corresponding to the fillet corners and mounting holes, described in Section 2.2 on page 12, and afterwards cutting the cruciform geometry with a band saw. The process is shown in Figure 3.3 and 3.4.



Figure 3.3 Square GFRP plate with holes for fillet corner and mounting

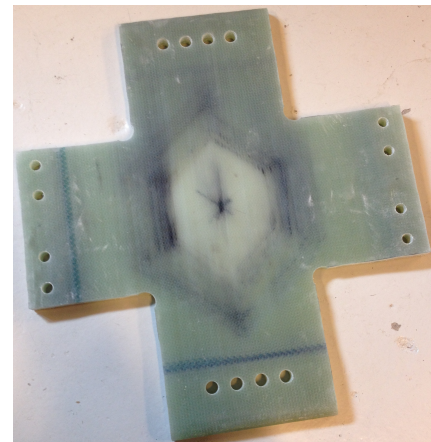


Figure 3.4 Finished specimen ready for testing

The fillet corners in the designed specimen, shown in Figure 2.5 on page 13, has the curvature as shown in Figure 3.5. This fillet corner curvature was selected since it was planned to cut the manufactured specimen from squared to cruciform geometry by water cutting. But due to the limited project period it is selected to cut the specimens at Aalborg University, thus the designed curvature cannot be obtained, which yields the fillet corner curvatures for the specimens to be as shown in Figure 3.6.

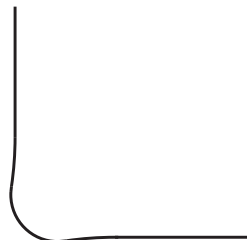


Figure 3.5 Designed fillet corners

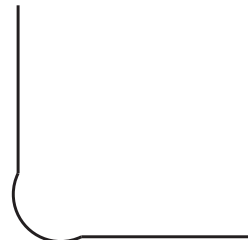


Figure 3.6 Tested fillet corners

It is assumed that this change has a negligible influence on the specimen w.r.t. number of cycles for first failure or the failure modes. This is supported by the FE shell model, where the maximum stress in the fillet corner is located within the radii.

Static Pilot Test 4

The static pilot test is conducted in order to gain knowledge for the fatigue tests and to gain experience with the test rig, as well as the test equipment. It is of interest to gain knowledge about the specimen strength and failure modes. The specimen strength is utilized in the setup for the fatigue tests. The failure modes are studied to be compared to the failure modes occurring in the fatigue tests, and to define the term first failure.

The setup and procedure for the static pilot test is described in Section 4.1. Camera observations are presented in Section 4.2 and failures are studied in Section 4.3. Strain gauge and DIC measurements are presented in Section 4.4 and compared in Section 4.5 together with the strains determined using an FE shell model.

4.1 Static Test of Specimen

The static pilot test is conducted by increasing the loads, with a constant loading rate, in the primary and secondary directions until total failure occurs. The load ratio is found by examining the strain ratio in the gauge zone, where a strain gauge rosette is positioned in the center. An initial guess of the load ratio, based on the load ratio determined in the optimization, is applied to the specimen at a relatively low load magnitude such that no damage occurs in the specimen, and afterwards the R_{strain} -result is examined. A new guess of the load ratio is then utilized and this procedure is repeated until the SWP specified strain ratio is obtained in the gauge zone. This results in $R_{Load} = 0.40$, which is in the vicinity of the optimized $R_{Load} = 0.445$, and is selected since it yields the SWP specified strain ratio.

The specimen used in the static pilot test is manufactured by SWP and cut into the cruciform geometry at Aalborg University, as described earlier. However, because a previous version of the working drawing is used to drill the holes, the arms in the primary direction ended up having a width of 140 [mm], instead of 200 [mm].

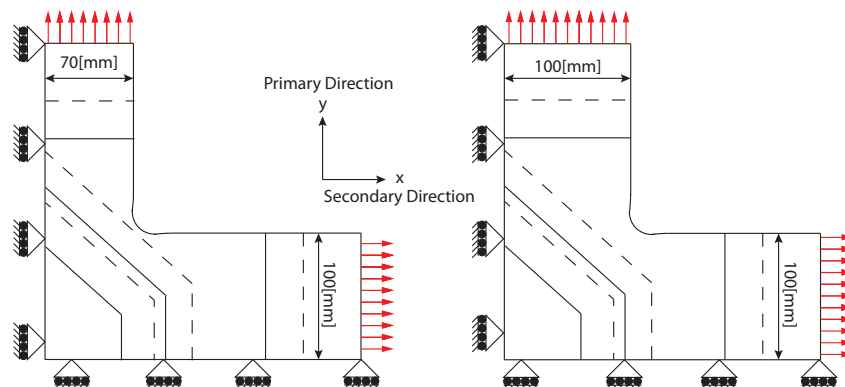


Figure 4.1 Comparison of primary arm widths

The difference is shown in Figure 4.1 and yields that the fillet corners are closer to the second ply drop boundary than intended, which can affect the static pilot test results.

The static pilot test is conducted even though the width of the arms is changed, since only a limited amount of specimens are available for the project.

4.2 Camera Observations

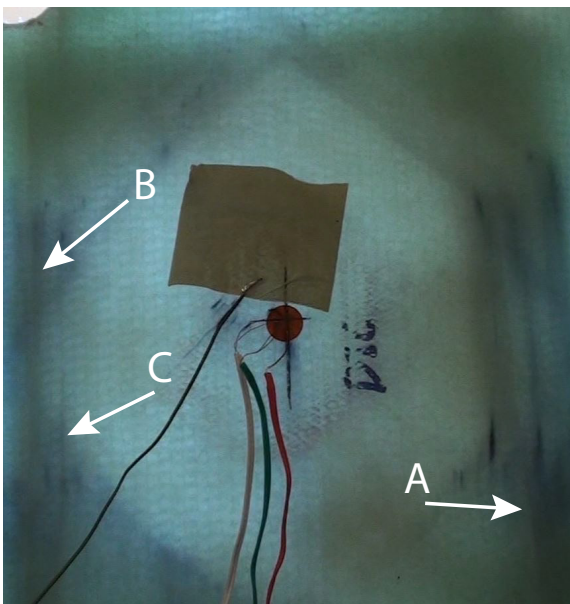
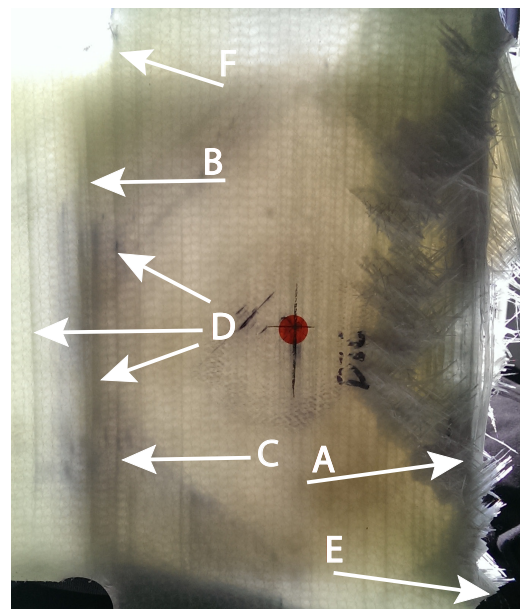
The goal of the fatigue test is to identify first failure together with the corresponding failure modes.

The static pilot test is therefore used to test and verify if this is possible. The camera observations are shown in Table 4.1 and the failures are studied in Section 4.3. The static pilot test ended due to total failure after approx. 1000 [s] corresponding to a load in the primary direction of 254 [kN]. Images of the failures are shown in Figure 4.2 and 4.3.

Table 4.1 Camera observations

ID	Time [s]	Observations	Primary Load [kN]	Secondary Load [kN]	Picture Reference
1	824	Crack in UD 0° lamina at lower part of specimen at third ply drop boundary near arm 2	208	85	Figure 4.3, (A)
2	886	Vertical crack similar to ID 1, but positioned at third ply drop boundary at upper part of specimen near arm 4	223	91	Figure 4.3, (B)
3	904	Crack at lower part of gauge zone at third ply drop boundary near arm 4	228	93	Figure 4.3, (C)
4	940-951	Further vertical crack initiation and propagation in the left and right side of the third ply drop boundary, i.e. near ID 1 and 2. The failure observations are more or less symmetric in and around the gauge zone	237-240	96-97	Figure 4.3, (D)
5	998	Crack initiation and propagation in fillet corners	251	102	Figure 4.3, (E) (F)
6	1002	Total failure propagated from the lower left fillet corner vertically through the width of the arm, where fiber failure can be seen	254	103	Figure 4.3

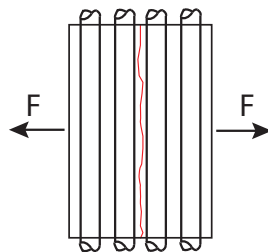
The forces shown in Table 4.1 are approximate values, which corresponds to the measurements shown in Figure 4.11.

**Figure 4.2** After first failures**Figure 4.3** Observed failures after total failure

4.3 Failure Mode Investigation

The failures observed during the static pilot test are analyzed in this section to get an understanding of the failure mechanisms occurring when the specimen is loaded.

In Table 4.1 the observed failures from the static pilot test are presented, where failure ID 1, 2, 3 and 4 are inter fiber failures (IFF). This failure mode mainly occurs when a lamina is loaded in the matrix dominated directions, i.e. transverse to the fibers and in-plane shear, as shown in Figure 4.4. The strength of the ply in the fiber direction is a lot higher than the transverse strength of the ply. This can also be assessed by the UD strength data presented in Table B.5 in Appendix B.5, where the UD material in the fiber direction has a strength of 914 [MPa] and a transverse strength of 45.7 [MPa]. Thus a small transverse load is needed for failure to occur, whereas a high load in the fiber direction is needed for failure to occur. Transverse loads often lead to IFF.

**Figure 4.4** IFF in a UD ply

The IFF's appear in the gauge zone and propagate until the second ply drop starts. This means that the IFF's start at the gauge zone, where the lay-up consists of 5 UD 0° and 4 BIAX 0° plies, and ends where the lay-up starts to include UD 90° plies, as shown in Figure 2.22 on page 22. Because the stiffness in the secondary direction is increased significantly.

IFF appears only in the UD laminae since no observations of failure in BIAX laminae are present.

Thus, it is assumed that the IFF's appear due to the secondary load, which is determined through $R_{Load} = 0.4$ and is approx. 9 times larger than the strength ratio of 0.05, i.e. (Y_t / X_t) .

The failures in the fillet corners (ID 5 in Table 4.1) appear in the UD 0° lamina and are IFF. This is assumed, since the cracks are only visible in the UD 0° laminae and the crack propagation is vertical, i.e. parallel to the 0° fibers. These failures occur after ID 1, 2, 3 and 4 because the lay-up around the fillet corners consists of 15 UD 0° , 8 UD 90° and 4 BIAX 0° plies, as shown in Figure 2.22, hence a higher strength in the secondary direction is present, due to the 8 UD 90° plies.

Total failure occurs in the left side of the specimen with a vertical cut between the two fillet corners. The total failure is a combination of the previous failures, as shown in Figure 4.5, where ID 1 and 5 failures are shown. ID 1 is a vertical IFF in the UD 0° lamina in the gauge zone and ID 5 is vertical IFF's in the UD 0° lamina around the fillet corners. Due to the above-mentioned smaller arms of the specimen, the fillet corners are closer to the gauge zone than for the designed specimen. Thus, it is assumed that total failure is caused by a strength reduction in a vertical region near arm 2, due to ID 1 and 5 failures. To get a better understanding of the total failure the specimen is studied under a microscope in Section 4.3.1.

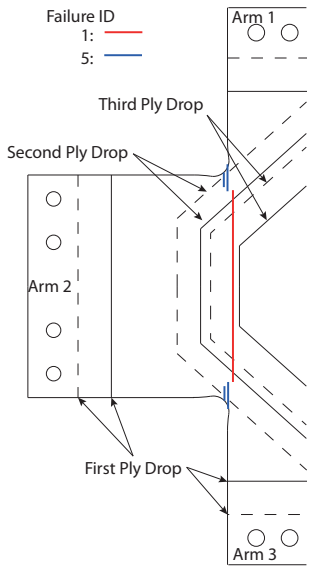


Figure 4.5 Static pilot test failures

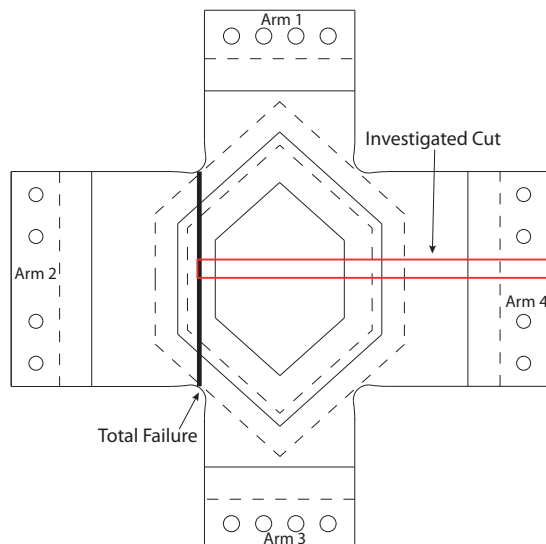


Figure 4.6 Cutout section of the specimen

The focus for the project is to obtain failure in the gauge zone, since this lay-up is of interest for SWP. The static pilot test showed failure in the gauge zone (failure ID 1-4), as intended, which means that the strength of the lay-up in the gauge zone is tested. After these failures the test becomes a structural test of the specimen geometry and the lay-up outside the gauge zone. However, the static pilot test is continued after first failure to clarify how and where total failure occurs, since it could occur in the gauge zone.

Total failure appeared between the lower and upper fillet corners in the left side, which is considered to be a structural failure. If total failure appeared in the gauge zone, both first and total failure would be of interest, but for this project it is selected to consider first failure for the tested specimens.

4.3.1 Microscopic Examination

A section going through the middle of the gauge zone of the static pilot test specimen, see Figure 4.6, is cut with a band saw and polished to be used in a microscopic examination of the failure modes occurring during the test. This is done in order to verify the above observations. The cut section is shown in Figure 4.7, where A indicates where total failure occurs, B shows where the strain gauge is positioned (close to the gauge zone center), C and D show IFF cracks in the middle of the gauge zone and E, F and G show IFF cracks in the ply drops at the gauge zone boundary close to where total failure occurs.

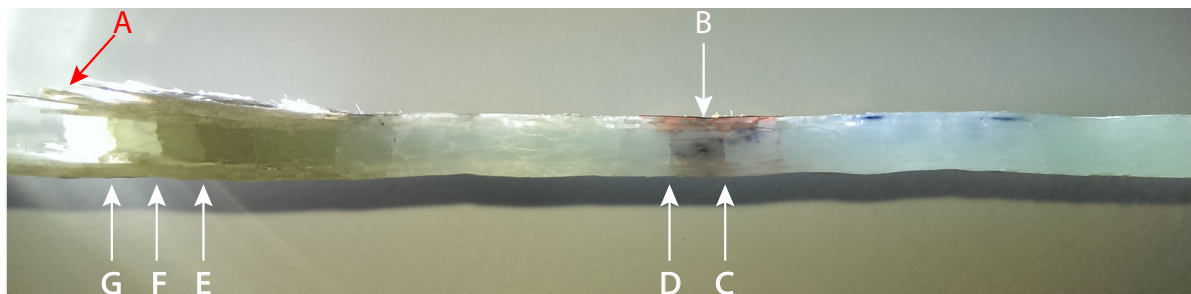


Figure 4.7 Failure modes observed in cutout section of the specimen

The marked cracks in Figure 4.7 are a few among many. These are chosen to give an idea of how the cracks appear in the specimen. Furthermore, some of the cracks cannot be seen from the camera observations. This is due to the failure sizes or position of the failures that make it impossible for the camera to observe them, since the light reflection through the specimen does not change when the failure occurs.

Crack C and D are examined under a microscope, as shown in Figure 4.8. The two IFF cracks start in the UD 0° lamina and propagate in the thickness direction until they reach the BIAX 0° lamina. At the upper end of crack C the BIAX 0° lamina shows indications of further crack propagation, which is most likely due to the UD 0° lamina crack. This is also the case for the lower end of crack D. The white branches in the middle of the UD lamina is the stitches in the glass fiber mats.

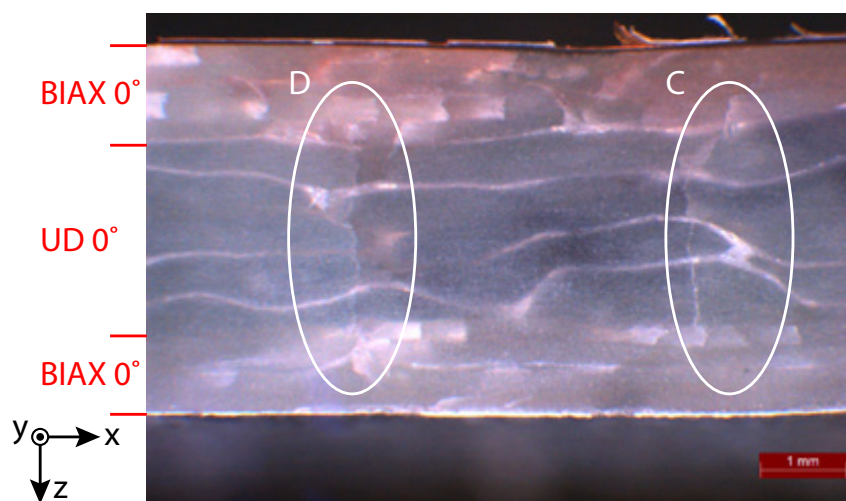


Figure 4.8 Crack C and D under microscope

The cracks E, F and G are shown in Figure 4.9, which are in the vicinity of the total failure area. These are similar to crack C and D with the exception that the BIAX 0° laminae are destroyed and a large amount of delamination is present. It is assumed that this mainly comes from the total failure, but as the section is cut with a band saw, delamination could also have occurred during this process.

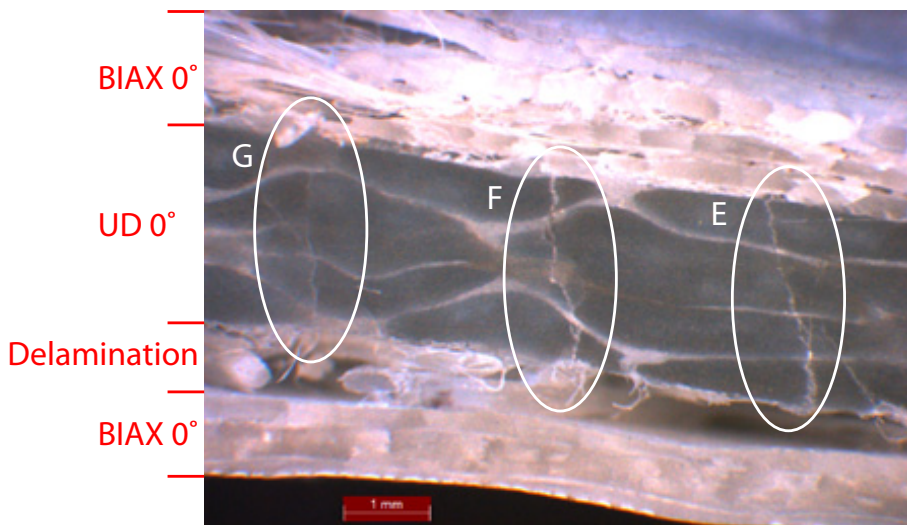


Figure 4.9 Crack E, F and G under microscope

It is assumed that the cracks propagate, as shown in Figure 4.8 in the thickness direction for the fatigue tests, if the cracks observed, with the naked eye, on the surface of the fatigue tests resemble the cracks observed on the surface of the static test.

4.4 Measurements

The measurements conducted during the static pilot test involve the results from the strain gauges attached to the specimen, the DIC equipment and the test rig controller output. The measurements are compared to the observations, shown in Section 4.2, to clarify whether or not failures can be detected by the DIC and strain gauges measured strain.

A load ratio that corresponds to a strain ratio equal to what SWP has specified, has been found by the use of the strain gauge rosette at the back of the specimen. However, when the test is conducted the strain ratio result shows a non-linear behavior at low load magnitudes, as shown in Figure 4.10. The non-linear behavior can be caused by several factors. It is to be expected that the specimen and the mounting plates are going to settle, when loads are applied in the beginning of the test. The settling of the specimen is caused by various imperfections in the specimen, as described in Appendix A.3. However, a biaxial load condition was applied to the specimen before the static test was conducted, so some of this settling should have already taken place. Furthermore, the hydraulic cylinders and the load cells on the test rig are designed for high loads, which means that there could be some deviations when small loads are applied.

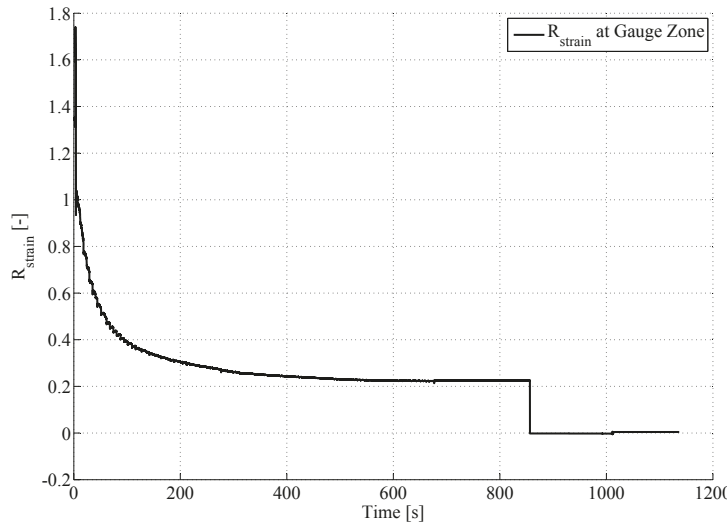


Figure 4.10 Strain ratio calculated based on strain gauge measurements

The asymptotic R_{strain} value is 0.22, which is less than the SWP specified $R_{strain} = 0.34$. Thus it is of interest to increase the load ratio in the fatigue tests in order to be in the vicinity of 0.34. Furthermore, the strain ratio is not known after approx. 856 [s], because the rosette strain gauge circuit in the primary direction failed. This is due to the configuration of the strain gauge measurement software Catman, as described in Appendix D.8, where a constant in the configuration of the strain gauges hindered data acquisition after a strain value of approx. 8000 [μ strain]. This constant is changed for the remaining tests to 40000 [μ strain].

The force subjected to the specimen is measured from the test rig controller and depicted w.r.t. time in Figure 4.11. First failure is marked with a green dotted line and the time where the rosette strain gauge circuit in the primary direction fails marked with a blue dotted line.

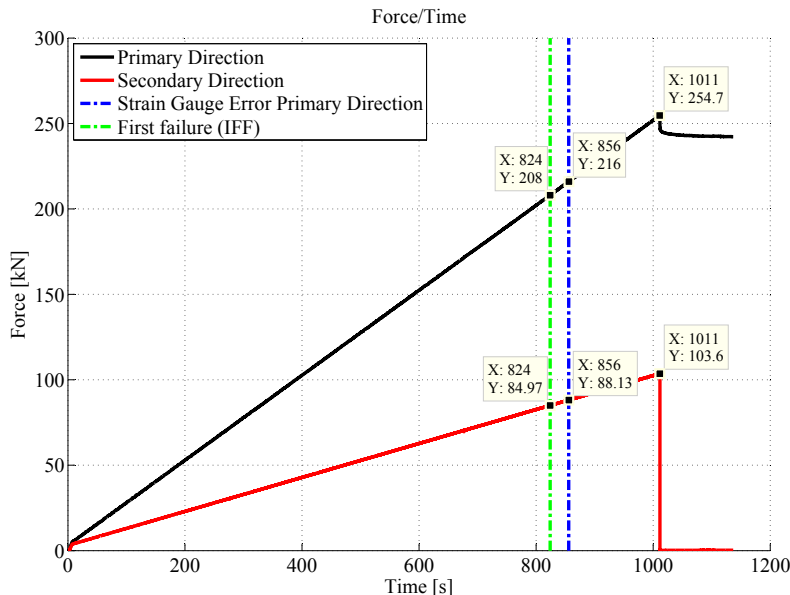


Figure 4.11 Force in primary and secondary directions vs. time

Total failure (ID 6 in Table 4.1) occurs at 1011 [s], which is different from the camera observations where total failure occurs after 1002 [s]. This is due to the time reference for the camera and the strain gauge measurements are offset by 9 [s], which has no further effect on the measurements.

4. Static Pilot Test

The primary and secondary loads obtained from the test rig controller are plotted against the measured strains from the strain gauge rosette in the primary and secondary directions as shown in Figure 4.12 and 4.13, respectively. For the force-strain in the secondary direction the graph is cut just before total failure occurs.

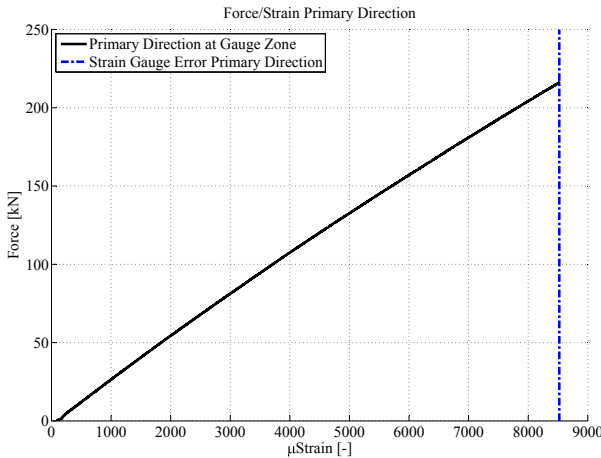


Figure 4.12 Force vs. strain in primary direction

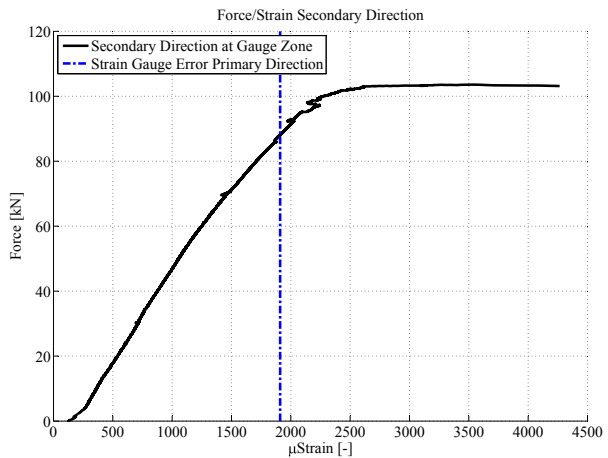


Figure 4.13 Force vs. strain in secondary direction

The result for the primary direction shows a general linear tendency until the primary strain gauge failed. Likewise for the secondary direction, but a non-linear tendency occurs when the specimen is close to total failure. Noise is present in Figure 4.13, but between 85 [kN] and 103 [kN] it could be due to the occurring failures.

As mentioned in Section 3.1, on page 28, strain gauges are positioned on two arms to determine whether or not in-plane bending is to be considered. The results from these strain gauges are shown in Figure 4.14 and 4.15.

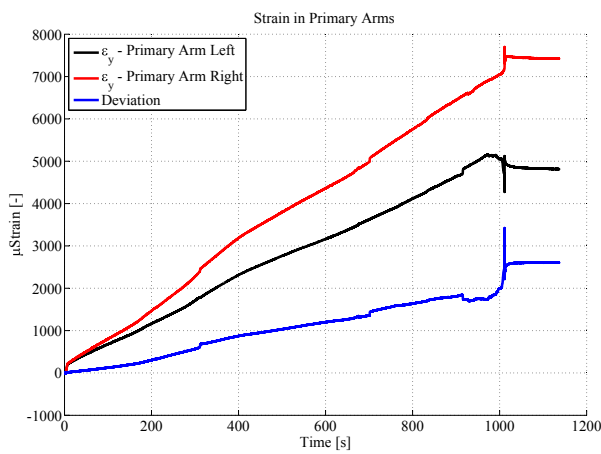


Figure 4.14 Strain in primary arms

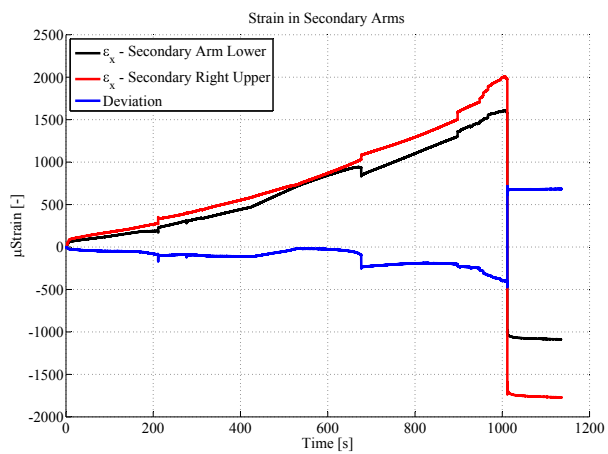


Figure 4.15 Strain in secondary arms

Bending is present in the primary and secondary directions. An estimate of the stresses that correspond to the strain deviation between the two sets of strain gauges has been calculated, which yields the bending stress to be roughly 20 [MPa] and 5 [MPa] in the primary and secondary direction, respectively. The equivalent stiffness used to calculate the bending stress is determined

as described in Appendix C.1.1.

Other sources for the moments could be placement error when strain gauges are mounted on the arms, due to different distance to the center axis or one is angled w.r.t the other. The specimen thicknesses can be another issue, because this yields different strains if the thickness in the two strain gauge areas is not identical.

The bending moments could have an influence on the result, and if these increase it should be included in the FE model. For the fatigue test, bending moments are studied, to observe whether it affects the tests or not.

The in-plane bending could be caused by multiple things, such as the mounting holes, irregular surfaces and asymmetric geometry, as described in Appendix A.3. A mismatch between the angle of the centerlines of the mounting holes, can yield a bending moment to be introduced, if these are not parallel.

The specimen is manufactured with irregular surfaces, as described in Appendix A.3, which can make the strain gauge measured strains erroneous. Another reason could be asymmetry in the cutout of the gauge zone plies, because these are cut by hand. Therefore it is necessary to be aware of this in-plane bending to ensure a reasonable validity of the fatigue results.

The temperature is monitored with a thermocouple positioned in the gauge zone. The temperature did not show any significant variation during the test. The result is shown in Appendix C.1.1 together with the strain gauge results.

4.4.1 DIC - First Failure

DIC measurements are conducted during the static pilot test. The DIC noise images are shown in Appendix C.1.3. The noise is between -50 [μ strain] and 50 [μ strain] for the primary direction and between -100 [μ strain] and 100 [μ strain] for the secondary direction. Figure 4.16 to 4.19 show the DIC results before and after first failure for the primary and secondary directions. The y-index and x-index are the facet numbers in the primary and secondary direction, respectively.

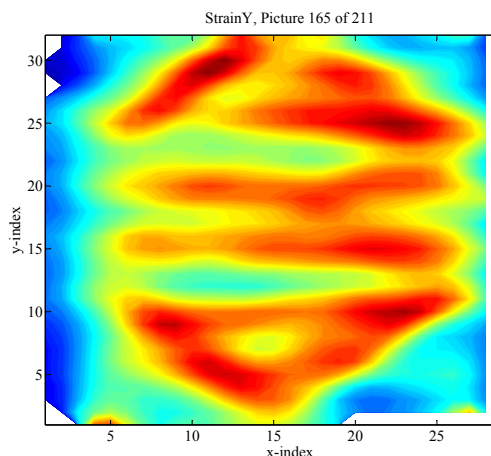


Figure 4.16 Contour plot in primary direction before first failure

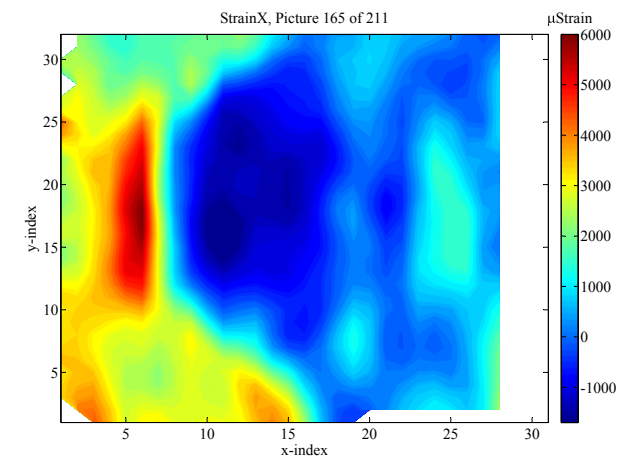


Figure 4.17 Contour plot in secondary direction before first failure

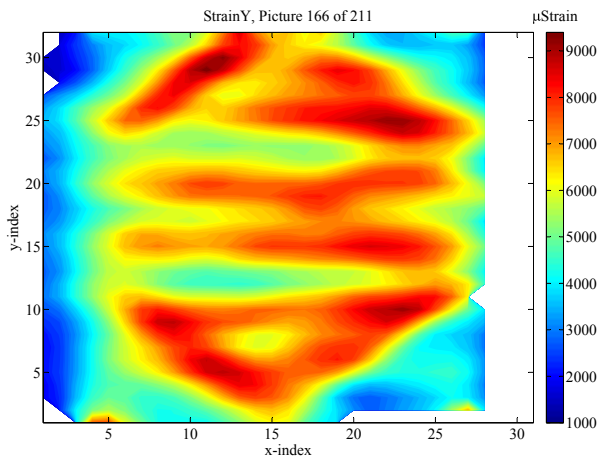


Figure 4.18 Contour plot in primary direction after first failure

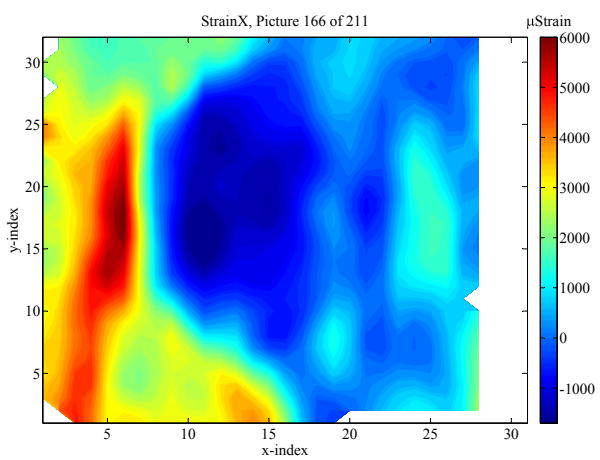


Figure 4.19 Contour plot in secondary direction after first failure

In the primary direction there is no noticeable differences before and after first failure. For the secondary direction it is clear that first failure can be seen in the left side of the DIC images. At index (4,7) in Figure 4.17 and 4.19, before and after first failure, respectively, the strain concentration increases which can indicate a crack initiation or propagation moving towards the lower left fillet corner.

This is in good agreement with the first failure, as shown in Figure 4.20. The failure is a vertical IFF crack, which goes through the third ply drop and into the gauge zone, which is similar to what the DIC shows.

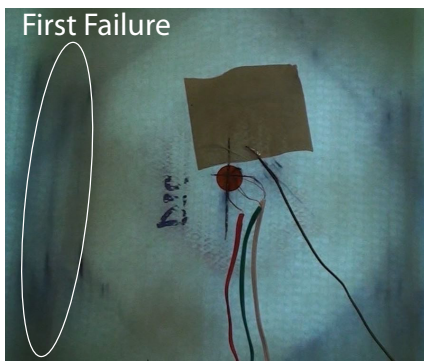


Figure 4.20 First failure (mirrored according to DIC result)

From the above-mentioned it can be concluded that it is possible to see this failure on the DIC, because the failure yields stiffness changes in the specimen, in which the strain field is changed.

As shown in Figure 4.17 and 4.19 the strain in the secondary direction is negative in an area within the middle of the gauge zone. It is assumed that the DIC equipment is not capable of finding the right correlation between the facets in the area with negative strain. A clarification of this assumption is not possible, since the DIC software does not allow the user to view the correlation values.

The negative strain does not make sense, since the specimen is loaded in tension in both directions with $R_{Load} = 0.40$, i.e. the Poisson's ratio effect from the primary direction is smaller than the resulting strain from the secondary load.

Due to these results it is assessed that the DIC equipment shows erroneous results in this area. Therefore a verification test of the DIC equipment is conducted in Appendix D.7, where improvements are found, to ensure that the equipment can measure reasonably correct strains. One of these improvements is to decrease the aperture, to enhance the depth of field, and increase the area in which the picture is in focus.

The flaws leading to the erroneous strain in the secondary direction can have affected the calculated strain in the primary direction as well. Even though the strain in the primary direction could be erroneous, the result still seems reasonable compared to the results from the strain gauge and it is therefore used in the further evaluation of the static pilot test.

It can be concluded that the DIC equipment can be employed to detect failure similar to the ID 1 failure in a specimen during test, by observing strain changes in the surface.

The shear strain does not show any significant change before and after first failure, but in order to give an idea of the shear strain distribution the result for shear strain is shown in Figure 4.21. The shear strain field in the center of the gauge zone has a negligible magnitude compared to the four corners, which are close to the fillet corners. This is in good agreement with the optimized FE result, where shear strain is negligible in the gauge zone and becomes larger near the fillet corners as well. The two blue spots near the center in Figure 4.21 are areas where the DIC equipment is unable to find a correlation.

The shear strain magnitude is insignificant compared to the strain in the primary and secondary directions, thus the measured shear strain in the gauge zone is not of interest for the remaining tests. The magnitude of the shear strain measured with strain gauge in the middle of the gauge zone is shown in Appendix C.1.1.

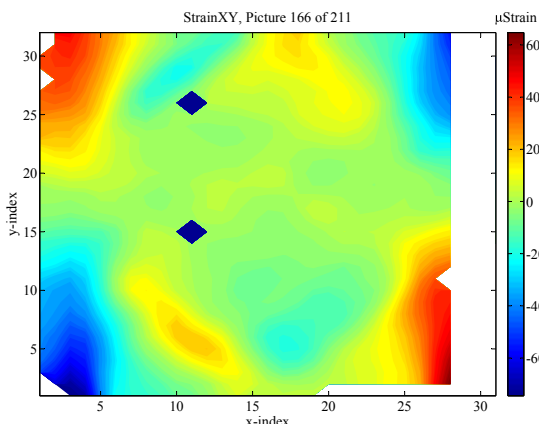


Figure 4.21 Shear strain after first failure

4.4.2 DIC - Total Failure

Figure 4.22 and 4.23 show the primary and secondary strains approx. 30 [s] before total failure. The strain distribution is similar to what is seen before and after first failure. However, one thing to notice is that the highest strain concentration in the secondary direction is moved closer to the fillet corner.

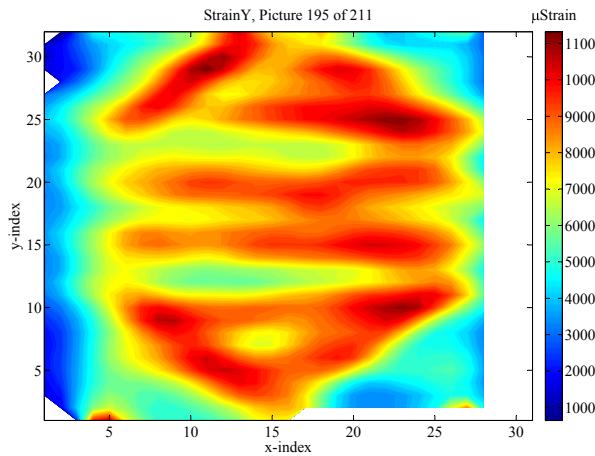


Figure 4.22 Contour plot of DIC strain in primary direction

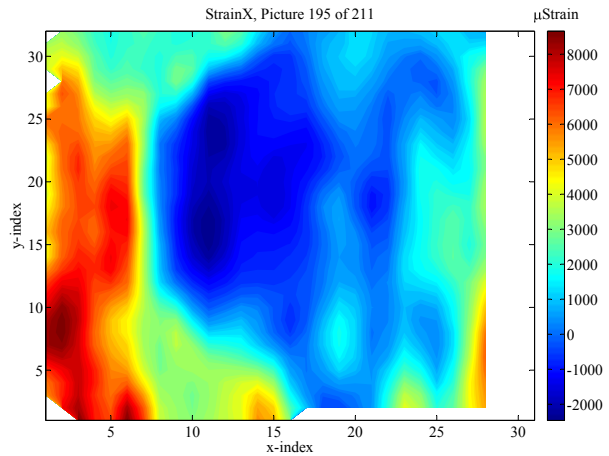


Figure 4.23 Contour plot of DIC strain in secondary direction

Furthermore, these are in strong contrast to the images just before total failure, as shown in Figure 4.24 and 4.25. The strain in the primary direction is negative at index (3,2), which is due to the previous failures. The secondary strain, in Figure 4.25, has a very high magnitude at index (3,1) compared to the strain in the remaining part of the strain field. From the camera observations it is shown that the total failure starts in the fillet corner and propagates vertically towards the upper fillet corner. This is in good agreement with the DIC images, where the high strain area is near the lower fillet corner and the strain contour is vertical.

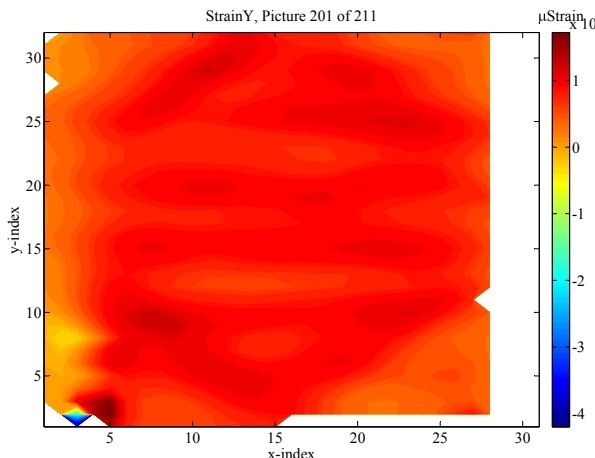


Figure 4.24 Contour plot of DIC strain in primary direction before total failure

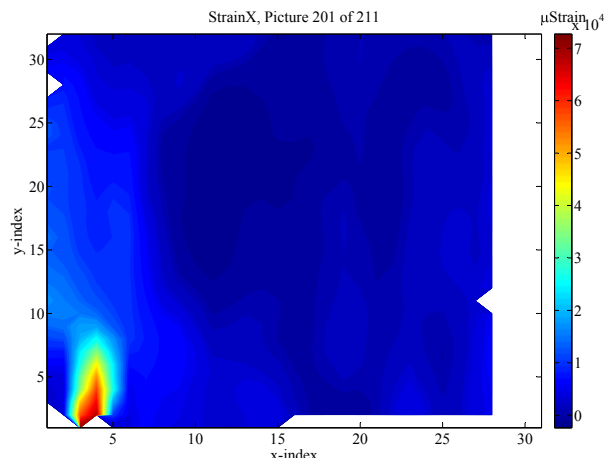


Figure 4.25 Contour plot of DIC strain in secondary direction before total failure

As a comparison to the strain gauge results the strains from DIC are extracted at the gauge zone center, and plotted against the time of the test. In Figure 4.26 the strain in the primary direction is shown for the strain gauge measured strain and the DIC. The DIC equipment calculates a strain field for each image, where the extracted strain value is probed for the center position of the gauge zone, for all 211 images and plotted w.r.t. time.

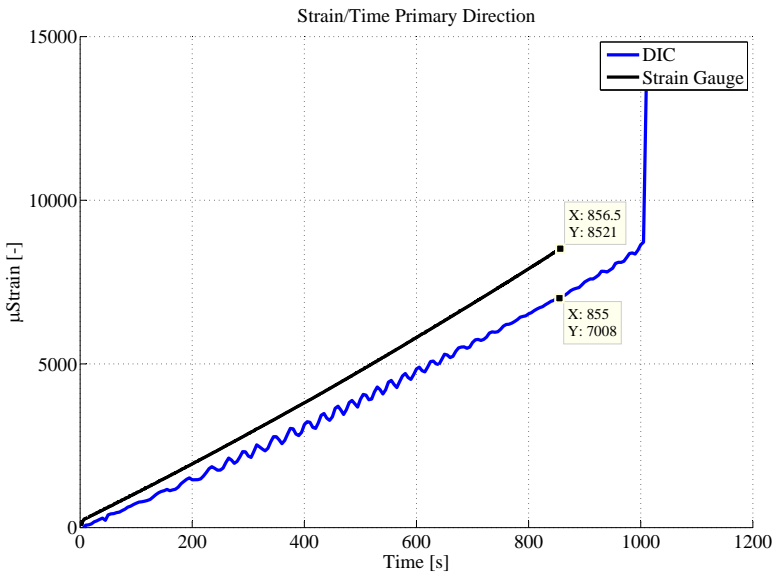


Figure 4.26 Strain in the primary direction in the gauge zone center

The strain gauge and DIC are not synchronized, and due to the aforementioned error with the strain gauge in the primary direction, no result is displayed after approx. 850 [s]. However, if the result at this point is compared to the DIC result at the same point, as shown in Figure 4.26, the deviation is approx. 18 [%]. The curves are close to being linear, where the slope of the strain gauge is approx. 8.6 and approx. 7.5 for DIC, thus the difference between the two measurement methods increases, when the load increases.

The measured strains for the secondary direction are not comparable due to the erroneous DIC result, hence these results are not shown.

The strain gauge results can be used to get the strain magnitudes in a minor area at the position of the strain gauge. If failure occurs somewhere in the specimen, the strain gauge result can include spikes, due to redistribution of loads. However, it is not possible to get a distribution of the strains or an indication of where the failure occurs.

On the other hand, it is possible to detect where failure occurs with DIC. Thus for the fatigue test, strain gauges are employed to monitor strain magnitudes at predefined positions, and DIC is employed to monitor strain distribution, magnitudes and failure in the gauge zone.

4.5 Comparison

In Table 4.2 the DIC obtained strains are compared to the strain gauge measured strains. Furthermore, two FE models are compared to the strain gauge measured strains. The first is a modified FE shell model, where the primary arm has the width of 140 [mm] as the static pilot test specimen. The second FE model is similar, but has a primary arm width of 200 [mm]. The simulated and measured strains are compared to clarify how the FE shell models predict the real strains.

All comparisons are performed for the strain gauge position in the center of the gauge zone, i.e., point measurements for DIC and FE in the center of the gauge zone.

In Appendix B.4 the FE shell model is validated to strain gauge and DIC monitored strains in five points. The validation shows that the FE model is better to predict strain in the primary direction compared to secondary direction and shear, since the largest deviation is 26 [%] and 12 [%] for strain gauge and DIC monitored strains, respectively. For the secondary direction and shear strain the deviations are larger, compared to the primary direction. This can be due to specimen imperfections and irregularities, which is experienced during testing and described in Appendix A.3.

Table 4.2 Comparison of strains for first and total failure

	Primary direction, ε_y [μstrain]	Secondary direction, ε_x [μstrain]	Shear, ε_{xy} [μstrain]	Primary direction deviation [%]	Secondary direction deviation [%]	Shear deviation [%]
First failure						
Strain gauge	8164	1842	107	-	-	-
DIC**	6749	-1471	1.0	17	180	99
FE shell model (modified)	9573	3119	1.9	17	69	98
FE shell model	5141	1604	0.4	37	13	100
Total failure						
Strain gauge*	N/A	4008	N/A	-	-	-
DIC**	8720	-860	3	N/A	121	N/A
FE shell model (modified)	11733	3768	2	N/A	6	N/A
FE shell model	6304	1934	0.5	N/A	52	N/A

* The strain gauge result stops recording in the primary direction around 850 [s], hence N/A.

** The DIC results are erroneous in the secondary direction.

The DIC deviates 17 [%] in the primary direction compared to the strain gauge, which is acceptable. The DIC measured erroneous strain in the secondary direction, where the shear strain is also affected by this, thus comparison between these and the strain gauge result makes no sense. This is seen by the large deviations of 180 [%] and 99 [%] for the secondary and shear strains, respectively, and 121 [%] for total failure.

The modified FE shell model overestimates the primary and secondary strains, but the shear strains is underestimated. Secondary and shear strains have large deviations compared to the strain in the primary direction. For total failure the secondary strain is within 6 [%] of the strain gauge measured strain.

The FE shell model underestimates all strains for both first and total failure, where the deviation for the secondary strain is acceptable for first failure, but not for the primary strain. Near total failure the specimen is exposed to different failures, which yields a non-linear strain behavior when monitored in the gauge zone. This non-linear strain behavior yields larger differences to the FE model strains, as the FE models are linear analyses.

The differences between the two FE models are caused by the different arm widths. The modified

FE shell model transfers higher stresses into the specimen in the primary direction than the FE shell model, as the area of the arms in this direction is smaller.

This comparison between FE, strain gauge and DIC measured strains show the same trend as the validation in Appendix B.4, where the strain in the primary direction has a small deviation compared to deviations in the secondary direction and for shear strain.

The strain ratio presented for the static pilot test in Figure 4.10 has a non-linear behavior at low loads, which is due to imperfections and irregularities in the specimen. It is not possible to eliminate all imperfections or irregularities, such as inclusions etc., when manufacturing a composite specimen, even though a lot of effort is put into doing so. When the specimen is loaded, micro cracks and general settling of the structure occurs, which could also create disturbances in the measured results.

The fundamental idea of the static pilot test is to gather knowledge of the specimen strength and failure modes, which are used for the fatigue tests, and this has been accomplished.

Fatigue Tests 5

In this chapter the fatigue tests are defined and the results are presented subsequently. Initially the general setup is defined for the fatigue tests in Section 5.1. Fatigue test 1 (FT1) is defined in details and results are presented in Section 5.2. Likewise for FT2, FT3 and FT4 in Section 5.3, 5.4 and 5.5, respectively. Finally the test data used for the fatigue simulations in Part III are summarized in Section 5.6.

5.1 General Setup for Fatigue Tests

For the four fatigue tests a maximum primary force, F_{max} , is selected, and since SWP has specified $R_{CL} = 0.1$, as described in Section 1.3 on page 8, the minimum primary force, F_{min} , is dependent on F_{max} .

The secondary load is determined through the SWP specified strain ratio in the gauge zone of 0.34, presented in Section 1.3. Due to the behavior of the strain ratio it is selected to have the specified strain ratio where the primary and secondary forces are at maximum.

During the static pilot test it is shown that the strain ratio dropped and settled at a constant level, as shown in Figure 4.10 on page 39. To ensure that the load ratio yields the specified strain ratio, a static test is performed. It is similar to the static pilot test, but this test is stopped when the primary load reaches 50 [kN]. From this test the strain ratio is studied and a load ratio for the fatigue test is selected. Thus, the secondary maximum and minimum loads are determined by R_{Load} and R_{CL} .

It is of interest to inspect the specimen for visual failures and to be able to take DIC images during the fatigue tests. The camera observations are supplemented by inspections of the specimen, which can yield that more failures can be observed. As described in Section 3.1 on page 28, DIC equipment is employed to monitor the strain field in the gauge zone. Furthermore, the static pilot test shows that IFF failures can be monitored by DIC, thus DIC is employed for the fatigue tests as well, since these observations can be used as another supplement to the camera observations.

This yields a testing procedure called a test sequence, as shown in Figure 5.1. A test sequence consists of a number of steps wherein one of the steps include a number of cyclic loads. When the test sequence is done, the fatigue test is paused.

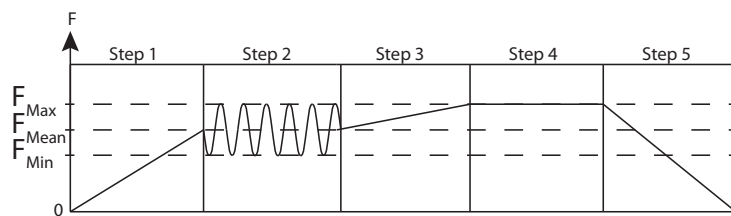


Figure 5.1 Step sequence procedure

In step 1 the applied force is ramped to the mean value of the sine wave in step 2. For the sine wave an amplitude, a frequency and a number of cycles are selected. The amplitudes for the fatigue tests are described in the individual sections for the fatigue tests. The frequency is set as high as possible, to decrease the test time, but the test rig has to be stable at all times. The number of cycles in the test sequence is a parameter which is changed through the fatigue tests. This is because it is of interest to inspect the specimen frequently in the beginning of the tests. Furthermore, a phase angle of 180° is employed for the secondary actuator movement, which ensures synchronized movement, i.e. F_{max} is reached simultaneously for the two actuators. Issues w.r.t. this is described in Appendix D.1.

In step 3 the force is increased to the maximum load, F_{max} , where it in step 4 is held for 5 [s]. This makes it possible to take a DIC image at the maximum load. Finally the specimen is unloaded in step 5, which completes the test sequence and another can begin.

This is the test procedure for the fatigue tests for both actuators. Generally for all steps is that a new step can only begin when the previous step for both actuators is finished.

5.2 Fatigue Test 1

In this section FT1 is defined in Section 5.2.1 and results and experiences are presented in Section 5.2.2. FT1 is based on the static pilot test in order to have a starting point, since no knowledge of the specimen fatigue behavior or strengths are known.

5.2.1 Definition

The static pilot test first failure occurred with a primary load of 208 [kN]. FT1 is performed at 160 [kN] which is approx. 75 [%] of the load for first failure in the static pilot test. 75 [%] is selected, because it is of interest to perform FT1 fast, to gain knowledge about the specimen fatigue behavior and to get an idea of how many cycles the specimen can withstand. In Table 5.1 the parameters for FT1 are shown.

Table 5.1 Setup parameters for FT1

Load parameters		
Direction	F_{max} [kN]	F_{min} [kN]
Primary	160	16
Secondary	64	6.4
General parameters		
R_{Load}	Frequency [Hz]	Cycles in step 2
0.4	0.5 - 2.5	100-5000

FT1 is the first test where the project group has used the test rig for fatigue test, thus the project group has no knowledge of the test rig performance during fatigue tests. This yields that low frequencies and a low number of cycles are used at first and later higher frequencies and more cycles are used in each test sequence. This can be seen in Table 5.1, where the frequency and number of cycles are shown in intervals.

5.2.2 Results

FT1 is performed where 378000 cycles are achieved with the loads shown in Table 5.1, before FT1 is stopped. The test is continued after first failure to clarify if the specimen behaves similarly in fatigue as what is experienced for the static pilot test. The results from the different types of equipment are presented subsequently.

Camera Observations

The camera observations for first failure is presented in Table 5.2 and the failures are shown in Figure 5.2.

Table 5.2 FT1 failures

ID	Cycle	Observations	Picture Reference
FT1-1	102	First failure appeared in the lower right side of the gauge zone. The lower part of the crack appeared at 102 cycles and after 103 cycles it propagated to the upper ply drop boundary	Figure 5.2, (A)
FT1-2	124	Second failure appears through the entire gauge zone and third ply drop boundary	Figure 5.2, (B)
FT1-3	163	Third failure is similar to FT1-2, but positioned symmetric w.r.t. the vertical center axis	Figure 5.2, (C)
FT1-4	300	Vertical failure outside the gauge zone in the fillet corner between arm 3 and 4	No Image

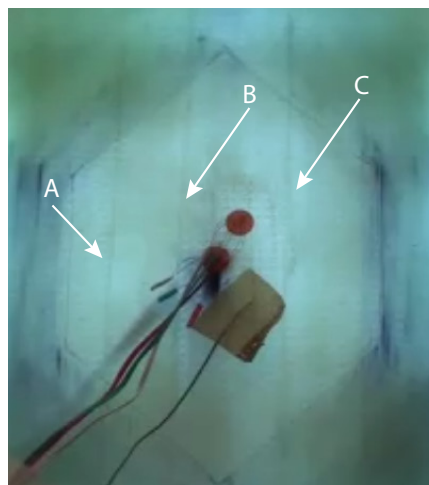


Figure 5.2 FT1 failures

First failure (FT1-1) is an IFF in the gauge zone, which is caused by the applied transverse load, as described in Section 4.3, on page 35. Failure ID FT1-2, FT1-3 and FT1-4 are also IFF failures, where failure ID FT1-4 is located in the fillet corner.

The failure modes and order are similar to what is observed for the static pilot test.

Measurements

The strain ratio during FT1 is shown in Figure 5.3, where it is plotted for a step sequence with 100 cycles, from cycle 200 to cycle 300. The strain ratio varies during each cycle, but

as mentioned above, it is of interest to have the specified strain ratio where both the primary and secondary actuator are at F_{max} . This strain ratio is shown by the red line, which has a value of 0.35 and is close to the SWP specified $R_{strain} = 0.34$. Thus, the strain ratio for FT1 is acceptable.

Furthermore, the strain ratio is spot checked during the test, which reveals no difference. In Appendix C.2.1 the strain ratio is shown after 59300 cycles, where the value of 0.35 is maintained.

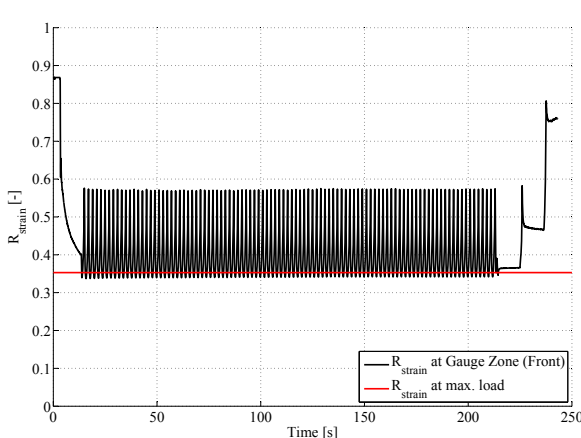


Figure 5.3 Strain gauge measured strain ratio after 200 cycles

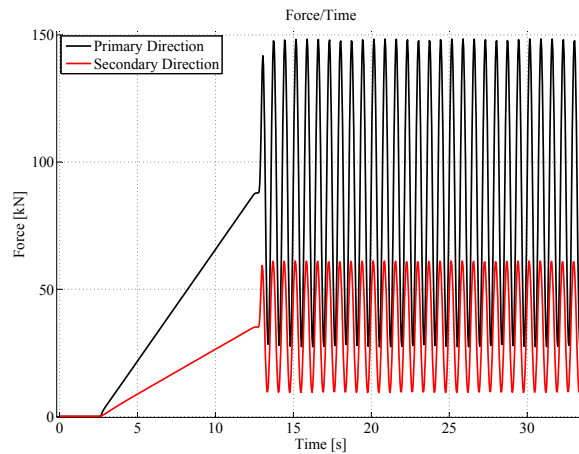


Figure 5.4 The primary and secondary forces during FT1

The primary and secondary forces are shown in Figure 5.4. The plot should have shown peaks as determined in Table 5.1, but this is not the case, due to multiple reasons. The primary force output from the test rig controller is a filtered signal, in which the real force signal cannot be obtained. This is changed in the controller output during the test from a filtered option to a tracked option, i.e. peaks near 160 [kN] and 16 [kN] appear.

Furthermore, FT1 is performed with frequencies between 0.5 and 2.5 [Hz]. In the high end of this frequency interval the output from the controller is too slow, i.e. it is not possible to sample the entire load tracks from the controller. Thus, the load peaks in Figure 5.4 do not reach the loads determined in Table 5.1.

The amplitude setting (Enable Amplitude Control) in the program for the secondary direction was not enabled, thus the secondary amplitude is smaller than what is expected, i.e. the specimen is not loaded as intended. This is realized during the test and enabled, which entailed that the peaks for the secondary actuator got near 64 [kN] and 6.4 [kN], as determined in Table 5.1.

Since the secondary load has been below the required value it is assumed that the fatigue life is increased, i.e. more cycles can be performed before first failure occurs.

The monitored bending moments during FT1 have small magnitudes and no deviation during the test is present, hence, these are neglected. The strain gauge measured strain in the arms is shown in Appendix C.2.1.

The static pilot test proved that DIC measured strain can be used to detect IFF's in the gauge zone. This can also be seen for FT1, as shown in Figure 5.5 and 5.6, which are the DIC strain fields from before and after first failure, respectively, for the secondary direction. The DIC noise is ca. $\pm 40\mu$ strain, the images are shown in Appendix C.2.2.

First failure occurs in the right side of the gauge zone, but it cannot be seen in the DIC strain field. This is because the strain field is not calculated in this area, since the DIC equipment was not able to recognize the pattern on the surface, due to the wires from the strain gauge.

The marked areas, B and C, in Figure 5.6 are in good agreement with FT1-2 and FT1-3, as shown in Figure 5.2. Strains in these areas are doubled, and it is assumed that these changes are due to the failures.

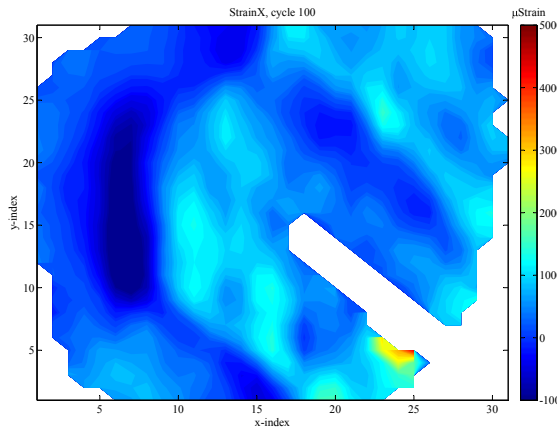


Figure 5.5 Strain field of secondary direction before first failure

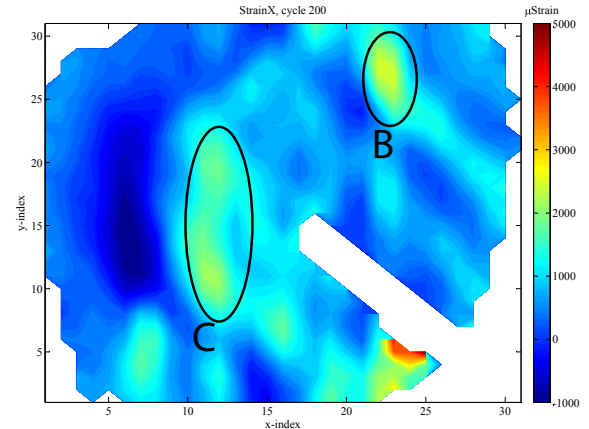


Figure 5.6 Strain field of secondary direction after first failure

In Figure 5.7 and 5.8 images from the thermal camera are shown from the start of FT1 and around 60000 cycles, respectively, where failures in the gauge zone and fillet corners appear. At the start of FT1 the specimen temperature is under 27 [°C] and only the strain gauge rosette circuits have a higher temperature. The specimen temperature increases during FT1, where the general temperature is between 27-30 [°C], which is in good agreement with the measured temperature from the thermocouple, presented in Appendix C.2.1.

There are two reasons why the temperature of the specimen increases. The first is that the temperature of the hydraulic cylinders increases, which directly causes the specimen temperature to increase because the primary cylinder is in direct contact with the specimen. The other reason is that the hydraulic fluid heats up the entire room. Furthermore, the strain gauge circuit temperature is again over 30 [°C].



Figure 5.7 Thermal image from FT1 start

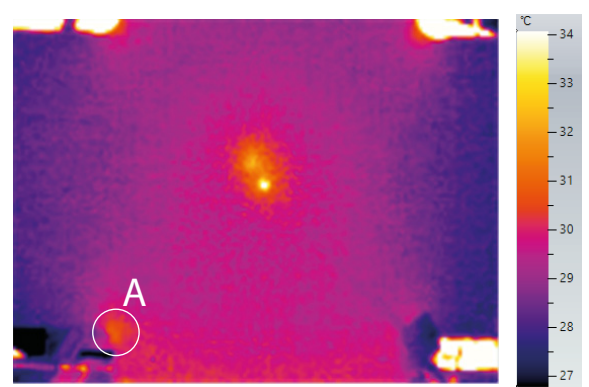


Figure 5.8 Thermal image around 60000 cycles

The highest specimen temperature is around the fillet corners. This can be due to failure in the fillet corners (FT1-4), where crack surfaces are rubbed against each other. This is illustrated in

the lower left fillet corner, marked A in Figure 5.8.

The increased temperatures can also be seen for the two upper fillet corners. However, these temperatures can be misleading, because the temperature gradients on the edge of the specimen are large, due to the hydraulic cylinder and hoses behind the specimen.

For the remaining fatigue tests the thermal camera is not employed, because it is not possible to track cracks in the gauge zone, because either no heat is produced due to friction, or the thermal camera is just not sensitive enough to detect the change in temperature. This could be due to the accuracy of $\pm 2 [^{\circ}\text{C}]$ as described in Appendix E.5. Henceforth, the thermocouple is the only temperature reference.

5.2.3 Gained Knowledge

During FT1 it is realized that the applied forces are close to the maximum of what the secondary test rig can handle. This can be seen by the failures of the secondary test rig occurring during FT1, which are described in Section 5.2.4. Thus, if testing with loads close to the loads applied in FT1, it is to be expected that failures occur in the secondary test rig, due to the lack of fatigue strength. This is also in good agreement with the setup for the remaining tests, because it is of interest to achieve more than 102 cycles for first failure in these.

The FT1 failures are similar to what is seen for the static pilot test, i.e. first failure is IFF in the gauge zone followed by similar IFF's in the gauge zone and finally IFF's in the fillet corners.

First failure occurred after 102 cycles, which is earlier than expected. The FT1 primary load of 160 [kN] is approx. 75 [%] of the primary load for first failure in the static pilot test.

This early first failure can be explained by the strain ratio in the gauge zone. A higher strain ratio yields higher strain/stress in the secondary direction, which results in earlier failure, due to the IFF failure mode.

The strain ratio during the static pilot test is 0.22, as presented in Figure 4.10, and 0.35 for FT1. This difference affects the number of cycles for first failure, thus the specimen strength from the static pilot test is misleading, due to the strain ratio. Furthermore, the changed arm widths, described in Section 4.1 on page 33, can also have affected the static pilot test result, which FT1 is based on.

5.2.4 Errors During FT1

During FT1 multiple errors occurred, which are described in details in Appendix D. Some of the errors are emphasized in the following.

- Asynchronous load configuration
- Mounting plates for secondary direction
- Bolt failure in bushing
- Arm failure
- Failure in rod end

The asynchronous load configuration is a programming error, which is detected after the first cycle step and changed for the remaining FT1 and employed for FT2, FT3 and FT4. This could have affected the number of cycles for first failure, since the specimen is not loaded as intended, i.e. first failure occurred after a different number of cycles, than if the actuator movements had been synchronous from first cycle.

The existing mounting plates for the secondary direction failed, thus new and stronger mounting plates are designed by the project group and manufactured in the workshop at Aalborg University.

The bushing consists of two parts, which are constrained by a screw. This screw failed because it is not prestressed properly. To ensure that this does not occur again, a different procedure for tensioning of the mounting plates are employed.

The load from the secondary actuator is distributed to the specimen through two arms, one in each side, as shown in Figure 1.4 on page 6. One of the arms failed and it is chosen to redesign the arms. New arms are designed by the project group and manufactured in the workshop at Aalborg University and mounted in the test rig.

Rod ends are used to distribute the load from the actuator to the specimen in the test rig for the secondary direction. One of the rod ends failed, due to the cyclic fatigue loads. The failed part is replaced with an identical part, which is a standard component from the manufacturer SKF. Five more rod ends failed during the rest of the tests, this is described in Appendix D.6.

5.2.5 Sub-Conclusion

First failure occurred after 102 cycles in the gauge zone as an IFF identical to what is seen in the static pilot test. Both second and third failure occurred in the gauge zone a few cycles after first failure. These failures appear similar to what is seen for the static pilot test, so it is assumed that the failure modes shown in Figure 4.8 on page 37 are valid for this test as well.

First failure occurred too early compared to what is of interest, thus for the remaining fatigue tests lower load magnitudes are employed.

The strain ratio for FT1 is 0.35 and is acceptable, even though SWP has specified $R_{strain} = 0.34$. The difference of 0.01 is acceptable, since the specimen has a non-linear behavior as described for the static pilot test, in Section 4.4 on page 38, thus it is difficult to achieve a certain strain ratio.

Furthermore, it is shown how the strain ratio cycles during FT1 and that $R_{strain} = 0.35$ is obtained when both actuators are in F_{max} , as it is intended.

5.3 Fatigue Test 2

5.3.1 Definition

FT2 is based on the experience from FT1, where first failure occurred after 102 cycles. 102 cycles for first failure is considered to be too few cycles for a fatigue test. To achieve more cycles before first failure occurs, the load magnitudes for FT2 are selected, as shown in Table 5.3. FT1

did not provide enough knowledge to the project group to enable a selection of load magnitudes. Therefore, load magnitudes are determined through a previous version of the FADAS algorithm presented in Chapter 8. The algorithm estimates first failure to occur at 30000 cycles, which is considered to be beneficial due to the limited testing time.

Table 5.3 Setup parameters for FT2

Load parameters		
Direction	F_{max} [kN]	F_{min} [kN]
Primary	125	12.5
Secondary	55.6	5.56
General parameters		
R_{Load}	Frequency [Hz]	Cycle steps
0.445	2.5	500-10000

5.3.2 Results

FT2 ran for 464500 cycles before the test is stopped, because it is realized that first failure cannot be obtained within the test time for FT2. The results for FT2 are presented subsequently.

Camera Observations

The camera observations for FT2 are presented in Table 5.4 and in Figure 5.9.

Table 5.4 FT2 failures

ID	Cycle	Observations	Picture Reference
FT2-1	7600	IFF appear in all fillet corners	Figure 5.9, (A)

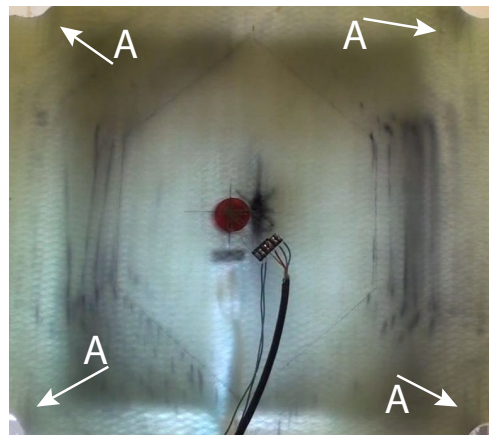


Figure 5.9 Camera observed failures

The FT2 loads are determined through a previous version of the FADAS algorithm, which showed failure around 30000 cycles in the gauge zone. In FT2 no failure appeared in the gauge zone after 464500 cycles. Therefore, this method to determine loads is not beneficial, since large differences between the used previous version of the FADAS algorithm and the reality appear.

In the static pilot test and in FT1 first failure in the gauge zone occurred before IFF in the fillet corners. In FT2 IFF occurred in the fillet corners around 7600 cycles and after 464500

cycles first failure in the gauge zone has not occurred. Thus the order of failures for FT2 are not similar to the static pilot test or FT1.

Measurements

Measurements from FT2 are shown in Appendix C.3 and the important observations are stated in this section.

The strain ratio for FT2 is determined before FT2 is initialized by a static test, similar to the one described in Section 5.1, where a satisfactory strain ratio is obtained. The load ratio resulting from this static test is employed for FT2. Thus it is assumed that a strain ratio close to the SWP specified is obtained during FT2.

After the first 500 cycles $R_{strain} = 0.24$. However, for these cycles the strain in the secondary direction is erroneous, because the strain cycles from positive to negative values. This effect subsides after 17000 cycles where the strain ratio is increased to 0.27 when the primary and secondary actuator is at F_{max} and this magnitude is maintained throughout the rest of FT2. The strain ratio is smaller than the SWP specified $R_{strain} = 0.34$, to a degree where it is not acceptable.

The strain gauge data shows that the initial monitored strains are erroneous and therefore not reliable until 17000 cycles. The reason for the erroneous strains could be due to noise in the measured strains or the configuration of the CatmanEasy software. It is assumed that the erroneous strains can have affected the static test where the FT2 load ratio is determined as well, in which the load ratio becomes erroneous and yields $R_{strain} = 0.27$.

Bending is present during FT2, but due to the magnitude of the bending stresses, these are neglected, since these do not exceed ± 2 [MPa] in the primary and secondary direction.

No failure in the gauge zone occurred during FT2, thus no relevant DIC results are post-processed.

5.3.3 Gained Knowledge

The previous version of the FADAS algorithm used to estimate the number of cycles for failure, showed a large difference between simulated and actual failure. Therefore, it is necessary to employ another method of estimating the required loads for the fatigue tests. This is described in Section 5.4.

The strain gauge measurements showed erroneous results, which yield that further focus has to be on configuration, mounting, etc. of strain gauges for the remaining tests.

5.4 Fatigue Test 3

5.4.1 Definition

The previous methods used to determine loads for FT1 and FT2 are not satisfactory because they yield first failure to occur too early or not at all, respectively. This yields that another approach is utilized for FT3.

First failure observed, in this project, is IFF in the UD lamina in the gauge zone, i.e. the transverse fatigue strength for the UD lamina can be used to estimate the number of cycles for failure. The transverse stress is determined from measured strains in the gauge zone. The stress is used to determine the number of cycles for failure based on an S-N curve for the transverse direction. The measured strains are monitored from the strain gauge rosettes on the front and back, when the specimen is loaded. The used S-N curve is determined from coupon tests performed by OptiDAT.

Multiple things can affect this approach. The strain gauges can be mounted on a surface irregularity, as described in Appendix A.3, in which the measured strain can be erroneous. Since two strain gauges are used the most reliable strains are employed for the stress calculation. An evaluation of the strains are performed to determine whether or not the strains are reliable by looking into the strain ratio, since it is known, from previous tests, that $R_{Load} = 0.445$ yields the strain ratio to be around the SWP specified strain ratio.

The stress is calculated using Classical Laminate Theory (CLT) where a plane stress assumption is employed, i.e. the measured strains are used together with the UD lamina stiffness and Poisson's ratio in the primary and secondary direction. These material properties can be erroneous, since only normalized material properties are delivered from SWP, as described in Appendix B.5.

The slope of the used S-N curve has a small magnitude, which means that a small change in stress magnitude yields a large change in number of cycles for failure. Furthermore, the S-N data used is based on a GFRP with slightly different material properties than the one used to manufacture the specimens. Therefore, the estimated cycles through the CLT calculation are used as a rough estimate.

The parameters for FT3 are shown in Table 5.5.

Table 5.5 Setup parameters for FT3

Load parameters		
Direction	F_{max} [kN]	F_{min} [kN]
Primary	150	15
Secondary	66.75	6.68
General parameters		
R_{Load}	Frequency [Hz]	Cycle steps
0.445	2.5	500-4000

5.4.2 Results

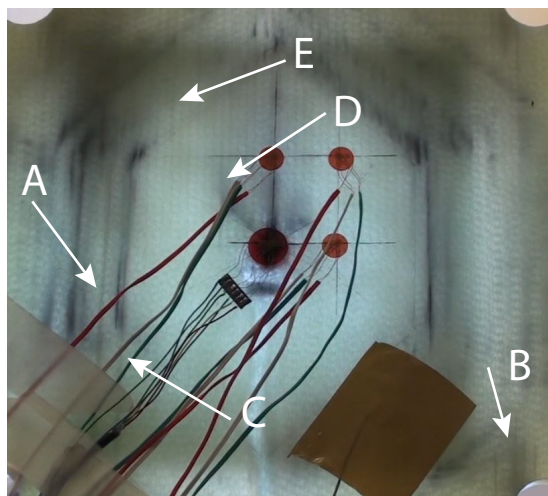
The results from FT3 are presented subsequently, where the test is stopped after 256000 cycles.

Camera Observations

Camera observations from FT3 are presented in Table 5.6 and shown in Figure 5.10.

Table 5.6 FT3 failures

ID	Cycle	Observations	Picture Reference
FT3-1	0	IFF is initiated from the start of FT3 and propagates vertical towards the top of the gauge zone after 11000 cycles	Figure 5.10, (A)
FT3-2	2250	IFF's in all fillet corners	Figure 5.10, (B)
FT3-3	32000	IFF in the right ply drop boundary	Figure 5.10, (C)
FT3-4	93500	First IFF inside the gauge zone close to the center	Figure 5.10, (D)
FT3-5	104000	IFF in top of the gauge zone, which propagates into the gauge zone around 120000 cycles	Figure 5.10, (E)

**Figure 5.10** Camera observed failures

Failure (FT3-1) is observed from the start of FT3, which can be due to the approach for determination of the FT3 loads, as explained in Section 5.4.1. An imperfection could have been present in the manufactured specimen and triggered by the initial loads before FT3 is started. This is supported by the fact that the initial failure does not propagate until after 11000 cycles. Thus, FT3-1 is not considered as first failure.

First failure (FT3-3) occurred in the ply drops outside the gauge zone, which must be due to imperfections around the start of a ply drop and yields an IFF along the ply drop boundary. Like FT2 failure in the fillet corners is seen before first failure for FT3.

Measurements

Measurements from FT3 are shown in Appendix C.4 and the important observations are stated in this section.

$R_{strain} = 0.39$ from the start of the test and after 96000 cycles it increases to 0.42. For FT3 the strain ratio is higher than the SWP specified strain ratio, thus the load ratio magnitude should have been decreased.

The FT3 specimen is exposed to bending throughout the test with a constant magnitude, both for the primary and secondary direction. Bending could have affected the specimen to fail more

in one side than the other, due to higher strain and stress. However, the bending stresses acting in the specimen in either direction is neglected because of the negligible magnitude, as shown in Appendix C.3.

The temperature during FT3 is similar to what is shown earlier for FT1 and FT2.

From the DIC calculated strain field the propagation of FT3-1 is detected. However, the remaining failures cannot be detected by the DIC.

5.5 Fatigue Test 4

5.5.1 Definition

As mentioned in Chapter 3 on page 27, it is of interest to perform FT4 identical to FT3 w.r.t. load magnitudes, etc., to study the difference between two identical tests. However, this is not possible, because identical loads on the two specimens, yield different strain magnitudes. In an attempt to get a strain field with magnitudes similar to FT3, the load ratio is increased and the primary load magnitude is decreased.

The setup for FT4 is shown in Table 5.7.

Table 5.7 Setup parameters for FT4

Load parameters		
Direction	F_{max} [kN]	F_{min} [kN]
Primary	148	14.8
Secondary	67.3	6.7
General parameters		
R_{Load}	Frequency [Hz]	Cycle steps
0.455	2.5	500-4000

5.5.2 Results

The results from FT4 are presented subsequently, where the test is stopped after 137000 cycles.

Camera Observations

Camera observations from FT4 are presented in Table 5.8 and shown in Figure 5.11.

Table 5.8 FT4 failures

ID	Cycle	Observations	Picture Reference
FT4-1	1600	IFF in all fillet corners	Figure 5.11, (A)
FT4-2	17150	IFF on the boundary between the gauge zone and the first ply drop	Figure 5.11, (B)
FT4-3	73000	IFF in ply drops	Figure 5.11, (C)

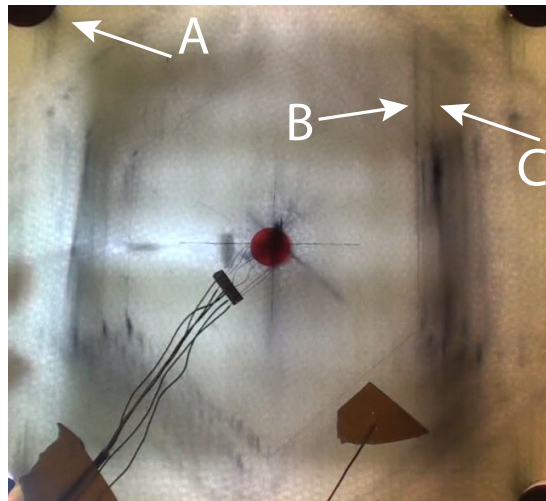


Figure 5.11 Camera observed failures

First failure (FT4-2) occurred after 17150 cycles and is an IFF in the ply drops. Second failure occurs after 73000 cycles close to the location of the first failure. FT4-2 is considered as first failure, even though it is most likely initiated due to an imperfection. This is assumed because FT4-3 is located right next to it, and appears more than 55000 cycles later. Because the large difference between when the failures appear it is assumed that first failure is triggered due to an imperfection in or around the ply drop boundary.

Failure in the fillet corners appeared after 1600 cycles, i.e. before first failure as observed for FT2 and FT3.

Measurements

Measurements from FT4 are shown in Appendix C.5 and the important observations are stated in this section.

$R_{strain} = 0.31$ when measured after 500 cycles and 0.39 after 57000 cycles. Again is it shown that the strain ratio is difficult to keep constant around the SWP specified strain ratio during a fatigue test.

Bending is present for FT4 with magnitudes similar to those for FT3. The bending moment is neglected, since it is difficult to determine the impact of the bending in the primary and secondary directions.

The temperature during FT4 is similar to what is shown for the other fatigue tests.

5.6 Fatigue Test Summary

In Table 5.9 the obtained results are presented in order to identify the data used for comparison between the fatigue tests and simulations in Chapter 10 on page 87. The location of the observed failures are shown in the table in the column FL (failure location).

Table 5.9 Fatigue Test Failures

Fatigue Test 1			
ID	Cycle	Observations	FL
FT1-1	102	First failure	
FT1-2	124	Second failure	
FT1-3	163	Third failure	
FT1-4	300	Failure in fillet corner	-
Fatigue Test 2			
ID	Cycle	Observations	FL
FT2-1	7600	Failure in fillet corner	-
Fatigue Test 3			
ID	Cycle	Observations	FL
FT3-2	2250	Failure in fillet corner	-
FT3-3	32000	First failure	
FT3-4	93500	Second failure	
FT3-5	104000	Third failure	
Fatigue Test 4			
ID	Cycle	Observations	FL
FT4-1	1600	Failure in fillet corner	-
FT4-2	17150	First failure	
FT4-3	73000	Second failure	

Part III

SIMULATION OF FATIGUE TEST

Introduction to FADAS

6

In order to simulate fatigue tests a state-of-the-art fatigue life prediction algorithm is implemented into ANSYS. This fatigue life prediction algorithm is based on the linear FAtigue DAmage Simulator (FADAS), which is a linear progressive damage simulation algorithm for composites under cyclic loading.

FADAS is based on a ply-to-laminate approach making it possible to estimate fatigue life of numerous laminates of different stacking sequences. "Ply-to-laminate" means that experimental characterization of the typical static and fatigue properties, such as strength, stiffness, etc. for the individual plies, are used in a stacking sequence which is solved numerically e.g. by FE software [V.A. Passipouliardis, 2010].

The main topics within the linear FADAS algorithm are:

- Progressive strength degradation
- Puck's failure criteria
- Stiffness degradation

Progressive strength degradation is based on a linear model calculating the residual strength due to the stress level and the number of cycles. The model is stated as the simplest model available and it requires no residual strength testing [V.A. Passipouliardis, 2010]. The strength degradation is described more in detail in Section 8.6 on page 78.

Puck's failure criteria are implemented into FADAS to determine if failure occurs at the ply level and to determine what type of failure mode is occurring. More details about the failure criteria are stated in Chapter 7 on page 67.

Stiffness degradation is dependent on the occurring failure modes stated by Puck's failure criteria. This is described more in detail in Section 8.8 on page 79.

In Chapter 1 on page 3 different categories of fatigue models are introduced. With respect to these categories the FADAS algorithm falls into a gray area, as it can be classified both as a phenomenological- and a mechanistic model. The problem with this classification is that no clear boundaries are stated between the different categories, making it hard to place FADAS under a specific category. The FADAS algorithm takes the actual fatigue damage of the material into account, but empirical data as S-N curves and empirical constants implemented in Puck's failure criteria are also used in the algorithm.

The FADAS algorithm is implemented into ANSYS by the use of a programmable subroutine called "UserMat". The subroutine allows the user to write specific material constitutive equations within a general framework using current-technology element types [ANSYS, 2011b]. The subroutine is written in the scripting language FORTRAN and it is called at every integration point of the used element type when the analysis is solved.

In order to run the subroutine in ANSYS the Newton-Raphson procedure is utilized. An example of the Newton-Raphson procedure is shown in Figure 6.1. The Newton-Raphson procedure makes it possible to divide the load into sub steps, shown as F_{sub_j} in this example, in order to solve non-linear problems. Each sub step is divided into a number of equilibrium iterations, shown as F_{eq_i} in the example. For each equilibrium iteration the Jacobian matrix (tangent stiffness matrix, shown as K^T in Figure 6.1), stresses and strains are calculated in the material routine and stored for use in ANSYS. The so-called state variable values (e.g. residual strength, residual stiffness) are continuously updated to the appropriate values at the end of each sub step. The procedure is continued until the specified load step, shown as $F_{Load\ step}$ in Figure 6.1, is obtained.

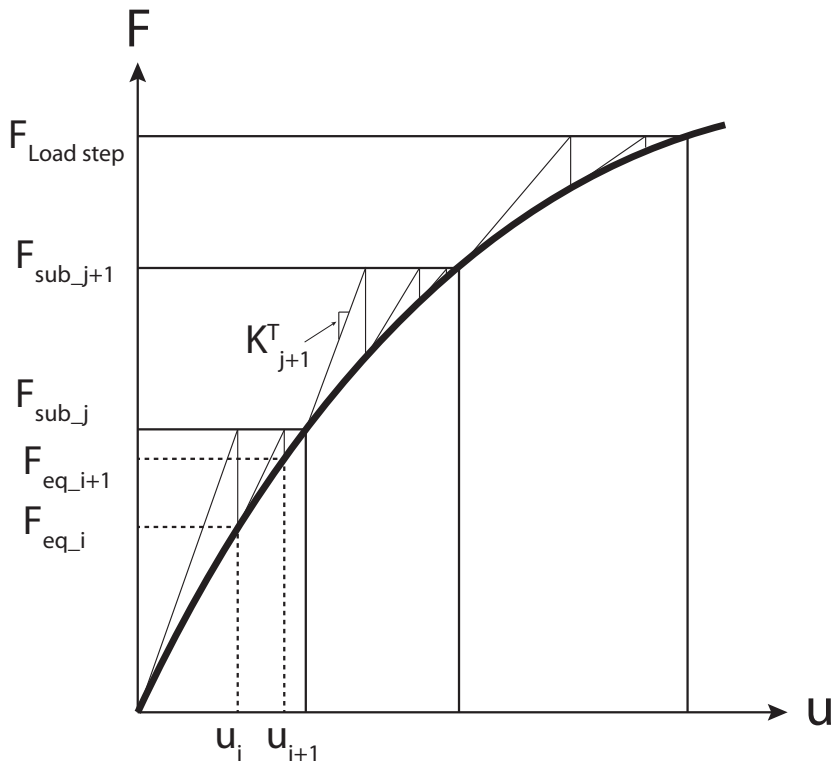


Figure 6.1 Newton-Raphson procedure, F and u are force and displacement, respectively

The FADAS algorithm is adapted to a shell model. The element type used for this model is SHELL181 with reduced integration, reducing the 4-node layered element to only have one integration point in the middle of the element and one through the thickness of each layer. This is done in order to keep the computational time at a reasonable level compared to a higher order element or if full integration is utilized.

Failure Criteria

7

The FADAS algorithm in Philippidis [2011] and V.A. Passipoulardis [2010] is based on Puck's failure criteria, this is also the case in this project. Puck's failure criteria are presently some of the best failure criteria. At the World Wide Failure Exercise Puck's criteria were evaluated as the best, especially because they can predict what kind of failure there occurs. [Knops, 2008] In this chapter Puck's failure criteria are presented. In Section 7.1 and 7.2, the different failure modes are introduced and the expressions used to determine whether failure has occurred or not are introduced as well.

The magnitudes of the constants used in the presented equations can be found in Appendix B.5 in Table B.7. Furthermore, the material strengths in the presented equations are the residual strengths calculated by the FADAS algorithm, which is presented in Chapter 8 on page 73.

Puck's failure criteria are derived in a general 3D form, and based on the assumption that FRP behave as a brittle material. However, Puck has simplified the criteria to a 2D case, which is utilized in this project. The simplified formulation utilizes that the out-of-plane stresses are assumed to be negligible, when dealing with thin laminates, which is the case for the specimen in this project, especially in the gauge zone.

When using the 2D formulation, no search for the fracture plane among the action planes is necessary. The fracture plane is, in short, defined as the action plane in a lamina where the risk of failure is highest, based on the stresses in the lamina. The theory behind the numerical search for the fracture plane is not described in this report, since, the fracture plane can be found analytically for the 2D case. A detailed description of the theory behind the fracture plane can be found in Knops [2008].

In the failure criteria, a parameter called the stress exposure factor is used. This factor indicates whether failure has occurred or not. There is a factor for each type of failure, and when this factor exceeds 1, failure of the given type is predicted.

Usually UD GFRP can be regarded as transverse isotropic, where it is an advantage to use the term, stressing, which is used because transverse stresses, σ_2 and σ_3 cause the same stress in the material. Therefore the stressings in Figure 7.1 are used in relation with Puck's failure criteria, especially w.r.t. IFF modes.

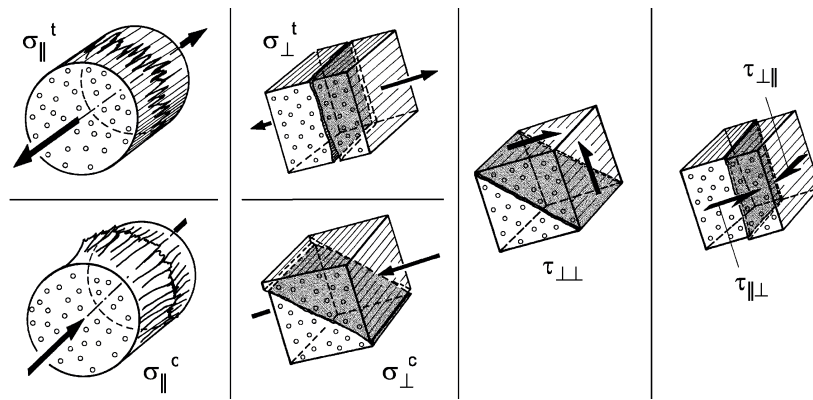


Figure 7.1 Stressings [Knops, 2008]

7.1 Fiber Failure (FF)

Depending on the stress condition in the lamina, the fibers can fail in different ways, as shown in Figure 7.2. However, the three compression dominated failure modes are calculated using the same failure criterion, as shown in Equation (7.2).

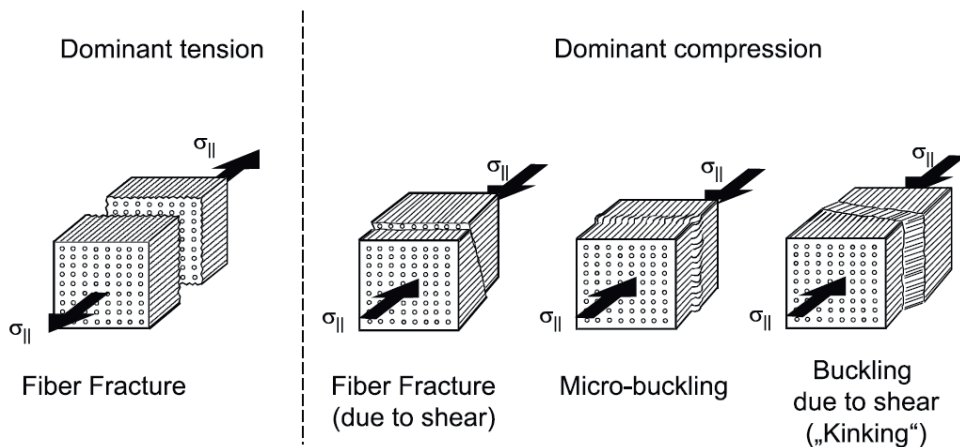


Figure 7.2 Different FF modes [Knops, 2008]

For a simple analysis regarding failure in the fiber direction, the stress and strength in the fiber direction is required. However, for a more accurate analysis, it is necessary to include stresses developed by strains transverse to the fibers and in shear, due to Poisson’s effect [Knops, 2008]. The FF criteria are based on the assumption that fibers fail when the stress in the fibers is higher than the strength of the fibers. This is why the material parameters of the actual fibers, E_{f1} and ν_{f12} , are used in Equation (7.1) and (7.2) along with the stiffness of the lamina. Furthermore, at the interface between fibers and matrix, there is a local effect that causes increased biaxial strain, this is simulated using a ‘stress magnification factor’, $m_{\sigma,f}$, that is included in the expression for fiber failure. E_{f1} , ν_{f12} and $m_{\sigma,f}$ are parameters which are determined through experiments. The criterion for tension FF is shown in Equation (7.1) and is only employed when an element is in tension. For compression FF Equation (7.2) is used and is only employed if an element is in compression.

$$f_{E(FF)} = \frac{1}{X_{tr}} \cdot \left(\sigma_1 + \left(\frac{E_{11}}{E_{f1}} \cdot \nu_{f12} \cdot m_{\sigma,f} - \nu_{12} \right) \cdot \sigma_2 \right) \quad (7.1)$$

$$f_{E(FF)} = \frac{1}{X_{cr}} \cdot \left| \left(\sigma_1 + \left(\frac{E_{11}}{E_{f1}} \cdot \nu_{f12} \cdot m_{\sigma,f} - \nu_{12} \right) \cdot \sigma_2 \right) \right| + (10 \cdot \gamma_{12})^2 \quad (7.2)$$

where:

$f_{E(FF)}$	Stress exposure factor for FF, [-]
X_{tr}	Residual tension strength in fiber direction, [MPa]
σ_1	Stress in fiber direction, [MPa]
E_{11}	Stiffness in the fiber direction, [GPa]
E_{f1}	Stiffness of fiber material, [GPa]
ν_{f12}	Poisson's ratio of fiber material, [-]
$m_{\sigma,f}$	Fiber/Matrix interface stress magnification factor, [-]
ν_{12}	Poisson's ratio of lamina, [-]
σ_2	Stress transverse to fibers, [MPa]
X_{cr}	Residual compression strength in fiber direction, [MPa]
γ_{12}	In-plane shear strain, [-]

When considering compression, experimental tests show that the compressive strength is reduced, when high shear stresses are present in the lamina. This is included in the failure criterion as the last part in Equation (7.2).

7.2 Inter Fiber Failure (IFF)

Puck operates with three different modes of IFF. These modes occur at different stress conditions in the lamina, as shown in Figure 7.3. Mode A occurs when tension stress is acting transverse to the fiber direction. Mode B and C occur when compression stress is acting transverse to the fibers.

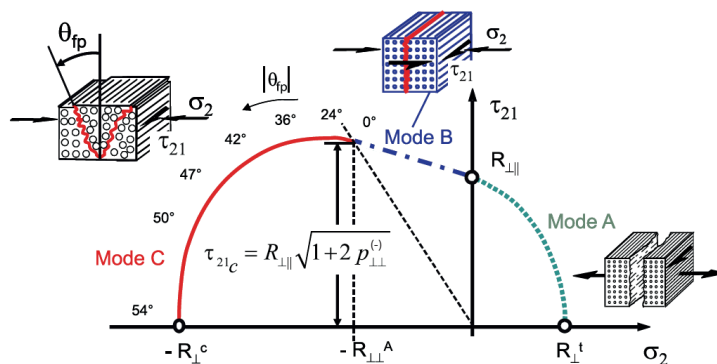


Figure 7.3 IFF fracture envelope [Knops, 2008]

where:

R_{\perp}^c	Fracture resistance of the fracture plane against σ_{\perp}^c , [MPa]
R_{\perp}^t	Fracture resistance of the fracture plane against σ_{\perp}^t , [MPa]
$R_{\perp\perp}^A$	Fracture resistance of the fracture plane against $\tau_{\perp\perp}$, [MPa]
$R_{\perp\parallel}$	Fracture resistance of the fracture plane against $\tau_{\perp\parallel}$, [MPa]
$p_{\perp\perp}^{(-)}$	Slope of the compressive part of the fracture envelope at $R_{\perp\parallel}$ for $\tau_{\perp\perp}$, [-]
θ_{fp}	The angle of the fracture plane, [-]
τ_{21c}	Shear stress at the 'turning point' of the fracture envelope, [MPa]

The angle of fracture for IFF mode C is determined based on the relation between the transverse stress and the shear stress, as shown in Figure 7.3. It can be seen that a higher compression transverse stress can be tolerated than a tensile transverse stress. Furthermore, when a compressive stress is acting in the lamina, a higher shear stress can be tolerated. This is not the case with tensile stresses.

Puck introduces two parameters, to determine what IFF mode is relevant to consider at the given stress conditions. One of them is τ_{21c} and it is calculated as shown in Figure 7.3. The second parameter, $R_{\perp\perp}^A$, is calculated as shown in Equation (7.3).

$$R_{\perp\perp}^A = \frac{Y_{cr}}{2(1 + p_{\perp\perp}^{(-)})} \quad (7.3)$$

where:

Y_{cr}	Residual transverse compression strength, [MPa]
----------	---

These two parameters are used in Equation (7.5) and (7.7) to determine which failure mode there occur. In the following sections the three failure modes are described in more detail.

7.2.1 IFF Mode A

IFF mode A (IFF A) can only occur when a tensile transverse stress is acting on a lamina. However, shear stress has a huge influence on when failure occurs as well. The crack surface is perpendicular to the transverse direction, because the stress exposure factor, $f_{E(IFF)}^A$, in this action plane is highest.

The failure criterion for IFF A is dependent on several factors which for the most part are included in the fracture envelope (Figure 7.3), as shown in Equation (7.4). However, the last part in the expression is of another nature. It is included to take a statistical breakage of fibers into account before X_{tr} or X_{cr} is reached. This is necessary because of the high amount of energy released when a fiber breaks that causes the interface between fibers and matrix to fail [Philippidis, 2011].

$$f_{E(IFF)}^A = \sqrt{\left(\frac{\tau_{21}}{S_{21r}}\right)^2 + \left(1 - p_{\perp\parallel}^{(+)} \frac{Y_{tr}}{S_{21r}}\right)^2 \left(\frac{\sigma_2}{Y_{tr}}\right)^2} + p_{\perp\parallel}^{(+)} \frac{\sigma_2}{S_{21r}} + (0.9 f_{E(FF)})^6 \quad (7.4)$$

where:

$f_{E(IFF)}^A$	Stress exposure factor for IFF mode A, [-]
S_{21r}	Residual shear strength, [MPa]
$p_{\perp\parallel}^{(+)}$	Slope of the tensile part of the fracture envelope at $R_{\perp\parallel}$ for $\tau_{\perp\parallel}$, [-]
Y_{tr}	Residual transverse tensile strength, [MPa]

In IFF A it is assumed that the two faces of the crack are not in contact. From that it is reasonable to assume that no load can be transferred from one crack face to another. This means that E_{22} , G_{12} and ν_{12} can be considered equal to zero at the crack. However, if the lamina is part of a laminate, it can be assumed that some of the load carrying capabilities of the lamina are maintained, this is described in Section 8.8 on page 79.

7.2.2 IFF Mode B

IFF mode B can only occur when the conditions in Equation (7.5) are met and the stress exposure factor is determined in (7.6).

$$\sigma_2 < 0 \text{ and } 0 \leq \left| \frac{\sigma_2}{\tau_{21}} \right| \leq \frac{R_{\perp\perp}^A}{|\tau_{21c}|} \quad (7.5)$$

The conditions above are also displayed in Figure 7.3. They describe that IFF mode B occurs when a high shear stress and a moderate compressive transverse stress is applied. The fracture plane is perpendicular to the transverse direction, which is the same as the action plane of the acting shear stress, τ_{21} [Knops, 2008]. The compressive transverse stress can not produce a mode B failure on its own, which can also be observed by the lack of Y_{cr} in Equation (7.6). The compressive transverse stress impedes fracture up to a point, which means that mode B failure is controlled by the shear stress, and hereby the shear strength.

$$f_{E(IFF)}^B = \frac{1}{S_{21r}} \left(\sqrt{(\tau_{21})^2 + (p_{\perp\parallel}^{(-)} \sigma_2)^2} + p_{\perp\parallel}^{(-)} \sigma_2 \right) + (0.9 f_{E(FF)})^6 \quad (7.6)$$

where:

$f_{E(IFF)}^B$	Stress exposure factor for IFF mode B, [-]
$p_{\perp\parallel}^{(-)}$	Slope of the compressive part of the fracture envelope at $R_{\perp\parallel}$ for $\tau_{\perp\parallel}$, [-]

When IFF mode B occurs, the crack faces are pressed together which means that the lamina can carry loads. Therefore, it is assumed that E_{22} and ν_{12} are unchanged. However, the crack faces can slide w.r.t. each other, when a frictional force is exceeded. This frictional force is not considered in Puck's criteria, so G_{12} is decreased as if no friction occurs between the two faces [A. Puck, H. Schürmann, 1999], as described in Section 8.8 on page 79.

It is possible that a fracture can start as a mode B, but end up as a mode C which is completely controlled by the compressive transverse stress. This transition results in a high fracture angle that has a high risk of causing delamination and local buckling in the laminate. [A. Puck, H. Schürmann, 1999]

7.2.3 IFF Mode C

IFF mode C can only occur when the conditions in Equation (7.7) are met and the stress exposure factor is determined in (7.8).

$$\sigma_2 < 0 \text{ and } 0 \leq \left| \frac{\tau_{21}}{\sigma_2} \right| \leq \frac{|\tau_{21c}|}{R_{\perp\perp}^A} \quad (7.7)$$

IFF mode C occurs when a high compressive transverse stress and low or no shear stress is applied. The angle of the fracture plane is controlled by the applied shear stress, as shown in Figure 7.3. When the shear stress increases, the stress condition moves towards the area of mode B which means that the angle of fracture is decreased, which makes sense since the angle of a mode B fracture is 0° .

IFF mode C is the most damaging IFF mode because, as mentioned, at high fracture angles there is a risk of delamination and local buckling in the laminate. This is called the 'wedge', or 'explosion' effect, because the high compressive transverse stress that is built up in the lamina is released after fracture as an out-of-plane force during a short period of time. [A. Puck, H. Schürmann, 1999]

$$f_{E(IFF)}^C = \left(\left(\frac{\tau_{21}}{2 \left(1 + p_{\perp\perp}^{(-)} \right) S_{21r}} \right)^2 + \left(\frac{\sigma_2}{Y_{cr}} \right)^2 \right) \frac{Y_{cr}}{-\sigma_2} + (0.9 f_{E(FF)})^6 \quad (7.8)$$

where:

$$f_{E(IFF)}^C \mid \text{Stress exposure factor for IFF mode C, [-]}$$

When IFF mode C occurs, the crack faces are in contact, but the crack faces can slide w.r.t. each other which means G_{12} is degraded. Furthermore, when compressive transverse stress is acting on the crack faces, the 'wedge' is able to move out of plane, which means that E_{22} is degraded as well, but ν_{12} is not degraded.

However, because of the 'wedge' effect IFF mode C is often considered as total failure of a laminate. Hence, there is no point in degrading the material parameters gradually, as it is done for mode A and B. Therefore, a constant factor is used instead [V.A. Passipoularidis, 2010], as described in Section 8.8 on page 79.

FADAS Implementation

8

In this chapter, all the main parts of the FADAS algorithm are described in detail. The FADAS algorithm is scripted as a subroutine for ANSYS which means that the calculations regarding elastic properties are performed during the FE computation of stresses and strains, which saves simulation time, compared to if the calculations were performed after the simulation in an APDL script [E. N. Eliopoulos, T. P. Philippidis, 2011]. The structure of the FADAS algorithm is shown in Figure 8.1, and the subroutine script can be found on the CD described in Appendix G.

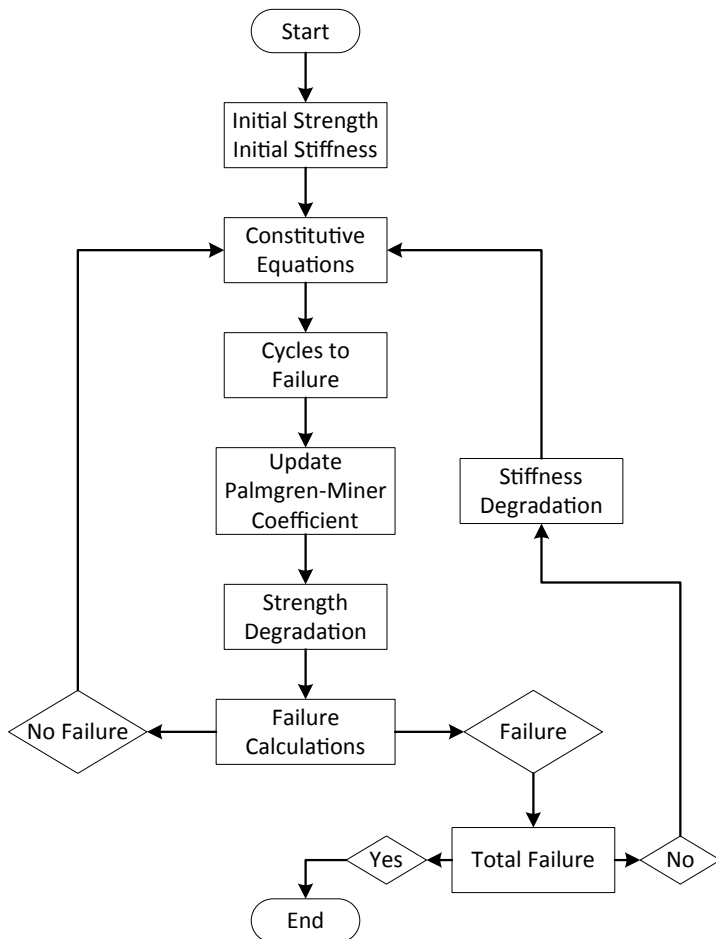


Figure 8.1 The FADAS algorithm structure

It is not possible to run an FE simulation for each cycle, due to the required computational time. In order to decrease the computational time of simulated fatigue tests, a cycle jump procedure is used. This is explained in more detail in Section 8.4. The implemented FADAS algorithm is categorized as a linear model in the literature, since a non-linear behavior of the material properties is not considered. However, because of the stiffness degradation described in Section 8.8 the model is solved non-linearly to take the change of stiffness into account.

Through the FADAS algorithm it is possible to take several parameters into account. These are described below:

The FADAS algorithm can take varying stress conditions, meaning tensile, compressive and mixed cyclic stresses, into account. This is done using the parameter, R_{CL} . Furthermore, data from several S-N curves can be used to determine, through interpolation, appropriate S-N data for the given stress condition. This is described in Section 8.3.

It is possible to take Constant Amplitude (CA) and Variable Amplitude (VA) into account by using the Palmgren-Miner linear damage rule, through the damage coefficient, $D_{j,l}$, as described in Section 8.4.

To determine the number of cycles simulated through the cycle jump procedure a parameter, Δn , is introduced. By changing this parameter the computational time required to simulate a given number of cycles is changed. Furthermore, it is possible to determine, how accurately it is known when a given failure occurs. This is described in Section 8.5.

A progressive strength degradation algorithm is implemented in the FADAS algorithm. It is based on strength data determined experimentally, and the Palmgren-Miner coefficient. For each simulated cycle the strength is degraded and the residual strength is updated. Since the strength degradation is cyclic, the degradation algorithm described in Section 8.6 is only employed for the last sub step of every other load step, i.e. at the end of every cycle.

Puck's failure criteria are implemented, which take the entire lay-up into account during the simulation. If failure occurs, the stiffness is degraded. For FF the stiffness is degraded with a constant. For IFF the progressive degradation is simulated for every equilibrium iteration of the FADAS algorithm, using a value that is calculated based on parameters derived from experimental data.

When the strengths and stiffnesses are degraded, it is utilized in the respective laminae within the elements in the FE model. The number of failed laminae within the elements are updated for every sub step. This is described in Section 8.8.

8.1 Initial Strength Initial Stiffness

All the initial material properties are defined as input parameters for the material routine, and later overwritten if necessary. The material properties are delivered by SWP, as described in Appendix B.5.

8.2 Constitutive Equations

ANSYS gives strains as input to the material routine and from that, stresses at each integration point are calculated based on the stiffnesses as shown in Equation (8.1). The equation is determined from classic laminate theory where a plane stress assumption is employed, which yields that in-plane stresses can be determined.

$$\begin{bmatrix} \sigma_1 \\ \sigma_2 \\ \tau_{12} \end{bmatrix} = \frac{1}{1 - \nu_{12} \cdot \nu_{21}} \begin{bmatrix} E_{11} & E_{11} \cdot \nu_{21} & 0 \\ E_{11} \cdot \nu_{21} & E_{22} & 0 \\ 0 & 0 & G_{12} \cdot (1 - \nu_{12} \cdot \nu_{21}) \end{bmatrix} \begin{bmatrix} \varepsilon_1 \\ \varepsilon_2 \\ \gamma_{12} \end{bmatrix} \quad (8.1)$$

The values for E_{11} , E_{22} , G_{12} and ν_{12} used in Equation (8.1), can be found in Table B.5 in Appendix B.5. ν_{21} used in the above equation is calculated as shown in Equation (8.2) to take the degradation of stiffnesses into account.

$$\nu_{21} = \frac{\nu_{12}}{E_{11}} E_{22} \quad (8.2)$$

The stiffnesses used in the constitutive calculations are subject to degradation if failure occurs in the element, which is described in detail in Section 8.8.

8.3 Cycles to Failure

The number of cycles the lamina can withstand before failure is dependent on the stress amplitude, σ_a , and S-N data obtained through coupon tests. Multiple S-N curves exist for a given lamina, depending on the load conditions. Normally three different S-N curves are made, at $R_{CL} = [0.1 -1 10]$. This is also the case in this project, and the values used for these S-N curves are shown in Table B.6 in Appendix B.5. The S-N data originates from a comprehensive database called OptiDAT [Nijssen, 2011]. Through these three sets of S-N data it is possible to generate an S-N curve for an arbitrary R_{CL} by interpolating between the known S-N curves. Depending on R_{CL} different S-N curves are to be used in the interpolation, which is shown in a Constant Life Diagram (CLD) in Figure 8.2.

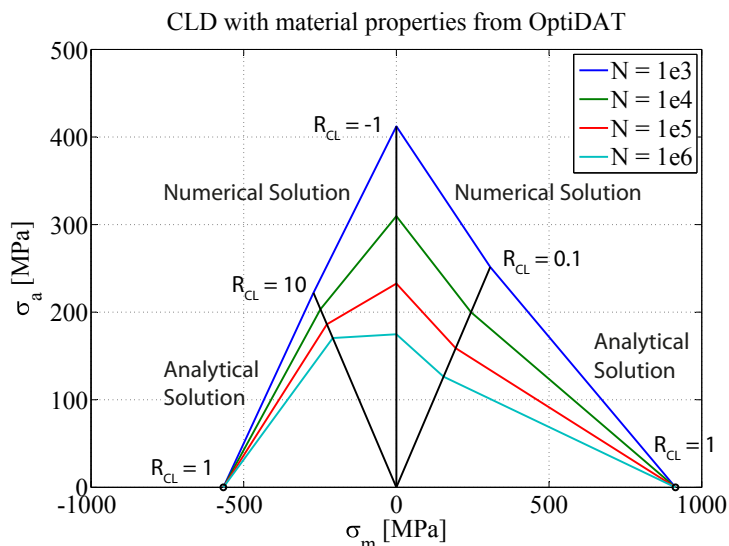


Figure 8.2 CLD parallel to fibers

In the intervals $[0.1 : 1]$, and $[10 : 1]$ it is possible to find an analytical solution based on the S-N data from, respectively, $R_{CL} = 0.1$ or $R_{CL} = 10$. However, when data from two S-N curves is used, there is no analytical solution because the S-N curves are based on a power law. Therefore, a numerical solution has to be found. An algorithm to find a numerical solution is presented in Wahl [2001]. The algorithm is slightly modified so that Sa and R_{CL} are the variables, as shown in Equation (8.3).

$$\begin{aligned}
N2 &= \left(\frac{-D2 \cdot N1^{\frac{-1}{k1}} - D3 \cdot N1^{\frac{-1}{k2}}}{D1} \right)^{\frac{1}{\frac{-1}{k1} - \frac{1}{k2}}} \\
D1 &= S1 \cdot S2 \cdot R_{int_2} - S1 \cdot R_{int_1} \cdot S2 \\
D2 &= S1 \cdot R_{int_1} \cdot Sa - S1 \cdot Sa \cdot R_{int} \\
D3 &= S2 \cdot Sa \cdot R_{int} - S2 \cdot R_{int_2} \cdot Sa \\
R_{int} &= \frac{1 + R_{CL}}{1 - R_{CL}} \\
R_{int_1} &= \frac{1 + R_{CL1}}{1 - R_{CL1}} \\
R_{int_2} &= \frac{1 + R_{CL2}}{1 - R_{CL2}}
\end{aligned} \tag{8.3}$$

where:

$N1$	Current guess for number of cycles for failure, [-]
$N2$	Resulting guess for number of cycles for failure, [-]
$k1$	Exponent in the expression for the first set of S-N data used in the numeric determination of N_i , [-]
$k2$	Exponent in the expression for the second set of S-N data used in the numeric determination of N_i , [-]
Sa	Stress amplitude, [MPa]
$S1$	Maximum stress amplitude in the expression for the first set of S-N data used in the numeric determination of N_i , [MPa]
$S2$	Maximum stress amplitude in the expression for the second set of S-N data used in the numeric determination of N_i , [MPa]
R_{CL}	Cyclic load ratio between minimum and maximum load in each direction, [-]
R_{CL1}	R_{CL} for the first set of S-N data used in the numeric determination of N_i , [-]
R_{CL2}	R_{CL} for the second set of S-N data used in the numeric determination of N_i , [-]

Equation (8.3) is solved numerically. For each iteration $N1$ is set equal to $N2$, and the problem is considered solved when the difference between $N1$ and $N2$ is less than 10. This is done twice in each iteration of the material routine, once for stresses parallel to the fibers and once for stresses transverse to the fibers.

When appropriate S-N data is determined, the number of cycles for failure is determined based on σ_a . As only one S-N curve is used for shear, the number of cycles for failure are found analytically through an interpolation.

8.4 Update Palmgren-Miner Coefficient

When an element fails during an analysis the stiffness of the element is decreased, as described in Section 8.8. This means that the stress in the surrounding elements is increased and the number of cycles for failure at this stress level is decreased, compared to before the first element failed. This means that even though CA is applied through the loads globally, a VA can occur in the individual elements locally. To take this effect into account the Palmgren-Miner linear damage rule is employed. At a given stress level the number of cycles simulated, Δn , is divided by the

number of cycles until failure, N_i . Thus, a part damage coefficient is found and added to the coefficient from the previous iteration. This coefficient is expressed as shown in Equation (8.4).

$$D_{j,l} = \sum_{i=1}^k \frac{\Delta n}{N_i} \quad (8.4)$$

where:

$D_{j,l}$	Palmgren-Miner Coefficient, [-]
j	Subscript to indicate tension (t) or compression (c), [-]
l	Subscript to indicate direction, parallel (p) or transverse (t) to fibers or shear (s), [-]
Δn	The number of cycles jumped in the FADAS algorithm, [-]
N_i	Number of cycles for failure at the i 'th stress level, [-]

The lamina has reached its fatigue limit when $D_{j,l} \geq 1$, and the lamina fails. This means that the appropriate material parameters are degraded, as described in Section 8.8.

In the FADAS algorithm five different Palmgren-Miner coefficients are used to be able to distinguish between different stress conditions. Two coefficients are used for tension, one for the fiber direction and one for transverse direction. Two are used for compression as well, and one is used for shear. Only one Palmgren-Miner parameter is used for shear because only one shear strength is used, and both compressive and tensile shear stresses affect the strength. This is implemented because the stress in an element can change from e.g. compression to tension throughout a simulation.

8.5 Cycle Jump Procedure

In the algorithm the number of cycles simulated is determined based on a parameter, Δn . Δn describes how many cycles are simulated by two load steps in ANSYS using the cycle jump procedure. Two load steps correspond to one cycle in the simulation, as shown in Figure 8.3, except for load step 1 and 2 which are used to initiate the simulation.

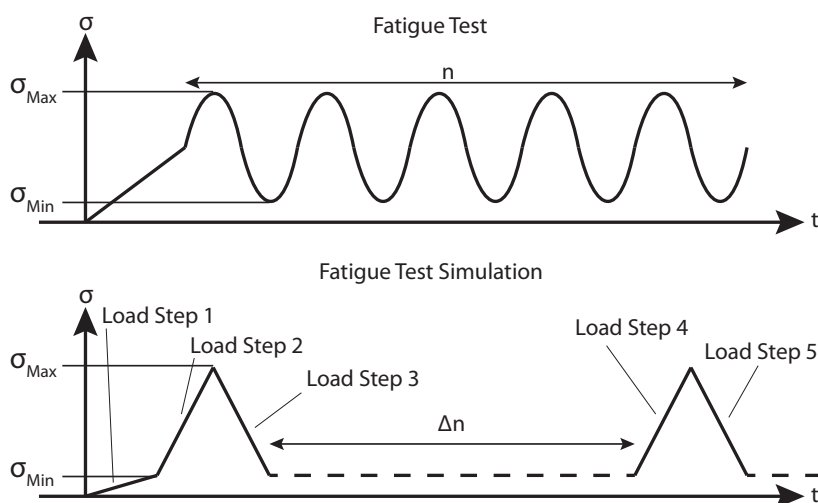


Figure 8.3 Cycle jump procedure

Δn and the number of load steps are defined in an APDL script before the analysis is performed. The magnitude of Δn and the number of load steps are determined as a compromise between computational time, how accurately it is required to know when a given failure occurs, and how many cycles it is necessary to simulate. The computational time is controlled by the number of load steps in an analysis, and the accuracy is controlled by Δn . Together they control how many cycles it is possible to simulate in an analysis.

Through the FADAS algorithm it is only possible to know in what interval of Δn the failure occurs. Furthermore, the propagation of failure throughout the FE model is very dependent on the size of Δn . With a small Δn fewer elements will fail compared to a large Δn , during each simulated cycle. This means that the stress redistribution happens more smoothly with a small Δn .

8.6 Strength Degradation

The strength degradation is calculated for tension and compression, parallel and transverse to the fibers, and in shear. Depending on R_{CL} some of the strength properties may not degrade, e.g. the tensile strength does not decrease if the load condition is pure compression. The expression to calculate the strength degradation is shown in Equation (8.5).

$$S_{j,l_r} = S_{j,l} - (S_{j,l} - \sigma_{j,l_{max}})D_{j,l}^k \quad (8.5)$$

where:

S_{j,l_r}	Residual strength parameter, [MPa]
$S_{j,l}$	Initial strength parameter, [MPa]
$\sigma_{j,l_{max}}$	Maximum stress, [MPa]
k	Sudden death eksponent, [-]

For example to calculate the residual tension strength parallel to the fiber direction, S_{t,p_r} , the following parameters are used. The initial tension strength, $S_{t,p}$, the maximum tension stress, $\sigma_{t,p_{max}}$, and the Palmgren-Miner coefficient for the number of cycles applied in tension parallel to the fiber direction, $D_{t,p}$. The sudden death exponent is set to 50 for compression loads and 1 for tension and shear loads [Philippidis, 2011].

8.7 Failure Calculations

As described in Chapter 7 on page 67, Puck's failure criteria are used to determine if failure has occurred. In the failure criteria, the residual strengths calculated in Section 8.6 are used. If failure occurs based on the failure criteria, then the appropriate stiffnesses are degraded as described in Section 8.8. If failure does not occur, then the stiffnesses are unchanged, and a new iteration is started.

For an element exposed to more than one failure mode, the one causing most damage to the lamina is prioritized. Total failure is reached when the FE model can not sustain any more damage. This is observed in the model when the deformations of the elements become so large that the simulation can no longer be solved, due to an equilibrium cannot be found.

8.8 Stiffness Degradation

Whenever failure is predicted some of the load carrying capabilities of an element are degraded. In the FADAS algorithm the stiffness degradation is dependent on the type of failure.

For FF the stiffness parallel to the fibers, E_{11} , transverse to the fibers, E_{22} , and the in-plane shear stiffness, G_{12} , are divided by 1000. In reality the stiffness is equal to zero after FF, but to avoid excessive distortion of failed elements, this non-zero stiffness is chosen, but decreased enough to not influence the results noticeably.

For IFF a slightly more advanced approach is used. It is assumed that after IFF has occurred in a lamina, the laminae surrounding it carry the redistributed loads. Thus, a given length away from the crack, the failed lamina can carry load again. [Knops, 2008]

This is included in the simulation as a stepwise degradation of the stiffness based on a parameter, η , practically giving a "smearing" effect to the stiffness around the failure. The expression used to determine η is shown in Equation (8.6). [A. Puck, H. Schürmann, 1999]

$$\eta = \frac{1 - \eta_r}{1 + c_{Puck}(f_{E(IFF)} - 1)\xi} \quad (8.6)$$

where:

η	Factor to determine stiffness degradation after IFF, [-]
η_r	Factor representing a small remaining stiffness, [-]
c_{Puck}	Parameter used to fit η -curve to experimental data, [-]
$f_{E(IFF)}$	Stress exposure factor for IFF, [-]
ξ	Parameter used to fit η -curve to experimental data, [-]

This factor, η , affects the algorithm as described in the itemization below.

1. When failure is predicted through Puck's failure criteria, the stress exposure factor, $f_{E(IFF)} \geq 1$. The magnitude of $f_{E(IFF)}$ is determined based on the stress at the integration point.
2. η is calculated based on $f_{E(IFF)}$, as shown in Equation (8.6). When $f_{E(IFF)}$ is increased η is decreased.
3. The stress is calculated based on the reduced stiffness as a result of η , as shown in Table 8.1. In the next iteration, the stiffness which is degraded, is the stiffness from the previous iteration, meaning not the initial.

Since the process described above is iterative, $f_{E(IFF)}$ is calculated in each sub step. As long as $f_{E(IFF)} \geq 1$ a new η is calculated which decreases the stiffness. When $f_{E(IFF)}$ is smaller than 1 no new η is calculated and $\eta = 1$. This means that the stiffness is kept constant, unless $f_{E(IFF)}$ becomes larger than 1 again.

The effect of η is shown in Figure 8.4. In the first part, the stiffness is constant and the stress and strain increases linearly. After $f_{E(IFF)} \geq 1$, the stiffness decreases and the stress-strain

curve shows non-linear behavior. The results shown in Figure 8.4 are based on multiple analyses of the FE model, shown in Figure 9.1 on page 81, where the load is increased linearly, and applied transverse to the fiber direction. Furthermore, the number of sub steps is varied to illustrate that this influences the stress strain relation. In this particular case, the stress should increase until the tensile strength transverse to the fibers is reached, where the stiffness should drop to zero because there are no other lamina to redistribute the load to, i.e. the stress should not increase any further. As shown, this behavior is best predicted when many sub steps are employed. 1 – 20 sub steps are employed in the analyses performed in this project, and ANSYS employs 7 sub steps for each load step, for the most part of the analyses.

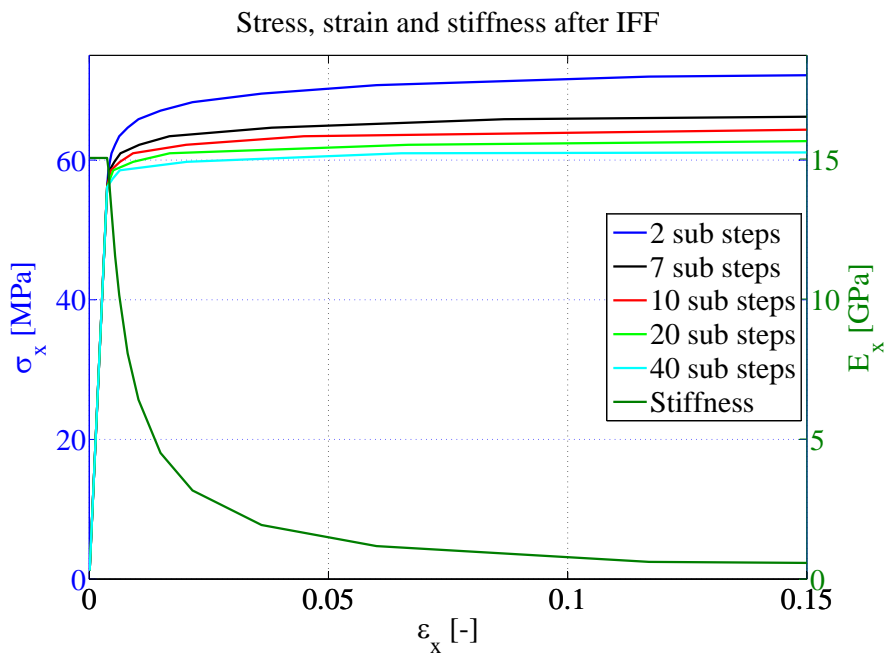


Figure 8.4 Influence of η on strain, stress and stiffness

Depending on the IFF mode, different material parameters are degraded, this is shown in Table 8.1.

Table 8.1 Material parameters being degraded at different IFF modes [A. Puck, H. Schürmann, 1999] and [V.A. Passipoularidis, 2010]

IFF mode	E_{22}	G_{12}	ν_{12}
Mode A	$\eta \cdot E_{22}$	$\eta \cdot G_{12}$	$\eta \cdot \nu_{12}$
Mode B	E_{22}	$\eta \cdot G_{12}$	ν_{12}
Mode C	$0.1 \cdot E_{22}$	$0.1 \cdot G_{12}$	ν_{12}

As it can be seen mode C failure does not utilize η because mode C is considered as total failure of the ply, as described in Section 7.2.3 on page 72, so the gradual degradation that yields from η is not relevant. Instead a constant factor is used to simulate total failure of the ply. Furthermore, the stiffness multiplied by the 0.1 factor is the initial stiffness, and not one that is reduced through iterations.

Validation of FADAS

algorithm 9

The FADAS algorithm developed in this project is verified in two steps, firstly it is verified w.r.t. its ability to calculate stresses and strains which is described in Section 9.1, and secondly it is verified that the strength degradation implemented in the FADAS algorithm matches the S-N data on which it is based, this is described in Section 9.2.

A single-element model is created with boundary conditions as shown in Figure 9.1. The stress-strain calculations and the strength degradation implemented in the algorithm, are verified on this FE model. A slightly different set of boundaries is used to validate that the shear stresses and strains together with the strength degradation in shear is calculated correctly, as shown in Figure 9.2.

9.1 Validation of Stress-Strain Relation

A simple load case is considered to verify that the FADAS algorithm created in this project is valid. This is done by comparing the stress and strain results from an ANSYS model to results from a Classic Laminate Theory (CLT) calculation.

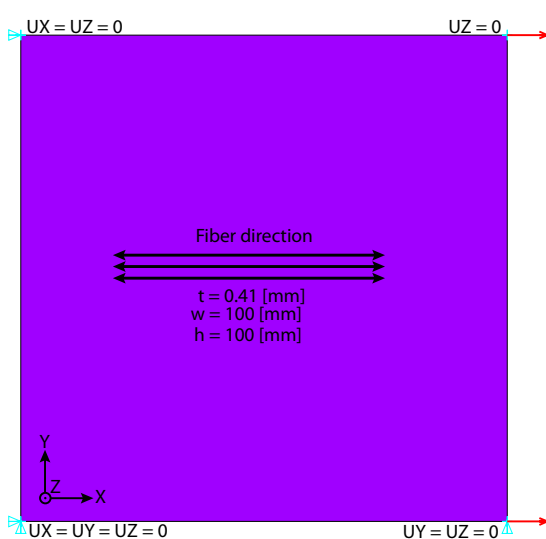


Figure 9.1 Boundary conditions for validation of FADAS algorithm

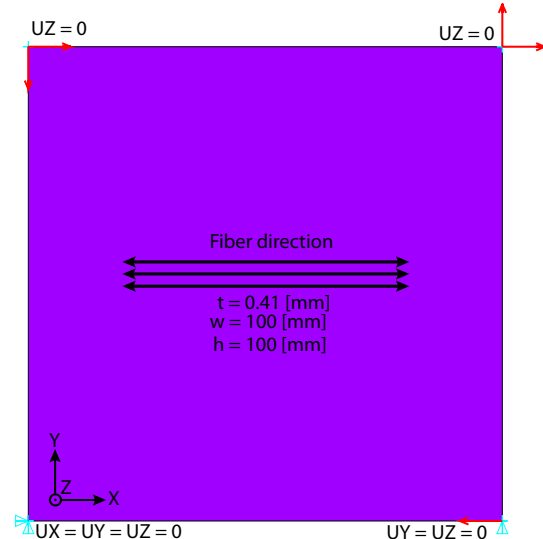


Figure 9.2 Boundary conditions for validation of FADAS algorithm in shear

The loads in the above figures, indicated with red arrows, are 500 [N] each, when validating the constitutive calculations.

With the boundary conditions shown in Figure 9.1, strain in the x- and y-direction can occur along with stress in the x-direction.

For shear, all in-plane stresses and strains are possible but the main part will be in shear. For both cases a uniform stress and strain field is obtained, this makes it simple to verify the FADAS algorithm.

The stresses and strains obtained in the models above are used to verify the algorithm. From the strains in the two cases, the relevant stresses in the x-, y- and xy-direction can be determined using CLT and the material properties in Table B.5 in Appendix B.5. The equations used for this are the same as shown in Equation (8.1) and (8.2) on page 74. The results from the algorithm and the CLT calculations are shown in Table 9.1.

Table 9.1 Results of the stress-strain verification

	Boundaries from Figure 9.1				Boundaries from Figure 9.2	
	ε_x	ε_y	σ_x	σ_y	ε_{xy}	σ_{xy}
FE model	$5.67 \cdot 10^{-4}$	0	24.4 [MPa]	$4.7 \cdot 10^{-16}$ [MPa]	$2.836 \cdot 10^{-3}$	12.2 [MPa]
CLT	$5.67 \cdot 10^{-4}$	0	24.4 [MPa]	0 [MPa]	$2.836 \cdot 10^{-3}$	12.2 [MPa]

There is a slight difference between the stresses in the transverse direction, σ_y . Since the edge is free to contract there should be no stress in the transverse direction. However, the algorithm estimates a negligible stress in the transverse direction, which is most likely due to rounding errors. Therefore, it is concluded that the implemented FADAS algorithm calculates correctly compared to CLT.

9.2 Validation of Strength Degradation

To verify that the algorithm calculates the strength degradation correctly, it is used on the FE models shown in Figure 9.1 and 9.2. The maximum stress applied to the models and the corresponding cycles for failure for loads applied in the fiber direction are shown in Table 9.2. The number of cycles for failure, predicted through the FADAS algorithm is compared to the estimated cycles for failure based on S-N data from Table B.6 in Appendix B.5 at the same stress level.

Table 9.2 Results of the strength degradation verification along the fiber direction

N _{estimated}	1000	5000	50000	1000000
$R = 0.1$				
σ_{max}	559 [MPa]	476 [MPa]	378 [MPa]	281 [MPa]
N _{FADAS}	1010	5050	50000	1000000
$R = -1$				
σ_{max}	412 [MPa]	337 [MPa]	254 [MPa]	175 [MPa]
N _{FADAS}	1010	5050	50000	1000000
$R = 10$				
σ_{max}	-494 [MPa]	-464 [MPa]	-425 [MPa]	-379 [MPa]
N _{FADAS}	1020	5050	50000	1000000

As it is shown, the estimated cycles for failure based on S-N data and the calculated cycles for failure through the FADAS algorithm do not match perfectly. This is because in the algorithm, as mentioned, there is a part that interpolates between different S-N curves. So for the S-N data used in the FADAS algorithm to be exactly the same as used to validate the algorithm, R_{CL} has to be equal to one of the R_{CL} -values used to determine the S-N data experimentally, i.e. [0.1 – 1 10]. However, because of rounding errors the R_{CL} used in the FADAS algorithm is not exactly the same, as any of the values used to determine the S-N data. This means that the S-N data is not identical, and therefore, different cycles for failure are predicted.

The data above is plotted in Figure 9.3, along with the S-N curves based on the data from Table B.6 in Appendix B.5. Similar plots for the transverse direction and for shear are shown in Figure 9.4 and 9.5

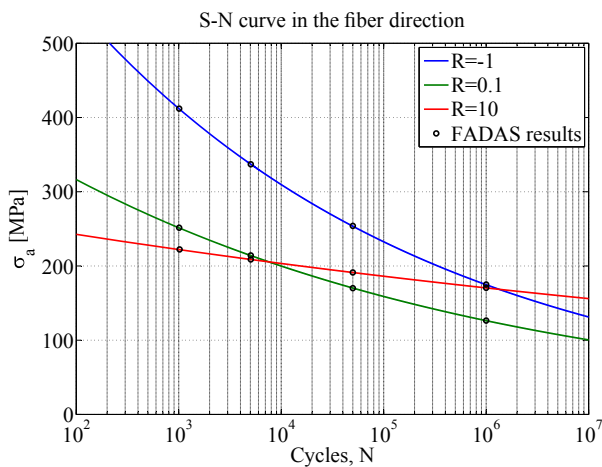


Figure 9.3 S-N curve for the fiber direction

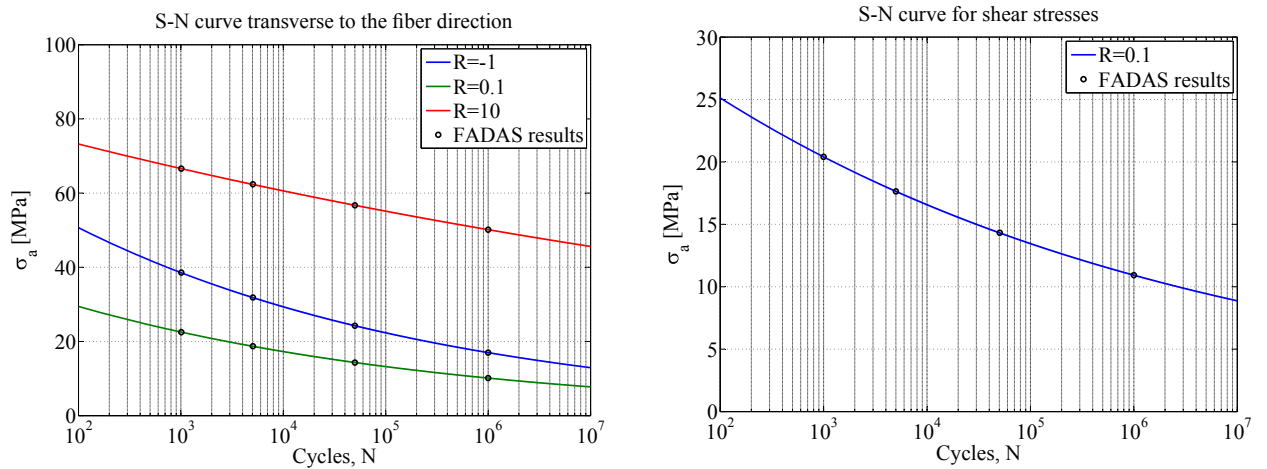


Figure 9.4 S-N curve transverse to the fibers

Figure 9.5 S-N curve for shear stresses

As it is shown in the above plots the chosen points from the FADAS algorithm fit very well to the S-N curves based on experimental data from Nijssen [2011]. This means that the implemented FADAS algorithm works as intended.

9.3 Comparison of FADAS Algorithm to Coupon Tests

The above verifications are more or less theoretical, so to determine how well the algorithm predicts physical tests, it is chosen to test the FADAS algorithm on an FE model of a coupon test specimen. The specimen geometry used to compare the algorithm to real life is the same as the R03 specimen defined in the OptiDAT wind turbine materials research database [Nijssen, 2011]. The specimen geometry with applied boundary conditions is shown in Figure 9.6.

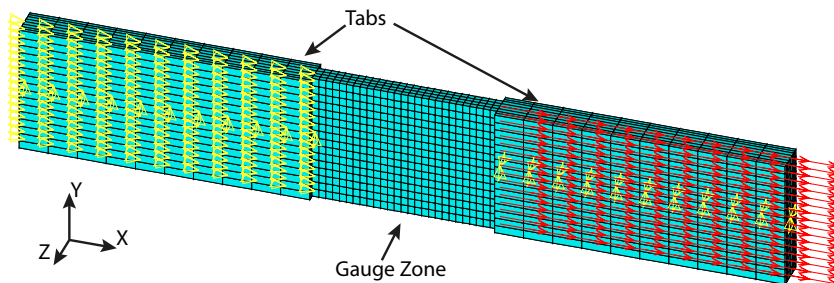


Figure 9.6 Boundary conditions for FE model for coupon test comparison

The load and constraint in the x-direction is distributed over all the nodes on the tabs to minimize the effect of singularities. The model is constrained in the y-direction along the center line to allow the specimen to contract due to Poisson's effect. Furthermore the strength degradation is not applied to the tabs to further ensure that failure does not occur outside the gauge zone.

It is chosen to evaluate the coupon test specimen model at four different stress levels that are expected to yield 1000, 5000, 50000 and 1000000 cycles, respectively. The S-N curve for $R = 0.1$ and the simulated cycles using the FADAS algorithm are shown in Figure 9.7.

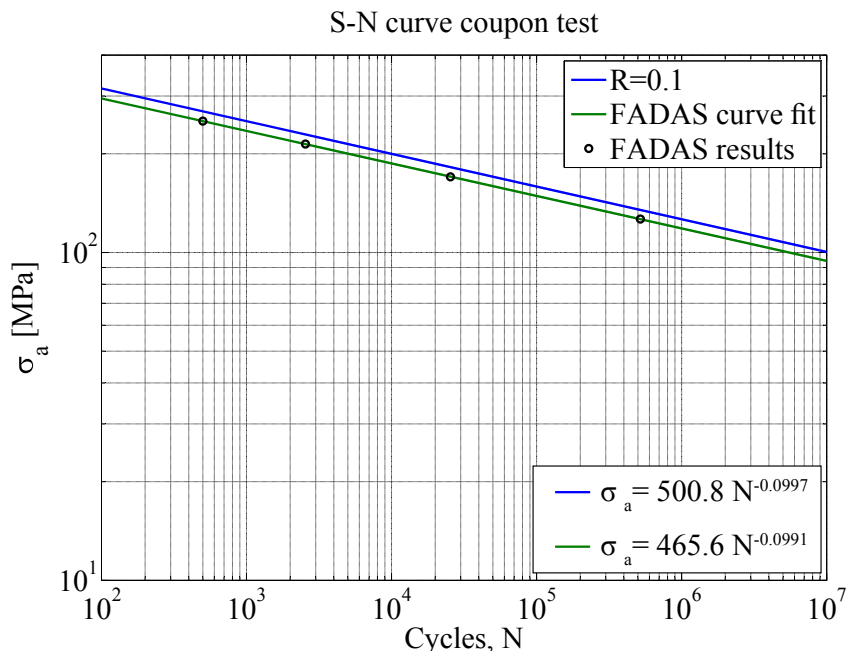


Figure 9.7 Comparison of FADAS results with S-N coupon test data

The cycles for failure when using the FADAS algorithm are 48-50 [%] less than estimated, based on the coupon tests made by OptiDAT [Nijssen, 2011]. The slope of the two curves shown in Figure 9.7 are very similar. However, there is a deviation for the intersection with the secondary axis of ca. 35 [MPa], which, due to the low magnitude of the slope, results in a large deviation in estimated cycles for failure. One of the reasons for this conservative result is that, due to the geometry of the model, there are stress concentrations at the ply drops between the tabs and the gauge zone, as shown in Figure 9.8, where the gauge zone is shown.

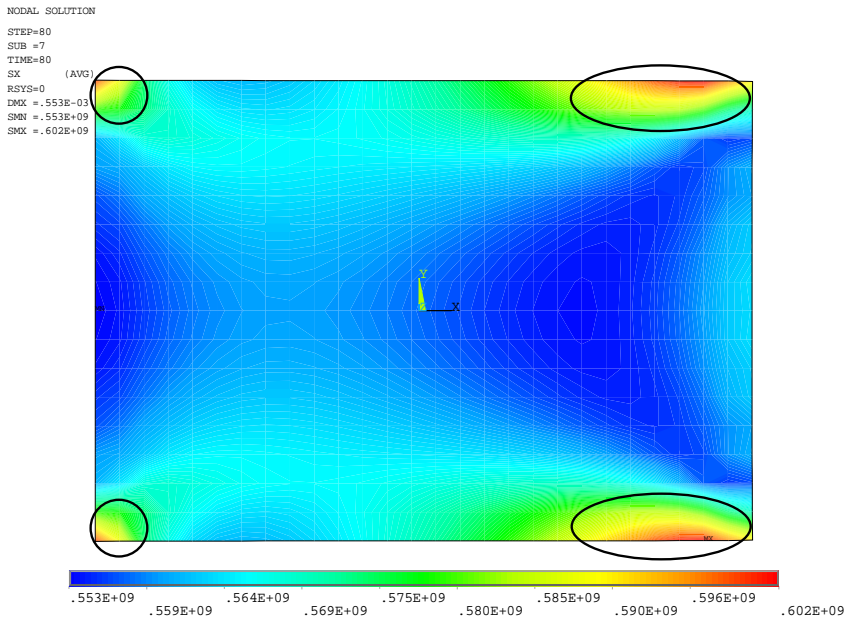


Figure 9.8 Stress in the gauge zone in the x-direction

The number of cycles that the FADAS algorithm predicts until failure is based on the stress amplitude, σ_a , which is dependent on the stress level. So, at the stress concentrations the algorithm predicts fewer cycles for failure. Some of this behavior can be explained by the fact that the FADAS algorithm used in this project is linear, whereas the FADAS algorithm in Philippidis [2011] is non-linear. The FADAS algorithm in that article is about 25 [%] conservative when used on a geometry similar to the one used in this section. If the FADAS algorithm is able to predict even a small amount of yielding at the stress concentrations then the stresses in the area would decrease and get redistributed to other areas and a longer lifetime would be achieved.

9.4 Sub-Conclusion

The FADAS algorithm is validated, and yields correct results when used on a single-element FE model. However, when used on an FE model of a coupon test specimen used in experiments there is a deviation between the simulation and the data from the experiments, where the simulation predicts failure of the specimen at about half the number of cycles. It is assumed that some of this error is caused by the stress concentrations in the FE model, where the FADAS algorithm cannot predict yielding. It is important to keep this in mind when comparing the results from the FADAS algorithm to the tests performed in the test rig.

Simulation of Fatigue

Tests

10

In this chapter fatigue simulations are conducted by utilizing the FADAS algorithm. The FE shell model presented in Appendix B.2 is used to simulate the fatigue tests presented in Chapter 5 on page 49. The simulated results for FT1 are presented in Section 10.1 and compared to the experimental results from FT1. The simulation of FT1 is presented to show how the FADAS algorithm interface works and how the results are interpreted. Subsequently, results and comparisons of FT2, FT3 and FT4 are presented. In this chapter when referring to the simulations of the fatigue tests e.g. sFT1 is used and for the experimental results e.g. eFT1 is used.

10.1 Simulation of FT1

In the modeling of the FE shell model, each ply drop is included by creating an area. Each area has a specified lay-up, which is presented in Appendix B.2. This is done in order to reduce the change in stiffness between different lay-ups and thereby reduce stress concentrations at the edges between areas.

The BIAX plies in the FE shell model are created by dividing the BIAX plies into a UD $+45^\circ$ ply and a UD -45° ply, as sketched in Figure 10.1 and 10.2. Initially a combined BIAX ply was implemented, but when subjected to IFF the entire stiffness transverse to 0° was degraded, which does not correspond to what happens in reality. This is illustrated by the red line in Figure 10.1. Instead, the alternative lay-up of the BIAX ply is created to be able to e.g. have a degraded stiffness transverse to the fibers of the UD $+45^\circ$ lamina, but the UD -45° lamina is still able to contribute to the stiffness in this direction. It is thereby possible to have a lamina that is non degraded and a lamina that is degraded. This is shown with the red line in Figure 10.2. A validation of the alternative modeling of a BIAX ply is shown in Appendix B.6. The validation showed that the deviations w.r.t. the strain in the x- and y direction, when changing the setup, is maximum 0.3 [%], when the combined BIAX ply is used as reference. The deviation w.r.t. the shear strain is relatively large, but as the shear strain values from the two setups are close to zero, it is assumed to be acceptable. In the FE shell model the UD $+45^\circ$ ply is the outermost ply of the specimen corresponding to layer 1.

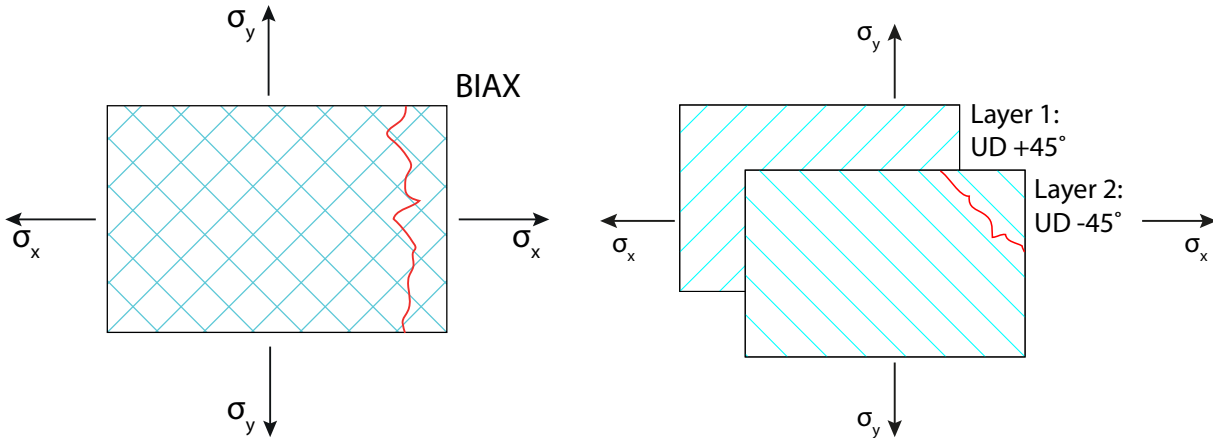


Figure 10.1 BIAX ply

Figure 10.2 BIAX ply divided into two UD plies

As described in Section 8.4 on page 76, Δn is specified to get a reasonable resolution of the fatigue results, and in order to due this, Δn is found by an iterative process.

There are two possible approaches for conducting the simulations, one where the loads are applied with the same magnitude as the loads in the tests, and another where the loads are fitted to obtain the same strain level as in the tests. The first approach is utilized because of the presence of uncertainties and flaws in the specimen, which are explained in Appendix A.3. This yields that the strain gauge measured strains could be erroneous and it would thereby not make sense to compare results with same stress level.

A recap of the setup and the observations conducted for eFT1, including the value of Δn for the simulations, are shown in Table 10.1.

Table 10.1 Setup parameters and observations for eFT1

Load parameters		
Direction	F_{max} [kN]	F_{min} [kN]
Primary	160	16
Secondary	64	6.4
Simulation parameters		
Δn	1, 300, 500 and 750	
Experimental results for FT1		
ID	Cycle	Observations
FT1-1	102	First failure
FT1-2	124	Second failure
FT1-3	163	Third failure
FT1-4	300	Failure in fillet corner

In sFT1 the value of Δn has been set equal to 1 in order to trace first failure, as this was observed relatively early in eFT1, and because it is experienced from the Validation of FADAS algorithm Chapter that it is conservative. sFT1 predicts failure at first cycle as an IFF mode A at the fillet corner for the UD $+45^\circ$ ply and for the UD 0° ply, as shown in Figure 10.3 and 10.5, respectively.

The failures indicated by the color bar in the results correspond to Puck's failure criteria presented in Chapter 7 on page 67.

sFT1 w.r.t. the fillet corner does not correspond to what is observed in eFT1, where failure occurs as IFF in the UD 0° lamina in the fillet corners at 300 cycles. One of the reasons for this deviation could be due to the issues with the synchronization of the cylinders in the start of eFT1, as explained in Section 5.2.4 on page 54.

Furthermore sFT1 predicts failure at first cycle in the gauge zone for both the UD $+45^\circ$ and the UD -45° laminae, i.e. layer 1 and 2 shown in Figure 10.2. These failures are shown in Figure 10.3 and 10.4, respectively.

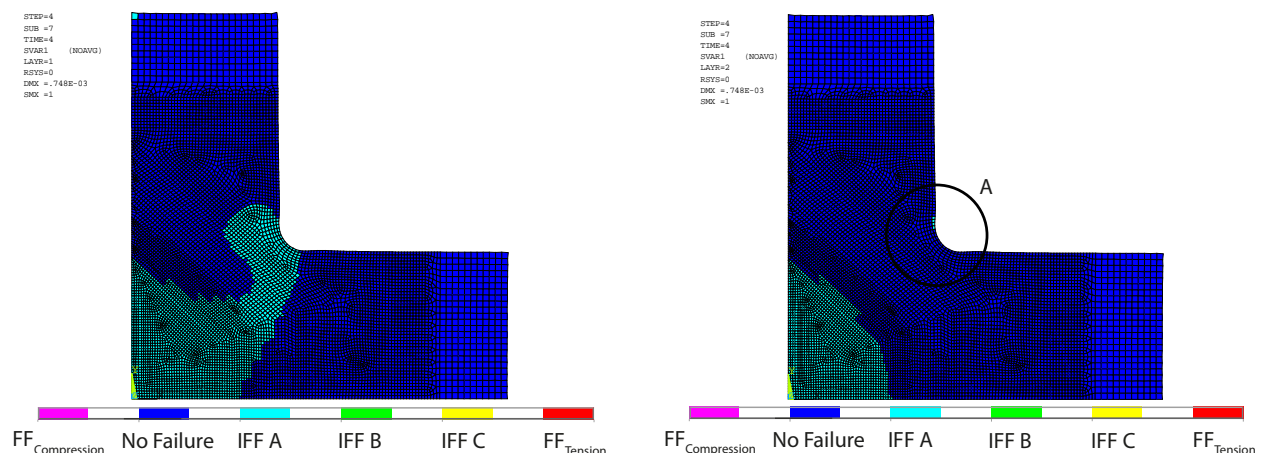


Figure 10.3 UD $+45^\circ$ lamina for sFT1 at cycle 1 showing failure at fillet corner and in the gauge zone

Figure 10.4 UD -45° lamina for sFT1 at cycle 1 showing failure in the gauge zone

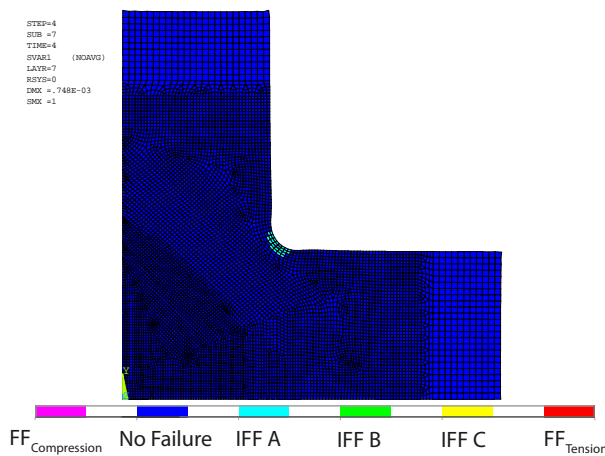


Figure 10.5 UD 0° lamina for sFT1 cycle 1 showing failure at fillet corner

In circle A in Figure 10.4 only a few elements have been subjected to IFF A compared to the result in Figure 10.3. The reason for the difference between the laminae is that the UD $+45^\circ$ lamina has the fibers oriented diagonally from the origin of the global coordinate system

towards the fillet corner, which the UD -45° lamina does not. This is shown in Figure 10.6. Because of load transfer between the primary and secondary arms, increased shear strains and stresses, are present at the fillet corner compared to the center of the gauge zone. This results in IFF in the UD $+45^\circ$ lamina and not in the UD -45° lamina at the fillet corner, because the fracture plane resulting from shear stress is oriented parallel to the fibers of the UD $+45^\circ$ lamina.

This is not observed during eFT1, meaning that it is not possible to determine when these cracks occurred with the utilized measurement equipment, but after the test, small undiscovered IFF cracks were present at the fillet corners and in areas in the gauge zone, as shown in Figure 10.7. Some of these cracks could be triggered by the IFF of the UD 0° lamina, but it is impossible to know for sure based on the experimental data.

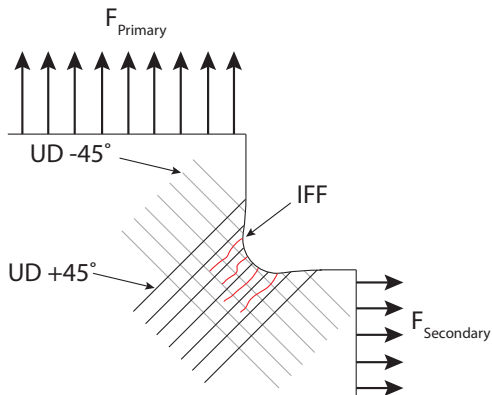


Figure 10.6 Sketch of IFF in UD $+45^\circ$ lamina at fillet corner

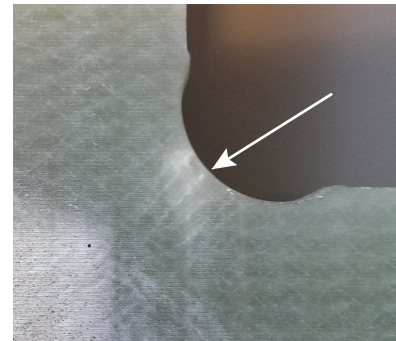


Figure 10.7 IFF in BIAX lamina at the fillet corner of the eFT1 specimen

A magnified view of circle A, in Figure 10.4, is used to show when failure is assessed to be present in the simulations. The simulation result of this magnified view after 1 cycle is shown to the left in Figure 10.8. It is assessed that no failure has occurred as only a few elements are subjected to IFF A. However, the result after 3300 cycles, presented to the right in Figure 10.8, involves one more element subjected to FF_{Tension}, which is a more critical failure mode than mode A, thus, failure is assessed to be present.

This way of qualitatively determining if failure has occurred or not is utilized in all the fatigue simulations.

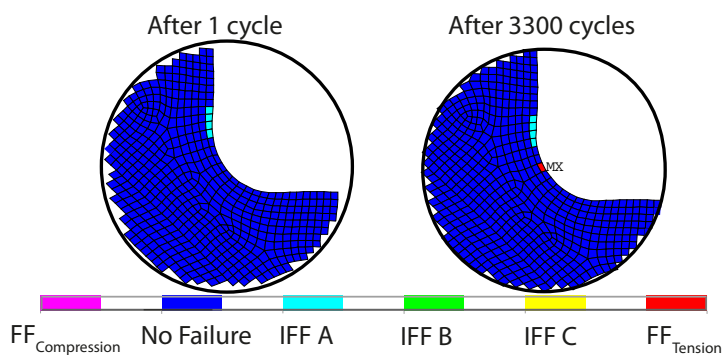


Figure 10.8 Progression of failure in UD -45° lamina for sFT1 (Highlighted circle A in Figure 10.4)

It is of interest to look into when first failure occurs in the gauge zone for the UD 0° lamina because this is defined as first failure in Section 1.2 on page 4. Hence, Δn has been changed

to 500 in order to reduce computational time. First failure in the UD 0° lamina is predicted at 19500 cycles in the gauge zone, as shown in Figure 10.9. This result does not correspond to what is observed in eFT1, where first failure occurred at 102 cycles.

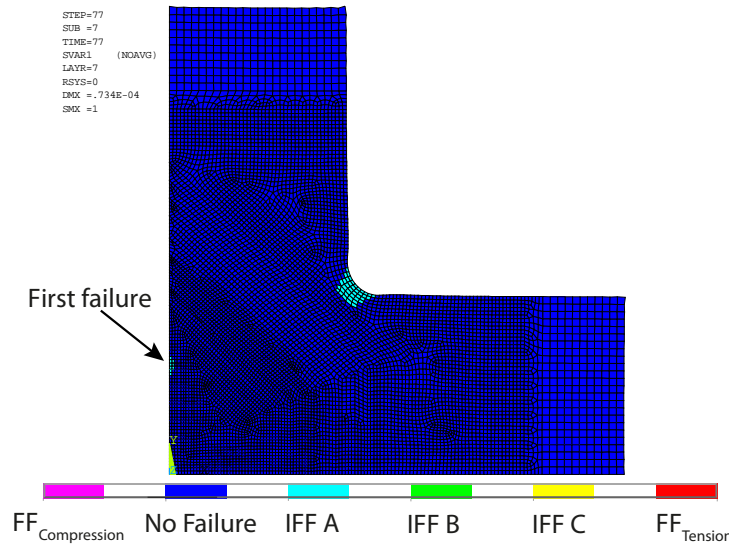


Figure 10.9 UD 0° lamina for sFT1 at 19500 cycles showing first failure in the gauge zone

The position of the different failures in sFT1 are studied and compared to the positions of the observed failures in eFT1. The failures in the UD $\pm 45^\circ$ laminae are not considered in this comparison, as these failures have not been observed in eFT1. First failure in the UD 0° lamina in the simulation is present below the tip of the gauge zone as shown in Figure 10.9. The position of this crack is close to the second failure (FT1-2) observed in eFT1. To verify if the model predicts similar failure initiation as shown in eFT1, a result after 29250 cycles is shown in Figure 10.10. Here it is shown that the failure beneath the tip of the gauge zone propagates and that a new failure is predicted in the right side of the gauge zone where the ply drop boundary is present. This is not observed in eFT1.

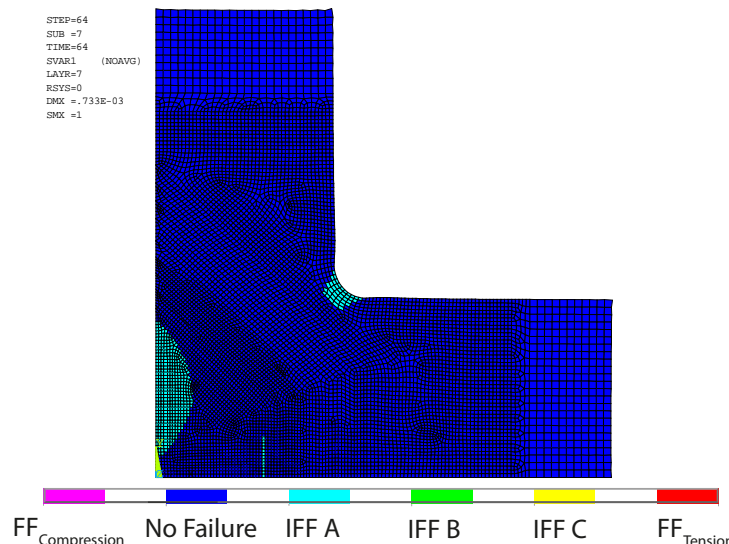


Figure 10.10 UD 0° lamina for sFT1 at 29250 cycles showing propagation of first failure in the gauge zone

The position of the failures in sFT1 are highly influenced by the stress concentrations in the model. This is discovered in Chapter 9 on page 81. These concentrations are typically present at ply drop boundaries and at the fillet corners, which is shown in Section 2.5 on page 23. First failure in the UD 0° lamina occurs at the tip of the gauge zone, where a stress concentration is present. The failure in the fillet corner also corresponds to where a stress concentration is present. Furthermore, the result for the UD 0° lamina after 29250 cycles shows that failure starts in the right side of the gauge zone close to the ply drop boundary, where another stress concentration is present.

In Table 10.2 the results from sFT1 are summarized and compared to the observed failures in eFT1. In the tests no observations are obtained for the BIAX laminae, which is why N/A is stated in Table 10.2. Furthermore, the strains from the first cycle in the simulations are extracted from a node in the model at the coordinate (0,0) and compared to the strain gauge measured strain from eFT1. It is preferable to get the strain gauge measured strain at the first cycle of eFT1, but due to the issues with the synchronization of the cylinders, as previously mentioned, the strain gauge measured strain is obtained at 300 cycles. This measured strain is not entirely comparable to the strain obtained from the model at first cycle, but it is presented in order to get an idea of the deviations between the strain in sFT1 and eFT1.

Table 10.2 sFT1 results and comparison

Cycles to failure:				
Lamina	Fillet corner	Fillet corner (Test)	Gauge zone	Gauge zone (Test)
UD +45°	1	N/A	1	N/A
UD -45°	3300	N/A	1	N/A
UD 0°	1	300	19500	102
Strain:				
Source	Direction	Value [μ strain]	Deviation [%]	
Model	ε_x	1164	22	
Test	ε_x	1498		
Model	ε_y	4155	2.6	
Test	ε_y	4264		

Another way to show the deviation between sFT1 and eFT1 is to use CLT to calculate the stresses from the strains in Table 10.2 and thereby the stress amplitude, which is used to estimate cycles until failure transverse to the fiber direction using S-N data. From the strains in the FE model, failure occurs at 36000 cycles and for the strains in the test, failure occurs at 11000 cycles. From this it is assessed that even if the strains in the model are fitted to the ones from the test, the number of cycles from eFT1 and sFT1 would still deviate a lot.

When presenting the rest of the fatigue simulations only the UD 0° lamina is compared to the tests, as the UD $\pm 45^\circ$ laminae failures have not been observed during the tests. In all the simulations the $\pm 45^\circ$ laminae fail in the gauge zone after 1 cycle.

10.1.1 Sources for Deviation

The different sources which are assessed to be causing the deviations in sFT1 are stated here and these sources are also a part of the reason for the deviations in the rest of the fatigue simulations.

As shown in Table 10.2 the strain, ε_x , corresponding to the secondary direction deviates 22 [%], when the reference is taken as the measured strain in eFT1. This is a relatively large deviation and it can be one of the main reasons that the simulation predicts failure in the UD 0° lamina at 19500 cycles instead of the 102 cycles, which is observed in eFT1. Another reason for the difference between the results is that the specimen can include flaws and imperfections, because of the manufacturing process, as described in Appendix A.3. The FE shell model is a perfect model, meaning that phenomena like imperfections etc. are not included.

It is assumed that some of the relatively large deviations in the predictions for sFT1 can be justified by the material properties used in the simulations. These do not correspond entirely to the material used in the specimen. The initial material parameters are provided by SWP in normalized values. Actual values are then calculated by the use of the material properties available in M. Leong et. al. [2012]. Furthermore S-N curves are utilized in the FADAS algorithm, but as this data has not been available for the used material, corresponding values from Nijssen [2011] have been used. This altogether gives a mismatch between the material data for the tested specimen and the material data for the simulated test and it could explain some of the deviations.

Another reason for the deviations is that a linear FADAS algorithm is utilized, meaning that non-linear material properties are not implemented into the simulations. As the model is highly influenced by stress concentrations, the implementation of non-linear material properties could reduce these stress concentrations and thereby reduce the deviations in the results.

10.2 Simulation of FT2

A recap of the setup and the observations conducted for eFT2, including the value of Δn for the simulations, are shown in Table 10.3.

Table 10.3 Setup parameters and observations for eFT2

Load parameters		
Direction	F_{max} [kN]	F_{min} [kN]
Primary	125	12.5
Secondary	55.6	5.56
Simulation parameters		
Δn	1 and 1200	
Experimental results for FT2		
ID	Cycle	Observations
FT2-1	7600	Failure in fillet corner

The strain gauge measured strains varies in the start of eFT2. This is because the loads tend to settle as the test progresses. Therefore the strains are obtained after the loads settle. Furthermore, as stated in Section 5.3.3 on page 57, issues with the strain gauge result in the secondary direction is present. The strain gauge result is therefore not entirely comparable to the strain at first cycle of sFT2, but it is used in order to give an idea of the strain deviations between sFT2 and eFT2.

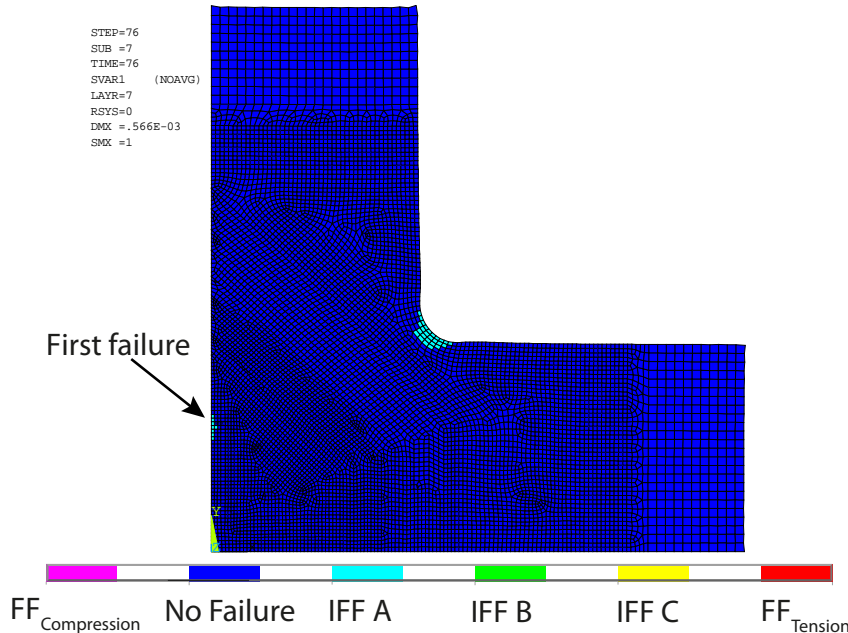


Figure 10.11 Simulated first failure for FT2 after 43200 cycles

In Figure 10.11 it is shown that failure occurs for sFT2 in the UD 0° lamina in the gauge zone after 43200 cycles. First failure has not been observed in eFT2 in the gauge zone, hence N/A is stated for this in Table 10.4.

Table 10.4 sFT2 results

Cycles to first failure:				
Lamina	Fillet corner	Fillet corner (Test)	Gauge zone	Gauge zone (Test)
UD 0°	1	7600	43200	N/A
Strain:				
Source	Direction	Value [μstrain]	Deviation [%]	
Model	ε_x	1289	96	
Test	ε_x	657		
Model	ε_y	3137	17	
Test	ε_y	2690		

If the number of cycles is calculated by the use of CLT and the S-N curve transverse to the fiber direction in the same way as done for FT1, the cycles for failure for the strain in the FE model is 71000 and for the strain in the test it is $2.7 \cdot 10^6$ cycles. Since first failure is not achieved in

eFT2 it is not possible to determine the deviation between cycles in eFT1 and sFT1.

In Table 10.4 it is shown that the strain deviates 96 [%] for the secondary direction, ε_x , which is a large deviation. This could explain some of the large differences between the results from sFT2 and eFT2. As mentioned the strain gauge shows erroneous results in the secondary direction, which could be caused by the aforementioned surface irregularities of the specimen, as described in Appendix A.3.

Furthermore the problems with the mismatch between the material properties and the lack of non-linear material properties in the model as presented in Section 10.1.1, could explain some of the deviations.

If the result for sFT2 shown in Figure 10.11 is compared to the result for sFT1 shown in Figure 10.9, the difference is that for sFT1 first failure occurs at the top of the gauge zone, whereas in the sFT2 it occurs in the right side of the gauge zone. This could be explained by the change in R_{Load} , which for sFT1 is 0.4 and 0.445 for sFT2, resulting in larger load in the secondary direction for sFT2.

10.3 Simulation of FT3

A recap of the setup and the observations conducted for eFT3, including the value of Δn for the simulations, are shown in Table 10.5.

Table 10.5 Setup parameters and observations for eFT3

Load parameters			
Direction	F_{max} [kN]	F_{min} [kN]	
Primary	150	15	
Secondary	66.75	6.68	
Simulation parameters			
Δn	1 and 275		
Experimental results for FT3			
ID	Cycle	Observations	FP
FT3-2	2250	Failure in fillet corner	-
FT3-3	32000	First failure	
FT3-4	93500	Second failure	
FT3-5	104000	Third failure	

The result for sFT3 in the UD 0° lamina, presented in Figure 10.12, shows that first failure occurs in the top of the gauge zone. Generally this result is similar to what is shown in Figure 10.9 for sFT1.

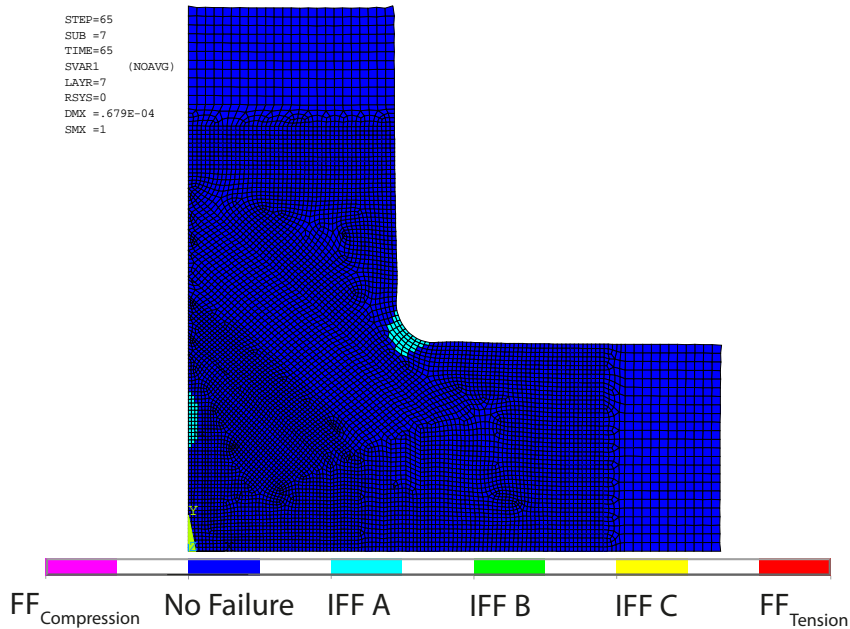


Figure 10.12 Simulated first failure for FT3 after 8525 cycles

The strain gauge measured results are obtained after the loads have settled, as explained in Section 10.2. In spite of this the deviations w.r.t. the strains shown in Table 10.6 are within a reasonable allowable tolerance, but still a relatively large difference in the number of cycles for failure is present.

Table 10.6 sFT3 results

Cycles to first failure:				
Lamina	Fillet corner	Fillet corner (Test)	Gauge zone	Gauge zone (Test)
UD 0°	1	2250	8525	32000
Strain:				
Source	Direction	Value [μ strain]	Deviation [%]	
Model	ε_x	1549	14	
Test	ε_x	1355		
Model	ε_y	3763	7	
Test	ε_y	3507		

If the number of cycles for failure transverse to the fiber direction is found from the stresses that correspond to the strains in Table 10.6, the number of cycles for failure for the strains in the FE model is 15000 and from the strains in the test, failure occurs at 37000 cycles. From this it is assessed that if the strains in the model are fitted to the ones from the test, the deviation of the number of cycles between eFT3 and sFT3 would be reduced noticeable.

As shown in Table 10.6, the deviations in amount of cycles between sFT3 and eFT3 are relatively large. The occurring failures in the simulations are highly influenced by the stress concentrations. A small change in stress level, i.e. stress amplitude, yields a large change in number of cycles for failure. This is due to the S-N curve w.r.t. the transverse direction of the fibers, as the slope of the curve has a low magnitude.

10.4 Simulation of FT4

A recap of the setup and the observations conducted for eFT4, including the value of Δn for the simulations, are shown in Table 10.7.

Table 10.7 Setup parameters and observations for eFT4

Load parameters			
Direction	F_{max} [kN]	F_{min} [kN]	
Primary	148	14.8	
Secondary	67.3	6.7	
Simulation parameters			
Δn	1 and 75		
Experimental results for FT4			
ID	Cycle	Observations	FP
FT4-1	1600	Failure in fillet corner	
FT4-2	17150	First failure	
FT4-3	73000	Second failure	

First failure in the UD 0° lamina for sFT4 occurs at the top of the gauge zone, as shown in Figure 10.13.

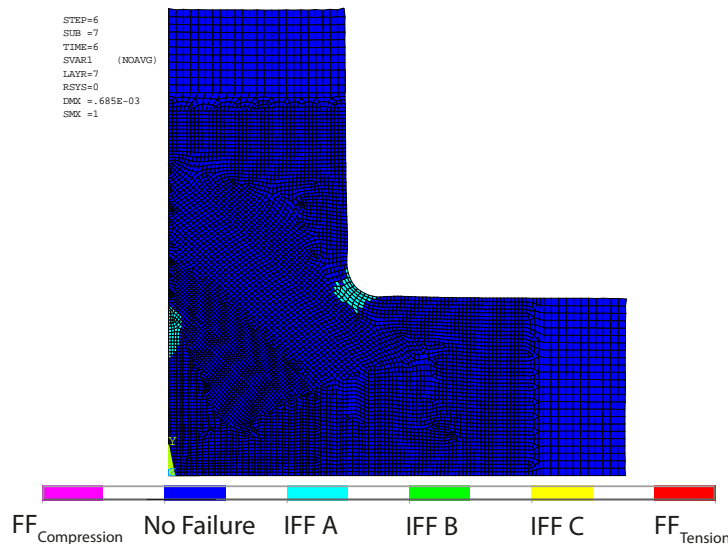


Figure 10.13 Simulated first failure for FT4 after 150 cycles

The procedure for obtaining the strain gauge measured strains is the same as explained in Section 10.2 and 10.3 and these are shown in Table 10.8. The deviations in strain for the secondary direction is 35 [%], which again could be explained by the erroneous strain gauge measurements, which is due to surface irregularities, or it could be due to the aforementioned mismatch between the material parameters presented in Section 10.1.1.

Table 10.8 sFT4 results

Cycles to first failure:				
Lamina	Fillet corner	Fillet corner (Test)	Gauge zone	Gauge zone (Test)
UD 0°	1	1600	150	17150
Strain:				
Source	Direction	Value [μ strain]	Deviation [%]	
Model	ε_x	1626	35	
Test	ε_x	1205		
Model	ε_y	3685	3	
Test	ε_y	3812		

If the number of cycles for failure transverse to the fiber direction is found from the stresses that correspond to the strains in Table 10.8, the number of cycles for failure for the strains in the FE model is 12000 and from the strains in the test failure occur at 45000 cycles. From this it is assessed that even if the strains in the model are fitted to the ones from the test, the number of cycles from eFT4 and sFT4 would still deviate a lot.

Generally there are no noticeable changes in the result for sFT4 compared to the previously presented fatigue simulation results.

10.5 Sub-Conclusion

The simulations of the presented fatigue tests in Chapter 5 on page 49 are conducted. It is difficult to conclude anything w.r.t. sFT1 when it is compared to eFT1, because of the issues with the synchronization of the cylinders in the start of the test, where most of the failures occurred.

The loads in the simulations have been set equal to the ones in the tests. For each test the number of cycles for failure have been calculated based on the strains in the simulations and in the tests, respectively. Based on these results, the best consistency seems to be between eFT3 and sFT3. However, it is difficult to conclude anything from this, as there have been large differences between each fatigue test even though it has been tried to obtain the same strains in eFT3 and eFT4.

The general tendency is that the utilized FADAS algorithm is conservative and underestimates the number of cycles for failure. In all the simulations the UD $\pm 45^\circ$ laminae fail in the gauge zone before the UD 0° lamina. Initially it has not been possible to observe this failure in the BIAX lamina during the tests, but after the tests, during a thorough inspection of the specimen, it was observed that failure in the BIAX lamina is present, both in the gauge zone and in the fillet corners.

The simulation is sensitive to stress concentrations, because of the low magnitude of the slope in the S-N curve w.r.t. the transverse direction a small change in stress level, i.e. stress amplitude, can create a large change in the simulated results.

Part IV

CLOSURE

Conclusion 11

In this chapter a conclusion for the project is presented. It is based on the performed work and on the knowledge and experience gained through the project period, which is presented in the report.

A specimen for biaxial testing is designed based on relevant literature. It meets the presented requirements, since it is designed with the SWP specified lay-up in the gauge zone and it fits into the existing test rig and mounting plates. Total failure can be achieved in a static test and first failure for static and fatigue tests appear in the gauge zone. Due to the imperfections in the specimen, especially in the ply drops near the gauge zone, some of the failures that should appear in the gauge zone, appear in the area between the ply drop and the gauge zone instead. The specimen is designed with a hexagonal gauge zone and it is selected to use internal ply drops.

To determine the final specimen design, an optimization is employed, where lamina thicknesses outside the gauge zone, the diameter of the fillet corners and the load ratio are parameters for the optimization. This is performed in order to ensure failure in the gauge zone and the SWP specified strain ratio.

The specimens are manufactured by SWP and delivered as square specimens, where the cruciform geometry is created by the workshop staff at Aalborg University and the project group.

Fatigue tests are performed where strains are monitored by strain gauges and DIC. Furthermore, failures are observed by a white light camera. Strain gauges are mounted in the gauge zone to monitor the strain ratio. On the arms strain gauges monitor the strain, in which it can be determined whether or not bending is present during a test. Bending is present for all the fatigue tests, but the magnitudes are negligible. DIC is used to monitor the strain field in the gauge zone, and to monitor where and when failure occurs. Failure can be observed by the camera, because the light reflection through the specimen changes when a failure occurs.

From the monitored strain ratio it is experienced that the SWP specified strain ratio is difficult to obtain and keep constant through a fatigue test. This is because the strain in the specimen varies cyclically with the applied loads.

The load magnitude for the primary and secondary actuator is controlled by the test rig controller, where the required cyclic loading ratio is achieved.

The specimen is designed to develop first failure in the gauge zone, but for some fatigue tests it is experienced that first failure occurs outside the gauge zone in areas where ply drops begin. Failure in these areas can be due to imperfections, etc. which is introduced, since it is selected to design the specimen with internal ply drops.

The state-of-the-art fatigue life prediction algorithm, FADAS, is implemented in an ANSYS material routine to be able to simulate the fatigue tests. Failure in the simulations are caused

by stresses in the FE shell model together with the progressive strength degradation and Puck's failure criteria. The FE shell model is modeled such that all ply drops are included in the geometry, which decreases the stress concentrations in the gauge zone. The stress concentrations are a major factor when the number of cycles for failure is determined, since the slope of the used S-N curve has a low magnitude. The progressive strength degradation is used to simulate the fatigue part of the simulations, where the magnitude of the cycle jump, Δn , has a significant effect on the simulation results. Puck's failure criteria are well known failure criteria which perform well compared to other failure criteria. Puck's failure criteria can predict failure and determine the actual failure mode, which is beneficial, because the simulation results then can be compared with the observed failures in the fatigue tests.

The implemented FADAS algorithm is validated w.r.t the stress-strain relation, the strength degradation and to physical coupon tests. The algorithm shows a negligible difference for the stress-strain relation and for the strength degradation. However, for the coupon test a larger difference appears, which is due to stress concentrations in the FE model of the coupon specimen.

The comparison between the performed fatigue tests and simulations show large deviations. This is due to stress concentrations in the FE model, imperfections in the specimen and deviation between the specimen material properties and the material properties employed for the simulations. The FE model is created so that stress concentrations are reduced as much as possible, by modeling areas for each ply drop. Imperfections yield failure to occur earlier in the fatigue tests compared to a specimen without imperfections.

SWP has delivered normalized material properties and these are de-normalized by material property magnitudes found in literature, therefore, a deviation can appear.

It is concluded that the implemented FADAS algorithm cannot be used to estimate when failure occurs in a specimen, because it predicts failure before the observed failure with a large deviation. Thus this algorithm is overly conservative.

It is concluded that the deviation of the implemented FADAS algorithm is too large, for it to be used as a tool when designing against fatigue damage. However, the algorithm can be used to achieve an insight in the interaction between the different failure types in a construction.

Future Work 12

A specimen is designed and fatigue tested in this project. It is concluded that the design of the specimen is not ideal, and some improvements are suggested below. Furthermore, suggestions on how to improve the fatigue testing and simulation of fatigue testing are presented.

Specimen Geometry

As mentioned earlier there are a lot of ways to design a biaxial test specimen. So far a good design has not been found, and the designed specimen in this project is no exception. One of the biggest problems with the design is the high probability of crack initiation in the ply drops, due to irregularities such as inclusions, and the resin rich areas in the internal ply drops. Furthermore, each specimen is manufactured individually, which means that a high deviation between the manufactured specimens is expected.

To avoid both these problems, external ply drops can be used. In this way, large GFRP plates can be manufactured, and several specimens can be cut from the same plate, and the gauge zone can be milled afterwards. However, when the ply drops are milled there is an increased probability of delamination in the ply drops, which also means that cracks initiate outside the gauge zone. A way to avoid this could be to mill the gauge zone and after that apply plies on either side of the specimen to encapsulate the ply drops. This, however, increases the time and complexity of the manufacturing process.

An alternative to drilling the fillet corners, is to get them water cut, which could decrease crack initiation in the fillet corners. To further decrease the crack initiation in the fillet corners, an entirely different fillet corner geometry could be applied as the one described in A. Makris et. al. [2009], where a spline is used to determine the geometry of the arms and fillet corners.

The hexagonal gauge zone geometry used in this project has the disadvantage of creating stress concentrations in the corners. The stress concentrations can be decreased and a more uniform strain field can be obtained by using a round gauge zone instead. However, it is difficult to make a circular gauge zone with internal ply drops without using e.g. a laser cutter.

The outer dimensions of the designed specimen are rather large, which means that high loads are required to produce failure within a reasonable number of cycles. Lower loads are required, if the overall size of the specimen is decreased, which means higher frequencies can be utilized, and there is a decreased risk of mechanical failure of the test rig. Furthermore, the resolution from DIC equipment would be increased if a smaller gauge zone is used, which means it is possible to obtain better results.

The focus of the optimization conducted in this project is on the lay-up of the specimen more than the geometry. In a second iteration of the optimization of the design, the geometry should be in focus. A lot of the load introduced into the specimen is distributed into the fillet corners, and some of this distribution could be avoided by designing the fillet corners differently. This optimization could also be conducted using topology optimization.

Fatigue Testing

Because of the relatively high strain ratio required in the gauge zone, the failures are primarily dependent on the load in the secondary direction, because the strength in this direction is a lot lower than in the primary direction. An increase in the strength and stiffness in the secondary direction, would entail that the load in the primary direction has a higher influence on the failures. The increased stiffness and strength could be obtained by introducing UD 90° plies in the gauge zone.

In this project only a few specimens were fatigue tested, which means that there is no way of knowing if the results are representative, or if they are misleading due to e.g. irregularities. Therefore, more tests should be conducted to ensure that the results from the tests are representative, so the potential diversions in the comparison with the simulation can be attributed to the simulation and not the tests.

Simulation of Fatigue Testing

The fatigue life prediction algorithm in this project is based on the FADAS algorithm. However, a few features are not included in the algorithm. This is the progressive stiffness degradation and non-linear material properties. The progressive stiffness degradation can be implemented as a curve fitting parameter. By including the non-linear material properties it is assessed that the fatigue life prediction algorithm can be made less conservative because it can take stress concentrations into account, and degrade the stiffness in an element before failure occurs, and hereby redistribute the stresses before failure occurs.

In the comparison of the fatigue tests and the simulation of the fatigue tests, it is chosen to compare the results by applying the same magnitude of loads. Instead, fitting of the loads in the simulations could be conducted and thereby obtain the strains in the gauge zone of the tests. The deviations could be reduced, but as the strain gauge results from the tests could be erroneous it is not necessarily the best approach.

In the project only first failure in the gauge zone is considered. It could be of interest to continue the tests and simulations until total failure, to determine if the fatigue life prediction algorithm can predict how the specimen fails at total failure.

Bibliography

- A. Makris et. al., 2009.** A. Makris et. al. *Shape optimisation of a biaxially loaded cruciform specimen*. Polymer Testing, 2009
- A. Puck, H. Schürmann, 1999.** A. Puck, H. Schürmann. *Failure analysis of FRP laminates by means of physically based phenomenological models*. Composites Science and Technology, 1999
- Andrew Hamilton, 2011.** Andrew Hamilton. *Introduction to Digital Image Correlation - MP5*. Aalborg University, 2011
- ANSYS, 2011a.** ANSYS. *ANSYS 14.0 Help*, 2011a
- ANSYS, November 2011b.** ANSYS. *ANSYS Mechanical APDL Programmer's Manual*, November 2011b. Release 14.0
- E. N. Eliopoulos, T. P. Philippidis, 2011.** E. N. Eliopoulos, T. P. Philippidis. *A progressive damage simulation algorithm for GFRP composites under cyclic loading. Part II: FE implementation and model validation*. Composites Science and Technology, 2011
- ESA, 1994.** ESA. *Structural Materials Handbook*. European Space Agency, vol. 1 edition, 1994
- Freissinet, 2011.** Sebastien Freissinet. *Worries about new composite made airplane*. 1001crash.com, 2011. <http://www.1001crash.com/index-page-composite-lg-2.html>
- GOM mbH, 2007.** GOM mbH. *ARAMIS User Manual*. GOM mbH, 2007
- GOM mbH, 2012.** GOM mbH. *ARAMIS Technical Data*. GOM mbH, 2012. Technical data for ARAMIS 4M system,
<http://www.gom.com/metrology-systems/digital-image-correlation.html>
- Jones, 1999.** Robert M. Jones. *Mechanics of Composite Materials*, 2nd edition, 1999
- Knops, 2008.** Martin Knops. *Analysis of Failure in Fiber Polymer Laminates*. Springer, 2008
- Lamkanfi et. al., 2010.** Lamkanfi et. al. *Strain distribution in cruciform specimens subjected to biaxial loading conditions. Part 1: Two-dimensional versus three-dimensional finite element model*. Polymer Testing, 2010
- Laustsen, 2014.** Steffen Laustsen. *Introduction to test rig*. Siemens Wind Power A/S, 2014
- Laustsen et. al., 2013.** Laustsen et. al. *Development of a High-fidelity Experimental Substructure Test Rig for Grid-scored Sandwich Panels in Wind Turbine Blades*. Strain - An International Journal For Experimental Mechanics, 2013
- M. Leong et. al., October 2012.** M. Leong et. al. *Investigation of failure mechanisms in GFRP sandwich structures with face sheet wrinkle defects used for wind turbine blades*. Composite Structures, October 2012
- MathWorks, 2014.** MathWorks. *R2014a Documentation*, 2014. <http://www.mathworks.se/help/gads>

BIBLIOGRAPHY

- Miel, 2013.** Rhoda Miel. *Composite-body BMW i3 starts production*. Plastics News, 2013.
<http://www.plasticsnews.com/article/20130918/NEWS/130919923/composite-body-bmw-i3-starts-production>
- Mouritsen, 2010.** Ole Ø. Mouritsen. *Grundlæggende usikkerhedsvurdering ved måling med strain gages*. Department of Mechanical and Manufacturing Engineering, Aalborg University, 2010
- Nijssen, February 2011.** Rogier Nijssen. *OptiDAT wind turbine materials research database*. Knowledge Centre Wind turbine Materials and Constructions, February 2011
- Norton, 2006.** Robert L. Norton. *Machine Design - An integrated approach*, 3rd edition, 2006
- Overgaard, 2014.** L. Overgaard. *Multiaxial fatigue in GFRP Materials*. Aalborg Universitet, 2014
- Philippidis, 2011.** T. P. Philippidis. *Verified Material model incorporating progression of damage due to static loading and the effect of fatigue on residual strength and stiffness*. University of Patras, 2011
- Richardson, N/A.** David Richardson. *The Fundamental Principles of Composite Material Stiffness Predictions*. University of the West of England, N/A. Lecture slides
- SKF, 2014.** SKF. *SKF Group*. SKF, 2014.
<http://www.skf.com/group/products/bearings-units-housings/spherical-plain-bearings-bushings-rod-ends/maintenance-free-rod-ends/female-thread/index.html?prodid=208300000>
- Sony, 2014.** Sony. *Sony 40GB Hard Disk Drive Full HD Camcorder Specification*, 2014.
<http://www.sony-meia.com/product/hdr-sr10e/specs>
- Testo, 2014.** Testo. *Testo Instruments - Test and Measurement Equipment*. Testo, 2014.
<http://www.testolimited.com/p/305/testo-875-thermal-imaging-camera#fulldescription>
- ToolBox, N/A.** The Engineering ToolBox. *Friction and Coefficients of Friction*. The Engineering ToolBox, N/A. http://www.engineeringtoolbox.com/friction-coefficients-d_778.html
- V.A. Passipouiaridis, T.P. Philippidis, 2010.** P. Brondsted V.A. Passipouiaridis, T.P. Philippidis. *Fatigue life prediction in composites using progressive damage modelling under block and spectrum loading*. International Journal of Fatigue, 2010
- V.A. Passipouiaridis, P. Brøndsted, November 2009.** V.A. Passipouiaridis, P. Brøndsted. *Fatigue Evaluation Algorithms Review*. Risø DTU - National Laboratory for Sustainable Energy, November 2009
- Wahl, 2001.** Neil Kelly Wahl. *Spectrum Fatigue Lifetime and Residual Strength for Fiberglass Laminates*. Montana State University, 2001

Part V

APPENDIX

Specimen Manufacturing

A

This appendix describes the manufacturing of the specimen and issues with this process. The content of the appendix is:

- | | |
|-----|---|
| A.1 | Manufacturing Process |
| A.2 | Gained Experience regarding the manufacturing process |
| A.3 | Sources of Error Due to Manufacturing Process |

A.1 Manufacturing Process

The specimens are manufactured by SWP, but in order to verify that it is possible to manufacture them w.r.t. geometry, lay-up, ply drops and the manufacturing process a pretest specimen is manufactured at Aalborg University by the project group and former Ph.D. student Steffen Laustsen. Furthermore, this enables the project group to get a hands on experience with the manufacturing of the specimen. For the specimens the manufacturing process vacuum assisted resin transfer molding (VARTM) is selected by SWP.

Ply Cutting and Placing

Plies are cut according to the outer geometry, the gauge zone or ply drop boundaries throughout the specimen and placed, as shown in Figure A.1.

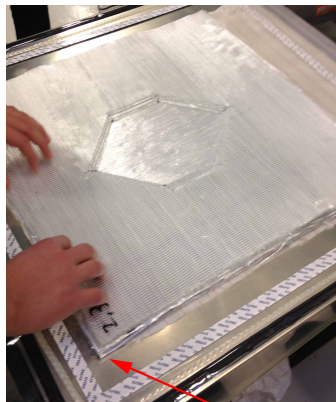


Figure A.1 Plies are placed on the mold. The red arrow shows the reference point for the lay-up

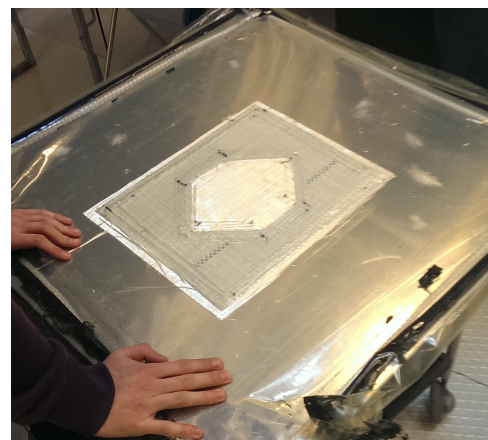


Figure A.2 The mold

Mold Creation and Specimen Casting

The mold is created on a thin steel plate, where cutouts from the gauge zone and ply drop boundaries are used to obtain the desired mold shape, as shown in Figure A.2. When the lay-up is placed on the mold, the VARTM process can be initiated, as shown in Figure A.3.



Figure A.3 The VARTM process, where the epoxy flow front is shown

A.2 Gained Experience regarding the manufacturing process

Ply Cutting

To ease the cutting process of the plies, it is necessary to use templates for the outer geometry, the gauge zone and the ply drops. The cutting is done with a tool, similar to a pizza cutter, designed to cut glass fiber. This is easier compared to a pair of scissors. As no BIAX plies are available, UD plies cut in $\pm 45^\circ$ are used instead.

The prefabricated glass fiber is delivered on reels, thus it is necessary to roll the fiber mats out on a table to be able to cut the mats. The fiber mats consist of UD fibers which are stitched with threads. The mats stretch significantly in the transverse direction of the fibers, and therefore it is necessary to roll out the mat and let it settle on the table before cutting the plies. This can be eased by two persons lifting the fiber mats, one in each side, and then lay it down on the table.

Mold Creation

When preparing the mold for the casting process it is necessary to get as much space around the outer geometry of the specimen as possible, in order to get the vacuum plastic to tighten properly. Therefore the mold needs to be positioned appropriately.

Placing the Plies

It was difficult to place the plies such that the reference point is used and fulfilled, but at the same time having the right ply drop distances in the specimen. The better the plies are cut, the better and easier it is to manufacture the lay-up.

Furthermore, when the plies are placed it is important that no extra fibers are spilled at the free areas, where the vacuum plastic is supposed to enclose to the mold. Small fibers can cause leakage, thus it is not possible to obtain the wanted vacuum within the mold.

Casting

When casting the specimen it is beneficial to have a relatively large area, without any fibers, for the epoxy to flow through before it reaches the outlet of the mold, as shown in Figure A.4.



Figure A.4 VARTM process, where the arrow indicates the clearance to the outlet of the mold

This may ensure that the epoxy reaches all the fibers in the specimen, because the flow resistance becomes higher at the area near the outlet.

Before the VARTM can be initiated the epoxy is degassed in order to remove air inclusions. This is done for approximately 15 [min] in a pressure chamber subjected to vacuum.

A.3 Sources of Error Due to Manufacturing Process

In this appendix uncertainties and flaws in the specimen are presented. These appear, due to the way the specimen is designed and manufactured.

A.3.1 Surface Irregularities

From the VARTM process the possibility of having irregularities on the surface of the specimen is present, which is due to the used mold. The mold is created, as shown in Figure A.2, from a thin steel plate where the curvature for the ply drops is constructed by placing fiber mats. These fiber mats are identical to the cutouts of the fiber mats used in the specimen e.g. cutouts of the gauge zone. The fiber mats in the mold can be laid up with small gaps between the fibers, which affects the surface of the specimen when the vacuum process is initiated.

Furthermore, in the manufacturing process of the specimen a one sided mold is used, i.e. one specimen side lies on the mold and the other is free, only constrained by the vacuum bag. An example of these surface irregularities are shown in Figure A.5.

The surface irregularities mainly appear on one side of the specimen, which is the specimen side turning upwards in the mold during the curing process. Also the side turning towards the mold has surface irregularities, which could be caused by the cutouts.



Figure A.5 Cutout of the specimen going through the gauge zone

To the right of the red line, in Figure A.5, is the start of the third ply drop boundary. To the left, the gauge zone is shown where surface irregularities can be seen. The irregularities are present as a wavy surface, where the thickness changes, as shown around the red arrows.

If a strain gauge rosette is attached on a wavy surface, it can show erroneous results. On a wavy surface like the one shown in Figure A.6 the thickness varies along the secondary direction,

meaning that the stress and strain varies as well. This means that a strain gauge placed on a cross section with a relatively high thickness, yields a strain with less magnitude in the secondary direction, than if it is placed on cross section with a low thickness. However, it is assumed that the strain in the primary direction is unaffected by the thickness change in the secondary direction.

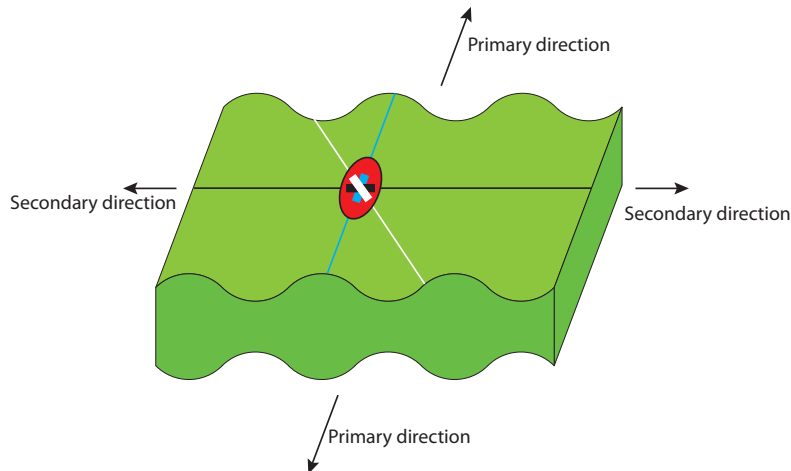


Figure A.6 Strain gauge on a surface with varying thickness

It is difficult to diminish surface irregularities due to the chosen manufacturing process, but when strain gauges are attached to the specimen the surface is polished in order to remove as much of the irregularities as possible. However, care has to be taken, as too much polishing can result in too much epoxy being removed such that the glass fibers are reached and damaged. To remove the surface irregularities completely a change in the manufacturing process has to be employed. During the curing process a plate could be placed on top of the specimen, i.e. a plate identical to the existing mold. This would even out the pressure on both specimen sides, in which the surface irregularities can be decreased.

Furthermore, the molds could be manufactured in a CNC milling machine where small tolerances can be obtained and two identical molds can be created, without using glass fiber cutouts.

A.3.2 Imperfections

Imperfections appear in the specimen and can be due to different issues. Internal ply drops are employed in the specimen, where a resin pocket can be in front of the ply drop, as shown in Figure A.7. This pocket consists entirely of epoxy and no fibers, thus the strengths in this pocket are determined by the material properties of the used epoxy.



Figure A.7 Resin pocket in an internal ply drop

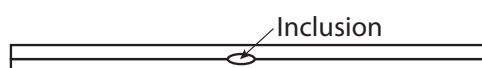


Figure A.8 Inclusion between two plies

Inclusions are another issue when dealing with composite specimens. An inclusion can be compared to a resin pocket, but it is not necessarily located in front of a ply drop. It can for example appear between two plies, as shown in Figure A.8, and it can consist of epoxy, air, water, etc. An inclusion is a weakness for the specimen, because the fibers are further from each other, thus the specimen strength is decreased. Furthermore, there is a very large likelihood of

crack initiation at the inclusion. The inclusion material properties determine the strength for the specimen in this area. [Jones, 1999]

The VARTM process is employed for the manufacturing of the specimens tested in this project, where it is assumed that the specimen is completely infused with epoxy. However, this is difficult to control during the process and curing, in which dry fibers can appear. Dry fibers can appear during the manufacturing process, if the epoxy cannot be sucked through the specimen lay-up because of the vacuum or the shape of the mold. Furthermore, two plies or a bundle of fibers can be pressed together where the epoxy cannot be sucked through, thus the epoxy cannot reach all fibers and dry spots appear.

The volume fraction of a composite has a significant effect on the performance w.r.t. strength and stiffness. For a composite the volume fraction describes the relation between the amount of fiber and epoxy. A change of volume fraction through a specimen can result in failures at different number of cycles for different areas in the specimen, when exposed to e.g. cyclic loads in a fatigue test. A method to determine the volume fraction in different areas of a specimen is to use a destructive approach, where elements are cut out of the specimen and burned in an oven.

A.3.3 Geometric Asymmetry

By asymmetrical geometry, it is meant that during the curing process there could be more epoxy present at the side of the specimen turning towards the mold than the side turning away from the mold and vice versa, thereby making the specimen asymmetrical. Furthermore, when the different plies are cut, the specified tolerances can be difficult to achieve and thereby making the specimen asymmetrical. If an asymmetrical geometry is present for a specimen, the risk of having out-of-plane bending is increased, and the possibility of getting results from the utilized measurement equipment which are not representative for the specimen is also increased.

Finite Element B

In this appendix FE related material is presented. The content of the appendix is:

B.1	The Solid Model
B.2	The Shell Model
B.3	Comparison of the Solid and Shell Model
B.4	Validation of FE Shell Model
B.5	Properties
B.6	Validation of BIAX Ply
B.7	Convergence Study
B.8	Force and Stress Distribution in Specimen
B.9	Calculations of Bolt Connections

B.1 The Solid Model

In this appendix the solid model is described. The solid model is employed in the optimization to determine the fillet corner diameter and number of plies in the individual layer groups.

The solid model is a 3D volume model where all laminae are modeled as volumes, on both sides of the mid lamina (5 UD 0°). As explained in Section 2.3 only a quarter of the specimen is modeled, because it is symmetric around the vertical and horizontal axis and it is of interest to reduce the computational time. The quarter specimen with BC's are shown in Figure B.1.

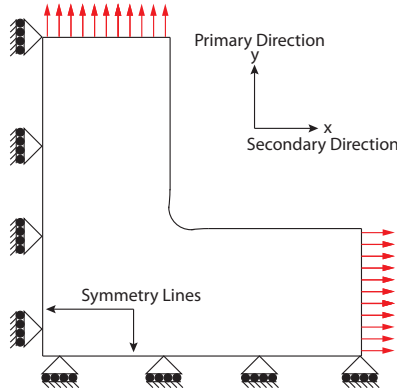


Figure B.1 FE geometry

The FE model can be divided into parts, as the flowchart in Figure B.2 shows. The different parts are not described in details, since only the essence of each part is of interest. For more details, the FE model can be found on the CD, see Appendix G.

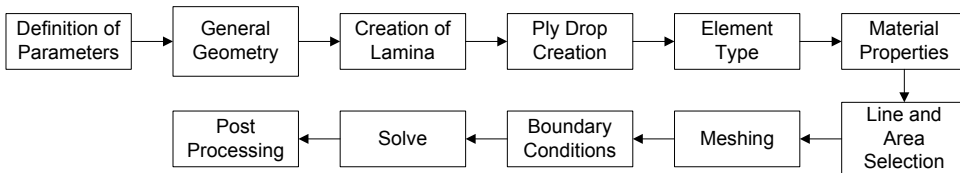


Figure B.2 Flowchart of the solid model

B.1.1 Definition of Parameters

The solid model is controlled by model parameters. During the optimization the algorithm controls the magnitude of each of the variable parameters such as, thicknesses of the three layer groups, the fillet corner diameter and the load ratio.

B.1.2 General Geometry

The general geometry is constructed in this part. Initially keypoints are created, then lines are created between the keypoints before areas are created from the lines. Finally the areas are extruded into volumes. These volumes are the mid lamina and consist of 5 UD 0°.

B.1.3 Volume (all Laminae) and Ply Drop Creation

In these parts, volumes are created for the remaining lamina together with ply drop volumes. The created mid lamina volumes have a surface which consists of multiple areas, as shown in

Figure B.3. These surface areas are a product of the above mentioned created lines. All other lamina volumes are created with use of one (or multiple) areas of the mid lamina surface, as shown in Figure B.4.

It is selected to implement ply drops in the solid model, which is done by creating a prism-like volume, as shown in Figure B.5. Furthermore it is selected to assign the same material properties to the ply drop and the layer group 1. This approach is performed for all the different ply drops.

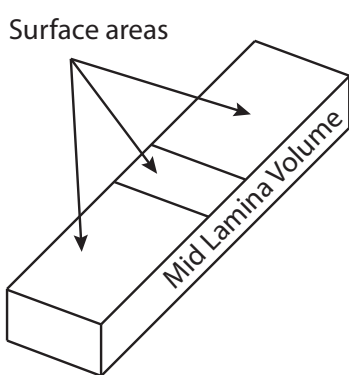


Figure B.3 Illustration of the mid lamina

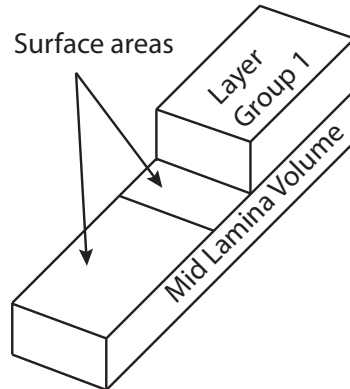


Figure B.4 Illustration of two created volumes

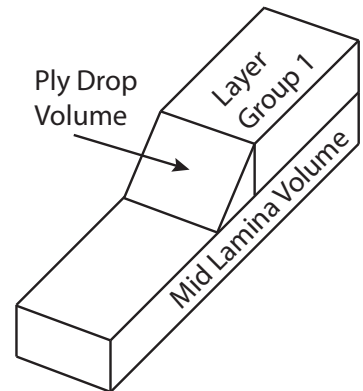


Figure B.5 Illustration of a ply drop

The geometry of the ply drop volume is shown in Figure B.6, where it is illustrated that the two cathetus have the same length, i.e. angle $A = B = 45^\circ$. This is implemented in an attempt to reduce the stresses in the corners of the ply drop volume.

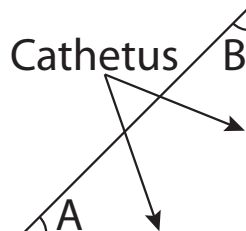


Figure B.6 2D view of the ply drop volume

B.1.4 Element Type and Material Properties

This is a 3D volume model, thus the solid brick element called SOLID186 is employed. It is a higher order element consisting of 20 nodes. The element has three degrees of freedom in each node, which is the displacements, U_x , U_y and U_z [ANSYS, 2011a]. The default key options are employed for the element.

The material properties employed in the solid model are described in Appendix B.5.

B.1.5 Line and Area Selection

Before meshing, a selection of line and area groups are performed. Different line and area groups are defined and used in the meshing part.

B.1.6 Meshing

The meshing sequence uses the VMESH command to mesh the created volumes. Each volume group represents a lamina and is meshed individually to ensure that the correct properties are assigned to the elements, e.g. material properties and coordinate system.

The element shape is mainly hexahedral and only in the ply drop volumes is the element shape changed to a prism. This is shown in Figure B.7, where a sectional view of the meshed volumes is shown.

In Figure B.8 the mesh mid lamina volume is shown. The element size is not constant throughout the specimen, i.e. a fine element size is employed in the gauge zone and the areas around it and a coarse element size is employed beyond the first ply drop boundary. This yields a reduction of elements in the FE analysis compared to a case where the fine element size is employed for the whole specimen, which reduce the computational time.

The element sizes are determined through a convergence study, see Appendix B.7.1, where a factor of two is implemented between the fine and coarse element sizes. The convergence study yields the fine element size to be 3.5 [mm] and 7 [mm] for the coarse element size.

The above-mentioned line and area selection is used to control where the fine and coarse element sizes are employed. Furthermore, a line selection is used to control the number of elements in the height of each volume, which is set to 1 element for all laminae.

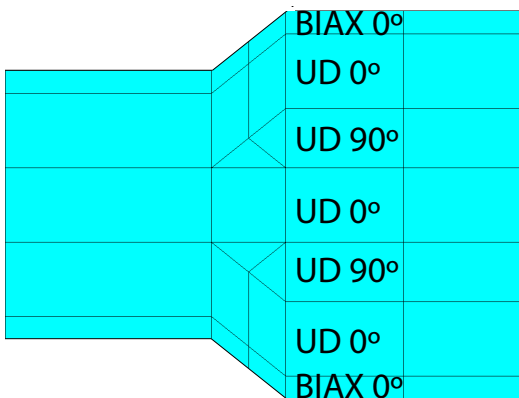


Figure B.7 Mesh around a ply drop

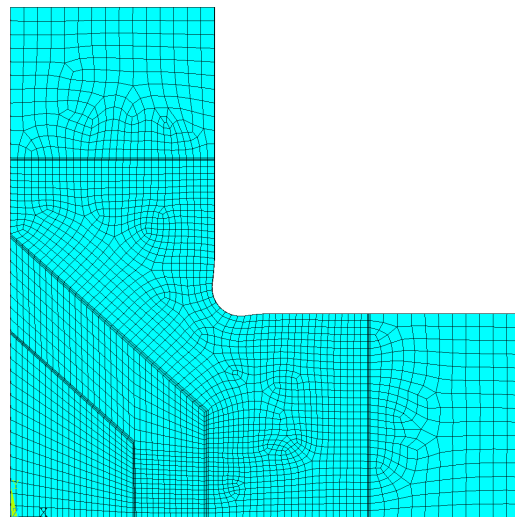


Figure B.8 Volume mesh of the UD mid lamina

B.1.7 Boundary Conditions

The applied BC's are shown in Figure B.1. The primary and secondary forces are applied to all nodes in their respective ends. Symmetric BC's are applied to all the nodes along the two symmetry lines. The horizontal line is fixed in the y-direction, thus it can only move along the x-axis. For the vertical symmetry line movement in the x-direction is prevented.

Furthermore, the nodes on the mid lamina are constrained in the z-direction to ensure that no out-of-plane displacements occur.

B.1.8 Solve and Post Processing

The model is solved as a static structural FE analysis. The solid model is used for the optimization, which is described in Section 2.4.

B.2 The Shell Model

In this appendix the shell model is described. It is used for the simulation of the fatigue test, where a fatigue simulation algorithm is implemented. The shell model is a simplification of a solid model, because the shell element type is a collapsed solid element, where a 2D assumption is employed. The assumption yields that only in-plane strain, stresses, etc. are calculated.

The shell model is an area model where a shell element is employed. A flowchart of the model is shown in Figure B.9. The different parts are not described in details, since only the essence of each part is of interest. For more details, the FE model can be found on the CD, see Appendix G.

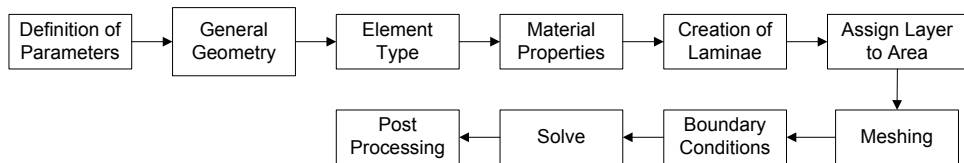


Figure B.9 Flowchart of the shell model

B.2.1 Definition of Parameters

The model parameters for the shell model are set to the optimization results, presented in Table 2.1.

B.2.2 General Geometry

The general geometry for the shell model consist of 18 areas, as shown in Figure B.10. As presented in Section 2.2 on page 12, the specimen consists of a gauge zone with the SWP specified lay-up and ply drop zones around it. To ensure that the stiffness change between areas with different lay-up is as small as possible, it is selected to have an area for each ply, i.e. where a new area is created for each ply drop.

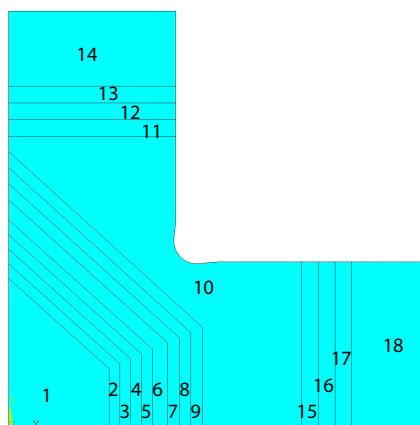


Figure B.10 Areas of the general geometry

B.2.3 Element Type and Material Properties

The ANSYS element type SHELL181 is employed for the shell model. It is a lower order element consisting of 4 nodes, where each node has six degrees of freedom, i.e. three displacements (U_x , U_y and U_z) and three rotations (Rot_x , Rot_y and Rot_z) [ANSYS, 2011a]. The default key options are employed for the shell element, except for the layer data storage option, where it is selected to store data from all layers including the mid layer.

The material properties employed in the shell model are described in Appendix B.5.

B.2.4 Creation of Laminae and Assign Lamina to Area

In these parts, laminae are created and assigned to areas. In Figure B.11 the lay-ups, determined in the optimization, are shown for the different areas. In area 2 to 6 UD 0° ply drops begin and yield that one to five UD 0° plies, respectively, are added to the gauge zone lay-up. Similar for areas 7-10 and 11-18 for UD 90° and UD $\pm 45^\circ$ plies, respectively.

Furthermore, material properties and element coordinate systems are assigned to each of the laminae.

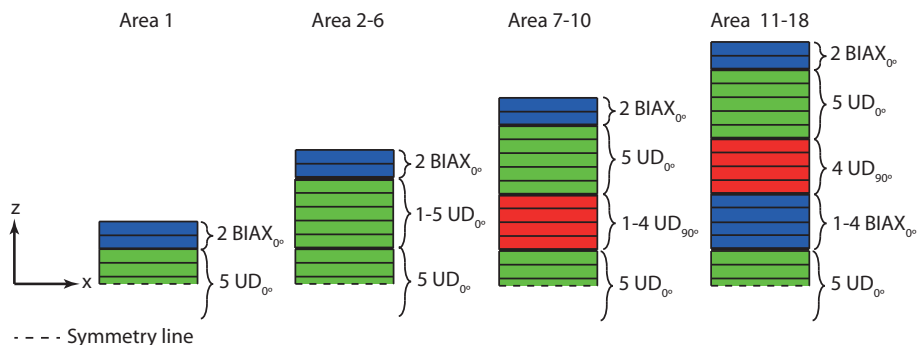


Figure B.11 The symmetric lay-up for the different areas

B.2.5 Meshing

The areas are meshed with the AMESH command, where the element size is determined through a convergence study, in Appendix B.7.2. The meshed specimen is shown in Figure B.12, where it can be seen that different element sizes are used. In the arms where the loads are applied the element size is 4.2 [mm]. In and around the gauge zone the element size is 1.7 [mm] and between the gauge zone and the arms the element size is 2.1 [mm].

Compared to the solid model the shell model is not as computationally heavy to solve, because the element type SHELL181 is a 4 node element and the solid element is a 20 node element SOLID186.

The created laminae for each of the areas are not a part of the meshing, since these are assigned to each of the elements.

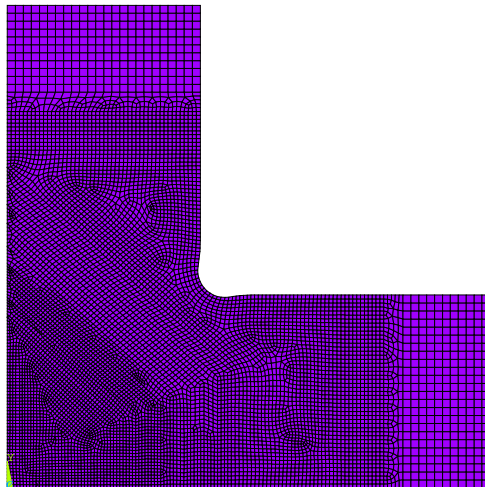


Figure B.12 ANSYS graphical output of meshed geometry

B.2.6 Boundary Conditions

The BC's for the shell model are similar to what is applied to the solid model, see Appendix B.1. However, the shell model uses an element type which has both displacement and rotational degrees of freedom in each node, compared to a solid element which only has displacement degrees of freedom.

B.2.7 Solve and Post Processing

The solving of the static system is performed and the post processing can begin. The shell model is used for the FADAS algorithm, where the post processing is explained in Part III.

B.3 Comparison of the Solid and Shell Model

In this appendix the solid and shell model are compared in order to clarify difference between the models. It is of interest to use a shell model, with only 4 nodes per element in order to reduce the computational time compared to the solid model with 20 nodes per element.

In this appendix it will be studied whether or not the solid model gives important information which the shell model does not provide. This is of interest since the computational demands for solving the shell model is substantially lower than for the solid model.

In Section 2.5, on page 23, the solid model strains and failure indices are presented, where the applied loads are 200 [kN] and 89 [kN] for the primary and secondary direction, respectively. These loads are applied in the shell model described in Appendix B.2, in which the strains and failure indices can be compared. The difference in strains and failure indices is shown and the strains are summarized in Table B.1.

In Figure B.13 and B.14 the strain in the primary direction is shown for the solid and shell model, respectively. The strain fields in the two models are not identical. The solid model strain field is between 3900 [μstrain] and 5400 [μstrain] where the strain field in the shell model is between 4800 [μstrain] and 5300 [μstrain]. These strain intervals are found by looking into the strain field away from the boundaries.

Furthermore, the magnitude for the stress concentrations in the shell model is smaller than those for the solid model. This is in good agreement how the solid and shell models are created. For the solid models the entire lamina is reduced in one ply drop, where it for the shell model is divided into multiple ply drops.

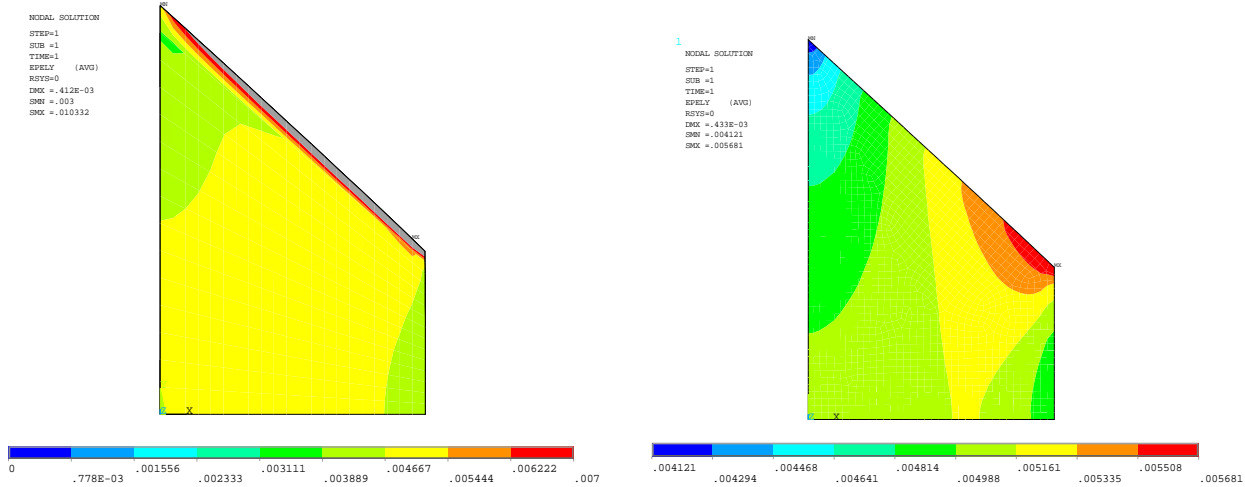


Figure B.13 The gauge zone strain in primary direction for the solid model

Figure B.14 The gauge zone strain in primary direction for the shell model

In Figure B.15 and B.16 the strain in the secondary direction is shown for the solid and shell model, respectively. Again, the strain fields in the two models are not identical. The solid model strain field is between 1700 [μ strain] and 2300 [μ strain] where the strain field in the shell model is between 1800 [μ strain] and 2200 [μ strain].

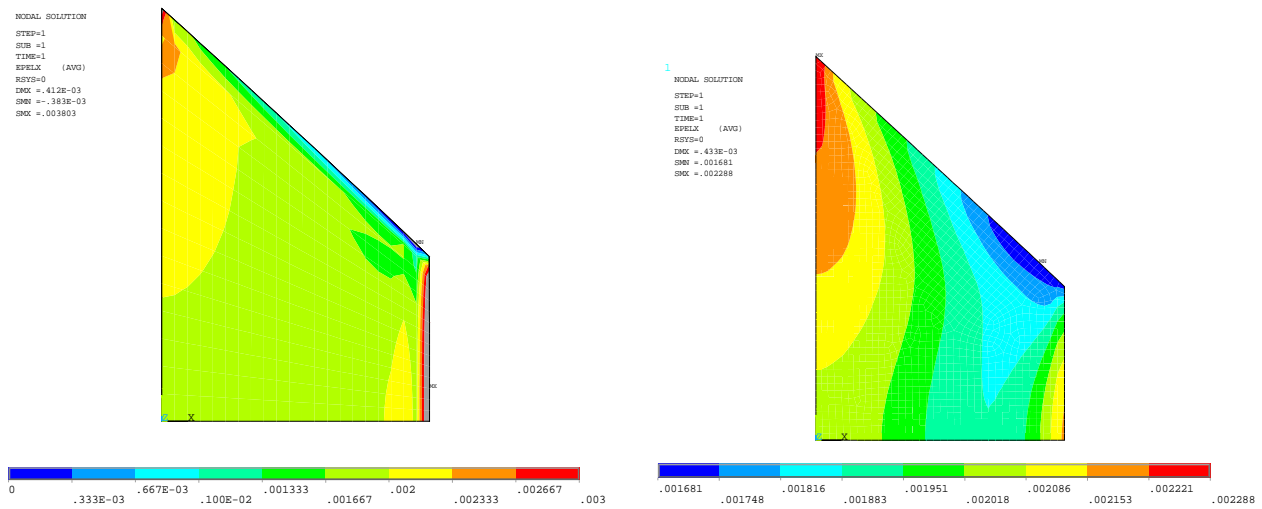


Figure B.15 The gauge zone strain in secondary direction for the solid model

Figure B.16 The gauge zone strain in secondary direction for the shell model

The deviation for the gauge zone strains are determined as the deviation between the mean values for the solid model and shell model intervals.

In Table B.1 a comparison of strains determined by the solid and shell model is shown. Strains

in the gauge zone are compared together with a point in the center of the gauge zone (0,0).

Table B.1 Comparison of strains determined in the solid and shell model

		Solid [μstrain]	Shell [μstrain]	Deviation [%]
Gauge Zone Strain	ε_x	1667 - 2333	1816 - 2153	0.8
	ε_y	3889 - 5444	4814 - 5335	8.7
	ε_{xy}	-421 - 515	-453 - 441	10.8
Center Point	ε_x	1940	2149	10.8
	ε_y	4805	4794	0.2
	ε_{xy}	$-0.639 \cdot 10^{-3}$	-32	-
	R_{Strain}	0.404	0.449	11.1

A deviation appears between the solid and the shell model, but the difference is between 0.2 [%] and approx. 10.8 [%], if the shear strain in the center point is neglected. The deviation between shear strains is larger, but the magnitude of the shear strains is minor compared to the magnitude of the strains in the primary and secondary direction, thus these are neglected.

For the failure indices the maximum stress criteria is employed. In Figure B.17 and B.18 the failure indices for the mid UD lamina are shown for the solid and shell model, respectively. There is a good agreement between failure in the two models, since the only differences are in the boundaries where the loads are applied and around the gauge zone. The shell model is a bit more conservative compared to the solid model, because a larger area around the gauge zone has a failure index above 1.

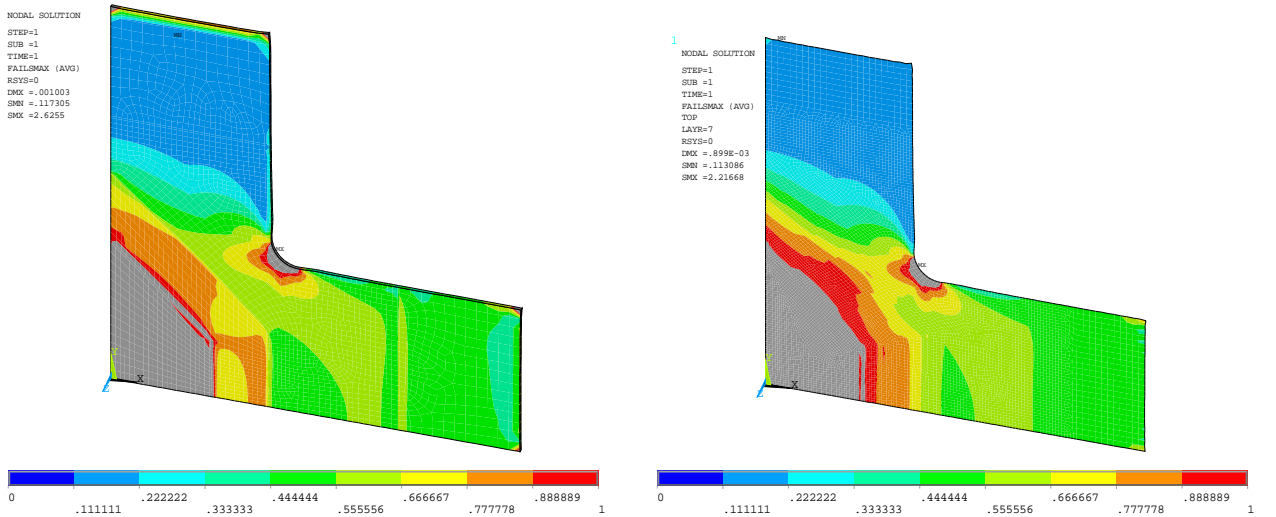


Figure B.17 Failure in the solid model UD lamina

Figure B.18 Failure in the shell model UD lamina

Differences and deviations appear between the two models, but it is assumed that the models predict similar strains and failure indices. Thus the shell model is used instead of the solid model, i.e. the lay-up and load ratio determined for the solid model is valid for the shell model as well.

B.4 Validation of FE Shell Model

In this section the FE shell model is validated against strain gauge and DIC monitored strains during a test of the specimen.

During the test the load is ramped up to 130 [kN] in the primary direction and 57.85 [kN] in the secondary direction with a constant load rate. The loads correspond to $R_{Load} = 0.445$. These loads are held in approx. 5 [s] and then the specimen is unloaded. Five strain gauge rosettes are attached to the specimen in the gauge zone, as shown in Figure B.19. The test is conducted on the FT3 specimen where 3 additional strain gauge rosettes are employed, e.g. rosette 1, 2 and 3. The front and back strain gauge rosette is used during this study and during FT3.

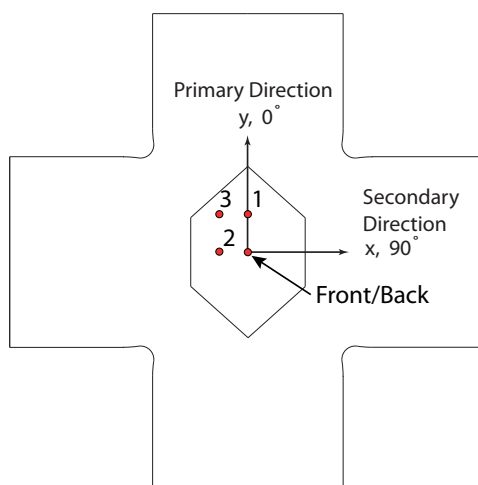


Figure B.19 Position of strain gauge rosettes

The points shown in Figure B.19 are described in Table B.2.

Table B.2 Measuring points in [mm]

Front/Back	Strain gauge rosettes positioned at (0,0) on the front and back
Point 1	Strain gauge rosette positioned at (0,40)
Point 2	Strain gauge rosette positioned at (-30,0)
Point 3	Strain gauge rosette positioned at (-30,40)

The results from the strain gauges are shown in Figure B.20 to B.23.

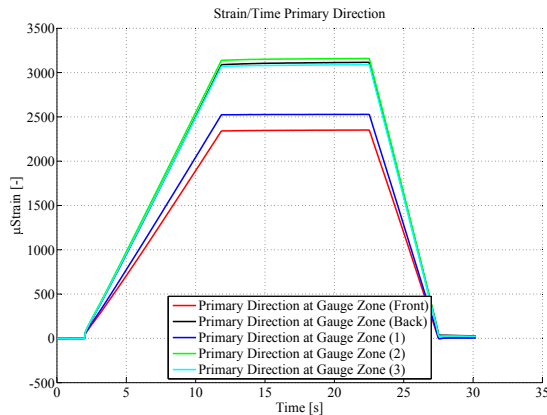


Figure B.20 Strain in primary direction

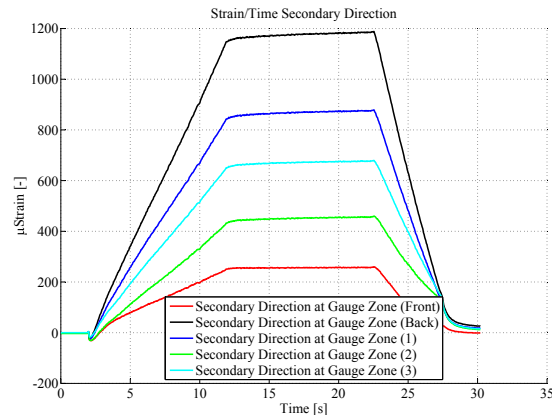


Figure B.21 Strain in secondary direction

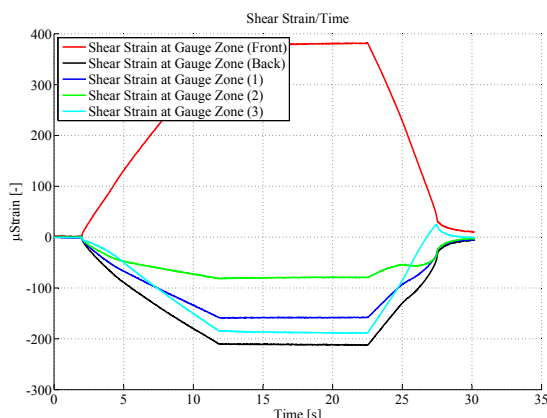


Figure B.22 Shear strain

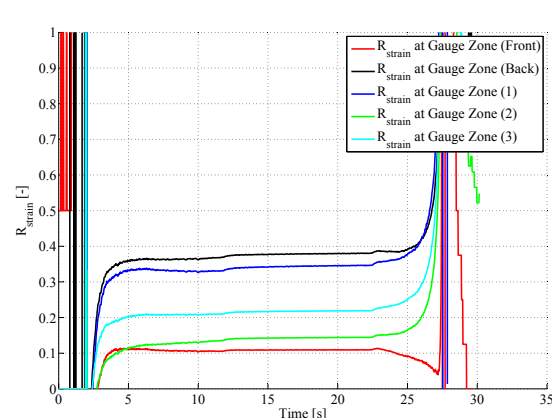


Figure B.23 Strain ratio

The shear strain, shown in Figure B.22, for the strain gauge on the front has positive values, while the others have negative values. This is because the strain gauge rosette on the front is placed differently compared to the ones on the back, i.e. the strain gauge positioned in 45° on the front is subjected to tension and the one on the back is subjected to compression. The magnitude of the shear strain result is almost twice as much on the front compared to the other results. In general all the results from the strain gauge on the front seem erroneous, which can be seen in Table B.3. This could indicate that this strain gauge rosette is positioned on a surface irregularity, etc. as described in Appendix A.3.

The DIC results from the test are shown in Figure B.24 to B.26.

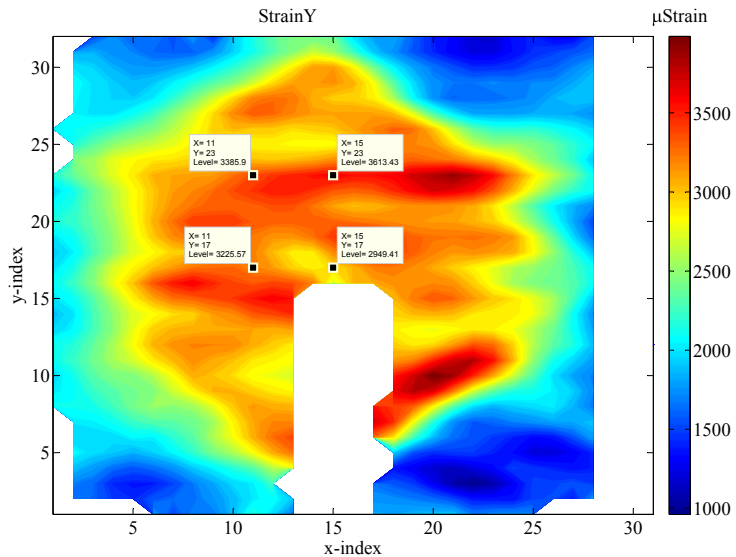


Figure B.24 Strain in the primary direction

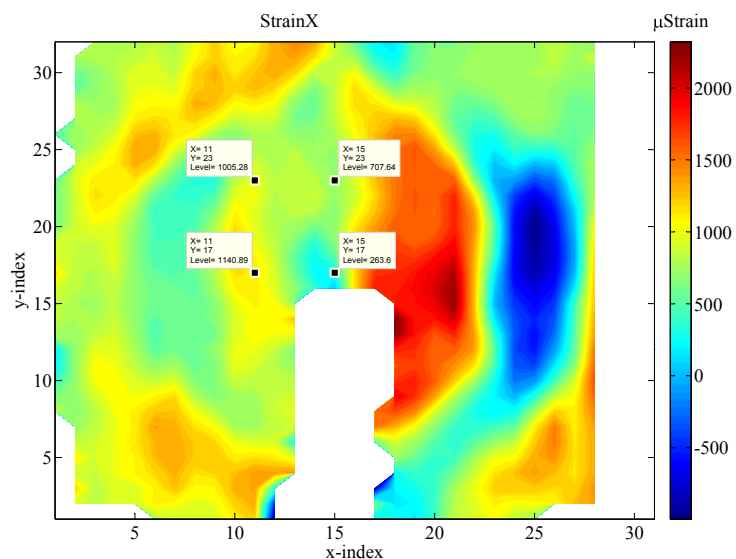


Figure B.25 Strain in the secondary direction

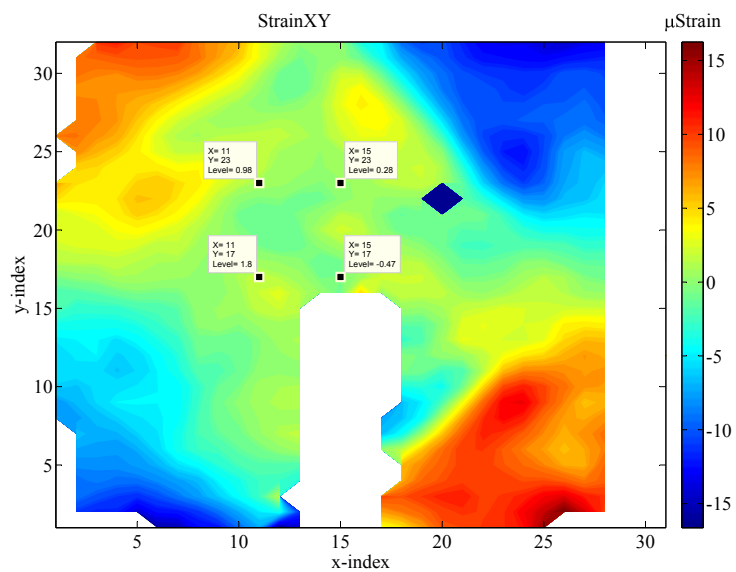


Figure B.26 Shear strain.

The DIC result for the primary direction and the shear strain generally show a symmetric strain distribution. However, a tendency of increased strains at index (20,10) and (20,24) is present in Figure B.24, and this is also shown in the result for the secondary direction in Figure B.25. Furthermore the result for the secondary direction does not have a symmetric strain distribution, which could be due to the manufacturing process of the specimen, resulting in an asymmetrical geometry. Asymmetrical geometry is described in detail in Appendix A.3.

B.4.1 Comparison

The FE shell model is compared to the strain gauge and DIC monitored strains, shown above, since it is of interest to determine how the FE model deviates w.r.t. to the monitored strains. The strain gauge results correspond to the values at 17.5 [s]. The FE shell model and DIC results are extracted at the points corresponding to the points shown in Figure B.19 and as shown in the DIC results.

In the comparison, the above-mentioned loads are applied in the FE shell model and the comparison is shown in Table B.3.

Table B.3 FE shell model results at the four measurement points

	Point	FE model	Strain gauge	DIC	Deviation w.r.t. strain gauge [%]	Deviation w.r.t. DIC [%]
Primary direction, ϵ_y [μstrain]	Front	3261	2349	2949	39	11
	Back	3261	3110	2949	5	11
	1	3192	2527	3613	26	12
	2	3342	3155	3226	6	4
	3	3358	3083	3386	9	1
Secondary direction, ϵ_x [μstrain]	Front	1343	257	264	423	409
	Back	1343	1117	264	20	409
	1	1402	869	708	61	98
	2	1253	453	1141	177	10
	3	1270	673	1005	89	26
Shear, ϵ_{xy} [μstrain]	Front	0.25	380	-0.5	100	-153
	Back	0.25	-212	-0.5	-100	-153
	1	10	-158	0.3	-106	3471
	2	5	-80	1.8	-106	178
	3	232	-188	1.0	-223	23573

Generally the FE shell model overestimates the strains in the primary and secondary directions when compared to the strain gauge results. However, the shear strains are underestimated.

The largest deviation for the primary direction is 26 [%], if the front strain gauge is neglected. The deviations for the secondary direction and the shear strain could be due to the imperfections on the surface of the specimen resulting in reasonable results in the primary direction, but erroneous results in shear and in the secondary direction. These imperfections are unavoidable during the manufacturing process, which is described in Appendix A.3. When the FE shell model is compared to the DIC results the maximum deviation in the primary direction is 12 [%].

In the secondary direction the deviations are larger, where the largest deviation is 409 [%]. The shear strains deviated even more than the primary and secondary direction, but as these strains are relatively small a large percentage deviation is depicted.

Deviations between the FE shell model and the measured results from the DIC and strain gauges are definitely present. The primary direction is within acceptable tolerances, when taking into account that the FE shell model is an ideal model, where no imperfections or irregularities are present, which appear in the specimen. The results in the secondary direction and the shear strain results make it difficult to conclude anything else than these exceed a reasonable allowed tolerance when validating an FE model. As described in Appendix A.3, the loads are distributed better in the primary direction to the gauge zone than for the secondary direction, which can be a reason for the presented results in this appendix.

In order to make a more comprehensive quantitative assessment, multiple identical tests should be conducted. However, due to limited number of specimens this has not been done.

B.5 Properties

In this section the material properties are presented. These are employed for all the FE simulations in this project.

B.5.1 Material Properties

SWP has delivered normalized material properties, as shown in Table B.4. The individual stiffnesses (Young's and shear modulus) are normalized with respect to the UD stiffness in the primary (E_{11}) direction and likewise for the BIAX stiffnesses. Similar normalizations are performed for Poisson's ratio and the material strengths.

The normalized material properties cannot be used in the FE simulations, thus denormalized material properties have to be found. From the article, written by M. Leong et. al. [2012], Young's modulus is found for E_{11} for both materials together with Poisson's ratio (ν_{12}) and the material strengths (X_t). The denormalized material properties are shown in Table B.5.

The article, M. Leong et. al. [2012], is performed in cooperation with SWP, where the UD and BIAX mats used are similar to what is used in this project, hence it is assumed reasonable to use these material properties within this project.

Table B.4 Normalized material properties

	E_{11} / E_{11}	E_{22} / E_{11}	E_{33} / E_{11}	G_{12} / E_{11}	G_{13} / E_{11}	G_{23} / E_{11}
UD	1.00	0.31	0.29	0.10	0.09	0.06
BIAZ	1.00	1.02	1.02	0.79	0.23	0.23
	ν_{12} / ν_{12}	ν_{21} / ν_{12}	ν_{13} / ν_{12}	ν_{31} / ν_{12}	ν_{23} / ν_{12}	ν_{32} / ν_{12}
UD	1.00	0.31	0.91	0.27	1.47	1.37
BIAZ	1.00	1.02	0.52	0.53	0.57	0.57
	Thickness [mm]	X_t / X_t	X_c / X_t	Y_t / X_t	Y_c / X_t	$S12 / X_t$
UD	0.41	1.00	0.62	0.05	0.13	0.05
BIAZ	0.32	1.00	-	0.99	-	-

Table B.5 Denormalized material properties

	E_{11} [GPa]	E_{22} [GPa]	E_{33} [GPa]	G_{12} [GPa]	G_{13} [GPa]	G_{23} [GPa]
UD	43	13.3	12.5	4.3	3,9	2,6
BIAZ	13	13.3	13.3	10.3	3	3
	ν_{12}	ν_{21}	ν_{13}	ν_{31}	ν_{23}	ν_{32}
UD	0.3	0.09	0.27	0.08	0.44	0.41
BIAZ	0.6	0.61	0.31	0.32	0.34	0.34
	Thickness [mm]	X_t [MPa]	X_c [MPa]	Y_t [MPa]	Y_c [MPa]	$S12$ [MPa]
UD	0.41	914	566.7	45.7	118.8	45.7
BIAZ	0.32	150	-	148,5	-	-

B.5.2 S-N Data

In the FADAS algorithm it is necessary to have experimentally obtained fatigue data. S-N data from Nijssen [2011] is used. The S-N values are shown in Table B.6.

Table B.6 S-N data for different R-ratios and orientations

R-ratio	σ_x		σ_y		σ_{xy}	
	σ_0 [MPa]	k	σ_0 [MPa]	k	σ_0 [MPa]	k
0.1	500.8	10.03	50.2	8.63	38.1	11.06
-1	972.2	8.05	87.5	8.43	N/A	N/A
10	289.5	26.08	88.5	24.32	N/A	N/A

B.5.3 Parameters for FADAS Algorithm

Presented in Table B.7 are the values of the parameters used in Puck's failure criteria. The values are determined based on curve fitting of experimental data. The values are taken from A. Puck, H. Schürmann [1999] and Philippidis [2011].

Table B.7 Values for parameters used in Puck's failure criteria

c_{Puck}	ξ	η_r	E_{f1} [GPa]	ν_{f12}	$m_{\sigma,f}$	$p_{\perp\parallel}^{(+)}$	$p_{\perp\parallel}^{(-)}$
4	2	0	72.45	0.22	1.3	0.3	0.25

where:

c_{Puck}	Parameter used to fit η -curve to experimental data, [-]
ξ	Parameter used to fit η -curve to experimental data, [-]
η_r	Factor representing a small remaining stiffness, [-]
E_{f1}	Stiffness of fiber material, [GPa]
ν_{f12}	Poisson's ratio of fiber material, [-]
$m_{\sigma,f}$	Fiber/Matrix interface stress magnification factor, [-]
$p_{\perp\parallel}^{(+)}$	Slope of the tensile part of the fracture envelope at $R_{\perp\parallel}$ for $\tau_{\perp\parallel}$, [-]
$p_{\perp\parallel}^{(-)}$	Slope of the compressive part of the fracture envelope at $R_{\perp\parallel}$ for $\tau_{\perp\parallel}$, [-]

B.6 Validation of BIAX Ply

SWP required that two times two plies of BIAX were used in the gauge zone. The normalized material properties of the BIAX specified by SWP are shown in Table B.4 and the de-normalized properties are shown in Table B.5. However, for the reason described in Section 10.1 it is necessary to split each BIAX ply up into two UD plies. At first the material properties of the UD defined by SWP was used. However, as shown in Table B.8 there is a rather large difference in strains. To determine material properties for UD plies to be used as a BIAX ply, an optimization is conducted. The optimization problem is stated as shown in Equation (B.1) and (B.2):

$$\begin{aligned} \text{Minimize : } & C_{X_{ref}}(\nu_{12}, E_{11}, E_{22}, G_{12}) \\ & C_{Y_{ref}}(\nu_{12}, E_{11}, E_{22}, G_{12}) \end{aligned} \quad (\text{B.1})$$

$$\begin{aligned} \text{subject to : } & 0.2 \text{ [-]} \leq \nu_{12} \leq 0.4 \text{ [-]} \\ & 30 \text{ [GPa]} \leq E_{11} \leq 50 \text{ [GPa]} \\ & 10 \text{ [GPa]} \leq E_{22} \leq 20 \text{ [GPa]} \\ & 3.5 \text{ [GPa]} \leq G_{12} \leq 7 \text{ [GPa]} \end{aligned} \quad (\text{B.2})$$

where:

$C_{X_{ref}}$	Optimization parameter, $(\varepsilon_X / 0.23567 \cdot 10^{-2})$, [-]
$C_{Y_{ref}}$	Optimization parameter, $(\varepsilon_Y / -0.14140 \cdot 10^{-2})$, [-]
ε_X	Strain in the x-direction of the 2 x UD simulation, [-]
ε_Y	Strain in the y-direction of the 2 x UD simulation, [-]

A simulation using the BIAX properties from Table B.5 is performed on the FE model used to verify that the FADAS algorithm calculated the constitutive equations correctly, with the same boundary conditions and loads applied, as shown in Figure 9.1. The resulting strains from the simulation are used as a reference in the optimization. The objective function is as shown in Equation (B.3).

$$fval = \text{abs}(1 - C_{X_{ref}}) + \text{abs}(1 - C_{Y_{ref}}) \quad (\text{B.3})$$

The SQP algorithm is used with a forward difference method to determine the gradients for the optimization. Standard values are used except for the minimum step size where 0.01 is used instead of 0. The material properties used in the optimization have been normalized, so that all the parameters in the optimization can vary from 0 to 1.

A starting guess of [0.1 0.1 0.1 0.5] is used and the results shown in Table B.8 are obtained.

Table B.8 Results from the optimization

	E_{11} [GPa]	E_{22} [GPa]	G_{12} [GPa]	ν_{12} [-]	ε_X [μstrain]	ε_Y [μstrain]	ε_{XY} [μstrain]
2 x UD	43	13.3	4.3	0.3	1914	-927	-0.06
2 x UD opti	39.5	14.4	4.13	0.33	2365	-1418	-0.09
BIAX	13.3	13.3	10.3	0.6	2357	-1414	$-7 \cdot 10^{-13}$

The difference between the BIAX ply and the 2 x UD plies is within an acceptable tolerance. However, the difference in shear strain is major, which can be explained by E_{11} and G_{12} where major deviation occurs.

The function value and the values of the optimization parameters are shown in Figure B.27

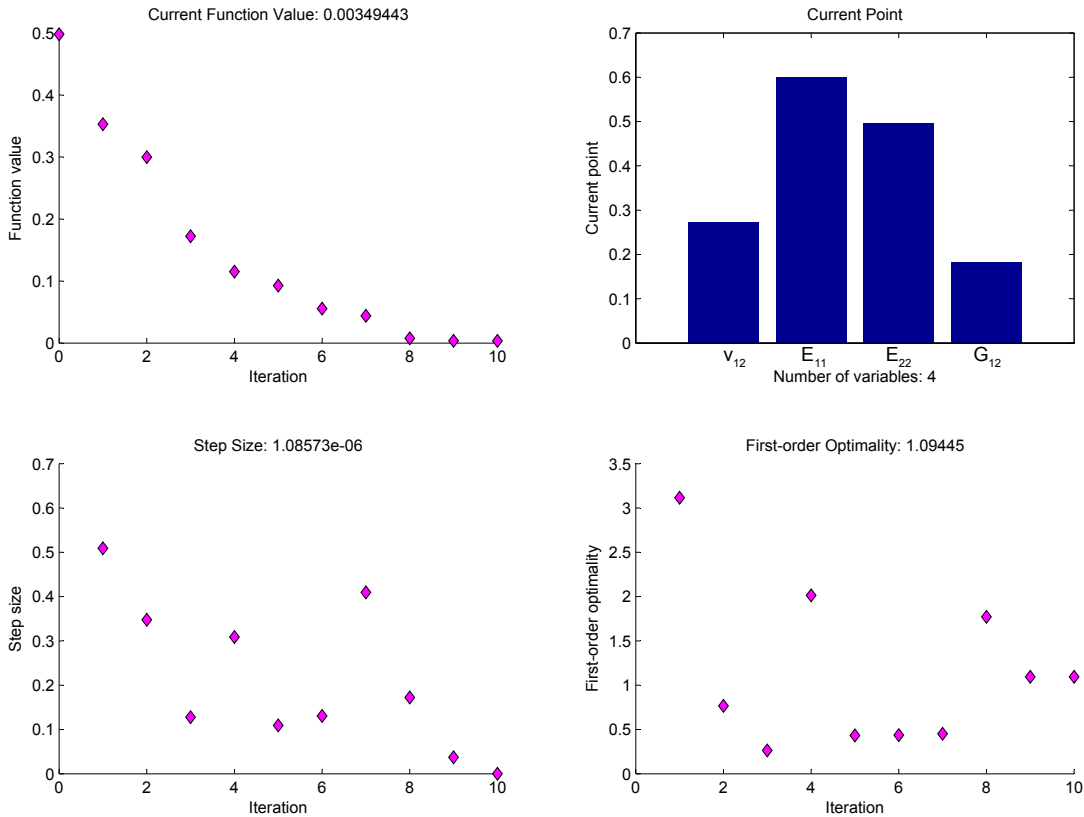


Figure B.27 Objective function value and optimization parameter values

After the optimization, the strain in the x- and y-direction are considered acceptable, as shown in Table B.8. However, there is still a considerable difference in the shear strain. The optimization is not able to determine material properties that correspond to a UD ply, when ε_{XY} is included in the optimization. Instead, the properties converged towards material properties resembling the original BIAX. Therefore ε_{XY} is not included in the objective function, and it is accepted

that there is a rather large difference between ε_{XY} calculated for the BIAX and the two UD plies.

B.7 Convergence Study

In this appendix the convergence studies for the solid and shell model are presented. The purpose of these studies is to determine the element size for the models. The FE models are described in Appendix B.1 and B.2.

B.7.1 Solid Model

The convergence study of the solid model is based on the strains with respect to the number of elements in the model. The strains are extracted at the center of the gauge zone by the use of a path involving four data points going through the thickness of the specimen. Four points are selected, due to the lay-up in the gauge zone. The strain result from these four points in the x-, y-, xy-direction are shown in Figure B.28, B.29 and B.30, respectively.

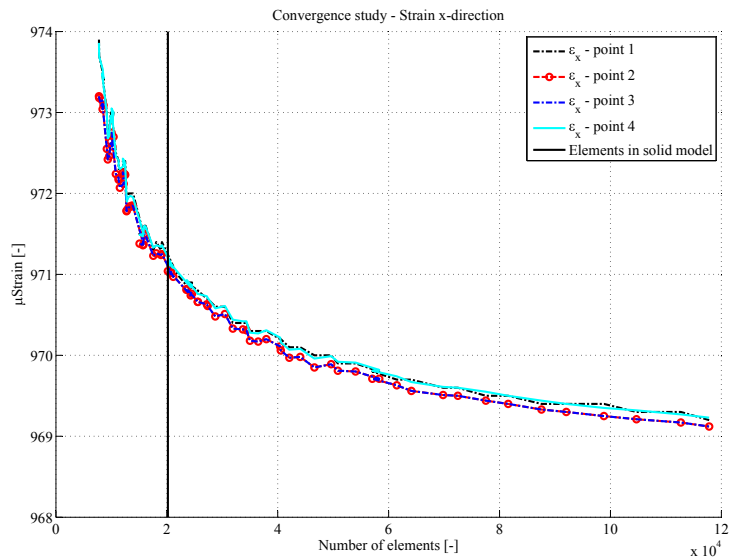


Figure B.28 Convergence study of strain in x-direction

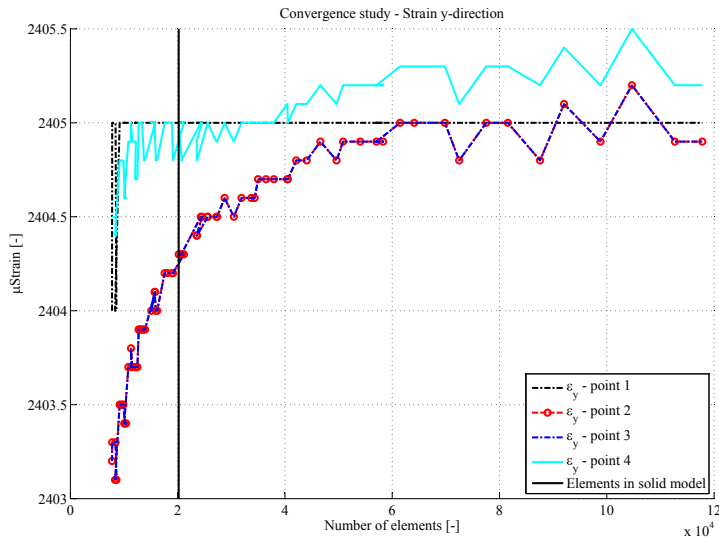


Figure B.29 Convergence study of strain in y-direction

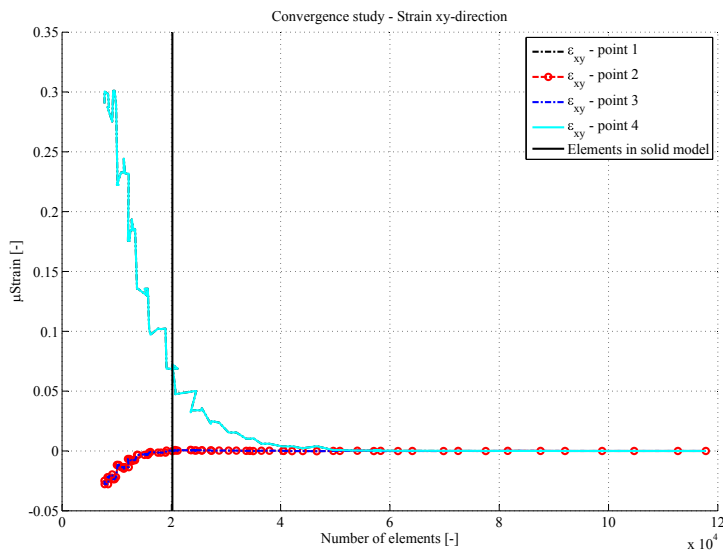


Figure B.30 Convergence study of strain in xy-direction

The number of elements is 20189 in the solid model, as shown with the black line in the above figures. The amount of elements correspond to having an element size equal to 3.5 [mm] in the gauge zone.

As shown in Figure B.28 the strains in the x-direction have a tendency to converge after approx. 40000 elements. In Figure B.29 it is harder to distinguish when the strain in the y-direction converges, but a tendency occurs at approx. 30000 elements. For the strain in the xy-direction in Figure B.30 it occurs at approx. 20000 elements.

Furthermore it is shown that a small deviation is present for each strain component through the thickness, which might be due to the different stiffnesses of each ply or round off and averaging of the results at the four extraction points. This deviation is neglected due to the magnitude.

In general the tendency is that the number of elements should be minimum 40000. However, this amount makes the model very computationally heavy, and the available student license version of ANSYS does not support that many elements. Additionally the deviations shown in

the above figures are so small that the error from this might be minimal compared to measuring errors when testing w.r.t. strain gauges, DIC etc.

The chosen number of elements is therefore assumed reasonable as a compromise between the tendency shown in Figure B.28, B.29 and B.30, and the limitation of using the student license version in ANSYS.

B.7.2 Shell Model

The convergence study for the shell model is conducted by selecting a node in the center of the gauge zone (0,0) and extracting the strain in the x-, y-, xy-direction. The results are shown in Figure B.31, B.32 and B.33.

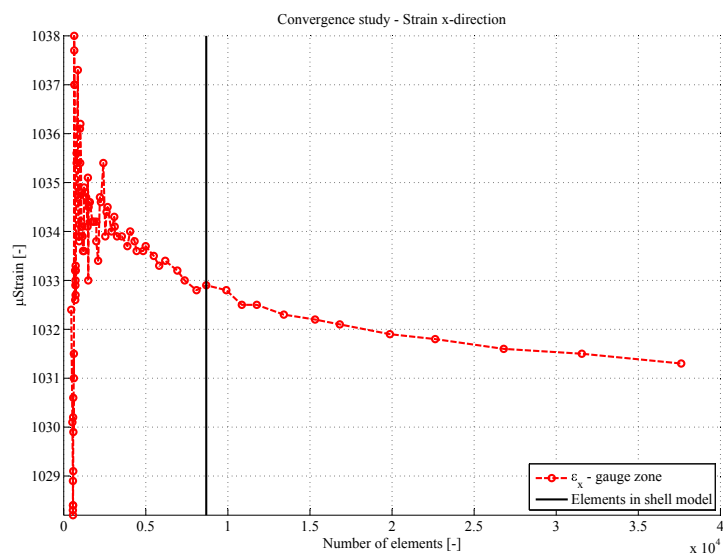


Figure B.31 Convergence study of strain in x-direction

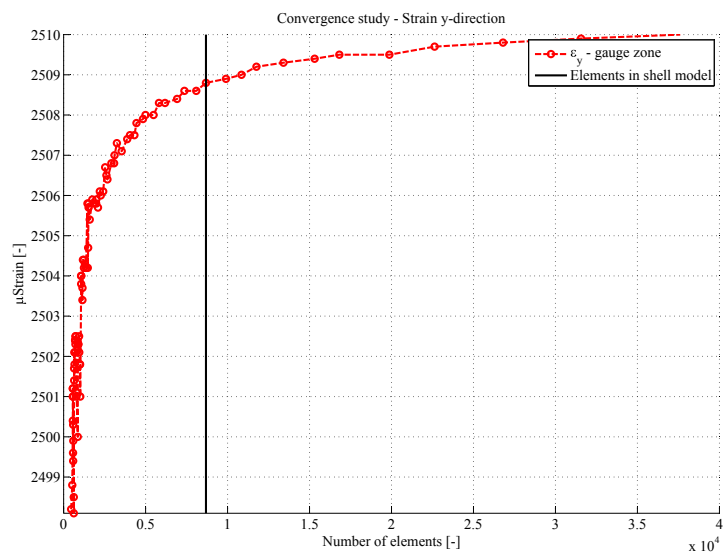


Figure B.32 Convergence study of strain in y-direction

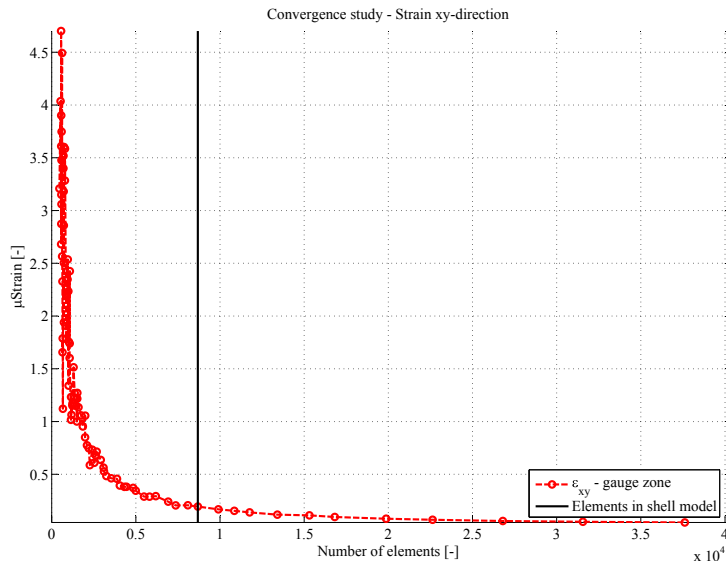


Figure B.33 Convergence study of strain in xy-direction

The number of elements in the shell model is equal to 8684 as shown with the black lines in the above figures. The amount corresponds to an element size of 2.1 [mm] within the gauge zone.

As shown above the tendency is that the strain in the x-, y- and xy-direction converges after approximately 10000 elements.

If the general tendency should be fulfilled, the amount of elements should be 10000 elements. The deviation between 8684 and 10000 elements is minor, therefore it is assumed that an element size of 2.1 [mm] is sufficient. Furthermore the error in the model would be small compared to the errors of the testing measurements w.r.t. strain gauges, DIC etc.

The chosen amount of elements in the shell model is assumed reasonable as a compromise between computational time and the results shown in Figure B.28, B.29 and B.30.

B.8 Force and Stress Distribution in Specimen

This appendix serves the purpose of documenting the stress due to changing the geometry and stiffness of the specimen. This is done by degenerating the actual geometry of the specimen, shown in Figure B.34, to a simple 2D beam geometry with four different configurations, as shown in Figure B.35. Static tests are performed where the stiffness of the rod for the four cases is changed and stresses in the center are monitored.

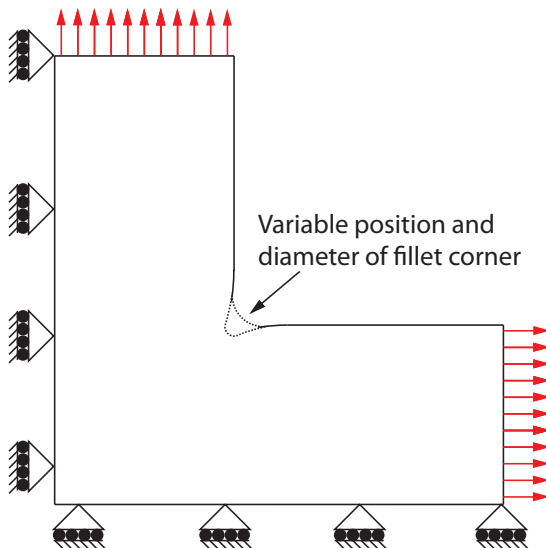


Figure B.34 Specimen with applied BC's

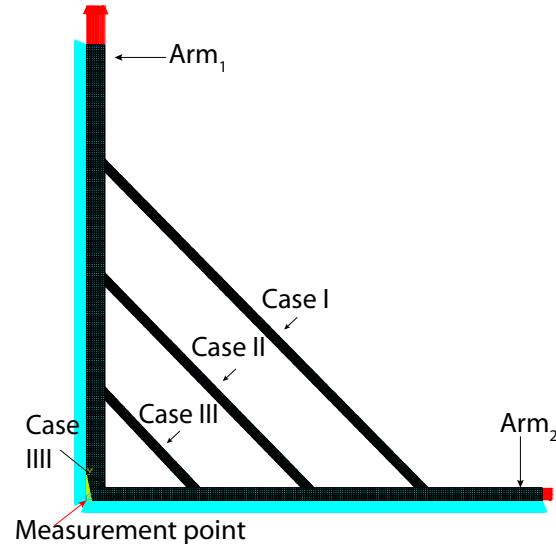


Figure B.35 Simplified beam model with applied BC's and measurement point

There are four different test cases which are analyzed. For each case the rod going from Arm_1 to Arm_2 is positioned at different locations as follows:

Case I: Rod positioned at $\frac{3}{4} \cdot L_{Arm_1}$ and $\frac{3}{4} \cdot L_{Arm_2}$

Case II: Rod positioned at $\frac{1}{2} \cdot L_{Arm_1}$ and $\frac{1}{2} \cdot L_{Arm_2}$

Case III: Rod positioned at $\frac{1}{4} \cdot L_{Arm_1}$ and $\frac{1}{4} \cdot L_{Arm_2}$

Case IIII: No rod

For each case the stiffness of the rod is increased incrementally and compared to the stress at the measurement point shown in Figure B.35. This comparison is shown for σ_x , σ_y and σ_{xy} in Figure B.36, B.37 and B.38.

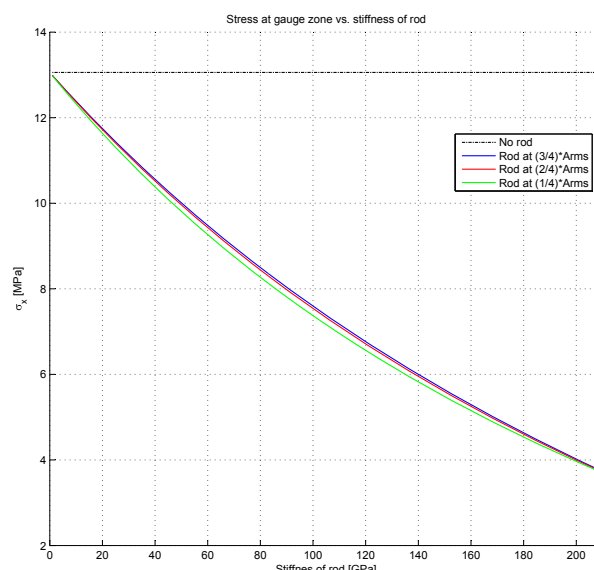


Figure B.36 σ_x vs. stiffness of various positions of the rod

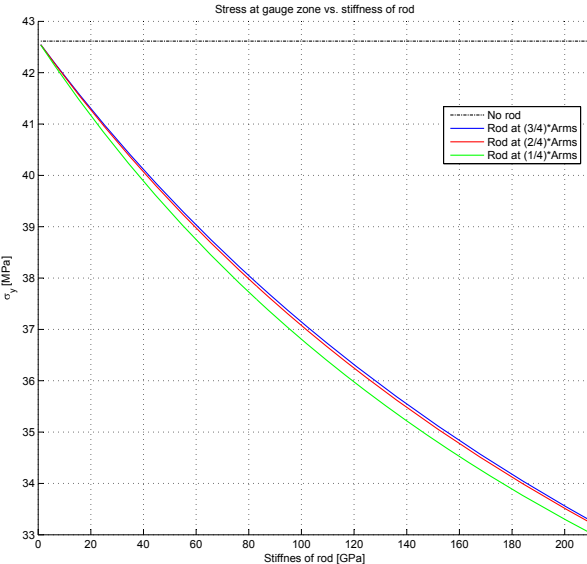


Figure B.37 σ_y vs. stiffness of various positions of the rod

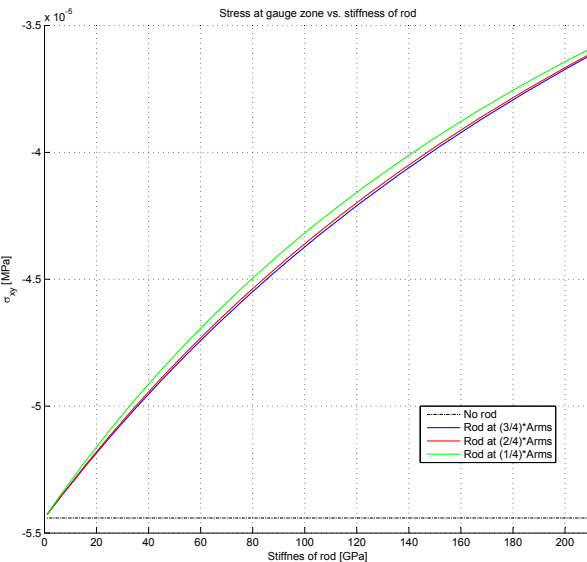


Figure B.38 σ_{xy} vs. stiffness of various positions of the rod

As seen in Figure B.38, the shear stress for each test case is small compared to the stresses in the x- and y-directions, which is because of the chosen measurement point. With respect to case III, where no rod is present, the stress in all directions is constant, as expected. The noticeable results are that the stress is reduced as the stiffness is increased. When changing the rod at the three specified positions, the stress does not change significantly. The maximum deviation w.r.t. case I, is shown in Table B.9.

Table B.9 Maximum deviation w.r.t. case I

Position	σ_x [%]	σ_y [%]	σ_{xy} [%]
Case I: Rod at $\frac{3}{4} \cdot Arms$	-	-	-
Case II: Rod at $\frac{1}{2} \cdot Arms$	0.19	0.795	0.284
Case III: Rod at $\frac{1}{4} \cdot Arms$	0.934	3.02	1.26

The deviations in Table B.9 are only used to indicate the difference of positioning the rod at

different locations. The closer the rod is positioned to the measurement point the more it deviates, as expected. It means that the applied forces at the arms are redistributed more through the rod if it is positioned closer to where the force is applied.

Furthermore, the stresses in the measuring point are reduced when the stiffness of the rod is increased. Thus, it is of interest to reduce the fillet corner stiffness as much as possible, from this point of view.

B.9 Calculations of Bolt Connections

In this appendix calculations are performed for the bolt connection in each arm. A study of direct shear leading to cutting of the bolt are performed, together with a study of tearout of the bolts in the specimen. The used analytical equations and approaches are found in Norton [2006], together with properties such as, bolt area and strength. The used forces in this appendix are the ones used for the static test, described in Chapter 4. This yields the results to be conservative, since the fatigue test loads are lower than the static loads, as described in Chapter 5.

The static maximum forces in the primary and secondary directions are 240 [kN] and 100 [kN], respectively. In each arm four bolts are mounted, where the eight bolts in the primary and secondary directions are M14 and M12, respectively. The applied forces can be divided by the four bolts, due to equilibrium, in each direction, by assuming an even load distribution between the four bolts. This yields the force for each bolt to be: $F_{M14} = 60$ [kN] and $F_{M12} = 25$ [kN]. The setup for the bolts is shown in Figure B.39, where the specimen is constrained by the bolt. Washers are used to ensure a direct connection between the specimen and the mounting plates.

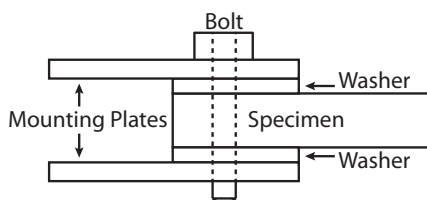


Figure B.39 Bolt connection

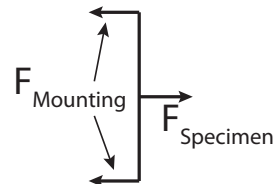


Figure B.40 Free body diagram of the bolt

The direct shear failure is due to forces acting transverse to the length of the bolt. This is shown in Figure B.40 with a free body diagram. The forces can cut the bolt in shear, i.e. direct shear of the bolt, due to transverse forces. The shear applied to the bolts can be calculated as shown in Equation (B.4).

$$\begin{aligned}\tau_{M14} &= \frac{F_{M14}}{At_{M14}} = \frac{60 \text{ [kN]}}{115.44 \text{ [mm}^2\text{]}} = 519.8 \text{ [MPa]} \\ \tau_{M12} &= \frac{F_{M12}}{At_{M12}} = \frac{25 \text{ [kN]}}{84.27 \text{ [mm}^2\text{]}} = 296.7 \text{ [MPa]}\end{aligned}\tag{B.4}$$

where:

τ	Bolt shear force, [MPa]
At	Bolt tensile stress area, [mm^2]

The strength class for the bolts are 12.9, in which the bolts have a yield strength of 1100 [MPa].

The safety factors against direct shear are:

$$SF_{DS\ M14} = \frac{\sigma_y\ Bolt}{\tau_{M14}} = 2.1 \quad (B.5)$$

$$SF_{DS\ M12} = \frac{\sigma_y\ Bolt}{\tau_{M12}} = 3.7$$

where:

SF_{DS}	Safety factor, [-]
$\sigma_y\ Bolt$	Yield strength for bolt in strength class 12.9, [MPa]

The safety factors for direct shear cut are 2.1 and 3.7 for the M14 and M12 bolt, respectively. Furthermore, the bolt tensile stress areas are conservative, because it is determined using the thread minor diameter, as shown in Figure B.41. But for the bolts used for the mounting of the specimen the mounting area is used, thus the loaded area has a greater diameter than the thread minor diameter, which yields the shear stresses in Equation (B.4) to decrease.



Figure B.41 Illustration of a bolt

Tearout is prevented by two things: the friction force from the prestressed bolt connection and the material between the bolt and the outer geometry. In Figure B.42 an element is shown where a normal force, F_N , and a force, F , are applied. The normal force creates a friction force, F_{fric} , and the element will not move as long as it is higher or equal to the force, $F_{fric} \geq F$.

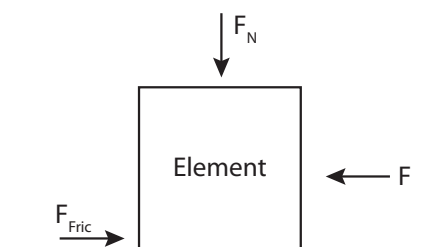


Figure B.42 Forces on an element

A normal force appears in a bolt connection due to prestressed bolts, thus the friction force is determined on the basis of the prestressed bolt force and is calculated as in Equation (B.6). The factor of 0.75 is employed, since the bolts are used for more than one test. 0.75 is used when it is required that the bolt and nut can be separated and used again. μ between GFRP and steel is 0.5 [ToolBox, N/A].

$$F_{fric\ M14} = \mu \cdot 0.75 \cdot \sigma_{proof} \cdot At_{M14} = 0.5 \cdot 0.75 \cdot 970 \text{ [MPa]} \cdot 115.44 \text{ [mm}^2\text{]} = 42.0 \text{ [kN]}$$

$$F_{fric\ M12} = \mu \cdot 0.75 \cdot \sigma_{proof} \cdot At_{M12} = 0.5 \cdot 0.75 \cdot 970 \text{ [MPa]} \cdot 84.27 \text{ [mm}^2\text{]} = 30.6 \text{ [kN]} \quad (B.6)$$

where:

F_{fric}	Friction force, [kN]
μ	Friction coefficient, [kN]
σ_{proof}	Bolt proof strength, [MPa]

By dividing the friction forces with the bolt forces the safety factors become 0.7 and 1.2 for the M14 and M12 bolt connections, respectively. The safety factor for the M14 bolts is not acceptable, since the friction force cannot hold the mounting plates and bolt connection. Thus it has to be ensured that the specimen material can prevent tearout.

In Figure B.43 a specimen constrained by a bolt is shown. If the applied force is larger than the friction force, the material between the bolt and the outer geometry has to be able to prevent a bolt tearout. This shear area is shown in Figure B.44, where the bolt area is highlighted.

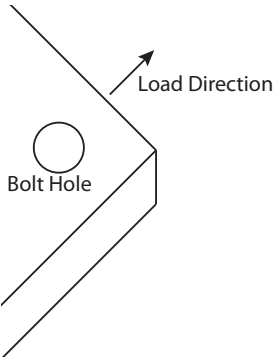


Figure B.43 Bolt hole in specimen

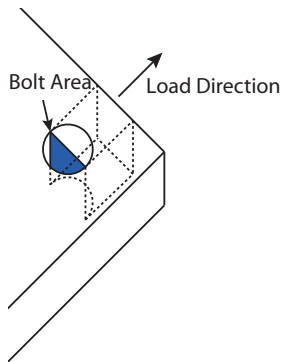


Figure B.44 Tearout shear area

The bolt will press on the surface inside the hole, thus only the shear area prevents a tearout. To determine the stresses in the material Equation (B.7) is employed.

$$\begin{aligned}\sigma_{Tear\ M14} &= \frac{F_{M14}}{Ab_{M14}} = \frac{60 \text{ [kN]}}{238 \text{ [mm}^2\text{]}} = 252.1 \text{ [MPa]} \\ \sigma_{Tear\ M12} &= \frac{F_{M12}}{Ab_{M12}} = \frac{25 \text{ [kN]}}{204 \text{ [mm}^2\text{]}} = 122.5 \text{ [MPa]}\end{aligned}\quad (\text{B.7})$$

where:

σ_{Tear}	Tearout stress, [MPa]
Ab	Tear out bolt area, [mm^2]

The safety factors against tearout are 1.9 and 2.4 for the M14 and M12 bolts, respectively, with material strengths of 478.3 [MPa] and 290.1 [MPa] for the primary and secondary directions, respectively. The material strength is approximated by an estimated volume fraction times the tensile strength for each of the three different laminae (UD 0°, UD 90° and BIAX 0°). This is explained further in Appendix C.1.1.

It can be concluded that the all safety factors are above one w.r.t the static test forces, which is satisfactory since the fatigue tests are performed at lower force magnitudes.

Test Results C

In this appendix test results are presented for all tests and it is an addition to the results presented in the report. The content of the appendix is:

C.1	Static Pilot Test
C.2	Fatigue Test 1
C.3	Fatigue Test 2
C.4	Fatigue Test 3
C.5	Fatigue Test 4

C.1 Static Pilot Test

In this section, results from the static pilot test is presented. The content consists of strain gauge results, camera observations and DIC noise images.

C.1.1 Strain Gauge Results

In Figure C.1 the displacement from the test rig controller output is shown. In Figure C.2 the estimated in-plane bending stress in the primary and secondary arms are shown. In Figure C.3 the result from a thermocouple is shown. In Figure C.4 the shear strain obtained by the strain gauge rosette is shown.

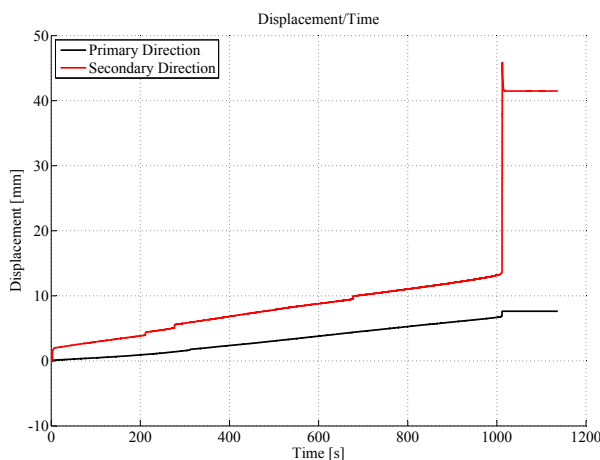


Figure C.1 Displacement vs. time in static pilot test

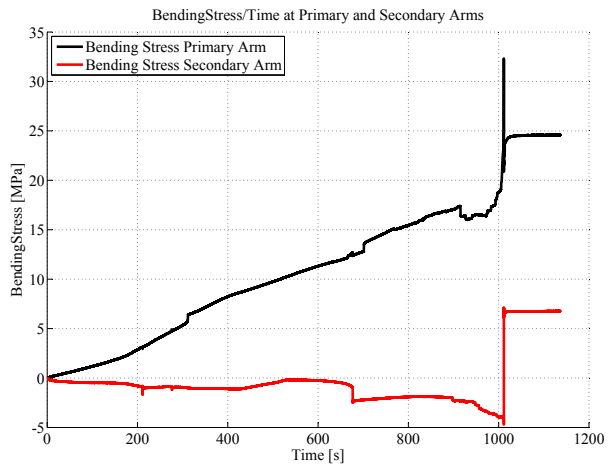
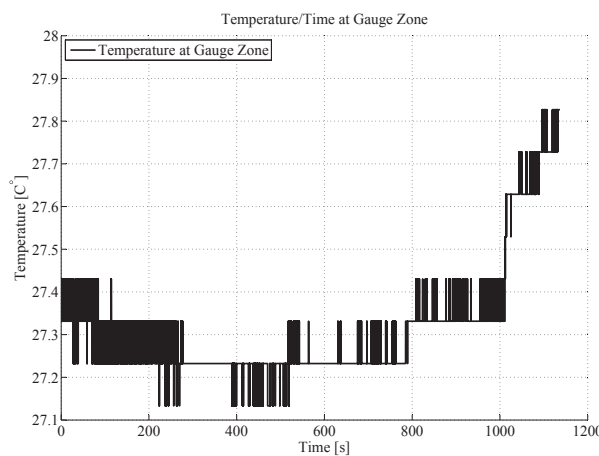
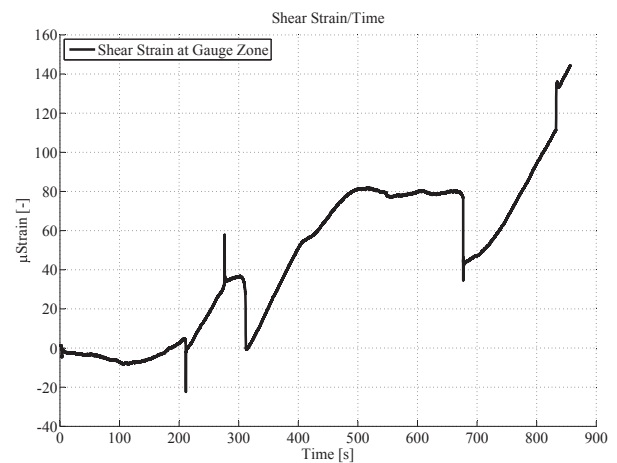


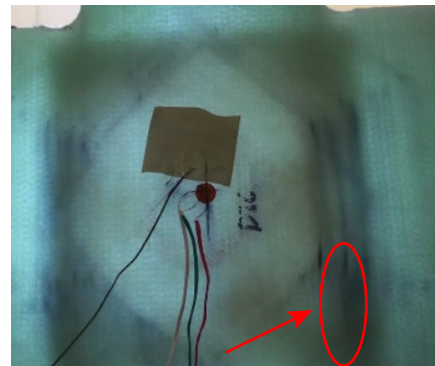
Figure C.2 Estimated in-plane bending stress in the primary and secondary arms

The bending stress is calculated by an approach where an estimation of the equivalent stiffness is calculated by the use of an efficiency factor, also called Krenchel factor. The efficiency factor is used to take the effect of fiber orientation into account when calculating the stiffness [Richardson, N/A]. The efficiency factor is calculated by the layer fraction present at the position of the strain gauges and the orientations of the fibers in the plies at this position i.e. empirical fiber orientation factors are multiplied to the layer fractions and an efficiency factor is thereby calculated. The stiffness from the UD 0° fibers are used and corrected with the efficiency factor. The equivalent stiffness, the resistance against bending calculated at the position where the strain gauges are positioned and the strain difference between the two strain gauges are used to calculate the bending stress. This is under the assumption that the strain gauges are positioned parallel to each other and with the same distance from the neutral axis of the specimen. This procedure is conducted for the rest of the presented results w.r.t. bending stress calculations.

**Figure C.3** Temperature in the gauge zone**Figure C.4** Shear strain in the gauge zone

C.1.2 Camera Observations

In this section the camera observations of first and total failure are presented. Snap shots of the camera observations, located on the back of the specimen, before first failure, are shown in Figure C.5. Total failure is shown in Figure C.6 and C.7 before and after it occurred.

**Figure C.5** Identification of first failure**Figure C.6** Crack initiation at fillet corner before total failure**Figure C.7** Further crack initiation at fillet corner before total failure

C.1.3 DIC Noise Results

In Figure C.8 and C.9 the noise of the DIC measurements with respect to the static pilot test is shown.

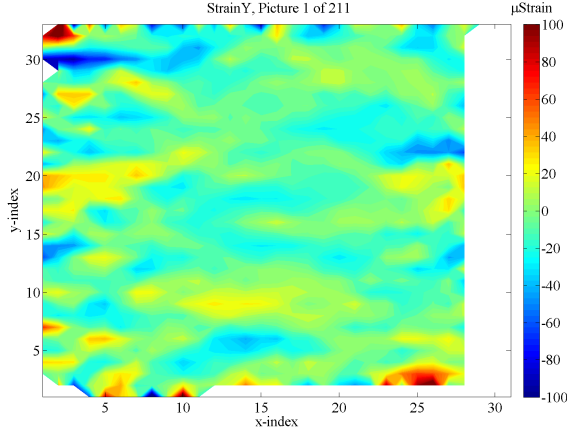


Figure C.8 Contour plot of DIC strain noise in primary direction

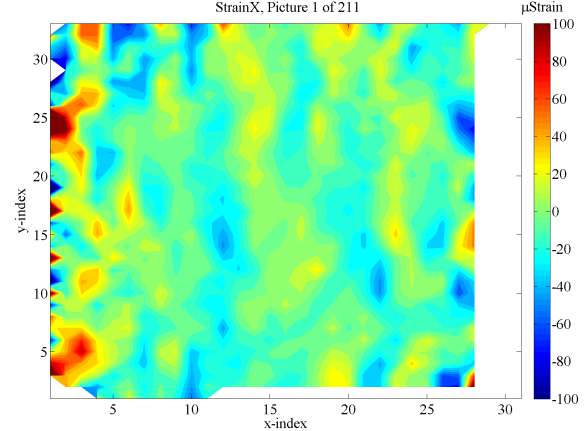


Figure C.9 Contour plot of DIC strain noise in secondary direction

C.2 Fatigue Test 1

In this section, results from FT1 are presented. The content consists of strain gauge results, camera observations and DIC noise images.

C.2.1 Strain Gauge

The strain ratio after 59300 cycles is shown in Figure C.10, with $R_{strain} = 0.35$ at load peaks. In Figure C.11 the temperature monitored by the thermocouple is shown after 59300 cycles. The specimen temperature does not change significantly during the test, thus the specimen temperature is not an issue for FT1.

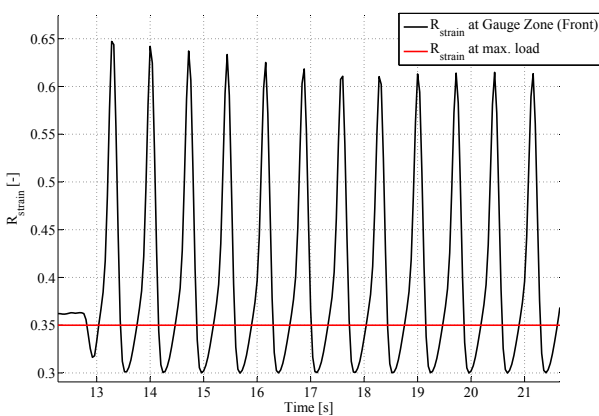


Figure C.10 Strain ratio after 59300 cycles

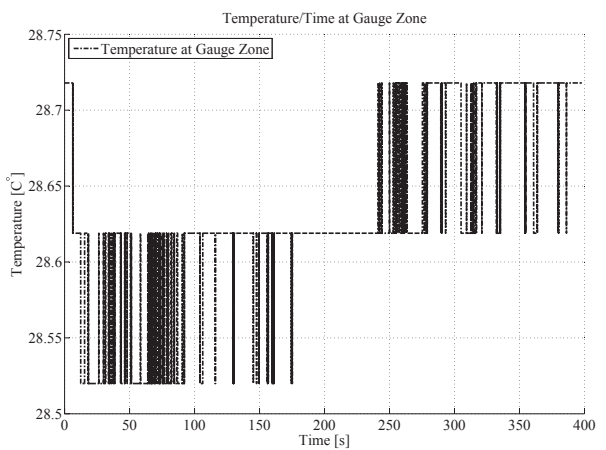


Figure C.11 Temperature after 59300 cycles

The strain in the primary arms is shown in Figure C.12 and C.13. It can be seen that there is no difference in the strains from the two strain gauges, hence, in-plane bending in the primary direction can be neglected. Through FT1 these strain magnitudes does not change, thus in-plane bending in the primary directions does not appear in FT1.

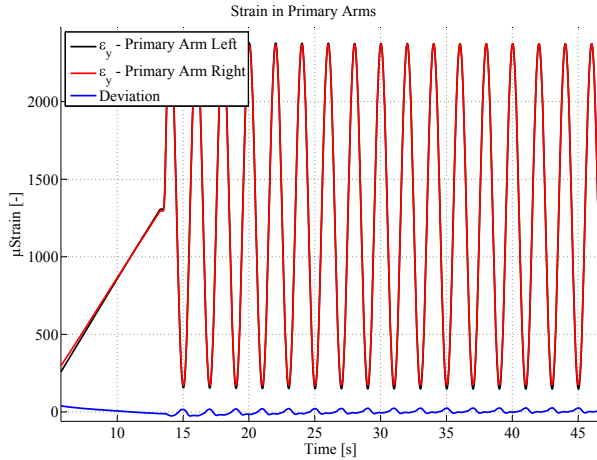


Figure C.12 Strain in the primary arms after 300 cycles

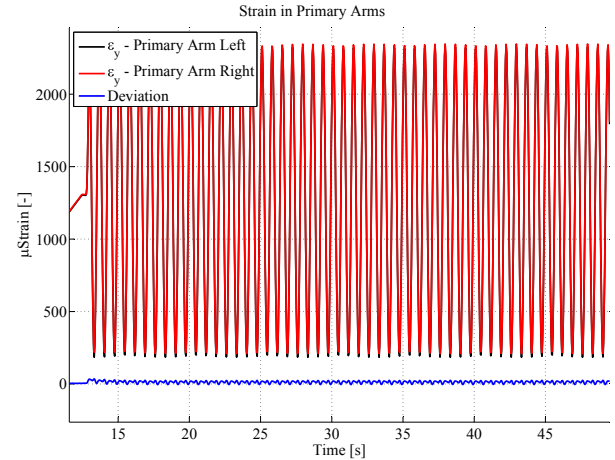


Figure C.13 Strain in the primary arms after 59300 cycles

Likewise for the secondary direction, i.e. the difference between the strains are negligible during the test. Thus, no in-plane bending in the secondary direction appears during FT1.

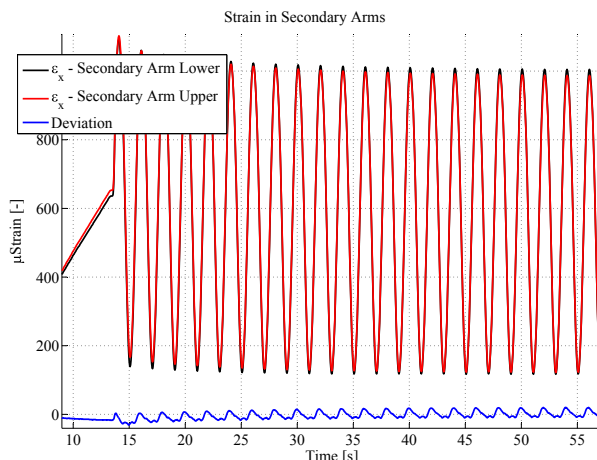


Figure C.14 Strain in the secondary arms strain after 300 cycles

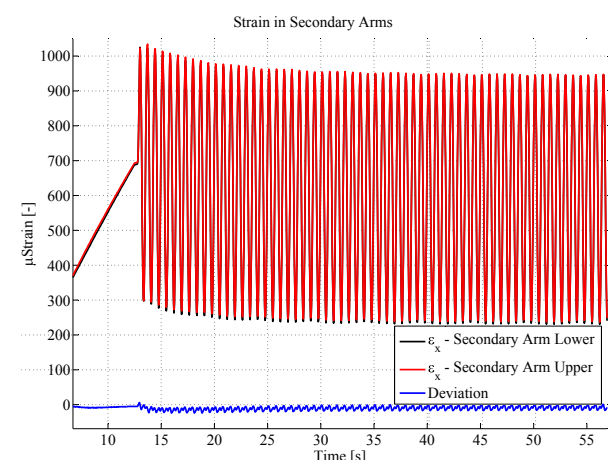


Figure C.15 Strain in the secondary arms after 59300 cycles

C.2.2 DIC

The DIC noise images for the primary and secondary directions are shown in Figure C.16 and C.17.

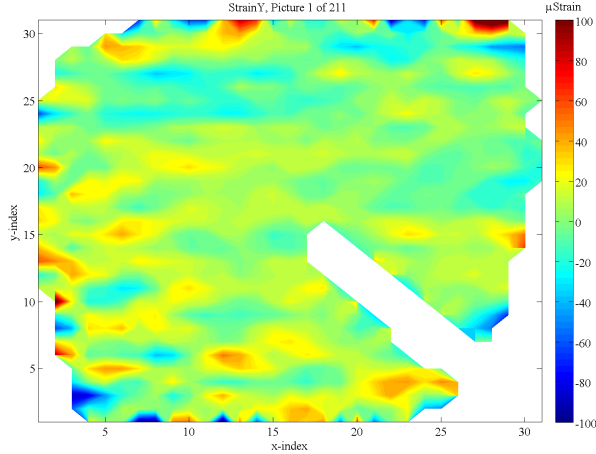


Figure C.16 Primary directional DIC noise

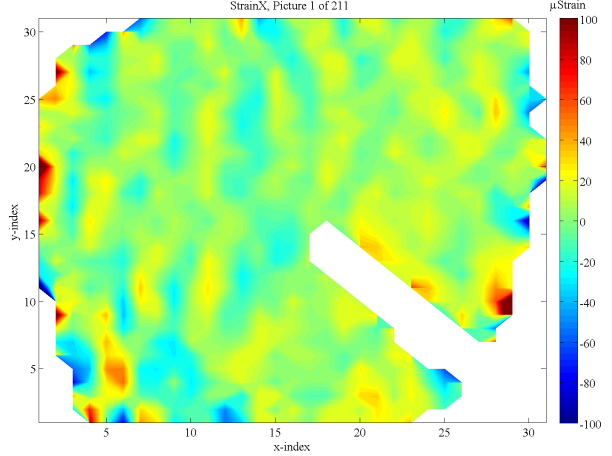


Figure C.17 Secondary directional DIC noise

C.3 Fatigue Test 2

In this section results from FT2 are presented. The content consists of strain gauge results, camera observations and DIC noise images.

C.3.1 Strain Gauge

The strain ratio is shown after 17000 and 80000 cycles in Figure C.18 and C.19, respectively. $R_{strain} = 0.27$ throughout FT2 and is considered to be too small, since it is of interest to be around the SWP specified strain ratio.

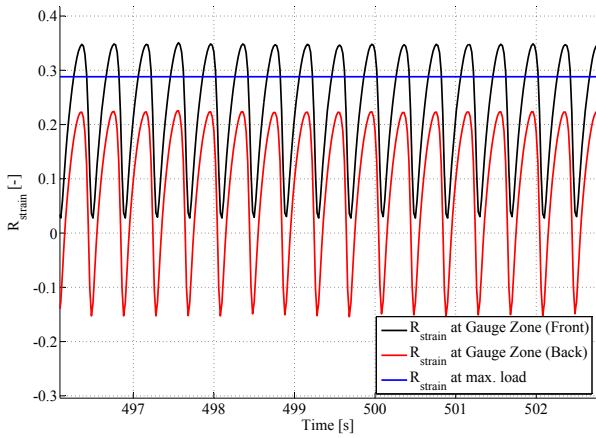


Figure C.18 The strain ratio after 17000 cycles

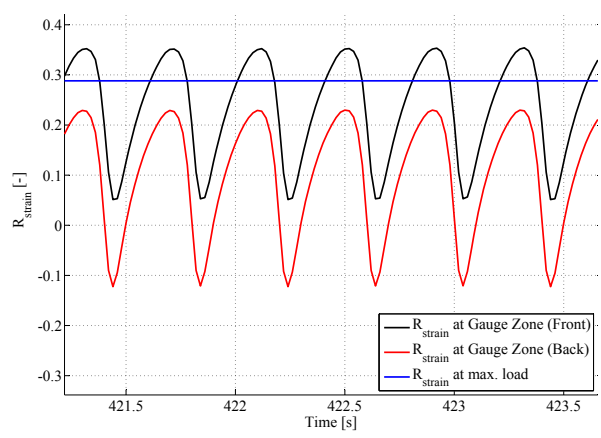


Figure C.19 The strain ratio after 80000 cycles

In Figure C.20 the load for the primary and secondary direction is shown. Temperature from the thermocouple is shown in Figure C.21, where it increases during the cycle step up to 80000 cycles.

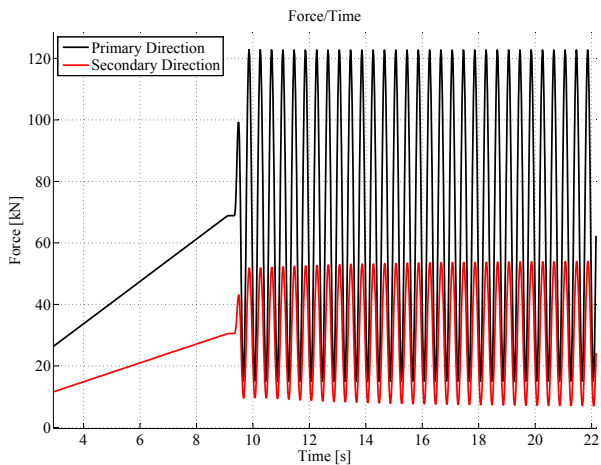


Figure C.20 The load magnitudes after 17000 cycles for the primary and secondary direction

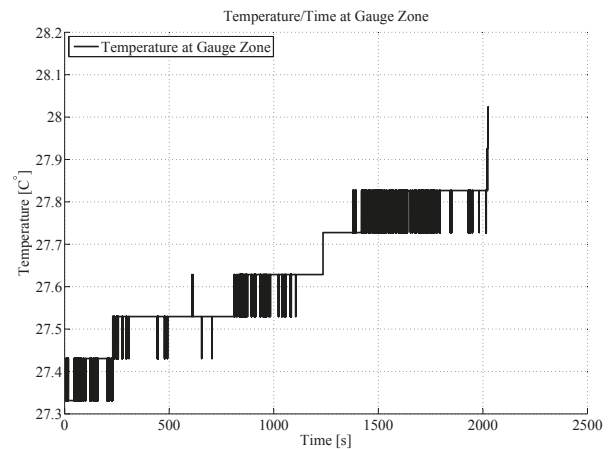


Figure C.21 The temperature during FT2 up to 80000 cycles

The strain for the primary arms is shown in Figure C.22 and C.23 for 17000 cycles and 80000 cycles, respectively.

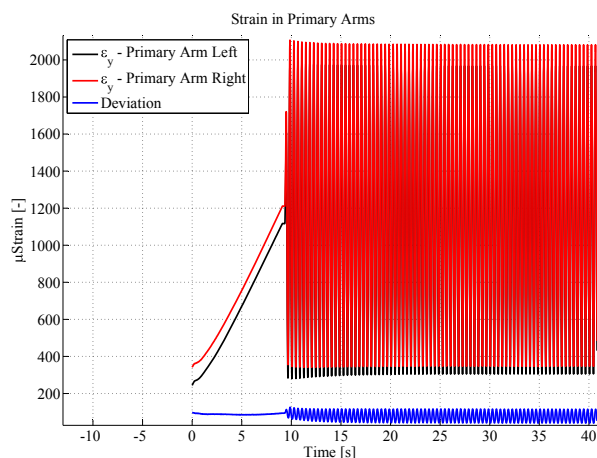


Figure C.22 Strain in the primary arms after 17000 cycles

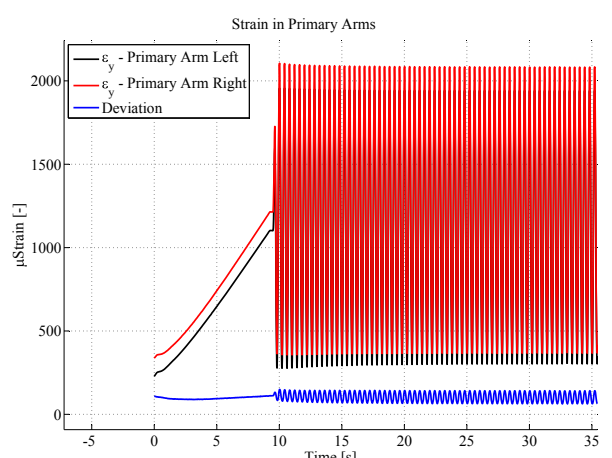


Figure C.23 Strain in the primary arms after 80000 cycles

The strain for the secondary arms is shown in Figure C.24 and C.25 for 17000 cycles and 80000 cycles, respectively.

C. Test Results

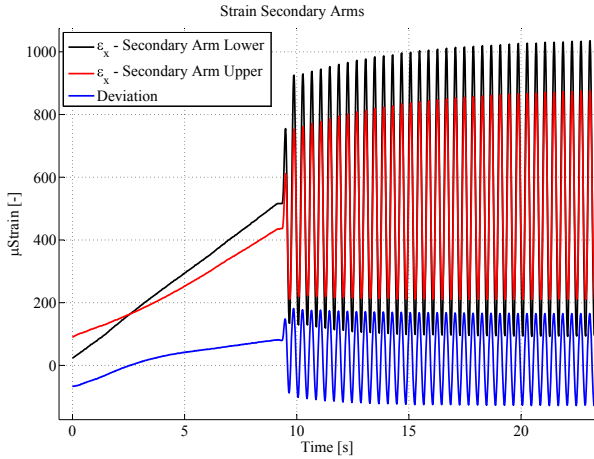


Figure C.24 Strain in the secondary arms after 17000 cycles

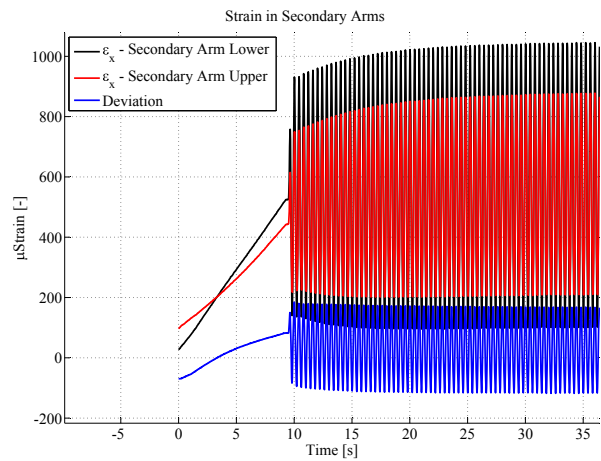


Figure C.25 Strain in the secondary arms after 80000 cycles

The differences between the above presented strains are converted into bending stress in Figure C.26 and C.27 for cycles up to 17000 and 80000 cycles, respectively. The stress magnitudes are minor, in which these are neglected. Furthermore, the bending stress for the primary direction is increased at 80000 cycles compared to at 17000 cycles, but the magnitudes are still neglected.

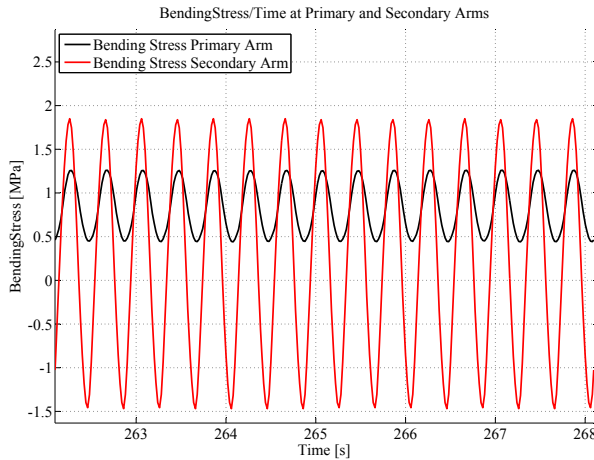


Figure C.26 Bending stress for 17000 cycles

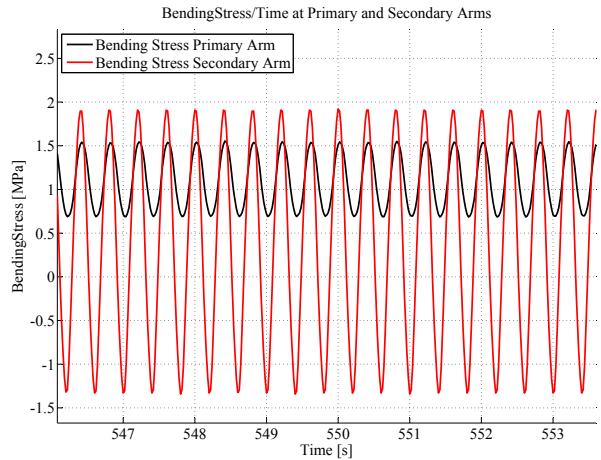


Figure C.27 Bending stress for 80000 cycles

C.4 Fatigue Test 3

In this section results from FT3 is presented. The content consists of strain gauge results, camera observations and DIC noise images.

C.4.1 Strain Gauge

The strain ratio for FT3 is 0.39 after 4000 cycles and 0.42 after 96000 cycles as shown in Figure C.28 and C.29, respectively. The strain ratio can be due to multiple reasons. The obvious reason would be that the loads are redistributed in the specimen, due to failures, which results in another strain field around the strain gauge.

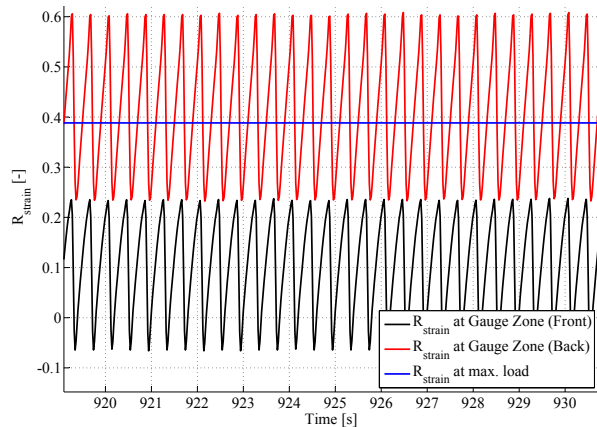


Figure C.28 Strain ratio after 4000 cycles

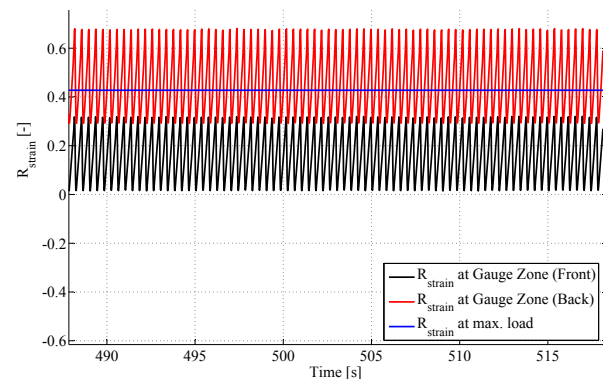


Figure C.29 Strain ratio after 96000 cycles

In Figure C.30 the loads for the primary and secondary actuators are shown, which correspond to the loads defined for FT3.

The temperature increases during FT3, but the tendency is to settle around 31.6° , as shown in Figure C.31.

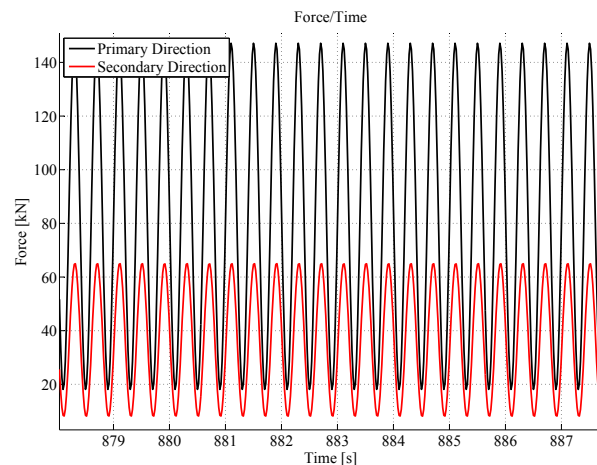


Figure C.30 The load magnitudes after 4000 cycles for the primary and secondary direction

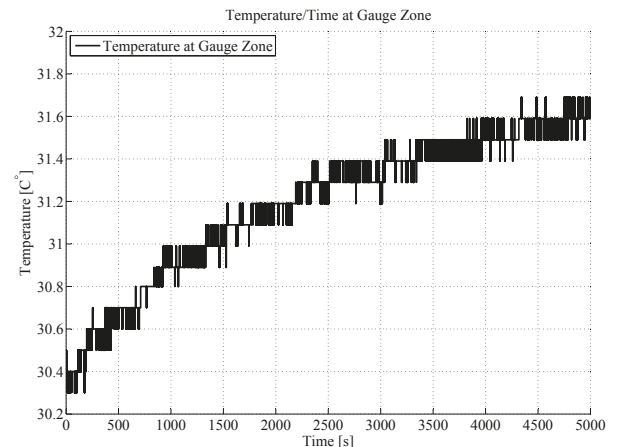


Figure C.31 The temperature during FT3 up to 96000 cycles

The strain for the primary arms is shown in Figure C.32 and C.33 for 4000 cycles and 96000 cycles, respectively.

C. Test Results

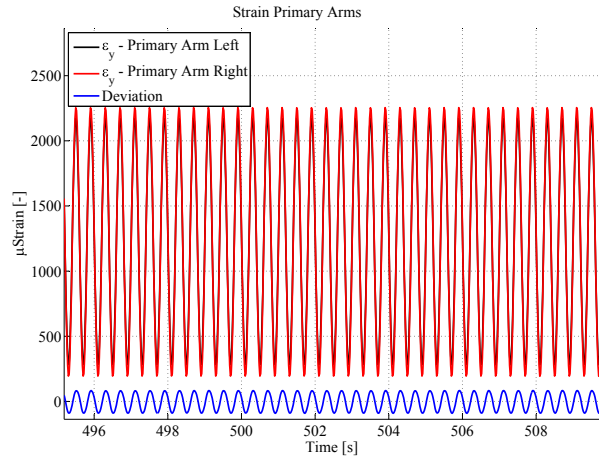


Figure C.32 Strain in the primary arms after 4000 cycles

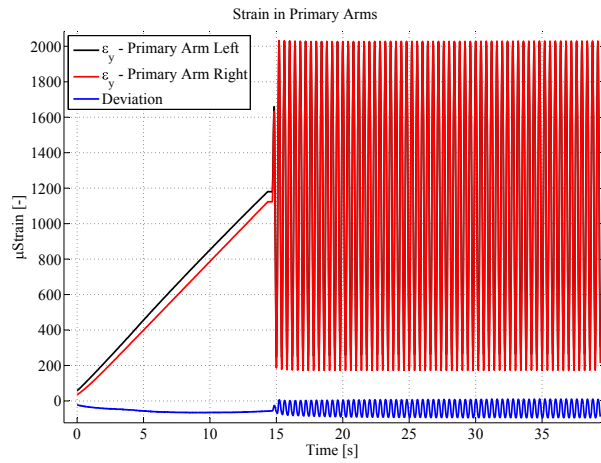


Figure C.33 Strain in the primary arms after 96000 cycles

The strain for the secondary arms is shown in Figure C.34 and C.35 for 4000 cycles and 96000 cycles, respectively.

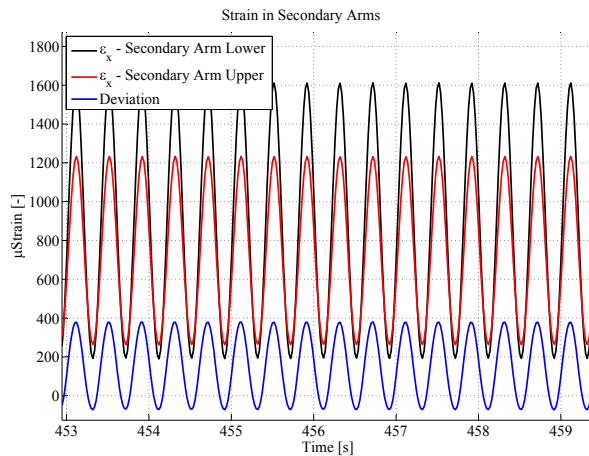


Figure C.34 Strain in the secondary arms after 4000 cycles

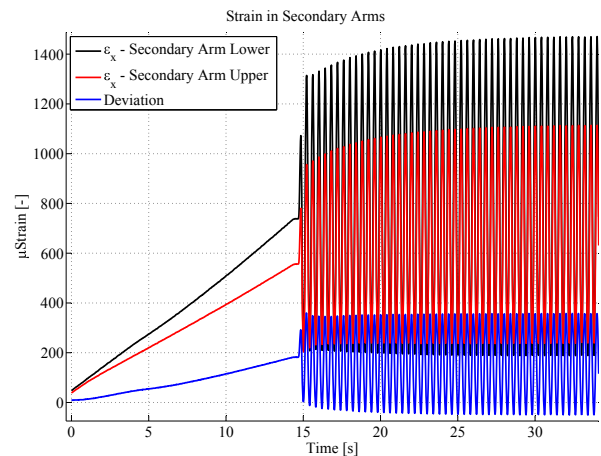
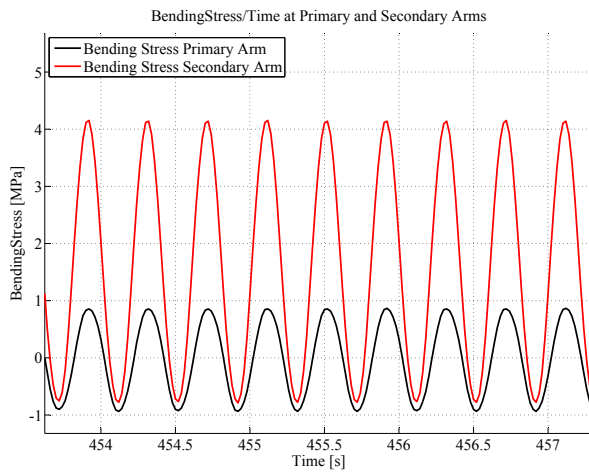
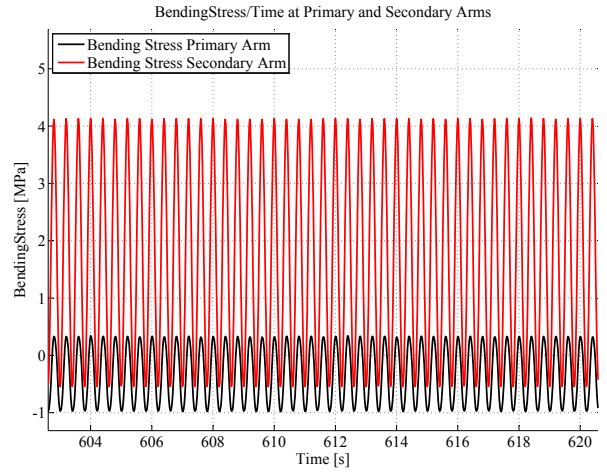


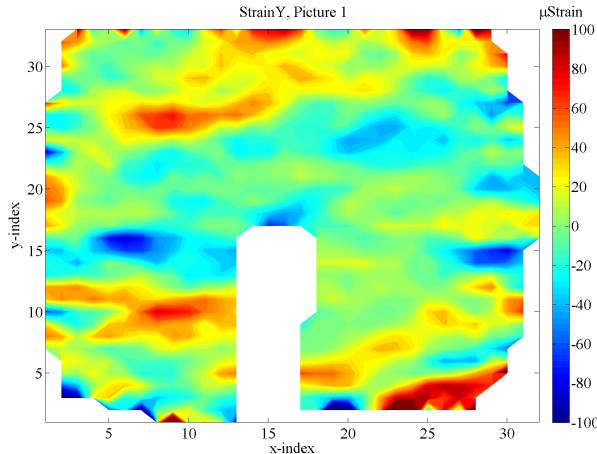
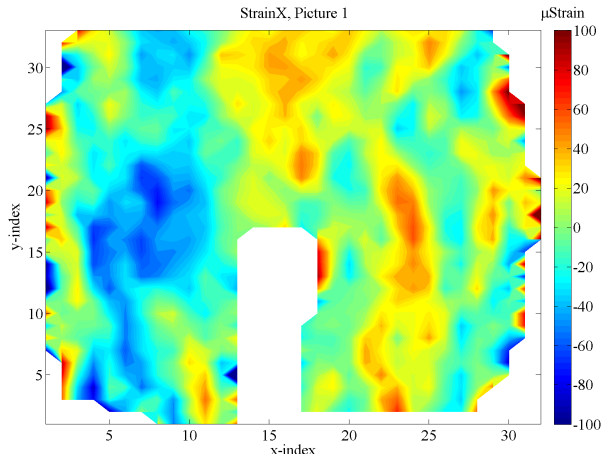
Figure C.35 Strain in the secondary arms after 96000 cycles

The differences in the above presented strains are converted into bending stress in Figure C.36 and C.37 for cycles up to 4000 and 96000 cycles, respectively. The stress magnitude for the primary direction is negligible. The magnitude for the bending stress in the secondary direction is up to 4 [MPa] which is the highest for all fatigue tests in this project. This is still neglected, since the bending stress is minor compared to the stress from the applied loads.

**Figure C.36** Bending stress for 4000 cycles**Figure C.37** Bending stress for 96000 cycles

C.4.2 DIC

The DIC noise for primary and secondary direction is shown in Figure C.38 and C.39, respectively.

**Figure C.38** Primary directional DIC noise**Figure C.39** Secondary directional DIC noise

DIC calculated strain fields from before and after first failure propagation is shown in Figure C.40 and C.41, respectively. First failure occurs in the right side around index (29,6-15), where the strain increases because the first failure appears in the UD 0° .

C. Test Results

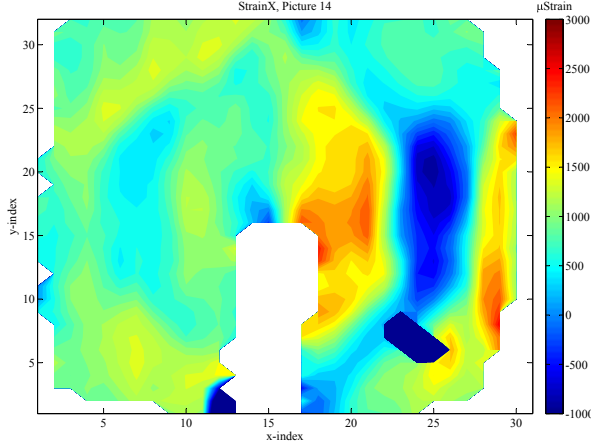


Figure C.40 Strain field in secondary direction before first failure

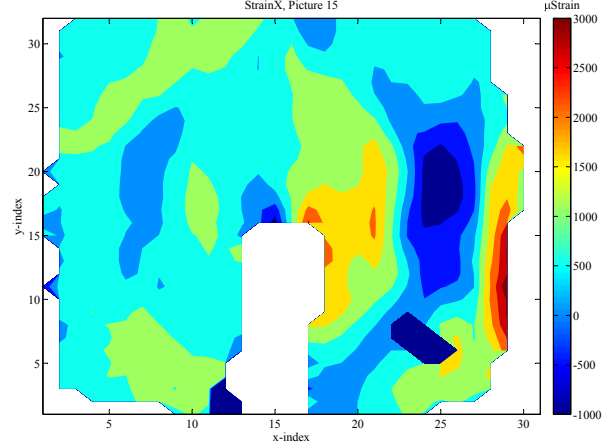


Figure C.41 Strain field in secondary direction after first failure

C.5 Fatigue Test 4

In this section results from FT4 are presented. The content consists of strain gauge results, camera observations and DIC noise images.

C.5.1 Strain Gauge

The strain ratio for the first 500 cycles is 0.31 and after 57000 cycles is it 0.39, as shown in Figure C.42 and C.43, respectively. The initial strain ratio is too low compared to the SWP specified strain ratio and around 57000 cycles it is higher. The strain ratio is difficult to control, in which deviations between the obtained and the specified strain ratio are acceptable. The strain ratio at F_{max} for FT4 varies throughout the test, which is also the case for FT3.

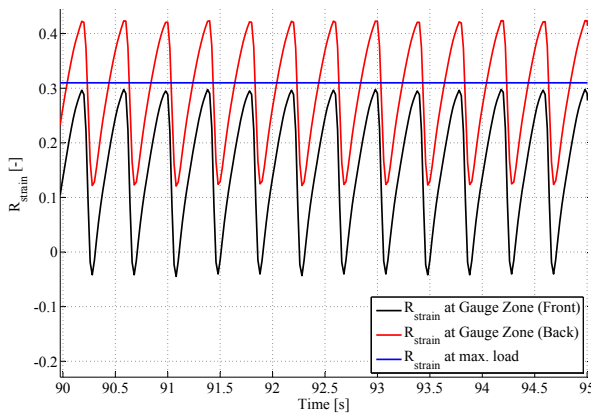


Figure C.42 The strain ratio after 500 cycles

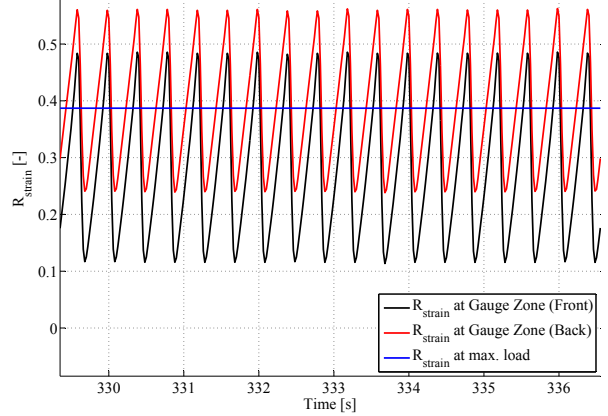


Figure C.43 The strain ratio after 57000 cycles

In Figure C.44 the loads for the primary and secondary actuators are shown, which correspond to the defined loads in FT4.

Initially the temperature is around 31° , as shown in Figure C.45, but after 250 [s] of FT4 the temperature suddenly increases and settles around 38° . The temperature jump is due to the thermocouple is held on the specimen with tape, which failed during FT4. After that, the thermocouple measured the temperature of the primary direction test rig, where heat from the hydraulic fluid is present. For the remaining parts of FT4 the temperature is maximum 31° , which also is shown for the other fatigue tests.

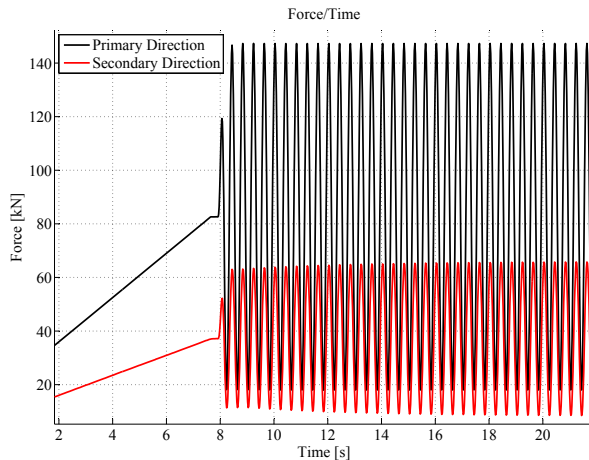


Figure C.44 The load magnitudes after 500 cycles for the primary and secondary direction

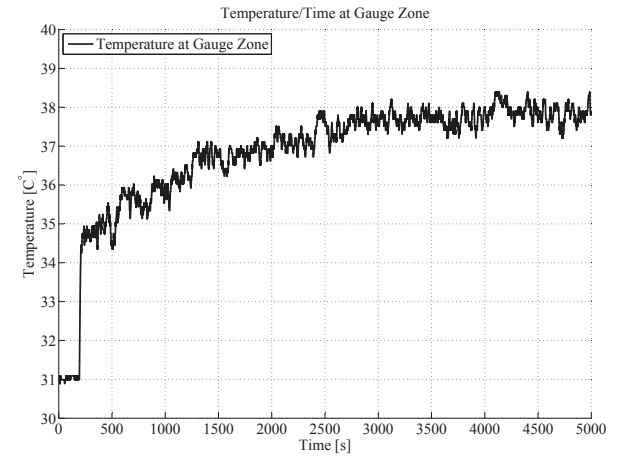


Figure C.45 The temperature during FT3 up to 57000 cycles

The strain for the primary arms is shown in Figure C.46 and C.47 for 500 cycles and 57000 cycles, respectively.

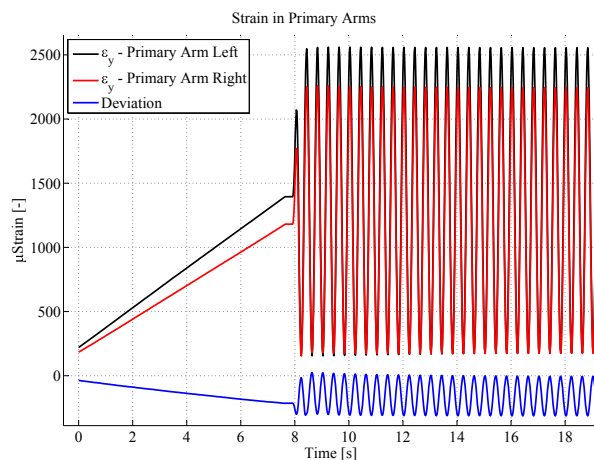


Figure C.46 Strain in the primary arms after 500 cycles

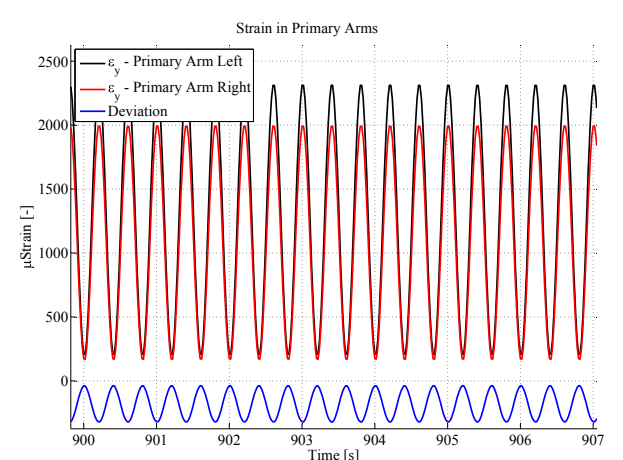


Figure C.47 Strain in the primary arms after 57000 cycles

The strain for the secondary arms is shown in Figure C.48 and C.49 for 500 cycles and 57000 cycles, respectively.

C. Test Results

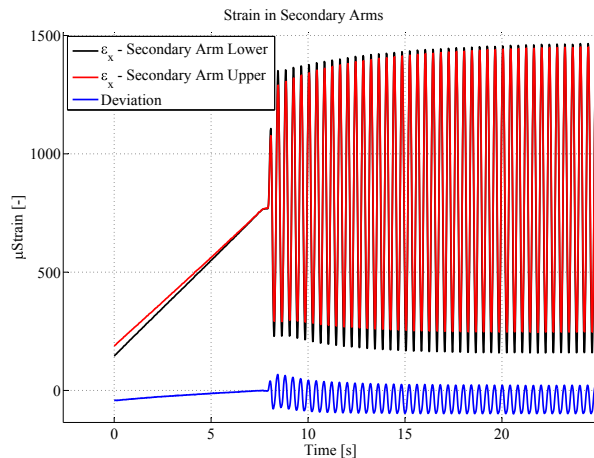


Figure C.48 Strain in the secondary arms after 500 cycles

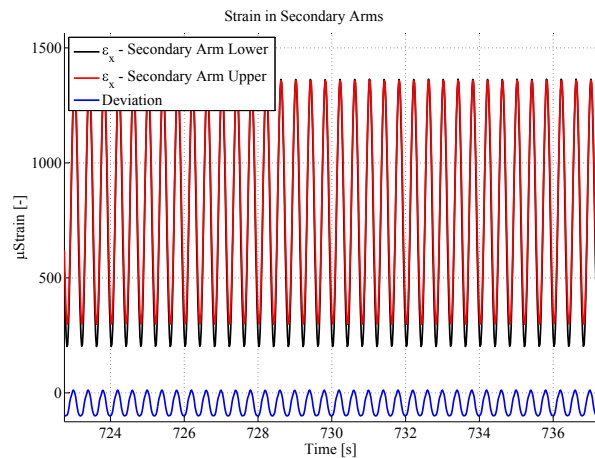


Figure C.49 Strain in the secondary arms after 57000 cycles

The differences in the above presented strains are converted into bending stress in Figure C.50 and C.51 for cycles up to 500 and 57000 cycles, respectively. The stress magnitudes for the primary and secondary direction are neglected again, since these magnitudes are minor compared to the stresses which correspond to the applied forces.

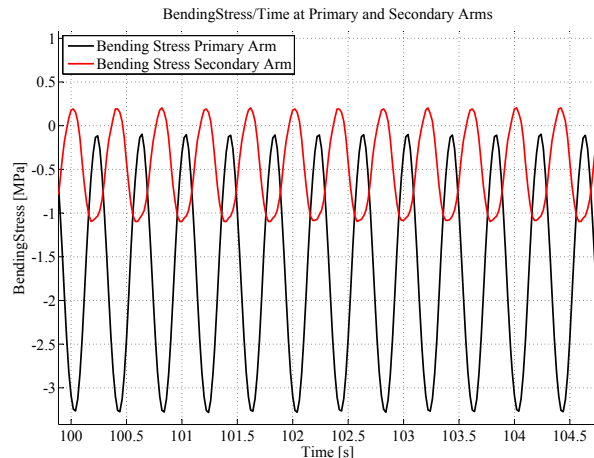


Figure C.50 Bending stress for 500 cycles

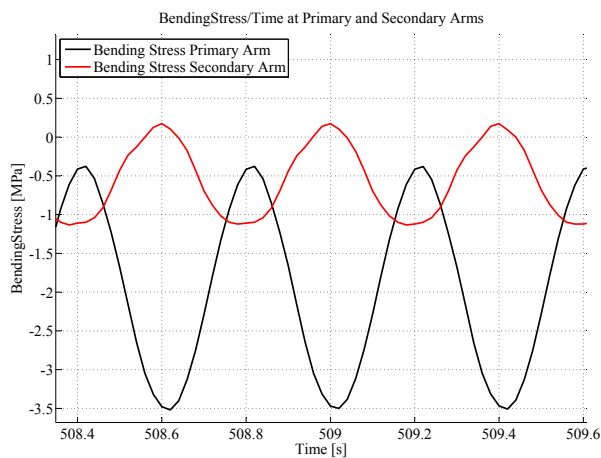
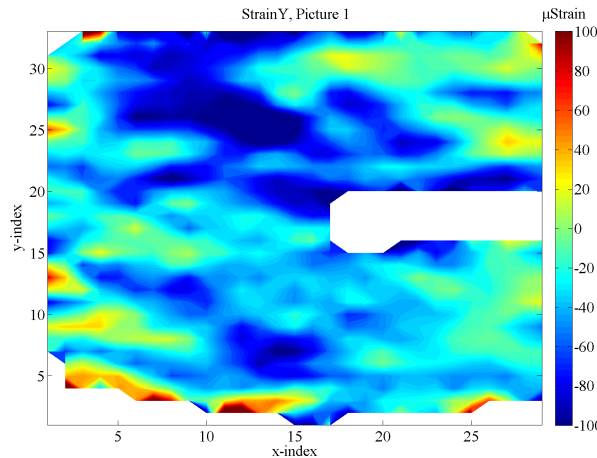
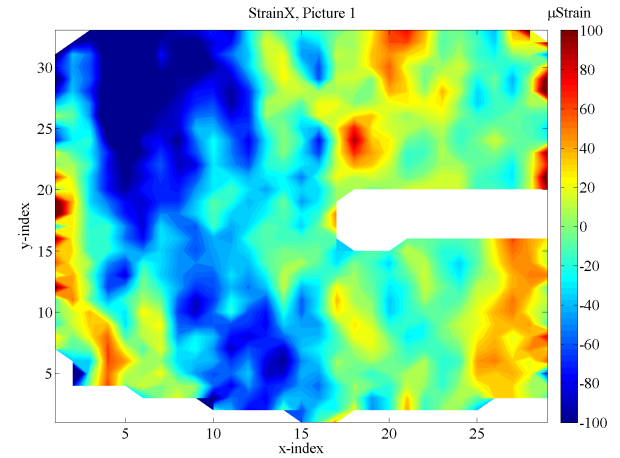


Figure C.51 Bending stress for 57000 cycles

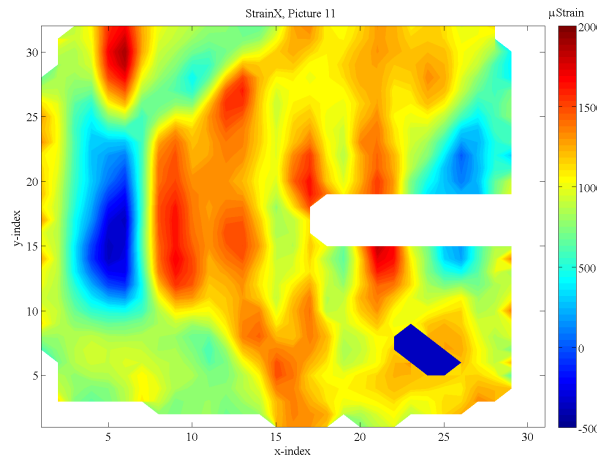
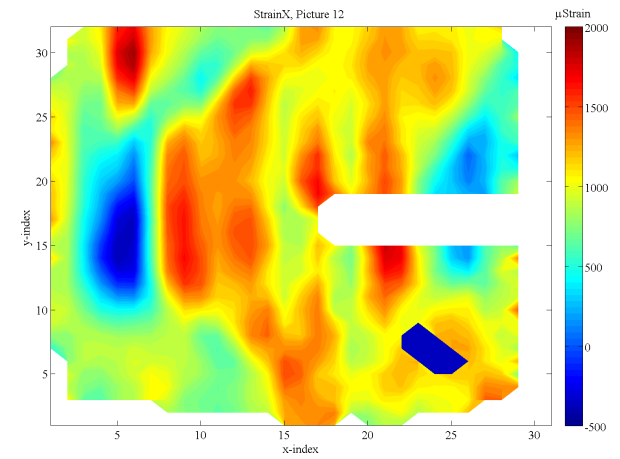
C.5.2 DIC

The DIC noise for primary and secondary direction is shown in Figure C.52 and C.53, respectively.

**Figure C.52** Primary directional DIC noise**Figure C.53** Secondary directional DIC noise

First failure cannot be seen in the DIC strain fields from before and after it occurs. Thus, these strain fields are not shown. In Figure C.54 and C.55 the DIC calculated strain fields before and after second failure are shown. Difference between the figures are difficult to see and it is only around index (5,24) noticeable differences occur. The second failure occurs in this area, but from the shown DIC images it can not be concluded that the difference is due to the second failure.

Figure C.54 and C.55 are plotted w.r.t the reference image from the start of the test. In Figure C.56 a strain field is shown, where the difference between Figure C.55 and Figure C.54 is shown. Here it is clear that a difference is present, which changes the strain field in the area around index (5,24) and it is assumed that it must be due to the second failure.

**Figure C.54** Strain field in secondary direction before second failure**Figure C.55** Strain field in secondary direction after second failure

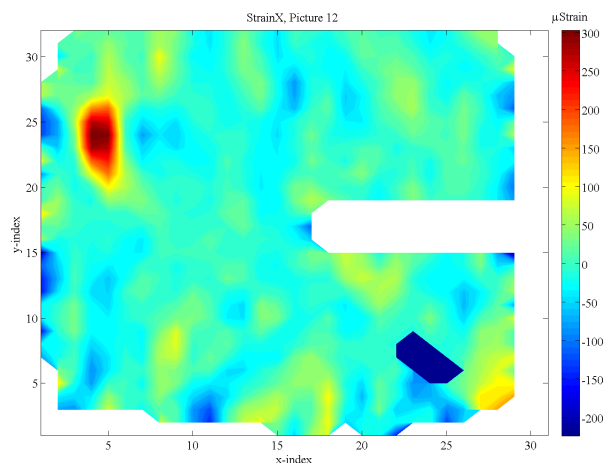


Figure C.56 Difference in strain fields in secondary direction before and after second failure

Experimental Log D

In this appendix problems with the test equipment are presented. The problems are described and a solution is presented. The content of the appendix is:

D.1	Asynchronous Load Configuration
D.2	Mounting Plates for Secondary Direction
D.3	Bolt Failure in Bushing
D.4	Arm Failure
D.5	Changing the Suspension System for the Secondary Actuator
D.6	Rod End Failure
D.7	DIC Data for the Secondary Directions
D.8	Strain Gauge Configuration

D.1 Asynchronous Load Configuration

During the first 100 cycles of FT1 an error is found in the programming. The error resulted in the actuators moved, as shown in Figure D.1, where the load peaks at F_{Max} are offset by a half period.

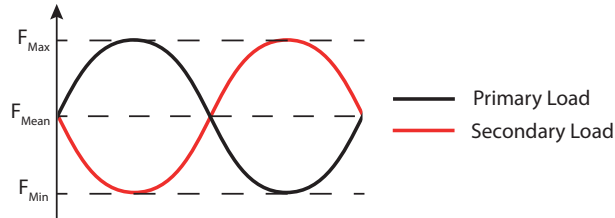


Figure D.1 Asynchronous load configuration

The reason for this error is a combination of the test rig construction and a wrong assumption. The test rig is constructed in a way where the primary actuator force is positive and the secondary actuator force is negative, when the specimen is loaded in tension in both directions. The assumption, which proved to be wrong, is about the moving of the actuators. It was believed that the numerically largest value was actuated first, i.e. F_{Max} was applied to the specimen in both directions simultaneously. But, the program actuated the absolute largest value for the primary and secondary actuator instead. Thus, F_{Max} for the primary and secondary directions are not applied simultaneously.

This error is solved by adding a phase angle of 180° in the program configuration for the secondary actuator. This phase angle is employed for the remaining fatigue tests.

D.2 Mounting Plates for Secondary Direction

A test is performed to get familiar and to get experience with the test rig and its controller. This test is not described in the report or appendix. During the test the existing mounting plates failed in the secondary directions. The existing mounting plates are shown in Figure D.2, where they are mounted on the specimen. The mounting plates are constrained by eight M6 screws, where four of them failed due to bolt cutting, as shown in Figure D.3.



Figure D.2 Existing mounting plates in test rig

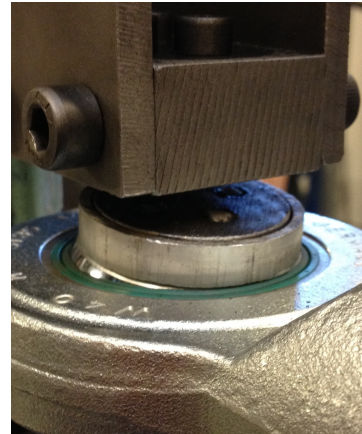


Figure D.3 Failed mounting plates

The mounting plates do not have the required strength, thus new bolts are not an option. A new set of mounting plates are designed for the secondary direction as shown in Figure D.4. The new designed mounting plates consist of two plates which are connected by four cylinders, eight screws and four bolts in the specimen. The drawings for these mounting plates can be found on the CD, see Appendix G.



Figure D.4 Designed mounting plates



Figure D.5 Failed screw

D.3 Bolt Failure in Bushing

In Figure D.4 the bushing is shown, when mounted in the test rig. It consists of two parts, which are constrained by a screw. During FT1 the screw failed (after approx. 41000 cycles) and the test was stopped, the screw was replaced by a new screw and the test was continued. Thus it is assumed that the failed bolt was not pre-tensioned correctly in the bushing. The failed screw is shown in Figure D.5.

After 149000 cycles in FT1 it is detected that both bushing screws failed, as shown in Figure D.6. Again the screws are replaced by new screws and FT1 is continued. A new procedure is employed regarding when the screws and bolts are fastened. The bushing screws are fastened before the remaining screws and bolts, to ensure a proper pre-tensioning.



Figure D.6 Failed bushing screws

D.4 Arm Failure

In the secondary direction the load is transferred from the actuator through two arms to the specimen, as shown in Figure D.7. One of these arms failed during FT1, due to a fatigue crack, as shown in Figure D.8. The crack is initiated near the fillet corner in the milled opening and the crack has propagated into the arm, until the test was stopped.

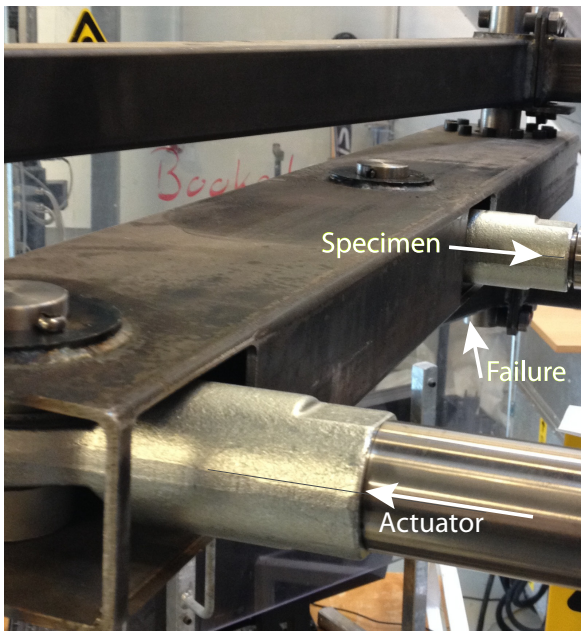


Figure D.7 Existing arm



Figure D.8 Failed arm

It is chosen to redesign the arm, as shown in Figure D.9, since it is of interest to increase the fatigue strength of the arm. So that a similar failure does not occur during the remaining fatigue tests. Furthermore, this yields that the intact arm is replaced as well. The redesigned arm consists of two plates, two spacers and a hingebox which are connected by 12 M12 bolts and 24 M8 screws, respectively.

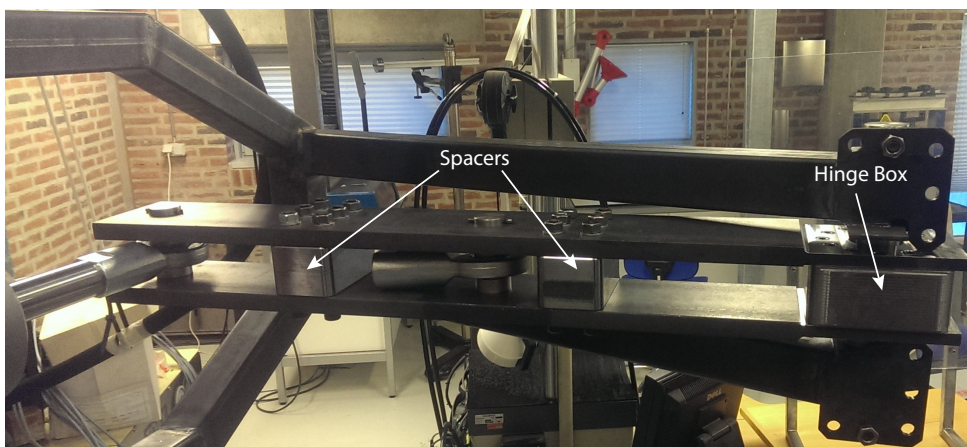


Figure D.9 The redesigned arm mounted in the secondary test rig

To ensure that the redesigned arm does not fail due to fatigue, an FE analysis is performed to determine the stress amplitude in the arm, in which a Goodmann life time estimation can be performed.

The FE analysis is performed in ANSYS Workbench, as shown in Figure D.10, where the Von Mises stress is plotted for the maximum load of 64 [kN]. The Von Mises stresses (382 [MPa]) are higher than the yield strength of 355 [MPa], which is due to stress concentrations and singularities on sharp edges, and at the load introductions and constraints, respectively. The singularities are neglected, since the sharp edges appear between the spacers/hinge box and the two plates. These are considered as one material in the FE analysis, but in reality they are different materials which are constrained by bolts and screws in which the load is transferred. Thus the maximum stress is located around the load transfer to the specimen and is $\sigma_{Max} = 155$ [MPa]. A similar FE analysis is performed to determine the minimum stress. Here, the applied load is 6.4 [kN], which yields $\sigma_{Min} = 15$ [MPa]. The loads for the two FE analyses are taken from FT1, and $R_{CL} = 0.1$ is employed.

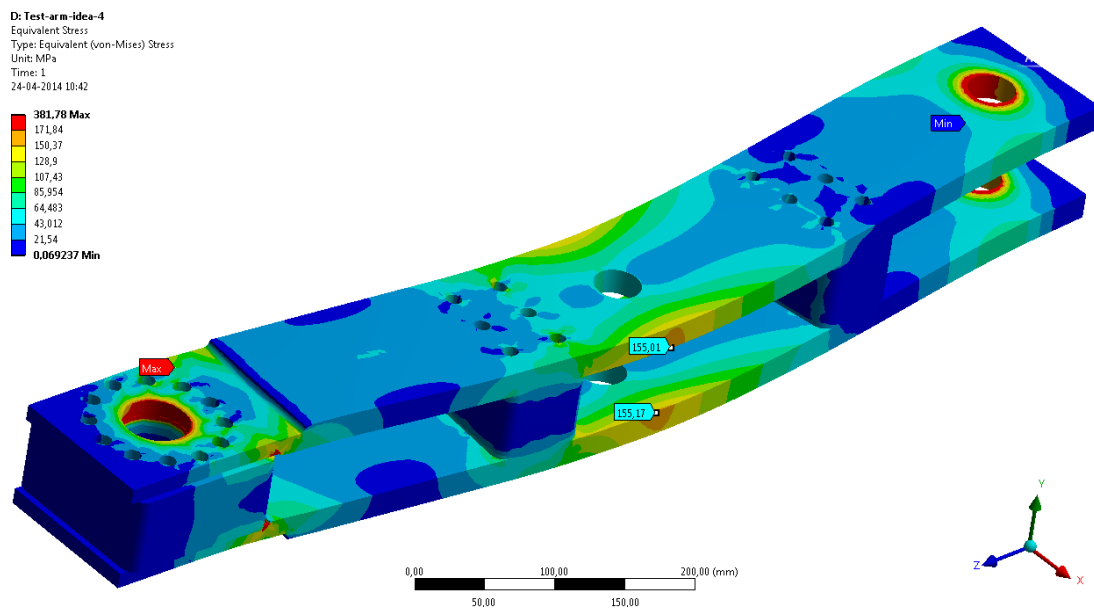


Figure D.10 Von Mises plot of the redesigned arm

Figure D.11 shows the created Goodman diagram for the redesigned arm and Equation (D.1) is employed to ensure that failure does not occur for the given load configuration for the arms. S_e is the endurance limit, where fatigue failure does not occur if a component is loaded below it, i.e. the number of cycles has no influence. Failure occurs when $SF_{Arm} = 1$, which is the case if the stress is multiplied by a factor of 1.22, thus the maximum stress allowed in the arm is approx. 190 [MPa]. These calculations are based on Norton [2006].

The ultimate strength of the material is used to determine the endurance limit (S_e) where 490 [MPa] is employed. This is a conservative value, since the material manufacturer informs that the ultimate strength is between 490-630 [MPa].

$$SF_{Arm} = \frac{\sigma_a}{S_e} + \frac{\sigma_m}{S_{ut}} = 0.82 \quad (\text{D.1})$$

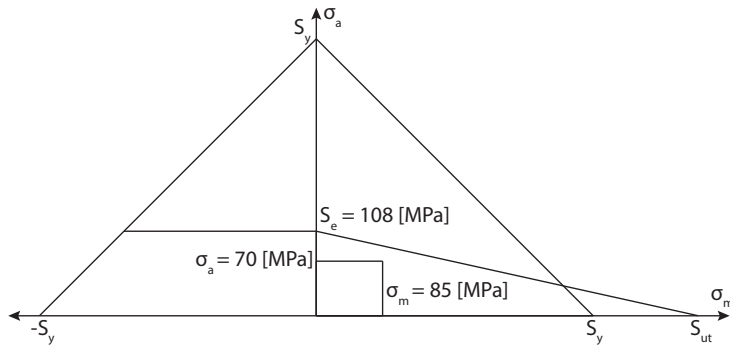


Figure D.11 Goodman diagram for the redesigned arm

The drawings for the redesigned arm can be found on the CD, see Appendix G.

D.5 Changing the Suspension System for the Secondary Actuator

The secondary actuator is installed in the test rig by a suspension system, as shown in Figure D.12, where one of the two supports is seen. When the redesigned arms are mounted in the test rig, it is detected that the secondary actuator is laying on the arms, i.e. the force from the actuator is not applied in the center of the arms as it should to ensure that no moments are applied to the arms. The suspension system is changed, in which the force from the actuator is applied in the center of the arms.

Furthermore, this changes the movement of the test rig during the fatigue test, in which the movement becomes more smooth.



Figure D.12 Suspension system for the secondary actuator

D.6 Rod End Failure

The secondary force is applied to the specimen through push/pull rods, where a rod end is used to connect the push/pull rod and the mounting plates as shown in Figure D.13. After approx. 380000 cycles in FT1, one of the rod ends failed, as shown in Figure D.14. The failed rod end

is replaced with an identical rod end. It is assessed that the rod end failed partly due to a manufacturing error or weak point, and partly due to fatigue part damage sustained during the tests of former Ph.D. student Steffen Laustsen.

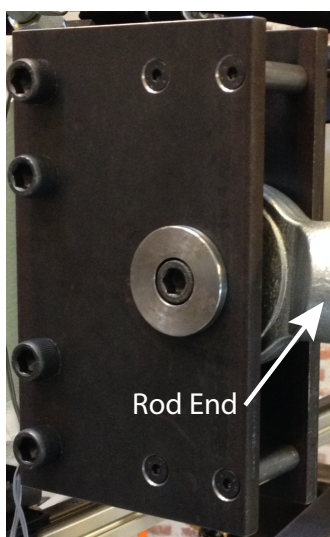


Figure D.13 Rod end in the test rig



Figure D.14 Failed rod end

In FT2 another rod end failed after approx. 60000 cycles, as shown in Figure D.15. Again, the failed part is replaced with an identical rod end.



Figure D.15 Second failed rod end

By studying the failure surfaces it is shown that it is a brittle fracture, since no fatigue striations are visible. This is in good agreement with cast iron which tends to be brittle and is the material used for the rod ends.

The above-mentioned assumption about a manufacturing error or a weak point in the rod ends is strengthened by the failure of the second rod end. Because the two failed rod ends failed at the same point and the failure surfaces are similar. However, the failure could also still be caused by part damage sustained in previous tests.

A possible solution could be to replace all the existing rod ends with stronger rod ends. However, these are larger as well compared to the already used rod ends. This yields a redesign of the components used in the test rig configuration. The arms designed in Appendix D.4 have to

be modified or bushings have to be designed, together with a redesign of the mounting plates for the specimen in the secondary direction, described in Appendix D.2. Furthermore, the rod connection between the mounting plates and the arm has to be redesigned.

This solution is very time consuming, which is a problem due to the limited project period, hence it is decided not to employ this solution.

Additional four rod ends have failed including three that were new from the previous failures. One of the rod ends used by Steffen Laustsen outlived one of the newly installed rod ends. This contradicts the assumption of part damage sustained during previous tests. Therefore, a more comprehensive assessment of the fatigue strength of the rod ends has been conducted.

The manufacturer of the rod ends is SKF and the specifications for the rod ends are shown in Table D.1.

Table D.1 Rod end specifications [SKF, 2014]

Dynamic load rating, C:	Static load rating, C_0
224 [kN]	134 [kN]

SKF prescribes the following calculation for estimation of the maximum permissible load for the rod ends:

$$p_{perm} = C_0 \cdot b_2 \cdot b_6 = 134 \text{ [kN]} \cdot 1 \cdot 0.5 = 67 \text{ [kN]} \quad (\text{D.2})$$

[SKF, 2014]

where:

p_{perm}	Maximum permissible load for rod end in the direction of the shank axis, [N]
C_0	Basic static load rating, [N]
b_2	Temperature factor depending on the sliding contact surface combination, [-]
b_6	Factor for the type of load, [-]

The temperature at which the rod end is operating is approx. 30 [°C] which means that according to SKF the constant b_2 is equal to 1 and because the load type is either alternating or pulsating, the constant b_6 is equal to 0.5 [SKF, 2014].

The permissible load for the rod ends is fairly below what has been expected and because the employed test loads are close to this value the lack of fatigue strength is more likely to be the reason why the rod ends fail during the tests.

D.7 DIC Data for the Secondary Directions

During the static pilot test the DIC equipment took images of the specimen. When the DIC data was post processed, problems with the strain in the secondary direction was identified. In Figure D.16 a plot of the strain in the primary direction is shown and for the secondary direction in Figure D.17. The strain in the primary direction is plausible compared to the strain gauge measurements and the FE shell model result. In the secondary direction the strain is erroneous, since negative (compression) strains are obtained in the gauge zone. The load configuration is tension-tension (primary-secondary), thus negative strains make no physical sense.

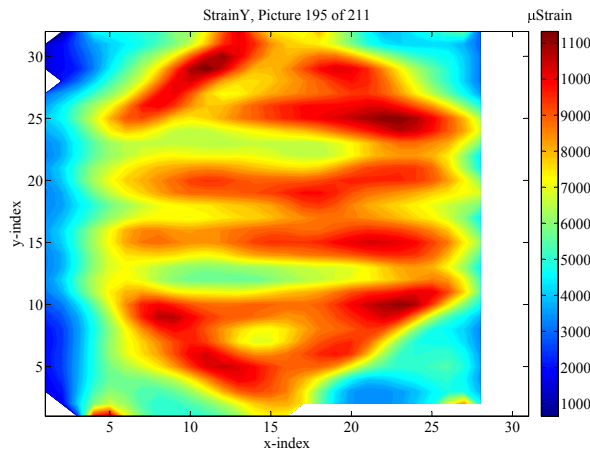


Figure D.16 Contour plot of DIC strain in primary direction in gauge zone

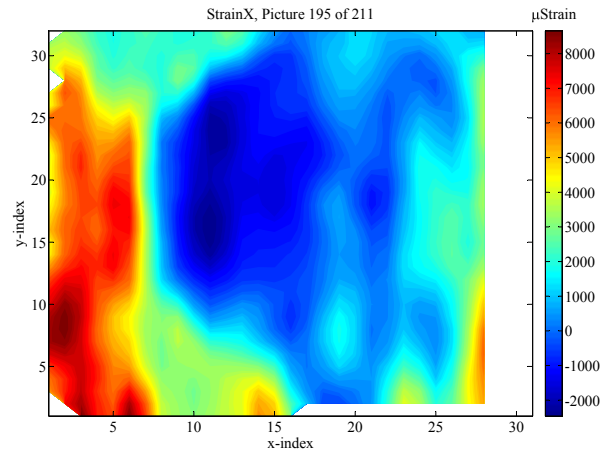


Figure D.17 Contour plot of DIC strain in secondary direction in gauge zone

To ensure that the DIC can measure strain in the secondary direction a simple test is performed. A 2 [mm] aluminum plate is mounted in the test rig and the DIC equipment is calibrated carefully. For this test the aperture configuration is different compared to previous calibrations, by decreasing the aperture size, the depth of field is increased. The procedure for the test can be seen in Table D.2, where it is shown in which directions loads are applied. The focus is not to measure the precise strains in every facet, but to study the measured strain field.

Table D.2 DIC test procedure

	Load in test sequence:		
Direction	I	II	III
Primary	Yes	No	Yes
Secondary	No	Yes	Yes

The purpose of test sequence I is to clarify whether or not the DIC can measure strain in the secondary directions. This strain is caused by the Poisson's ratio, since the aluminum plate is only loaded in the primary directions. Thus an isotropic plate is of interest in this study and explains why the aluminium plate is selected. In Figure D.18 and D.19 the results are shown for the strain in the primary and secondary direction, respectively. The images show that the DIC can measure positive strain in the primary direction and negative strain in the secondary direction. The negative strain is approx. 1/3 of the positive strain, which agrees with the Poisson's ratio of 0.3.

D. Experimental Log

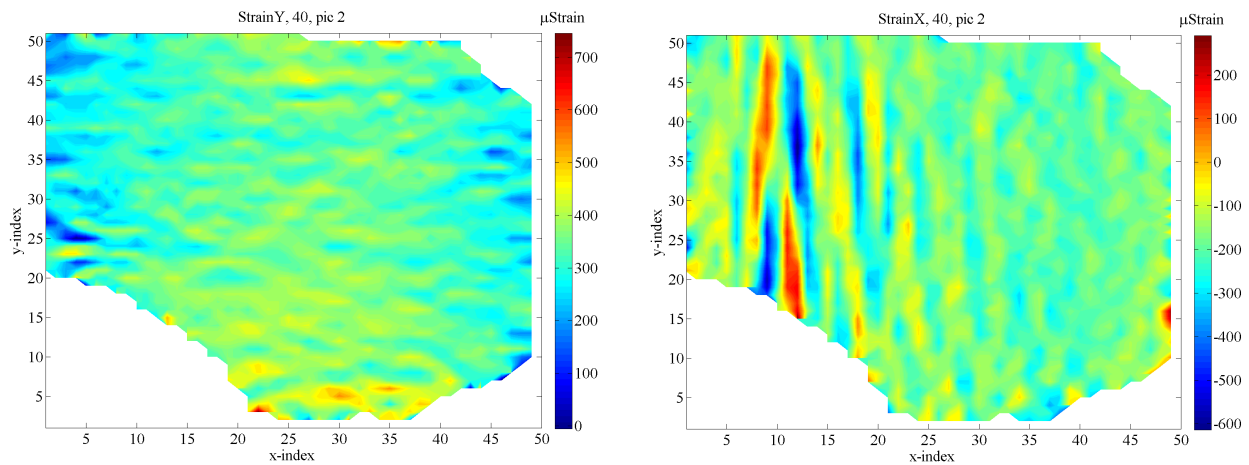


Figure D.18 Strain in the primary direction for test sequence I

Figure D.19 Strain in the secondary direction for test sequence I

Test sequence II is performed to clarify whether or not the DIC equipment can measure strain when loaded only in the secondary direction. Thus, strain in the primary direction must be due to the Poisson's effect. The measured strain is shown in Figure D.20 and D.21 for the primary and secondary direction, respectively. The measured strains are negative and positive for the primary and secondary direction, respectively, which agrees with the load configuration.

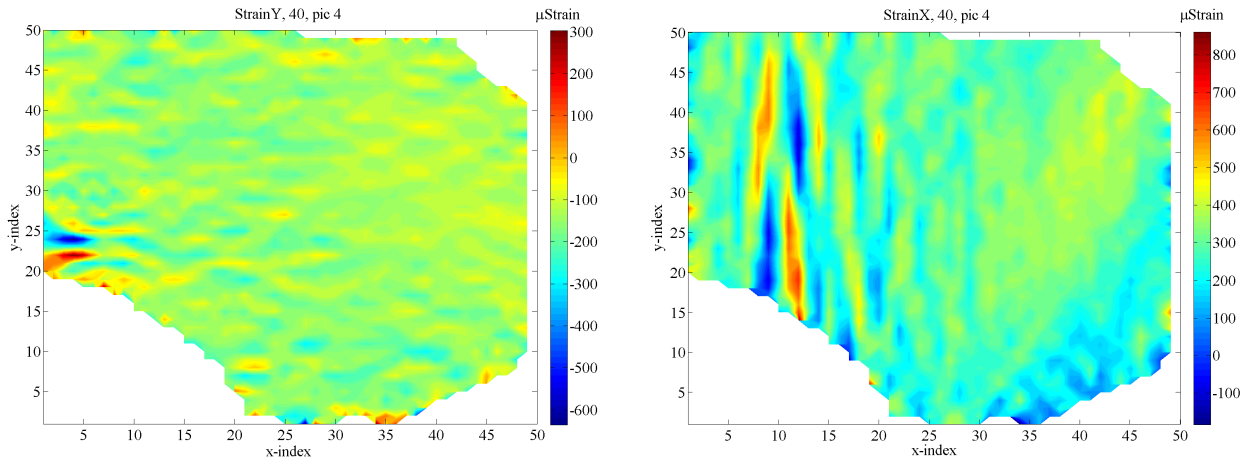


Figure D.20 Strain in the primary direction for test sequence II

Figure D.21 Strain in the secondary direction for test sequence II

Test sequence III is performed to clarify whether or not the DIC equipment can measure strain, when the specimen is loaded in both directions. The measured strain is shown in Figure D.22 and D.23 for the primary and secondary direction, respectively. Positive strain is measured for both directions as expected.

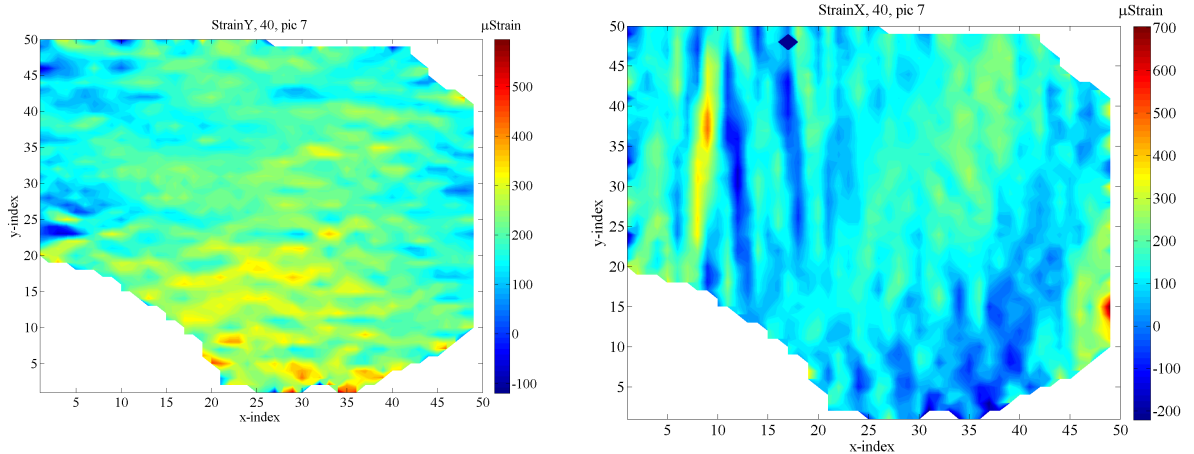


Figure D.22 Strain in the primary direction for test sequence III

Figure D.23 Strain in the secondary direction for test sequence III

From this study, the procedure for setting up the DIC and the post-processing is validated, thus DIC is employed for the remaining tests. The changed aperture configuration is kept, i.e. the aperture configuration for the aluminum test is employed for the remaining tests. Furthermore, a strain gauge rosette is employed on the front, together with the DIC pattern, i.e. rosette gauges are glued on both sides of the specimen during tests.

D.8 Strain Gauge Configuration

The strain gauge measurements are monitored and stored by the computer software Catman Easy. During the static pilot test the software stopped the recording of the strain in the rosette strain gauge in the primary direction. In the data file it can be seen that the software records the strain until it reaches approx. 7800 [μ strain] and then a value of -100000 is written instead of the strain gauge measurement. This is due to a default configuration of the strain gauge in the software, where a measurement limit of 4000 [μ strain] is employed. This means, that it maximum can measure 7000-8000 [μ strain]. To prevent this, the strain gauge measurement limit is set to 40000 [μ strain] for the remaining tests.

Specifications for Measurement Equipment E

The specifications for the measurement equipment used in this project are presented in this appendix. The content of the appendix is:

E.1	Test Rig
E.2	Video Camera
E.3	Strain Gauge
E.4	DIC
E.5	Thermal Camera
E.6	Thermocouple

E.1 Test Rig

The tests are conducted in the test rig shown in Figure E.1, which is located at Fibigerstræde 14 room 13, Aalborg University.

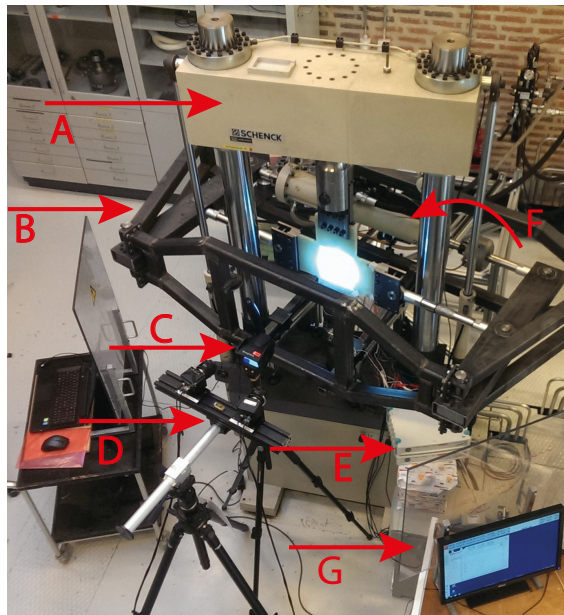


Figure E.1 The test rig used for testing

The primary load frame and actuator is a uni-axial servo-hydraulic 400 [kN] (Instron Hydropuls® PL 400) testing machine (A) which has been extended with an additional secondary 63 [kN] horizontal actuator (Instron Hydropuls® PL 63) and associated loading frame (B). [Laustsen, 2014]

To monitor heat during fatigue tests a thermal camera (C) is used. For the monitoring of strains both (D) Digital Image Correlation (DIC) and strain gauges (E) are used. (E) indicates the control box which is the connection between the strain gauges on the specimen and the computer, where the data is stored. Furthermore a regular white light camera (F) is mounted on the back of the test rig. The test rig is controlled by the actuator controller (G), where programming for the movement of the test rig is performed.

E.2 Video Camera

A white light video camera has been used during the tests to observe failure. The video camera is a Sony HDR-SR10E High Definition 4 Megapixel video camera, as shown in Figure E.2. It is able to record 40GB data, corresponding to approx. 15 hours of video. The specifications for the video camera are shown in Table E.1.



Figure E.2 The used video camera [Sony, 2014]

Table E.1 Specification for the used camera [Sony, 2014]

HD Recording Format	AVCHD (1920 / 1440 x 1080i)
Media Storage Type	40GB Hard Disk Drive
HD Video Codec	MPEG-4 AVC / H.264

E.3 Strain Gauge

Three different types of strain gauges have been used during this project. A single 3 [mm] strain gauge, a 3 [mm] strain gauge rosette and a 10 [mm] strain gauge rosette are the three used types, where the specifications are presented in Figure E.3, E.4 and E.5, respectively.

TYPE FLA-3-11-1L	
LOT NO.	A515511
GAUGE LENGTH	3 mm
GAUGE FACTOR	2.10 ±1 %
GAUGE RESISTANCE	119.8±0.5 Ω
TEMP. COMPENSATION FOR	11 ×10 ⁻⁶ /°C
TRANSVERSE SENSITIVITY	0.1 %
LEAD WIRES	10/0.12 1m

Figure E.3 Specifications for single strain gauge

TYPE FRA-3-11-3L	
LOT NO.	A601531
GAUGE LENGTH	3 mm
GAUGE FACTOR	1=2.12 2=2.12 3=2.12 ±1 %
GAUGE RESISTANCE	119.9±0.5 Ω
TEMP. COMPENSATION FOR	11 ×10 ⁻⁶ /°C
TRANSVERSE SENSITIVITY	0.1 %
LEAD WIRES	7/0.12 3m

Figure E.4 Specifications for 3 [mm] rosette

TYPE FRA-10-11		TEST CONDITION 23°C 50%RH
LOT NO.	A51583A	BATCH NO. LJ30K
GAUGE LENGTH	10 mm	GAUGE FACTOR 1=2.10 2=2.10 3=2.10 ±1 %
GAUGE RESISTANCE	120±0.5 Ω	TEMP. COMPENSATION FOR 11 ×10 ⁻⁶ /°C
QUANTITY	10	TRANSVERSE SENSITIVITY -0.6 %

Figure E.5 Specifications for 10 [mm] rosette

Two different sizes of strain gauge rosettes are used, because the 3 [mm] ones are available at Aalborg University from the start of the project period. The 10 [mm] strain gauge rosettes are delivered from SWP later in the project period in an attempt to yield better strain gauge measurements. Bigger gauges are able to mean over a larger area and thereby reduce the influence from the surface irregularities, described in Appendix A.3.

A parallel setup of multiple HBM Spider 8-30 data acquisition modules are used to connect the strain gauges to the computer software CatmanEasy.

The HBM Spider 8-30 data acquisition module has three different internal resistances (dummy gauges), meaning that it is possible to use these together with the strain gauges in what corresponds to a quarter bridge setup. In order to do so the strain gauge wires need to be connected into a 15-pin socket, which is set up as shown in Figure E.6.

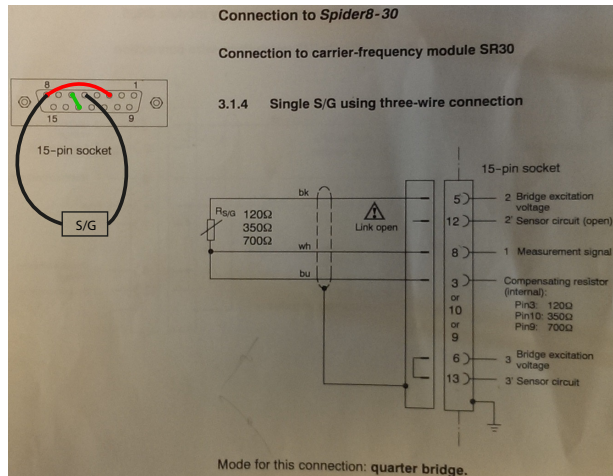


Figure E.6 Setup of strain gauge connection to 15-pin socket

The PC software used together with the strain gauges and the data acquisition modules is CatmanEasy v3.3.5. Thereby, strains can be monitored during tests and saved afterwards. Initially, the strain gauges are calibrated in CatmanEasy, in which a shunt calibration is performed, i.e. to set the point of origin before measurements start.

E.3.1 Strain Gauge Uncertainties

The biggest uncertainty w.r.t. strain gauge measurements is the uncertainty of the gauge factor as stated by the manufacturer. This uncertainty is so big that the uncertainty of the measured strains can be set equal to the uncertainty of the k-factor. To calculate the uncertainties, the following quote is used: *"It is known to be good practice, to calculate the uncertainty, i.e. the empirical spread, as half the tolerance."* [Mouritsen, 2010]

Therefore the uncertainty of the gauge factor, hence the strain, is calculated by taking half the uncertainty and dividing it with the actual gauge factor. This is shown in Equation (E.1), (E.2) and (E.3), where the gauge factor uncertainties are calculated for the single 3 [mm], the rosette 3 [mm] and the rosette 10 [mm] strain gauges, respectively.

$$\frac{s(k_{single})}{k_{single}} = \frac{0.5 \cdot 2 [\%]}{2.10} = 0.476 [\%] \quad (\text{E.1})$$

$$\frac{s(k_{rosette,3mm})}{k_{rosette,3mm}} = \frac{0.5 \cdot 2 [\%]}{2.12} = 0.472 [\%] \quad (\text{E.2})$$

$$\frac{s(k_{rosette,10mm})}{k_{rosette,10mm}} = \frac{0.5 \cdot 2 [\%]}{2.10} = 0.476 [\%] \quad (\text{E.3})$$

where:

s	Uncertainty, [%]
k_{single}	Gauge factor for single gauges, [-]
$k_{rosette,3mm}$	Gauge factor for strain gauge rosette 3mm, [-]
$k_{rosette,10mm}$	Gauge factor for strain gauge rosette 10mm, [-]

As an example a strain measure is, $\varepsilon = 1000 \text{ } [\mu\text{Strain}]$, and as the uncertainty of the gauge factor is so big compared to the uncertainty of the measured strain, the uncertainty of the measured

strain is set equal to the uncertainty of the gauge factor, as shown in Equation (E.4).

$$\frac{s(\varepsilon)}{\varepsilon} = \frac{s(k_{single})}{k_{single}} = 0.476 [\%] \quad (\text{E.4})$$

The actual uncertainty of measured strain is determined in Equation (E.5).

$$s(\varepsilon) = \varepsilon \cdot 0.476 [\%] = 1000 [\mu\text{Strain}] \cdot \frac{0.476}{100} = 4.76 [\mu\text{Strain}] \quad (\text{E.5})$$

The uncertainties are not included in the results presented in this project, but only stated here to give an estimation of the uncertainties.

E.4 DIC

DIC is used during the tests in this project. A 3D measurement setup is used during the tests, meaning two cameras are used to compute out-of-plane deformations as well as in-plane deformations. Alternatively one camera can be used, where no calibration is needed, but only in-plane displacements can be monitored, which is not sufficient for this project. The out-of-plane deformations are used internal in the DIC software, to calculate deformations in the primary and secondary direction. The specifications for the DIC equipment is shown in Table E.2.

Table E.2 Specifications for the DIC equipment [GOM mbH, 2012] [Andrew Hamilton, 2011]

DIC system	ARAMIS 4M
PC version	ARAMIS v6.2.0-6
Cameras	4 megapixel, f2.8/50 [mm] Lenses
Camera resolution	2048x2048 pixels
Calibration object	GOM / CP 20 / MV 175x140 [mm ²]
Strain accuracy	up to 0.01 [%]

The camera lens and the calibration object is shown in Figure E.7 and E.8.



Figure E.7 DIC camera lense

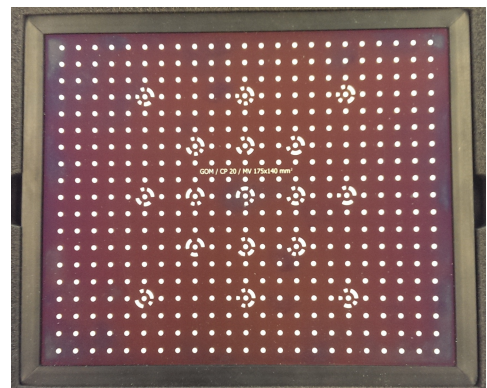


Figure E.8 DIC calibration object

The DIC system is calibrated with the calibration object shown in Figure E.8. The calibration object is held by hand in different positions and angles corresponding to the instructions shown

in the PC software. The calibration deviation is supposed to be between 0.01 and 0.04 pixels [GOM mbH, 2007]. Due to the calibration object is held by hand it is difficult to perform two identical calibrations, but as long as the calibration deviation is within the stated tolerance, reasonable results are to be expected.

To ensure that the DIC software identifies the facets between the different images, a pattern on the specimen surface is required. The pattern is created with white spray painting as a base where black paint is sprayed on top, as shown in Figure E.9. If the software can not recognize the sprayed pattern within a facet from image to image no strain is calculated for this facet.



Figure E.9 DIC pattern

Lights are used to make the pattern clear, in which the DIC software can identify the entire field of interest. Light reflection can occur, which reduce the ability to identify the pattern. This can be solved by reducing the light intensity, which also can reduces the ability to identify the pattern. Thus it is a compromise between enough light, where reflections do not occur.

Before every test is initiated, two images are taken with the DIC to get an estimation of the error/noise of the results. In order to determine the facet size, three different facet sizes are utilized and then the strain is extracted at one point in the gauge zone. These results are shown in Figure E.10, E.11 and E.12, for a facet size of 40x40 pixels, 60x60 pixels and 80x80 pixels, respectively.

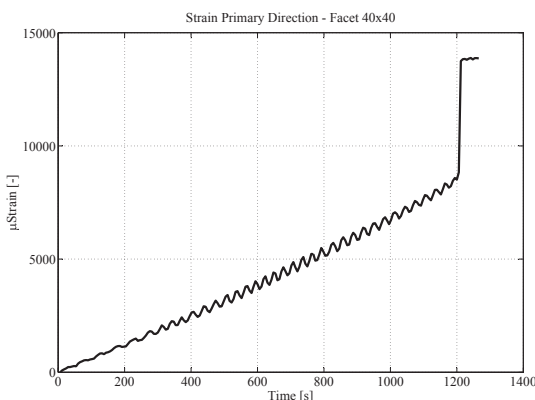


Figure E.10 DIC facet size 40x40 pixels

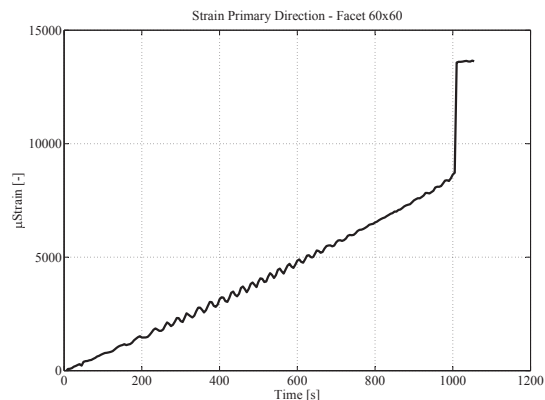


Figure E.11 DIC facet size 60x60 pixels

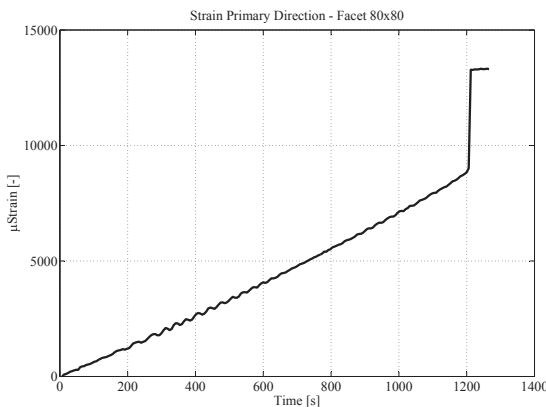


Figure E.12 DIC facet size 80x80 pixels

A small facet size compared to a larger facet size yields a solution where local effects are included, such as stress concentrations etc., but at the expense of accuracy. It means that the DIC attempts to match a subset of few pixels compared to a subset of many pixels, which increases the precision, but at the expense of reduced spatial resolution.

The above is shown in Figure E.10, where the facet size is the smallest amongst those presented, a more varying result is present compared to the result with the largest facet size in Figure E.12, where a more smoothed result is present. As a compromise between having a high precision and a high spatial resolution, the facet size of 60x60 pixels has been chosen in the results presented in this project.

E.5 Thermal Camera

The thermal camera used during FT1 is a Testo 875 - Thermal Imaging Camera as shown in Figure E.13.



Figure E.13 Testo 875 - Thermal Imaging Camera [Testo, 2014]

The specifications for the thermal camera are shown in Table E.3.

Table E.3 Specifications for Testo 875 - Thermal Imaging Camera [Testo, 2014]

Field of vision/min. focusing distance	Standard lens: $32^\circ \times 23^\circ / 0.1$ [m]
Detector type	FPA 160x120 pixels
Temperature range	0 - 280 [$^\circ$ C]
Accuracy	± 2 [$^\circ$ C]
Measuring point minimum diameter	Standard lens: 10 [mm] at 1 [m]
Measuring functions	Standard measurement (1-point), Cold-/Hotspot
Setting emissivity	0.01 - 1.00 (0.9 for plastic and/or glass is used)

E.6 Thermocouple

A K-type thermocouple has been used during the tests. The thermocouple is attached to the surface of the specimen with tape in order to trace the temperature and thereby verify if this has any effect on the obtained results. In order to obtain the data from the thermocouple it is plugged into the HBM Spider 8-30 data acquisition module as the strain gauges, with the difference that a DC terminal is used instead of a strain gauge terminal.

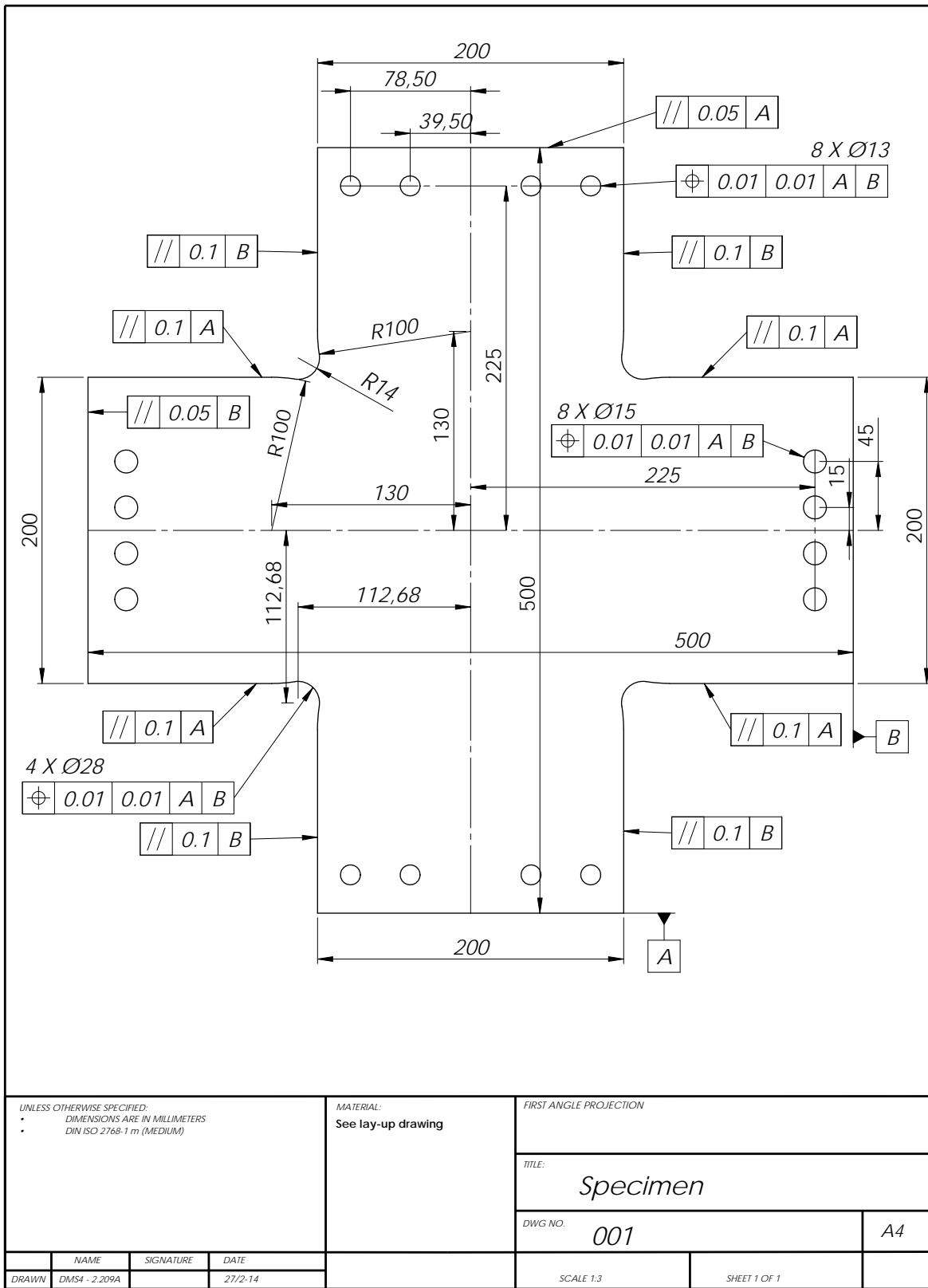
Working Drawings F

In this appendix the working drawings are presented. The content of the appendix is:

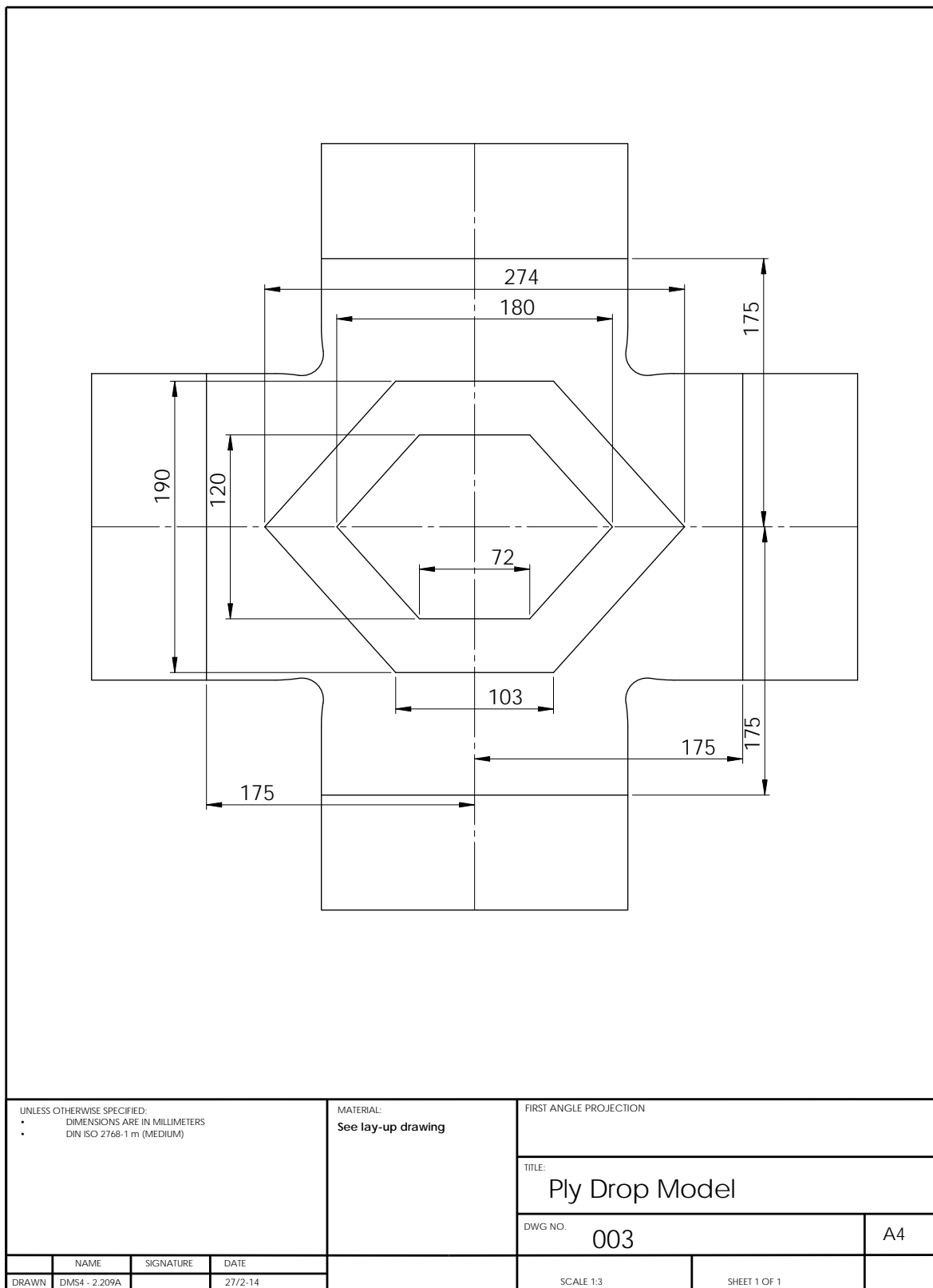
F.1	Specimen Geometry
F.2	Specimen Ply Drop Boundaries
F.3	Ply Drop Specifications

- * The scales specified on the working drawings cannot be used, since the working drawings in this appendix are scaled. Working drawing with the correct scales can be found on the CD, as presented in Appendix G.

F.1 Specimen Geometry

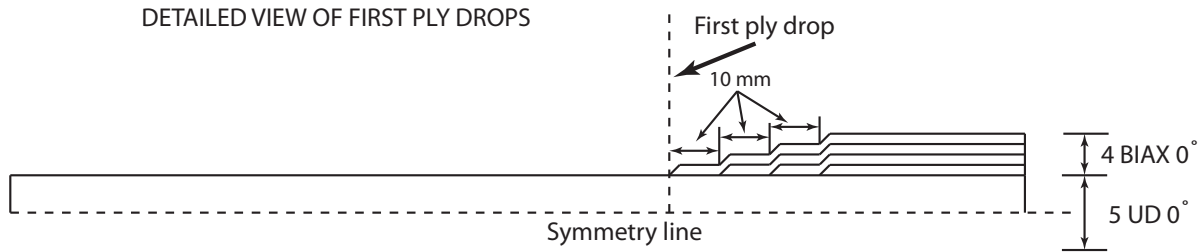


F.2 Specimen Ply Drop Boundaries

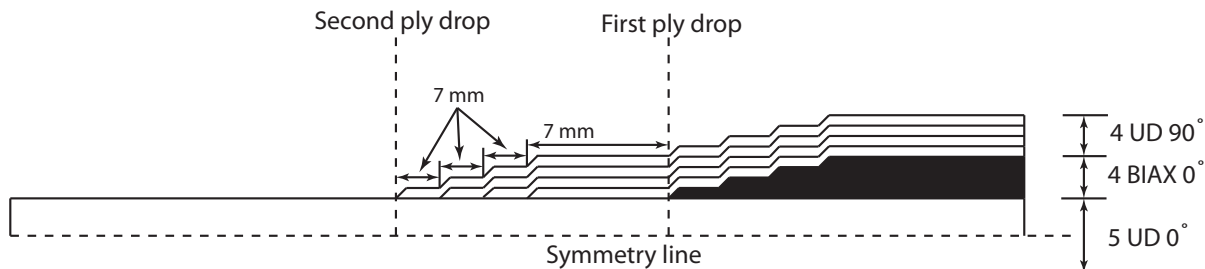


F.3 Ply Drop Specifications

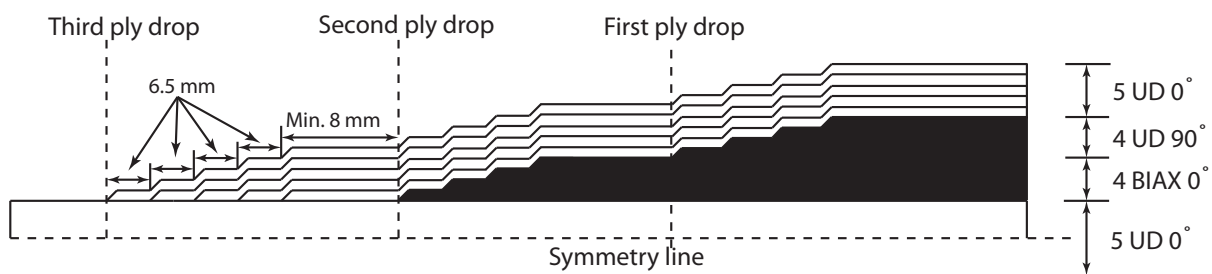
DETAILED VIEW OF FIRST PLY DROPS



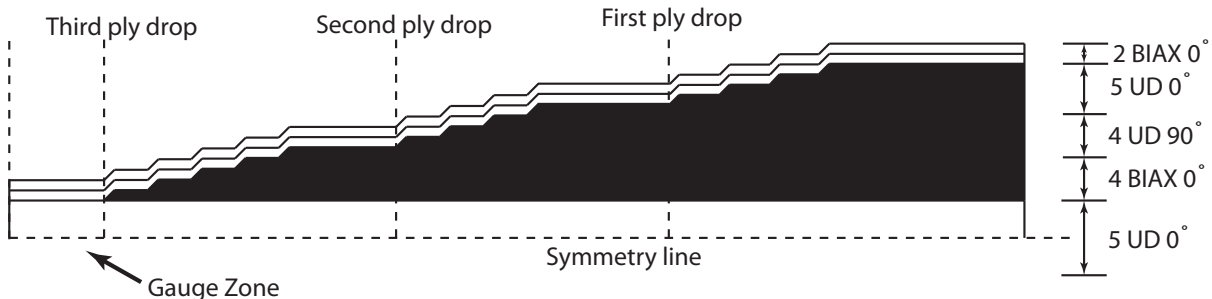
DETAILED VIEW OF SECOND PLY DROPS



DETAILED VIEW OF THIRD PLY DROPS



DETAILED VIEW OF OUTER BIAX



The content of the CD is described in this appendix, and it is divided as shown below:

- **Report.pdf:** Digital version of the report
- FADAS algorithm
 - **ReadMe.txt:** Text file containing brief instructions on how to get the material routine to work
 - **usermat.f:** The FORTRAN code of the FADAS algorithm
 - **usermatLib.dll:** The dll-file containing the user material routine
- FE models
 - **FE-MODEL_SHELL.mac:** Macro file for the shell model
 - **FE-MODEL-Solid.mac:** Macro file for the solid model
 - **MatStrengthStiffnessGFRP_SHELL.mac:** Material properties used for the shell model
 - **MatStrengthStiffnessGFRP_SHELL.mac:** Material properties used for the solid model
- Working drawings
 - Specimen and Lay-up
 - * **Lay-Up Mold.pdf:** Working drawings for the cutouts in the gauge zone
 - * **Lay-up Specifications.pdf:** Detailed view of the ply drops
 - * **Specimen.pdf:** Working drawing of the test specimen
 - * **Specimen-Lay-up Boundaries.pdf:** Dimensions of the ply drops
 - Test Rig Equipment
 - * Arm
 - **Arm.pdf:** Working drawing of the designed arm
 - **Assembly.pdf:** Drawing describing how to assemble the arms
 - **Spacer.pdf:** Working drawing of the spacer
 - * Mounting Plates
 - **Afstandsrør.pdf:** Working drawing of the pipe spacers for the mounting plates
 - **Beslag.pdf:** Working drawing of the mounting plates